Tesi di Dottorato di CHIARA SAGGESE
Matricola 785658

POLITECNICO DI MILANO

**DIPARTIMENTO
DI
CHIMICA,
MATERIALI
E
INGEGNERIA CHIMICA
"Giulio Natta"**

Detailed Kinetic Modeling of Soot Formation in Combustion Processes

**Dottorato di Ricerca in
Chimica Industriale e
Ingegneria Chimica (CII)**

XXVII ciclo
2012 - 2014

Coordinatore: prof. Tiziano Faravelli
Tutore: prof. Luca Lietti
Relatore: prof. Tiziano Faravelli

to my beloved family and friends

Acknowledgements

First, I would like to thank Professors Tiziano Faravelli and Eliseo Ranzi for their support and guidance in my research. I thank Professors Alessio Frassoldati and Alberto Cuoci for the constant support and advice during my PhD. I also warmly thank Professors Katharina Kohse-Höinghaus and Andrea D'Anna, members of my reading committee, for their critical and interesting comments.

I am also grateful to Professor Hai Wang to have given to me the opportunity to pursue and complete some aspects of my research in his laboratory and for his guidance and the inspiring discussions. It was a pleasure to work with Dr. Sanchez and Dr. Camacho and I thank them for the very interesting discussions.

Thanks to all my colleagues of Politecnico di Milano and Stanford University, with whom I spent these years in an pleasant and unforgettable way. Thanks to Mattia Bissoli, Alessandro Stagni and Stefano Langè for sharing all these years together and encourage each other. Thanks also to Matteo Pelucchi, Giancarlo Gentile, Sara Ferrario, Stefania Moioli, Giorgia De Guido, Davide Papasidero and Gabriele Lodi. Special gratefulness to my beloved italian friends and Nicolas, whose friendship and love overcame distances.

Finally, special thanks to my family, that encouraged me to follow this path since the beginning and supported me in every single moment of these years.

List of Publications

Camacho, J.; Liu C.; Gu, C.; Lin, H.; Huang, Z.; Tang, Q.; You, X.; **Saggese, C.**; Li, Y.; Jung, H.; Deng, L.; Wlokas, I.; Wang, H., Mobility Size and Mass of Nascent Soot Particles in a Benchmark, Premixed Ethylene Flame, submitted to *Combustion and Flame* (2015).

Salenbauch, S., Cuoci, A., Frassoldati, A., **Saggese**, C., Faravelli, T., Hasse, C., Modeling Soot Formation in Premixed Flames using an Extended Conditional Quadrature Method of Moments, *Combustion and Flame* (2015), accepted.

Saggese, **C.**, Sánchez, N. E., Frassoldati, A., Cuoci, A., Faravelli, T., Alzueta, M. U., Ranzi, E., Kinetic modeling study of polycyclic aromatic hydrocarbons and soot formation in acetylene pyrolysis, *Energy Fuels* **28**(2) (2014) pp. 1489-1501.

Stagni, A., **Saggese, C.**, Bissoli, M., Cuoci, A., Frassoldati, A., Faravelli, T., Ranzi, E., Reduced kinetic model of biodiesel fuel combustion, *Chemical Engineering Transactions* **37** (2014) pp. 877-882.

Pelucchi, M., Somers, K. P., Burke, U., **Saggese**, **C.**, Frassoldati, A., Ranzi, E., Curran, H. J., Faravelli, T., Kinetic modelling of biofuels: pyrolysis and auto-ignition of aldehydes, *Chemical Engineering Transactions* **37** (2014) 871-876.

Saggese, **C.**, Frassoldati, A., Cuoci, A., Faravelli, T., Ranzi, E., A wide range kinetic modeling study of pyrolysis and oxidation of benzene, *Combustion and Flame* **160** (7) (2013) pp. 1168-1190.

Saggese, **C.**, Frassoldati, A., Cuoci, A., Faravelli, T., Ranzi, E., A lumped approach to the kinetic modeling of pyrolysis and combustion of biodiesel fuels, *Proceedings of the Combustion Institute* **34**(1) (2013) pp. 427-434.

Lepore, E., Giorcelli, M., **Saggese**, **C.**, Tagliaferro, A., Pugno, N., Mimicking water striders' legs superhydrophobicity and buoyancy with cabbage leaves and nanotube carpets, *Journal of Materials Research* **28**(7) (2013) pp. 976-983.

Grana, R., Frassoldati, A., **Saggese**, **C.**, Faravelli, T., Ranzi, E., A wide range kinetic modeling study of pyrolysis and oxidation of methyl butanoate and methyl decanoate. Note II: Lumped kinetic model of decomposition and combustion of methyl esters up to methyl decanoate, *Combustion and Flame* **159** (2012) pp. 2280-2294.

Congresses and Symposia

B. Franzelli, A. Cuoci, A. Stagni, **C. Saggese**, A. Frassoldati, T. Faravelli, M. Ihme, *Accounting for strain-rate effect in soot modeling of turbulent flames*, 15th International Conference on Numerical Combustion, April 19-22, 2015, Avignon (France).

S. Salenbauch, M. Pollack, A. Cuoci, A. Frassoldati, **C. Saggese**, T. Faravelli, C. Hasse, *An Eulerian bivariate soot model based on a method of moments*, Proceedings of the European Combustion Meeting 2015, March 30-April 28, 2015, Budapest (Hungary).

C. Saggese, S. Ferrario, A.Cuoci, A. Frassoldati, E. Ranzi, T. Faravelli, *A kinetic modeling study of soot formation in cyclic C6 hydrocarbon flames*, 8th International Seminar on Flame Structure, September 21-24, 2014, Berlin (Germany).

C. Saggese, J. Camacho, T. Faravelli, E. Ranzi, H. Wang, *An Experimental Study of Soot Formation in Propene Flames*, 35th International Symposium on Combustion, August 3-8, 2014, San Francisco (CA).

C. Saggese, S. Ferrario, A. Frassoldati, A.Cuoci, T. Faravelli, E. Ranzi, H. Wang, *A Kinetic Modeling Study of Soot Formation in a Burner-Stabilized Stagnation Ethylene Flame*, 2014 International Sooting Flame (ISF) Workshop, August 2-3, 2014, Pleasanton (CA).

S. Ferrario, **C. Saggese**, A. Frassoldati, A. Cuoci, E. Ranzi and T. Faravelli, *Sensitivity Analysis on Soot Formation and PSDFs*. XXXVII Meeting of the Italian Section of the Combustion Institute, April 23-24, 2014, Pisa (Italy).

C. Saggese, J. Camacho, T. Faravelli, E. Ranzi, H. Wang, *The role of the surface growth reactions on soot formation*, Western States Section of the Combustion Institute - 2014 Spring meeting, March 24-25, 2014, California Institute of Technology (Pasadena, CA).

C. Saggese, T. Faravelli, E. Ranzi, H. Wang, *A Kinetic Modeling Study on PAHs and Soot Formation in Flames*, Thermal & Fluid Sciences Affiliates and Sponsors Conference, February 5-7, 2014, Stanford University (Palo Alto, CA).

C. Saggese, A. Frassoldati, A. Cuoci, T. Faravelli, E. Ranzi, *Detailed kinetics of PAHs and soot formation*, Colloquium on chemical Reaction engineering 2013, October 17-18, 2013, Politecnico di Milano (Milan, Italy).

N. E. Sanchez, **C. Saggese**, A. Frassoldati, A. Cuoci, T. Faravelli, E. Ranzi, A. Callejas, A. Millera, R. Bilbao, M. U. Alzueta, *Experimental and modeling study of acetylene conversion in a tubular reactor: Polycyclic aromatic hydrocarbon (PAH) and soot formation*, 4th annual meeting of the COST action CM0901, Perugia, Italy, 16-18 September 2013.

C. Saggese, A. Frassoldati, A. Cuoci, T. Faravelli, E. Ranzi, *A Comprehensive Modeling Study of Soot Formation from Different Fuels*, Proceedings of the European Combustion Meeting 2013, June 25-28, 2013, Lund (Sweden).

M. Pelucchi, **C. Saggese**, A. Frassoldati, E. Ranzi, T. Faravelli, K. P. Somers, U. Burke, H. J. Curran, K. Yasunaga, *Experimental and kinetic modelling study of n-butanal auto-ignition in a shock tube*, Proceedings of the European Combustion Meeting 2013, June 25-28, 2013, Lund (Sweden).

C. Saggese, A. Cuoci, A. Frassoldati, T. Faravelli and E. Ranzi, *Gas Phase Kinetics of Volatiles from Biomass Pyrolysis. Note II: Furan, 2-methyl-furan, and 2,5-dimethylfuran.* XXXVI Meeting of the Italian Section of the Combustion Institute, June 13-15, 2013, Isola di Procida (Italy).

C. Saggese, N. E. Sanchez, A. Callejas, A. Millera, R. Bilbao, M. U. Alzueta, A. Frassoldati, A. Cuoci, T. Faravelli, E. Ranzi, *A Kinetic Modeling Study of Polycyclic Aromatic Hydrocarbons (PAHs) and Soot Formation in Acetylene Pyrolysis*, COST Joint Working Group Meeting "Soot and PAHs", April 11-12, 2013, Sorrento (Italy).

C. Saggese, A. Frassoldati, A. Cuoci, T. Faravelli and E. Ranzi, *A kinetic modeling study of the oxidation and combustion of aromatic species*. Proceedings of the XXXV Meeting of the Italian Section of the Combustion Institute, October 10-12, 2012, Milano (Italy).

C. Saggese, A. Frassoldati, A. Cuoci, T. Faravelli, E. Ranzi, *Cinetica dettagliata di pirolisi e combustione di alta temperatura di idrocarburi aromatici*, Convegno nazionale GRICU 2012, September 16-19, 2012, Montesilvano (Pescara, Italy).

M. Bissoli, **C. Saggese**, A. Frassoldati, A. Cuoci, T. Faravelli, E. Ranzi, *Kinetic modeling study of the low and high temperature ignition of biofuels mixtures in a HCCI engine*, COST Third Annual Meeting, September 5-7, 2012, Sofia (Bulgaria) .

C. Saggese, G. Genova, R. Grana, A. Frassoldati, T. Faravelli and E. Ranzi, *A kinetic modeling study of mixtures of methyl esters with alcohol fuels*. Proceedings of the XXXIV Meeting of the Italian Section of the Combustion Institute, October 24-26, 2011, Rome (Italy).

Contents

List of Figures

List of Tables

Nomenclature

$BIN_{i,j}$	pseudo-species BIN of the i^{th} section and j^{th} hydrogenation level
$BIN_{i,j}$•	radical pseudo-species BIN of the i^{th} section and j^{th} hydrogenation level
$C_{p,k}$	specific heat of species k
d_c	collision diameter
D_f	fractal dimension
D_m	mobility diameter
d_p	equivalent spherical diameter
D_p	mobility diameter
f_v	soot volume fraction
$\widehat{H_k}$	specific enthalpy for species k
H_p	separation distance between the burner and the stagnation surface
k_B	Boltzmann constant
m	CPMA measured mass
M_k	molecular weight of species k
m_m	mobility mass
N	number density
nC	number of C atoms in the BIN
N_c	circles of benzene rings around coronene
nH	number of H atoms in the BIN
n_{met}	number of methylation
N_p	number of primary particles in each aggregate
N_s	number of species
P	pressure
$\dot{Q}$	radiative heat flux
r	radial coordinate
R_g	radius of gyration

t	time
T	temperature
T_b	burner temperature
T_{max}	maximum temperature
T_{sp}	sample probe temperature
u	axial velocity in the BSS flame
v	radial velocity in the BSS flame
v_0	cold gas velocity
V_k	mass diffusion velocity of species k
$\vec{V}_k^{(Th)}$	thermophoretic velocity of species k
x	axial coordinate
$\boldsymbol{x}$	vector of the external coordinates

Greek symbols

β	mixture parameter
γ	collision efficiency
$\boldsymbol{\xi}$	vector of the internal coordinates
λ	thermal conductivity
μ	gas mixture dynamic viscosity
μ_r	reduced mass
ν	gas mixture kinematic viscosity
ρ	gas density
ρ_{soot}	soot density
σ	mean collision diameter
Φ	equivalence ratio
ω_k	mass fraction of species k
$\dot{\Omega}_k$	molar production rate of species k

Subscripts

i	BIN section
j	BIN hydrogenation level
k	species

Acronyms

AFM	Atomic Force Microscope
AMPI	Atomistic Model for Particle Inception
APM	Aerosol Particle Mass analyzer
BC	Black Carbon
BSS	Burner-Stabilized Stagnation flame
BSU	Basic Structural Units
CPC	Condensation Particle Counter
CPMA	Centrifugal Particle Mass Analyzer
CQMOM	Conditional Quadrature Method of Moments
CS	Condensable Species
DCM	Di-Chloro-Methane
DMA	Differential Mobility Analyzer
DPF	Diesel Particulate Filter
DQMOM	Direct Quadrature Method of Moments
EELS	Electron Energy Loss Spectroscopy
EDS	Energy Dispersive x-ray Spectroscopy
ELS	Elastic Light Scattering
EQMOM	Extended Quadrature Method of Moments
FTIR	Fourier Transform Infrared spectroscopy
GA	Group Additivity method
HAB	Height Above the Burner
HACA	Hydrogen-Abstraction, C_2H_2-Addition
HCCI	Homogeneous Charge Compression Ignition

HIM	Helium-Ion Microscopy
HMOM	Hybrid Method of Moments
HRTEM	High Resolution Transmission Electron Microscopy
HTGA	High-Pressure Thermogravimetric Analyzer
IARC	International Agency for Research on Cancer
ISF	International Sooting Flame workshop
KMC-ARS	Kinetic Monte Carlo - Aromatic Site
LII	Laser Induced Incandescence
MC	Monte Carlo
MOMIC	Method of Moments with Interpolative Closure
NDF	Number Density Function
NSC	Nagle Strickland-Constable correlation
nsl	non-stacked layers
PAH	Polycyclic Aromatic Hydrocarbons
PBE	Population Balance Equation
PCAH	Pericondensed Aromatic Hydrocarbons
PM	Particulate Matter
PP	Primary Particle
PSDF	Particle Size Distribution Function
QMOM	Quadrature Method of Moments
ROPA	Rate of Production Analysis
SANS	Small Angle Neutron Scattering
SAXS	Small Angle X-ray Scattering
SEM	Scanning Electron Microscopy
SMPS	Scanning Mobility Particle Sizer
TEM	Transmission Electron Microscopy
WHO	World Health Organization
XPS	X-ray Photoelectron Spectroscopy

Abstract

Combustion is present in many large-scale processes, including internal combustion engines, power stations, waste incineration and residential burning of wood and coal. These, with field burning of agricultural wastes and forest and vegetation fires, are the main sources of airborne species, such as Polycyclic Aromatic Hydrocarbons (PAH) and Particulate Matter (PM or soot).

As by-product of fuel combustion, flame-generated carbon nanoparticles not only lower efficiency of many combustion devices but also can adversely impact global climate, air quality and human health. In particular, the smallest particles are the most dangerous ones because they can affect both the lungs and the heart.

Therefore a strong reduction of fine particulate matter emissions from combustion sources is needed and a fundamental understanding of soot formation process is required for the development of future clean combustion devices. Studying soot morphology and composition as well as its formation process in flames remains an intriguing problem in combustion chemistry research and significant progresses have been made over the last few years both experimentally and numerically.

Soot formation occurs at high temperature and in rich conditions and includes different processes: particle nucleation from the combustion of the initial gas phase mixture, surface growth by gas-surface reactions with C_2H_2 and PAHs, oxidation and dehydrogenation reactions. Moreover, along with chemical growth in a flame, soot particles coalesce or aggregate. The development of a reliable soot kinetic model is an ambitious task and involves not only a proper description of the gas phase kinetics and its coupling with solid phase but also a correct understanding of the experimental setup necessary for obtaining soot data to validate the model.

The aim of this thesis work is to have more insights on particle inception and growth through an improvement of a soot kinetic model, developed at Politecnico di Milano and based on the discrete sectional method, and an experimental activity carried out at Stanford University to measure soot produced under controlled flame conditions and to investigate the effect of the parent fuel structure on soot formation process.

The modeling activity is mostly focused on developing and further refining firstly the gas-phase kinetics of benzene and acetylene, important soot precursors, and secondly the soot kinetic model on the basis of recent experimental and theoretical evidences on aggregates formation in flames. Specifically, fractal aggregates are added to the scheme with their proper reaction kinetics and this allows to better describe the evolution of soot morphology.

The model validation is performed in terms of comparisons with data obtained in laminar premixed ethylene flames and among them the configuration of the Burner-Stabilized Stagnation (BSS) flame is considered as main case study. First, a proper one-dimensional method to describe the stagnation-surface configuration is defined through a set of conservation equations and boundary conditions. The approach consists in simulating it as a counterflow flame with zero velocity on the oxidizer side. It is very important to define correctly the boundary conditions, especially those for the species. In particular, for gaseous species, the sum of the convective and diffusive terms is zero on the air side, while for particles it is equal to the thermophoretic flux. This allows to take into account the flux of soot particles depositing on the water-cooled surface and to obtain a good agreement between soot mobility measurements and model predictions. Model and experimental uncertainties are respectively discussed and analyzed by means of a sensitivity analysis and the development of a new tandem technique to measure simultaneously soot mass and size distributions.

The goal of the experimental activity is to explore the influence of fuel molecule structure on the soot formation process. Soot is sampled and measured using a Scanning Mobility Particle Sizer (SMPS) in BSS pure propylene flames and ethylene/propylene flames for the first time. Similar flame operating and stoichiometric conditions have been chosen to compare soot volume fraction and size distributions from propylene with the ones from ethylene. Afterwards, the model capability to predict soot formation under different conditions is tested through comparisons with the performed measurements in BSS propylene flames and the literature data of cyclic C6 hydrocarbon premixed flames.

1. Introduction

This chapter provides information about soot origin and evolution in combustion systems with a particular focus on its impact on climate and human health. Particle morphology is also described relatively to the different stages of soot formation process because it affects the interactions of the particles with the environment.

1.1 Soot from combustion

Predominant sources of airborne species, such as Polycyclic Aromatic Hydrocarbons (PAH) and Particulate Matter (PM or soot), are combustion related, namely the use of fossil fuels and biofuels for transportation, solid fuels for industrial and residential uses, and open burning of biomass.

The term soot refers to the black particulate (Black Carbon, BC) produced as a result of incomplete combustion of organic matter in fuel-rich high-temperature environments. As products of combustion like CO, CO_2, NO_x, SO_x, PAHs and soot are considered primary pollutants because directly emitted in air from the sources.

The continuously growing global energy demand for each sector, mainly driven by emerging economies (e.g. India and China) [1], has raised one major concern, that is the increased level of pollutants in the atmosphere. Panel A of Figure 1.1 shows global BC emissions by region in 2000, indeed directly connected to the augmented energy consumption, whose expected trend until 2035 is presented in Panel B.

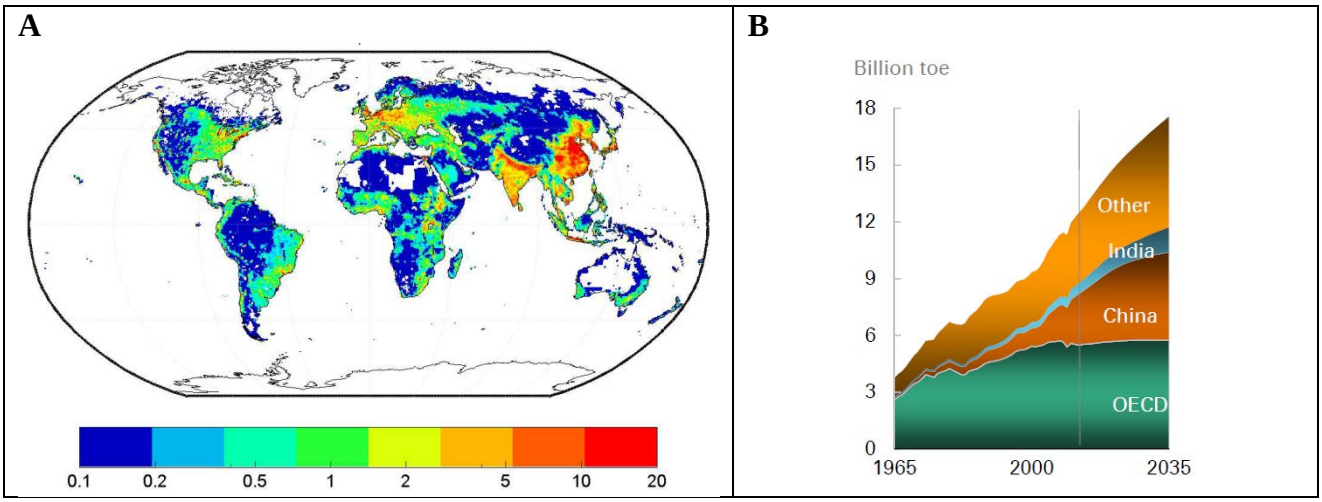

Figure 1.1 Panel A) Global BC Emissions based on Year 2000 Estimates, in Gigagrams (Gg). (Courtesy of Tami Bond, produced based on data from Bond et al. 2007 [2]). Panel B) Primary energy consumption by region until 2035. (OECD=Organisation for Economic Co-operation and Development) [1]

Dominant BC emitters from energy-related combustion depend on the location. Asia and Africa are dominated by residential coal and biomass fuels (60–80%), while on-road and non-road diesel engines are leading emitters (about 70%) in Europe, North America, and Latin America. Residential coal contributes significantly in China, the former USSR, and a few Eastern European countries [3]. Figure 1.2 shows BC emissions by regions and source in 2000.

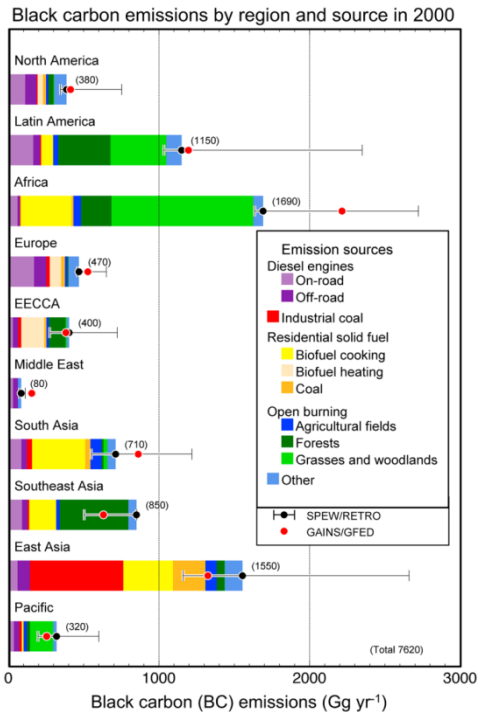

Figure 1.2 Emission rates of BC in the year 2000 by region, indicating major source categories in each region. (EECCA= Eastern Europe, Caucasus and Central Asia) [3]

As presented in Figure 1.2, diesel engines are the major causes of soot emissions in Europe and North America and also a view to 2040 shows that the demand for energy for transportation will rise by ~70% [4]. Up to now, the majority of the fuels are petroleum-based and the demand of diesel fuels is expected to rise through 2040 while gasoline consumption will most probably decrease [4].

Diesel engines replaced gasoline engines not only to reduce greenhouse and toxic gases emissions, but also for the possibility of using non-fossil fuels such as long-chain alkyl esters (biodiesel) that can have a lower carbon footprint than petrodiesel [5]. The major drawback of this technology with regard to environmental and health protection is the typically enhanced production of soot.

Not only in diesel engines, but also in all real devices the burning conditions are often locally non-ideal and the combustion results incomplete, thereby favoring the production of unburned carbonaceous compounds. This is mainly caused by:

- local cold spots, where the fuel is not fully oxidized;
- inadequate mixing of fuel and combustion air;
- insufficient pulverizing of solid fuels or atomizing of liquid fuels;
- too short residence time at high temperatures;
- sudden cooling of the flame gases through combustion chamber walls.

Moreover, the presence of aromatic compounds in the diesel fuel typically enhances soot emission through the condensation of aromatic units to form larger PAHs, whereas aliphatic compounds favor the growth mechanism through hydrogen abstraction and consecutive addition of (poly)acetylene.

PAHs and soot formation and depletion are kinetically controlled and they cannot be completely oxidized in the lean parts of the system. Therefore, soot formation in industrial systems affects the efficiency of the devices, for example worsening the heat exchange and increasing pressure drops in case of tubular reactors and maintenance is required to prevent its accumulation in the system [6].

There are two ways to decrease the amount of particulate matter emitted from diesel engines: optimizing the combustion of diesel fuel in the engine and through the after-treatment by installing particulate filters.

Combustion optimization can be obtained by improving the engine design, such as controlling better temperature and mixing as in the Homogeneous Charge Compression Ignition engine (HCCI), or creating new fuel formulations, such as adding oxygenated compounds to the fuel mixture. A large range of oxygenated compounds (of bio-fuels) has been proposed as possible additives to petroleum fuels, such as alcohols, methyl esters, acyclic and cyclic ethers [7-9]. On the other hand, the use of Diesel Particulate Filters (DPFs) is becoming necessary to control soot particle emitted from exhaust [10, 11]. Filter clogging can be avoided by continuously regenerating the DPF. However, conditions for the continuous regeneration depend not only on engine conditions, but also upon oxidative reactivity of particles on the DPF [12]. As a matter of fact, the exhausts from industrial activities are treated before being emitted into the atmosphere, but it is not possible to purify them completely or to retain even the smallest particles, which are the most dangerous in terms of health. Furthermore, depuration devices are very expensive and the cost increases with the depuration efficiency.

Hence, a better control of the combustion processes would lead to significant savings, both because it would improve energetic efficiency reducing fuel losses and because the costs for depuration devices would be reduced.

1.2 Soot impacts on environment and human health

As by-product of combustion, flame-generated carbon nanoparticles not only lower the combustion efficiency but can also adversely impact global climate, air quality, and human health.

As far as pollution increase is concerned, recently black carbon is classified “as the second most important individual climate-warming agent after carbon dioxide” [3]. Figure 1.3 summarizes the knowledge of the effects of BC emissions on climate.

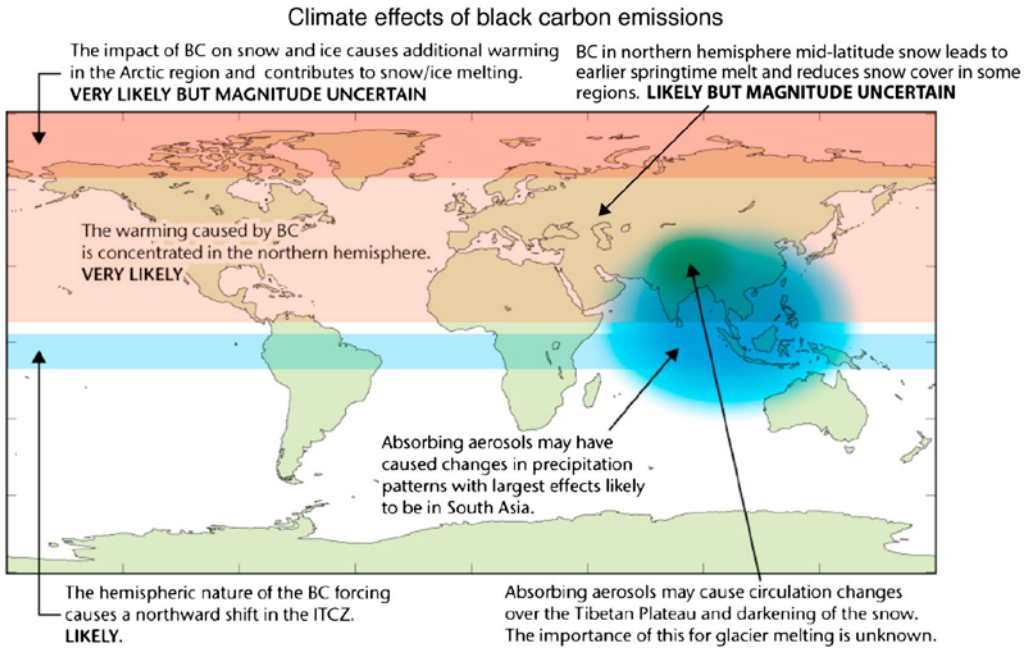

Figure 1.3 Qualitative summary of current understanding of the global climate impacts of BC emissions. [3]

The main quantified climate impact of soot is its atmospheric direct radiative forcing, that favors an increase of the absorption of incoming solar radiation, which causes warming and alters properties of ice clouds and liquid water. Moreover, soot deposition on snow and ice increases the light and heat absorption, therefore glacial retreat is enhanced with respect to what it would be considering the mere global warming.

Knowing this, soot can lead to local climate changes and precipitations variations, affecting the delicate biosphere equilibrium and contributing to all the bad effects of global warming. For these reasons, it appears clearly the necessity of controlling soot formation through the understanding of the underlying phenomena. In this context, an important step towards the control of pollution by the government is pollution regulation, that is realized through the issue of emission norms (such as Euro emissions standard of the European Union) which are being steadily tightened [13].

As soot belongs to the wider class of atmospheric aerosols, its properties, like mass concentration, number density, composition and dimensions, are important to evaluate its overall impact on environment and human health. Actually, the government restrictions for particulate matter emissions have been mainly imposed on size and amount.

Generally the distribution function of atmospheric aerosol dimensions is divided into four ranges that account for different formation mechanisms, as shown in Figure 1.4.

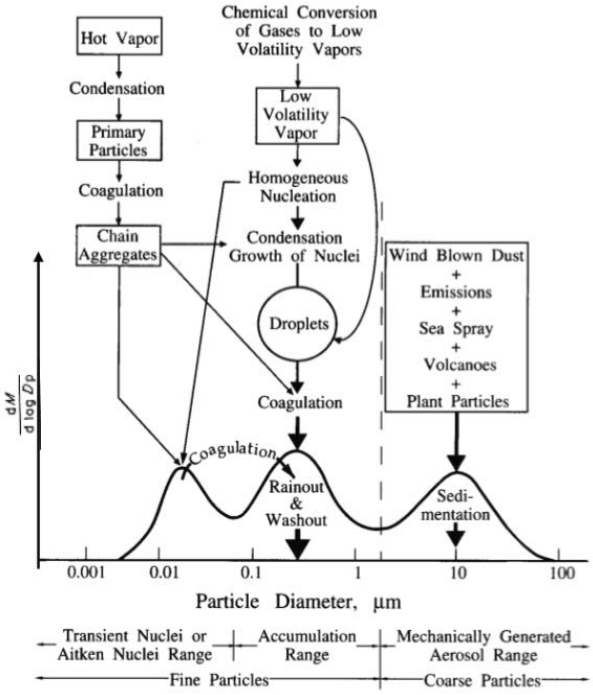

Figure 1.4 Size distribution expressed as mass per increment in log particle diameter and formation mechanisms for atmospheric aerosols [14].

The first range includes coarse particles, such as sea spray and desert dust, with diameters between 2 and 100μm are formed through mechanical processes. These dimensions facilitate the gravity deposition process and their mobility is due to convective phenomena.

Particles in the second range, defined as the accumulation range, have dimensions between 0.08 and 2μm. They are originated from coagulation of smaller particles and condensation of volatile compounds that deposit on preexisting particles and they are mainly constituted of organic matter. Their residence time in atmosphere is higher due to lower settling velocities, but they can be washed away by the rain.

Ultrafine particulate (10-80 nm) is in the third range. It comes from nucleation phenomena of supersaturated vapors at low temperature or from combustion processes. Particles in this range are called Aitken nuclei because they act like condensation nuclei, promoting the formation of bigger particles.

The last range includes particles made of organic carbon with diameters below 10 nm. They are also typical of nucleation phenomena.

The convention for dust sampling is to distinguish two main classes: inhalable and respirable particulate. Inhalable particulate is the fraction of a dust cloud that can be breathed into the nose or mouth (PM10, particles with dimensions less than 10μm), while respirable particulate is the fraction of inhaled airborne particles that can penetrate beyond the terminal bronchioles into the gas-exchange region of the lungs (PM2.5, particles with dimensions less than 2.5μm) [15].

Figure 1.5 shows the penetration areas of particles in the respiratory system, highlighting the dangerousness of respirable particulate.

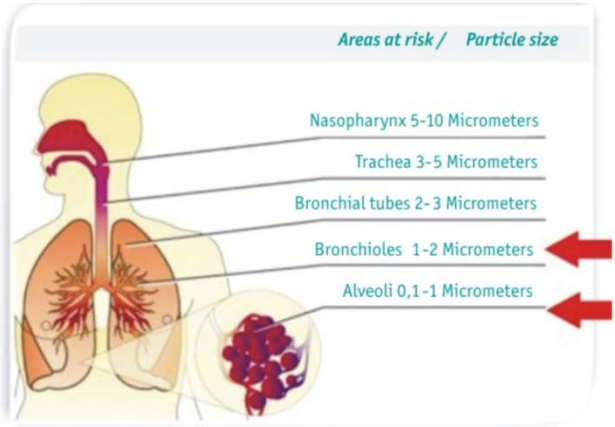

Figure 1.5 Penetration of particles in respiratory system depending on particles' size [16].

Regarding health concerns, soot carcinogenicity is well known. Actually a new report from the WHO's (World Health Organization) cancer research agency [17] announced the classification of outdoor air pollution and particulate matter as known human carcinogens, proving the connection between their levels in the air and cancer risks after the International Agency for Research on Cancer (IARC) independently reviewed over 1000 of the latest scientific studies on air pollution.

Furthermore, in a systematic review of the literature, Krzyzanowski et al. [18] concluded that combustion-related particles contribute to an increased risk of death, particularly from

cardiopulmonary causes. These particles also increase the risk of respiratory symptoms and diseases that are not related to allergies. Lung cancer and cardiopulmonary diseases are long-term effects, but there are also short-term effects including cardiovascular and respiratory diseases. Indeed, soot particles as small as 1 nm can enter the human body and gain access to the blood stream via inhalation or ingestion more easily than larger sized particles. They could also overload the body's phagocytes, cells that ingest and destroy foreign matter, triggering stress reactions that lead to inflammation.

Once in the blood stream, nanoparticles can also be transported around the body and be taken up by organs and tissues where they cumulate in time causing serious damages. This also shows the importance of regulating not only the mass quantity of emitted particles, but also their number since the smaller particles have negligible mass with respect to the bigger ones, but are more toxic by far [17].

1.3 Soot morphology

In order to understand how soot interacts with the surrounding environment and accordingly affects climate and human health, it is necessary to study its morphology and chemical composition. A review of the possible mechanisms that lead to soot formation and that account for this particular structure will be given in paragraph 2.1.

Soot is made of roughly spherical particles (called primary particles) with dimensions about 10 nm that afterwards coagulate into fractal aggregates with a chain-like structure, as the one shown in the Transmission Electron Microscopy (TEM) image in Figure 1.6.

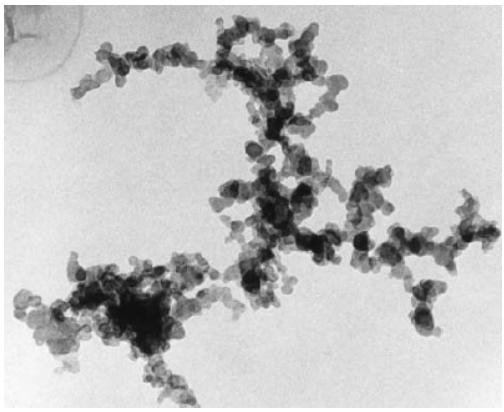

Figure 1.6 TEM picture of a fractal soot aggregate [19].

These primary particles have a soluble fraction constituted mainly of PAHs and their H/C ratio in mature aggregates is about 0.1 or less.

Transmission electron microscope pictures show that they can be amorphous or have a shell-core structure, meaning that is no identifiable long-range order like in graphite but there are graphene layers parallel to the surface in the outer shell and disordered in the core [20-22].

In some works, structural changes have been observed in dependence on fuel and synthesis conditions. Vander Wal and Tomasek [20], studying soot structure in pyrolysis conditions of different fuels, found that at low temperatures (around 1250°C, left panel in Figure 1.7) the particles have an amorphous structure, regardless of the fuel, while at high temperatures (around 1650°C, right panel in Figure 1.7) a shell-core structure appears and it depends upon the fuel and the flow rate. High flow rates favor the formation of PAHs with five-membered rings, thus the soot particles have a highly curved nanostructure, while slow flow rates lead to graphitic soot.

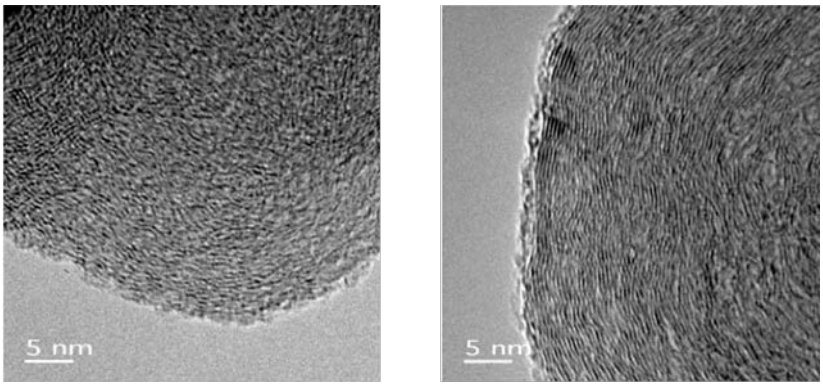

Figure 1.7 Soot formed in low (left) and high (right) temperature pyrolysis of acetylene. [20]

Also Alfè et al. [21] and Apicella et al. [22] confirmed that soot structure is dependent on the fuel and the aging. For instance, the onion-like structures are evident even in the young soot formed in benzene flames (left panel, image g in Figure 1.8), whereas soot in ethylene flames have a more amorphous and disordered structure. The onion-like structures in the benzene flame can be interpreted as two smaller particles that have been incorporated into a single spherical particle after coalescing together and due to surface growth.

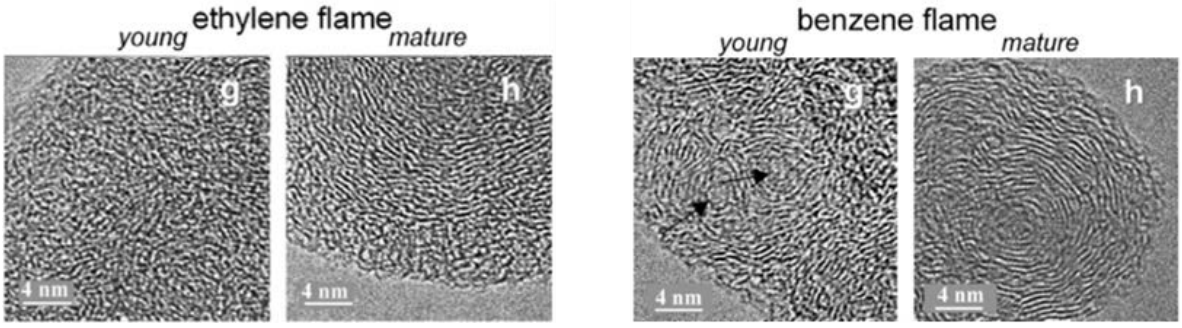

Figure 1.8 Structure of young and mature soot in ethylene and benzene flames. [21]

Different structures imply different reactive behaviors and interactions with the surrounding environment. Specifically, a correlation between soot nanostructure and soot reactivity toward oxidation has been proposed assuming that the reactivity toward oxidative attack depends on two main factors [23]:

- Accessibility of carbon in edge sites that are more reactive than the basal plane carbon atoms.
- Weakening of C-C bonds for effect of curvature due to five-member rings (driving to an increase of sp^3 character).

Indeed, Vander Wal and Mueller [24] showed that soot reactivity was related to its nanostructure. They found that soot with curvy and disordered structures was more reactive than soot with structures formed by planar graphitic layers.

1.4 Thesis organization

The rest of the thesis is structured as follows. Chapter 2 provides a brief overview of the different possible kinetic pathways of soot formation and growth and the approaches to modeling. The description of different experimental methods, used to analyze the physical and chemical properties of soot particles and aggregates formed in premixed flames, is also given. Successively, recent applications of soot theory are discussed. Chapter 3 describes the refinement of benzene and acetylene combustion and pyrolysis kinetics inside the POLIMI kinetic scheme, with a particular attention on PAHs formation. In Chapter 4, the coupling between gas- and solid-phase and the development of the soot kinetic model is presented. According to the discrete sectional approach, different classes of pseudo-species are defined as well as their thermodynamics and kinetics. Different comparisons of soot model predictions with experimental data in laminar premixed flames have been shown in Chapter 5. Firstly, the model is tested against soot measurements in laminar premixed ethylene flames, reported in literature. Among them, the BSS flame configuration is chosen as main case study and a sensitivity analysis has also been carried out to assess the effect of the uncertainties in the defined kinetic constants of the different reaction classes of the soot kinetic model. Experimental uncertainties are discussed using a new technique to measure soot mass and size distributions simultaneously, that involves the coupling of the Centrifugal Particle Mass Analyzer (CPMA) and the Differential Mobility Analyzer (DMA). Then fuel dependency on soot formation is explored in Chapter 6 by means of comparisons with experimental data in propylene flames and C6 cyclic hydrocarbon flames. Measurements in propylene flames have been carried out at Stanford University using the BSS configuration, while data in C6 flames have been taken from literature. Chapter 7 contains conclusions of the work presented and suggests some outlooks of the novel elements developed herein that might be taken forward.

2. State of the art

2.1 Theory of soot formation and growth

2.1.1 Thermodynamics

The formation of the first aromatic ring is the first step in soot nucleation, but not the only bottleneck of the process. On the contrary, there are several rate limiting steps [25] that must be analyzed taking into account also the thermodynamics of the problem.

The driving force for soot formation is either a decrease in the enthalpy due to chemical bond formation or an increase in entropy because of gas-phase species released during particle formation. The process of soot formation is entropy-driven, as shown in Figure 2.1.

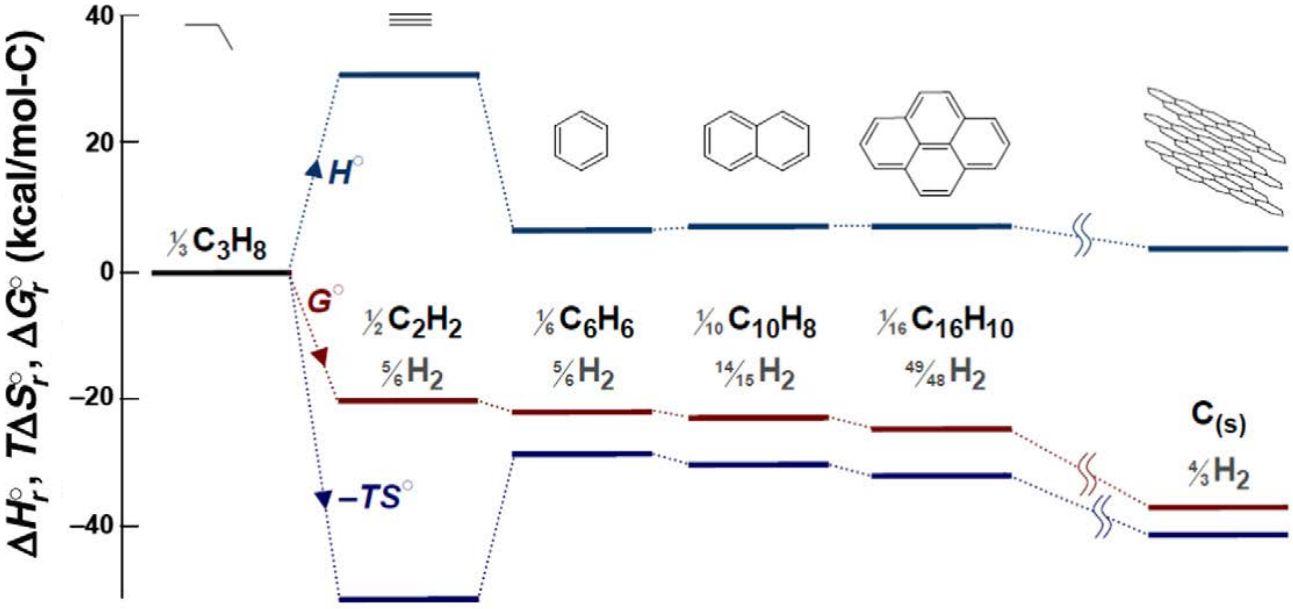

Figure 2.1 Enthalpy and entropy contributions to Gibbs free energy at 1600 K for the formation of solid carbon from propane. [26]

The overall process is slightly endothermic and the increase in entropy is not very strong, hence not only it is kinetically controlled, but the kinetics is also highly reversible [26].

2.1.2 PAH formation and growth

Benzene is the first aromatic compound, a relevant intermediate of several combustion processes and also a key precursor to soot formation. The primary focus is on the its formation in a flame by aliphatic molecules and radicals that are generated by the pyrolysis of fuel molecules [27].

The main contributing species are C2, C3 and C4 molecules or radicals, and the pathways for the formation of benzene from them are discussed in [25, 28].

Frenklach and coworkers proposed and developed a mechanism based on the role of acetylene as growth species, which is known as HACA (Hydrogen-abstraction, C_2H_2 addition) and involves an even-carbon-atom pathway for benzene ring formation. For instance, acetylene addition on n-C_4H_5 radical is similar to the one who had been proposed also by Cole et al. [29] for aliphatic fuels with the only difference of the simultaneous cyclization and hydrogen loss. Colket [30] reached similar conclusions, suggesting that acetylene addition to n-C_4H_3 is the major pathway leading to cyclic compounds.

Miller and Melius [31] proved that this pathway alone is not able to account for the formed benzene. They showed that, as Fahr and Stein [32] had suggested, in flames the first aromatic ring is mostly likely formed *via* an odd-carbon-atom pathway that consists in the self-recombination of propargyl radicals. Indeed, propargyl radical is resonantly stabilized and therefore very stable, thus its concentration in the system can be quite high. Later on, the role of all resonantly stabilized radicals besides propargyl was recognized [33, 34].

Melius et al. [33] proposed the first mechanism of cyclopentadienyl self-recombination mechanism to yield naphthalene, which was subsequently investigated in rich, sooting, premixed methane/ethane flames by Marinov et al. [33]. Specifically they confirmed the importance of cyclopentadienyl moieties in the formation of PAHs, as observed also by D'Anna and Violi [35]. The mechanisms for the formation of PAHs from cyclopentadiene and its radical were studied theoretically in [36], while a validation with experimental data is proposed in [37].

After the first ring is formed, the molecules can grow *via* different mechanisms. The well-known HACA mechanism captures the essence of the sooting process in the postflame region. However, at pyrolysis conditions the HACA mechanism cannot explain entirely the formation and build-up of PAHs [33, 38].

Recombination of resonance-stabilized radicals (e.g., propargyl, cyclopentadienyl, benzyl) as well as addition reactions between aromatic compounds with six π-electrons and compounds with conjugated double bonds (e.g., acenaphthylene) mainly contribute to the first formation and further growth of PAHs [26, 36, 39]. Colket and Seery [40] observed that resonance-stabilized radicals such as cyclopentadienyl, benzyl and similar radicals play a relevant role mainly in the pyrolysis region of diffusion flames. This work also indicates that the addition reactions of heavy unsaturated and aromatic species, such as phenyl addition to naphthalene, naphtenyl addition to benzene and similar, may need to be considered. The growth of PAHs through bimolecular reactions involving heavy radical and non-radical species has recently been the subject of several ab initio simulations based kinetic studies [33, 36, 41-43].

Despite all the recent advances, fundamental chemical kinetics of aromatics needs further research. Challenges remain especially in the context of soot precursor formation from real fuel combustion.

Furthermore, many isomers of aromatic compounds are formed with increasing the molecular mass. Although it is almost impossible to follow each of these species, some classifications are possible. Two broad classes of aromatic molecules can be considered: aromatics in which only π-bonds among C atoms exist, named pericondensed aromatic hydrocarbons (PCAH) and aromatics having both σ- and π-bonds between C atoms consisting of incompletely-condensed oligomers of PCAH [39]. The PCAHs having the lowest amount of H atoms are maximally condensed six-member ring structures. Their H/C ratio decreases as the molecular size increases; the largest of these compounds is a graphene sheet. If only six-member ring structures constitute the aromatic species, the molecules are planar. The presence of five-membered rings, instead, leads to a molecular distortion and induces a curvature in the molecule. Their active sites react with another aromatic compound or its radical originating non-completely condensed aromatic oligomers. Their H/C remains constant as the molecular weight of the oligomers increases. The number of C and H atoms furnishes a rough estimation of the molecular structure of aromatics. For a given C atoms number, molecules with large H/C ratios are oligomers of small aromatics whereas lower H/C molecules belong to the PCAH class. The value of the H/C ratio furnishes the structure of the aromatic compounds, as schematically shown in Figure 2.2.

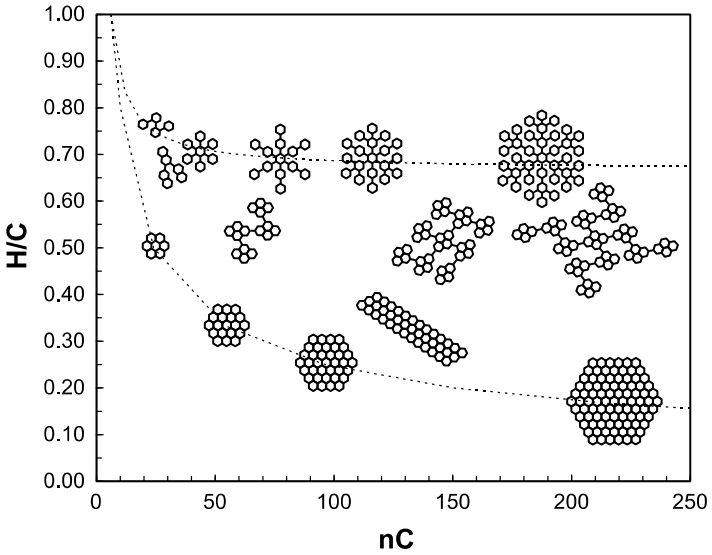

Figure 2.2 Representation of oligomers of benzene (high H/C values) and maximally PCAH (low H/C values). [39]

It is widely accepted that starting from the gas-phase molecules with size of a few angstroms, PAH molecules are first formed, followed by nucleation, coagulation, surface growth and oxidation, and finally aggregation into mature soot with the size of a few micrometers. The time scale of the entire process is on the order of milliseconds. Figure 2.3 shows soot particle evolution along the axis of a laminar premixed flame.

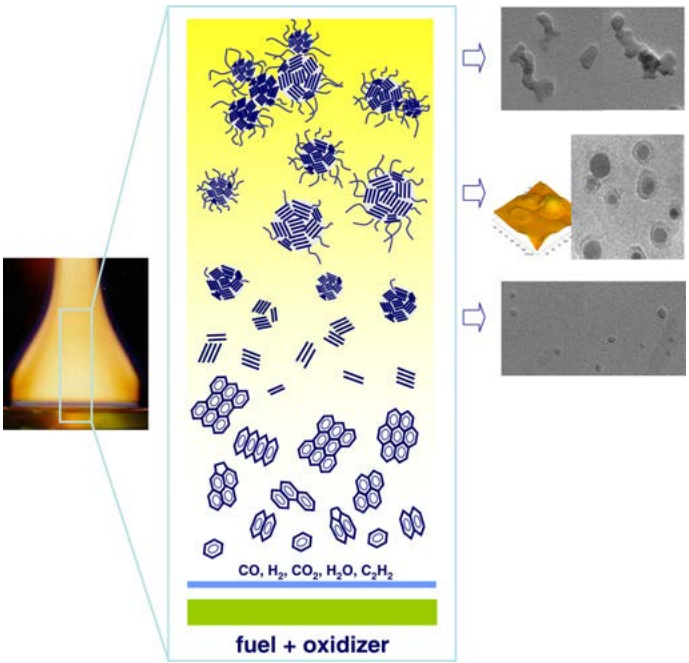

Figure 2.3 Schematic representation of soot formation and growth. [26, 44]

Nascent soot is represented with a core-shell structure. Firstly, an aromatic core composed of PAHs ranging from pyrene to ovaleneis is formed in the early stages of the flame where the gas temperature is high, then an aliphatic shell forms later on the aromatic substrate when the gas temperature becomes slightly lower [26].

2.1.3 Soot nucleation

The mechanism of soot nucleation (or particle inception) that represents the transition of gas-phase species to solid particles still remains elusive.

Initially, nucleation was thought to be the result of a purely chemical growth and soot was simply considered as the mass accumulated in PAH species above a certain size [28]. This assumption could predict very well the soot mass, but underestimated the particle size.

Nowadays, there are three different pathways that are the most discussed ones [26]:

- Path A considers the growth of two-dimensional PAHs into curved, fullerene-like structures that are the nucleus of spherical particles [45]. These particles cannot close into a layer of carbon, but develop in successive layers.
- Path B represents the nucleation as physical coalescence of moderate-sized PAHs into stacked clusters [46-48].
- Path C consists in the reaction or chemical coalescence of PAHs into cross-linked three-dimensional structures [49-51].

It is worth to notice that, as suggested by Frenklach [52], while Path A is substantially different, the other two might be considered as two extreme regimes of the same mechanism. In fact, Path B seems to be able to describe soot formation in high-temperature combustion, when the chemical growth is limited by an high degree of reaction reversibility. Path C becomes predominant when the formation of chemical bonds is not heavily counterbalanced by fragmentation, leading to the formation of a network of aromatic-aliphatic-linked structures.

The fullerenic growth (Path A) is too slow to explain the time scale of soot inception phenomena, also considering the concentrations of PAHs with growing number of rings. However, PAH dimerization as the initial nucleation step (Paths B and C) is supported by experimental evidence that shows a bimodality of particle size distribution functions of nascent soot particle in

premixed flames and jet-stirred reactors [53-58]. Indeed, a mechanism based on dimerization has a second-order kinetics in monomer concentration, consistent with a bimodal distribution that indicates a persistent nucleation parallel to the growth process of the particles already formed.

A theoretical study on PAHs dimerization as the initial step to soot nucleation (Path B) [48] has proposed that the intermolecular forces, such as electrostatic and dispersive forces, between a pair of moderate sized PAHs are strong enough to allow binding to occur even at flame temperatures. These stacked PAHs are, however, thermodynamically unstable at above 1600 K [26]. Assuming the dimerization as a phenomenon governed by equilibrium kinetics, PAH dimers can survive only when PAHs reach the size of circumcoronene ($C_{54}H_{18}$). To understand the non-equilibrium dynamics of PAH collision, Schuetz and Frenklach [59] carried out molecular dynamics simulation on pyrene dimerization. They demonstrated that this reaction is physically realistic inside the flames and that dimers' lifetime is compatible with soot formation time scale. However, further research has to be conducted to understand if a dimer would survive its non-reactive collisions with gas molecules that happen during its lifetime.

For Path C the presence of aliphatic groups joint with aromatic structures has been hypothesized. This conformation is explained through reactions of aromatic molecules with an aryl radical [49-51, 60] but the mechanism cannot explain the persistent nucleation in the post flame zone, where H• concentration drops drastically and cannot initiate these reactions.

In summary, though all these three conceptual pathways of nucleation are viable and important, additional pathways are needed for a comprehensive description. These pathways are likely to involve moderate-sized PAH‑PAH interactions, but such interactions must be as strong as those seen in typical covalent bonding.

Koley et al. [61] recently proposed a new pathway of nucleation in which several types of PAH molecules may bind together via covalent bonding, but without a deep discussion on how and why the bonding takes place. In this regard, many recent theoretical materials studies have shown that aromatic molecules can have radical or even diradical characteristics due to localized π-electron states. Considering the multiradical property of PAH mentioned above, Wang [26] proposed that the localized π electrons in PAHs may play an important role in soot nucleation, in that PAHs may be bound together by the covalent-like interaction of π electrons. As a matter of fact, recently Zhang

et al. [62] studied a possible pathway of soot nucleation involving PAH molecules having multiradical characteristics using density functional and semi-empirical methods. They showed that the number of covalent bonds formed in the dimerization of two identical PAHs is determined by the radical character, and the sites to form bonds are related to the aromaticity of individual six-membered ring structure.

2.1.4 Soot growth and oxidation

After particle inception, soot mainly grows *via* the following processes:

- Chemical growth by C_2H_2
- Chemical growth by PAHs (through biaryl formation)
- PAHs condensation (coagulation of a PAH molecule on soot particles)
- Coagulation of soot particles

Acetylene is the dominant mass growth species through the HACA mechanism that describes the soot surface as composed of aromatic basal planes and edges sites. Mass growth on soot surface requires H-abstraction to form an aryl radical site, followed by acetylene attack in a manner similar to the gas-phase mechanism [52]. Surface growth reaction rate is directly proportional to the concentration of hydrogen atoms. Experimental evidence shows that soot mass continues to increase even in the post-oxidative region of the flame, where H• concentration is very small.

This led to the hypothesis that there are persistent free radicals on soot surface and the theory has been confirmed by experimental measurements of the concentration of anthracite's free radicals [63] and of free aromatic radicals from ethylene and acetylene pyrolysis [64]. Despite the hypothesis of gas-phase similarity, there are some substantial differences with respect to the gas phase reactions in the definition of the active sites. In fact, in surface reactions the kinetics depends on the collision frequency while the sticking coefficient and the equilibrium constant might depend on the nature of the surrounding sites. Additionally, reactions or condensation of PAHs onto soot surfaces also contribute to soot mass, and the relative contributions appear to be dependent on the flame condition [27, 46, 52].

It is well-known that soot mass is determined by surface reactions, while the ultimate size of soot particles is governed by simultaneous particle-particle coagulation. The chain-like structure of

soot as observed in TEM images arises due to coagulation process. The continuous surface growth after particle coagulation leads to a structure where the fine particles constitute the inner core and PAHs form the outer shell [65]. As a soot particle grows, its surface reactivity towards the gas-phase reactants decreases [25, 66]. This happen because the H/C ratio decreases and less active sites are available. The decrease in the availability of reactive sites on soot particles may be due to steric hindrance: the reactive sites on PAHs present in the core of a soot particle may not be readily accessible and may get hindered due to the presence of nearby PAHs. Furthermore, bigger particles have a lower surface per volume unit and surface reactions become of secondary importance.

The rate of coagulation process can be calculated with the Smoluchowski formula [67]. For this calculation the particles are considered as spherical and small with respect to the gas mean free path and it is assumed that every collision results in a coagulation. Small particles or low-density gas verify this assumption. In particular this is valid in low-pressure flames [68, 69], in free-molecular regime.

There are two different types of coagulation: coalescence and agglomeration. Coalescence happens when a gas-phase molecule or a small particle collides against another particle to form a structure that, to minimize the free energy, tends to reduce its surface [70]. This means that smaller particles or gas-phase species are incorporated inside a bigger particle. The spherical shape is maintained also because surface reactions act on these structures “smoothing” the surface [26]. When bigger particles collide the interacting species maintain their own structure and aggregate into chain-like fractal structures [38, 52]. This is because particles are more graphitic, rigid, the coalescence is not effective anymore and the surface growth is too slow to smooth and reshape the structure into a spheroidal form [70]. The whole coagulation process is summarized in Figure 2.4.

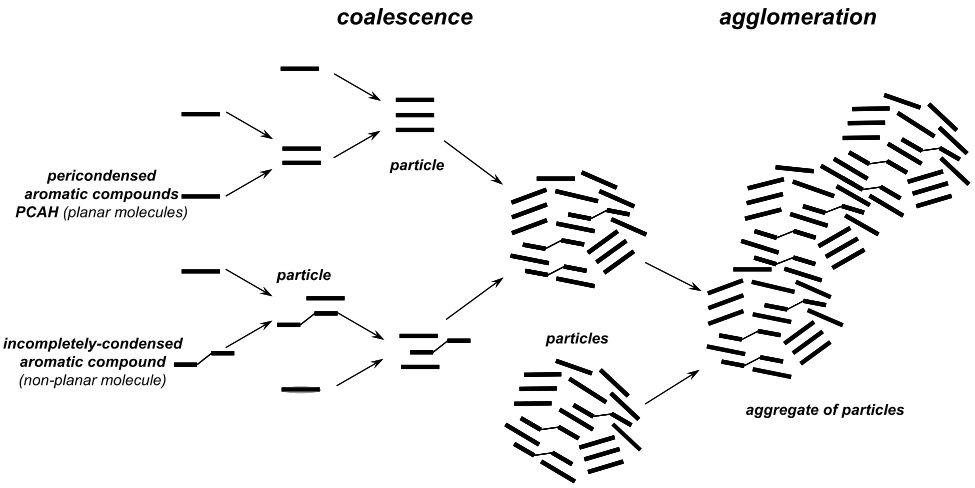

Figure 2.4 Scheme of the coagulation process [70].

2.1.5 Soot oxidation

Soot formation and growth processes are in competition with soot depletion due to oxidation reactions by OH•, O• and O_2 [71]. These mechanisms are poorly understood and the models' predictive capabilities are smaller than for the previous ones. Oxidation consists in particle mass removal due to chemical reactions at the surface [72]. Even though it has been measured that the collision efficiencies of OH• and radical oxygen are similar [73], the dominant radical in the process of soot oxidation is OH• because of its higher concentration.

A particular case is the oxidation-induced fragmentation [74], in which oxygen penetrates into particles and by removal of carbon atoms weakens the structure until it eventually breaks up, forming smaller particles. Only recently mechanisms that include both oxidation and oxidation-induced fragmentation have been developed [72, 75]. It is supposed that only oxygen participates in fragmentation, because OH• reactivity is too high. Therefore it cannot penetrate into particles but gets depleted near to the surface before reaching the core, whereas oxygen diffusion inside the particle pores is in a reaction limited regime [75].

Usually oxidation kinetics of soot is typically measured with well-aged soot as substrates, but nascent and mature soot show differences in details of interior and surface microstructures, as shown in paragraph 1.3.

Recently, a study on the kinetics of nascent soot oxidation by molecular oxygen was carried out at temperatures of 950, 1000 and 1050 K for molecular oxygen concentrations ranging from 1000 to

7800 ppm at ambient pressure in a coupled BSS flame burner and laminar aerosol flow reactor [76]. It was found that the specific oxidation rate has a first-order dependency on gas-phase O_2 concentration over the range of O_2 concentration studied. Moreover the surface of nascent soot resulted considerably more reactive towards oxidation than graphite or graphitized soot, as suggested by the greater measured rate than the classical Nagle Strickland-Constable (NSC) correlation.

On the other hand, the effect of fuel and pressure on oxidation rate was lately studied on soot samples formed in a premixed flat-flame of different liquid fuels and oxidized using a High-Pressure Thermogravimetric Analyzer (HTGA) [77]. It was shown that there was not a significant difference in the activation energies for oxidation of combustion generated soot for either pure components or as a mixture, with exception of soot from oxygen-containing fuels. The oxidation rate for *n*-butanol/*n*-dodecane mixture was found much higher than other fuels. The interpretation of such changes in terms of nascent physical (nano) structure and chemical composition of soot samples were investigated with the lattice fringe analysis performed on High Resolution Transmission Electron Microscopy (HRTEM) images and with X-ray photoelectron spectroscopy (XPS).

2.2 Modeling approaches for soot process characterization

Critical gaps in the fundamental understanding of the complex process of soot formation remain [26, 78]. In order to describe the process of soot formation, from nucleation mass/size growth to agglomeration, extensive numerical and experimental studies have been conducted. So far, no direct assessment of the validity of soot model and, to a large extent, sub-models can be made without comparing the computational results from these complex models with experimental measurements in terms of global and detailed properties of soot formed in low-dimensional laminar flames. Examples may be found in several workshops on the subject [79, 80].

The development of reliable and predictive kinetic models of soot formation requires a consistent description of the gas-phase chemistry that includes the kinetic behavior of gas-phase PAH species, and an appropriate coupling between gas-phase chemistry with aerosol dynamics and chemistry governing soot formation and growth.

As far as aerosol dynamics is concerned, there have been mainly three approaches proposed in literature: the method of moments [27, 46, 52, 81-83], the discrete sectional method [84-88] and the stochastic approach [89-94].

Nowadays, most of the detailed phenomenological soot models are based on techniques for solving the Population Balance Equation (PBE), which is a continuity statement written in terms of a Number Density Function (NDF) [95]. The evolution of the soot NDF $f(\xi) = f\,(t, \boldsymbol{x}; \boldsymbol{\xi})$ in fuel-rich premixed flames is represented by the following transport equation:

$$\frac{\partial f(t,\boldsymbol{x};\boldsymbol{\xi})}{\partial t} + \frac{\partial}{\partial x_i}\left(u_i\, f(t, \boldsymbol{x}; \boldsymbol{\xi})\right) - \frac{\partial}{\partial x_i} D_x \left(\frac{\partial\, f(t,\boldsymbol{x};\boldsymbol{\xi})}{\partial x_i}\right) = S_{\xi}(t, \boldsymbol{x}; \boldsymbol{\xi}) \qquad (2.1)$$

with $\boldsymbol{x}$ considered as the vector of the external coordinates and $\boldsymbol{\xi}$ as the vector of the internal coordinates. $\boldsymbol{\xi}$ contains the properties to characterize soot particles, such as soot particle diameter.

Soot particles can be defined with a univariate characterization by considering their volume V and in this way all particles are assumed to be spherical. Instead, in order to describe the shape of soot particles in a more realistic way, a bivariate description is needed, considering both particle volume V and particle surface S. The function $f(t, \boldsymbol{x}; \boldsymbol{\xi})$ is the Particle Size Distribution Function (PSDF) and the source term, $S_{\xi}(t, \boldsymbol{x}; \boldsymbol{\xi})$, accounts for all the chemical and physical phenomena that

modify the PSDF, such as nucleation, surface growth, PAH condensation, coagulation and oxidation. The transport equation expresses therefore a balance on the particles' number.

2.2.1 Method of moments

To solve the system numerically it is necessary to discretize not only time and space, but also the distribution function itself. The computationally most efficient approach to solving the PBE is given by the method of moments. The NDF is not solved directly; instead only a few lower-order moments of the distribution are tracked. The source term is in general an implicit and complex function of moments of the PSDF and particle dynamics is thus expressed through them.

If the PSDF shape is known then two moments are sufficient. The moment about zero, m_0, is the area of the distribution and represents the number of soot particles, while the third moment, m_3, is the soot volume fraction. A transport equation is written for each of these properties, and the source term for m_0 depends only on the mechanisms modifying the number of particles, like nucleation, coagulation and fragmentation, while the source term for m_3 accounts for nucleation, growth and oxidation, that change the soot volume fraction. The source term is then expressed through pseudo-reactions, but the exact evaluation of this term is numerically and experimentally very complex, therefore approximations, called closure moments, are needed.

The most widely used moment closure approach is given by the Method of Moments with Interpolative Closure (MOMIC), where unknown moments are interpolated from known ones [96]. Another way to achieve closure is given by the Quadrature Method of Moments (QMOM), where the unknown NDF is approximated either by a set of Dirac delta functions or, in newer developments, by kernel density functions [97, 98]. Within recent years, QMOM-based soot models have been applied increasingly [81, 99, 100].

Beside univariate approaches, which assume soot particles to be spherical, quasi-multivariate and multivariate approaches have also been developed. Multivariate models offer the possibility to consider aggregation and therefore lead to a more realistic description of the shape of soot particles. Multivariate moment problems are usually treated using the Direct Quadrature Method of Moments (DQMOM) [101]. However, DQMOM approaches are numerically challenging, since they require the inversion of a linear system, which may be extremely ill-conditioned. Mueller et al. [102]

therefore suggested a new bivariate approach called Hybrid Method of Moments (HMOM), in order to combine the numerical stability of MOMIC with the accuracy of the DQMOM method.

Besides numerical stability and accuracy issues, one of the most severe restrictions of state-of-the-art moment methods is the fact that source terms in the transport equations cannot be formulated as a continuous function of the particle size. Thus, effects such as the reduced collision efficiency of the smallest particles cannot be implemented accurately in standard moment methods with the same precision as in the Monte Carlo (MC). In order to overcome these limitations, Yuan et al. [98] proposed an Extended Quadrature Method of Moments (EQMOM), which enables the shape of the particle size distribution to be reconstructed from a moment set using kernel density functions instead of Dirac delta functions. However, EQMOM is a univariate moment method and, therefore, the aggregation of soot particles cannot be accounted for accurately.

It is known that even the smallest particles are no longer purely spherical and aggregation occurs as soon as nucleation takes place [103]. Therefore, aggregation needs to be considered in soot models in order to describe the evolution of soot particle ensembles properly. This implies the application of a bivariate NDF. Yuan and Fox [104] developed a multivariate moment approach called Conditional Quadrature Method of Moments (CQMOM) to handle bivariate moment formulations in a numerically robust way. Recently, a study in which EQMOM and CQMOM are applied to model soot formation in premixed flames was performed [105].

2.2.2 Discrete sectional method

The discrete sectional methods are based on the separation of the particle size spectrum into a set of size classes. A transport equation is written for each of the classes. This method has a very high computational cost, but it is accurate and gives detailed information about the particle size distribution, if an appropriate number of classes is chosen.

The soot model explained in Chapter 4 is developed using a sectional approach [84, 85], as well as other models recently proposed in literature [75, 106].

For instance, the advanced multi-sectional method developed by Sirignano et al. [75] was broadly validated in rich premixed and non-premixed ethylene flames. Particles were numerically treated as gas-phase species and by using lumped species, tracking the numbers of carbon and

hydrogen atoms. Also three different morphologies were considered with their appropriate kinetics: large molecules, cluster of molecules (i.e. single particles) and agglomerates of particles. The largest gas-phase species was determined by the chemical mechanism used, usually pyrene. All species with a larger molecular weight were conceptually treated as particles but numerically were treated as in the gas-phase. The mass range of these particles was defined by a range of sections and each section was assigned an average molecular weight and H/C ratio ranging from 0 to 1. The number of carbon atoms ranged from 24 in the first section to $2 \cdot 10^{10}$ in the last section. In each section, the three different morphologies were considered.

This model accounted for the inception, coagulation, condensation, and surface growth and oxidation of particles. Specifically, the inception process occurred both through the sticking of gas-phase PAHs and through the formation of large, polymer-like molecules that can coagulate forming the first particle. The coagulation efficiency was considered size-dependent, approaching unity as the size of colliding particles increases. The model took also into account the temperature and the interaction potential between the coagulation entities. Finally two different coagulation efficiencies were used for the coalescence and agglomeration times, allowing both single particles and agglomerates of particles to be considered.

This model accounted for the dehydrogenation process, which allows for the lowering of the hydrogen content in particles, typical of gas-phase PAHs, to very low values, typical of large soot aggregates.

The gas-phase chemistry and particle phase were fully coupled and the chemical evolution of PAHs and particles is tracked.

A novel aspect of this model was the ability to take into account oxidation-induced fragmentation of soot aggregates and particles.

2.2.3 Stochastic approach

Among the stochastic approaches, MC based models were developed in order to approximate the PBE-governed soot particle population using an ensemble of stochastic particles. Monte Carlo methods are known to yield very accurate results; however, due to their computational expense, their applicability has so far been limited to simple configurations.

Indeed several research groups have embarked on detailed modeling efforts aimed to add chemical resolution to nascent soot particles and to resolve chemical composition, size distribution, and morphology [26].

Using a combined kinetic Monte Carlo and molecular dynamics approach, named Atomistic Model for Particle Inception (AMPI), Violi and Venkatnathan [107] probed the structure of incipient soot in a benzene flame. AMPI provides atomistic level structures and morphological information including density and porosity as soot precursors evolve into a three-dimensional structure.

While Kraft and coworkers advanced a PAH-PP (Primary Particle) model [93, 108] and combined it with the Kinetic Monte Carlo - Aromatic Site (KMC-ARS) model, allowing the most detailed particle description in terms of their composition and shape. From this precise description, TEM images and mass spectra have been computationally generated. Primary particles are made up of PAH clusters and the connectivity between primary particles is stored using a binary tree structure. All processes such as inception, coagulation, condensation, and surface growth and oxidation of particles are considered. Inception is considered as the successful sticking of any two PAHs as determined by the collision efficiency model, and an empirical correlation is used with a dependence on the diameter and mass of the smaller of the two colliding PAH clusters. The parameters of the model were obtained by fitting to various features of experimental mass spectra. Characteristic coalescence and agglomeration times are calculated in a similar fashion to the one of the advanced multi-sectional method described in paragraph 2.2.2. This model accounts for the increase in sphericity between any two primary particles in addition to accounting for the increase in mass. Although the particle dynamics and the chemical evolution of PAHs are fully coupled, it is not coupled to the gas-phase. Finally, it is worth noting that the fragmentation process has yet to be added to this stochastic model.

2.3 Experimental techniques for soot diagnostic in premixed flames

The theoretical understanding of the whole soot process discussed earlier have inspired the development of a range of new experimental techniques over the last decade, allowing the mechanisms to be examined at much higher resolutions than previously possible. There are many different techniques both *in situ* and *ex-situ* used for detecting and characterizing soot formed in flames and its precursors. An example of classification of the diagnostics used in premixed flames for gas-phase species and soot particles is shown in Figure 2.5.

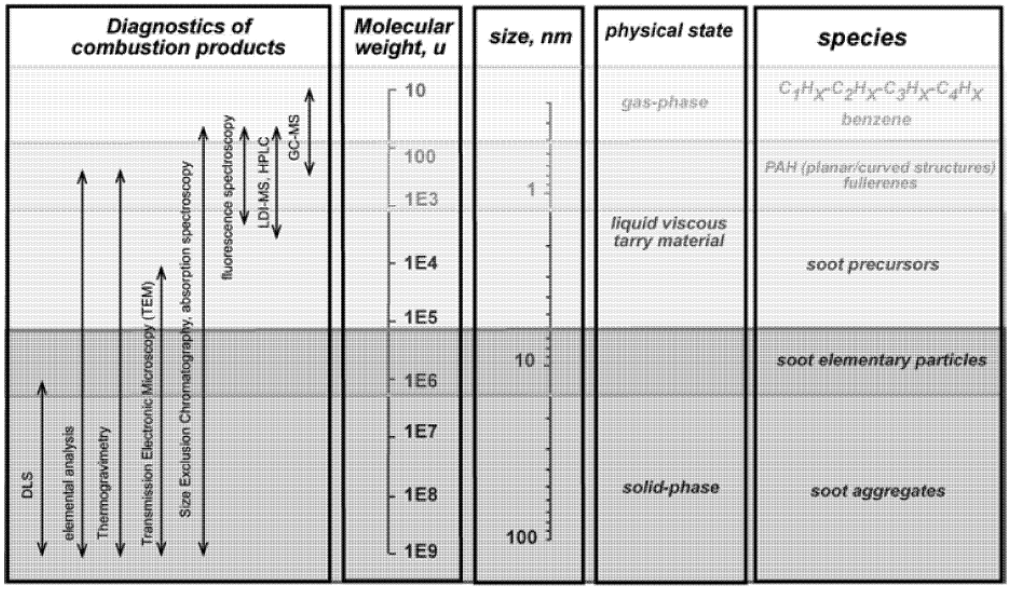

Figure 2.5 Example of classification of the condensed phases in soot formation with an indication of the proper diagnostics for their separation, identification and size evolution. [109]

In particular, this paragraph will focus on experimental techniques adopted for characterizing soot morphology and composition (imaging and spectroscopy techniques) and methods for quantitatively analyze soot formed in premixed flames (probe sampling and optical techniques). Moreover, observations which are relevant to this study will be presented and discussed.

2.3.1 Imaging and spectroscopy techniques

After collecting soot particles in the flame, using for instance the thermophoretic sampling [110, 111], they can be analyzed and characterized with different off-line techniques, such as microscopy and spectroscopy techniques. It is worth to notice that although off-line techniques involve

sampling and handling of the carbonaceous material that could modify soot structure, they offer the possibility to infer important information about the chemistry of the investigated material, not easily available by on-line and in-situ techniques [112].

As discussed in paragraph 1.3, three levels of structure describe soot particles. First is aggregate size - macrostructure. Second is the primary particle size - microstructure. Third is the nanostructure within the individual primary particle. These three descriptors provide continuity over a set of hierarchical length scales to represent aggregate geometry, morphology and atomic layer plane coordination. These are the metrics by which conditions of power and fuel are compared [113].

The electron microscopy allows to obtain information about micro- and nano-structure of soot samples, such as shape, size, distribution of the particles and also graphene layer orientation.

Both Scanning Electron Microscopy (SEM) and Transmission Electron Microscopy (TEM) use a beam of electrons to image the sample structure, while they differ in producing and magnifying images [114]. From a general point of view, SEM provides images of external morphology, whereas TEM looks into the internal structure of solids and analyzes the microstructural details. One of the most important advantages of TEM over other characterization techniques is that information can be obtained both from indirect and direct space. In indirect space, diffraction yields information on the crystallinity of the specimen. Besides this possibility, chemical information can also be acquired using the inelastic interaction of the incoming electrons with the atoms of the specimen. Here two techniques are typical, i.e. Electron Energy Loss Spectroscopy (EELS), and Energy Dispersive x-ray Spectroscopy (EDS). In direct space, two modes are typical, i.e. TEM and HRTEM, which can discern the structure and morphology of a material thanks to the high magnification and high resolution allowed by this technique. The drawback of HRTEM analysis is the projected nature of the micrographs i.e. only two-dimensional information can be extracted.

Instead, Atomic Force Microscope (AFM) is capable of scanning the surface of soot particles deposited on an atomically flat substrate with great resolution and accuracy, in order to obtain their 3D topological map with angstrom resolution in height and nanometer resolution in the plane parallel to the surface. AFM operates differently from SEM and TEM, because it has a

cantilever with a sharp tip that interacts physically with the sample, building up a map of the height of the sample's surface [115]. Nonetheless, AFM usage is not intuitive.

Recently, Helium-Ion Microscopy (HIM) was used to probe the morphological and size evolution of nascent soot in a number of well-characterized, premixed ethylene flames at the same stoichiometry but different flame temperatures [116]. Compared to electron microscopy, HIM allows for better contrast and surface sensitivity, and soot particles as small as 2 nm could be recognized [103]. Size distributions obtained from HIM are found in favorable agreement with previous mobility measurements obtained by Differential Mobility Analyzer in similar flame conditions. The results showed also that soot collected in a burner-stabilized ethylene flame exhibits quite irregular shapes and structures even for those just a few nanometers in size, suggesting that some degree of aggregation starts as soon as soot nucleates. Indeed, particle geometric properties, including sphericity and fractal dimension, exhibit no distinctive change with particle size.

Among all the listed imaging techniques, HRTEM presents the unique features in exploring the internal nanostructure of soot particles by measuring structural parameters like the layer length and the spacing of the Basic Structural Units (BSU) layers. The BSU consists of a local organization of stacked graphene layers, kept together by Van der Waals forces. Firstly, BSU was defined as 2-3 polyaromatic (coronene-like) stacked layers considered as the elemental bricks of the carbon materials [117]. Later on, Rouzaud and Clinard [118] on the basis of HR-TEM fringe analysis, redefined this classical structural model since it resulted to be much more complex than the stacked coronene-like structures.

In recent works, Toth et al. [119, 120] proposed a novel image processing framework for the analysis of soot HRTEM images in order to obtain structural information at native image resolution, increasing statistic robustness. Moreover, he introduced more efficient methods for extracting fringe orientation maps and symmetry parameters, as predicted by liquid crystal theory. The structural parameters obtained by lattice fringe analysis that allows to obtain more quantitative measure of the qualitative observation inferred by the HRTEM images are shown in Figure 2.6.

Figure 2.6 Schematization of the BSU in a skeletonized HRTEM soot image. L_a, L_c and d are the diameter, height and interlayer spacing of the stacked layers. [109]

L corresponds to the mean fringe length and has been evaluated by considering all the fringes larger than the size of 1 aromatic ring (L > 0.25 nm) and all the fringes larger than the size of 2 fused aromatic rings (L > 0.49 nm). L_a and L_c correspond to the diameter and to the height of the coherent domains formed by N stacked layers with an interlayer spacing of d. Graphene layers are considered as stacked to form a BSU only if their angle is smaller than 15° and the interlayer spacing lower than 0.7 nm.

Recently, soot structural parameters obtained by post-processing HRTEM images have been gathered in fuel-rich premixed flames of methane, ethylene and benzene [22, 121]. Usually, the BSU of soot are constituted of about 2–3 stacked layers having a layer length of about 1 nm. The spacing of the BSU layers is quite constant (0.38 nm) and larger than the graphitic spacing of 0.335 nm, due to the turbostratic character of flame-formed soot. The percentage of non-stacked layers (nsl) in respect to the total number of layers is observed to vary from about 40% to 60%. A slight increase of the layer length and the decrease of the nsl percentage can be noticed for the effect of aging and temperature increase. Regarding the fuel effect, it can be assessed that the higher order extent, in terms of higher layer size and lower nsl percentage, is shown by benzene soot in comparison to methane soot that exhibits the larger disorder degree. Among these fuels, ethylene soot shows an intermediate order degree [121].

X-ray Photoelectron Spectroscopy analysis for soot chemistry is complementary to high-resolution transmission electron microscopy for physical nanostructure. XPS can provide elemental composition and carbon bonding hybridization by high resolutions scans about the C1s core energy level. XPS can also reveal surface chemistry, such as oxygen functional groups, and differentiate their bonding state as well.

To investigate the local chemistry of the carbon materials, the Fourier Transform Infrared (FTIR) spectroscopy is also a fundamental tool. FTIR spectroscopy furnishes information about the occurrence of chemical functionality on the sample surface and for instance of adsorbed species on soot surface. It is useful to obtain qualitative and semi-quantitative evaluation of the aromatic and aliphatic hydrogen content [122]. In recent studies, Cain et al. [44] used this technique in conjunction with a micro-orifice uniform deposition impactor. Their results showed aliphatic components to be dominant in nascent soot.

2.3.2 Mobility techniques

Experimentally, probe sampling with scanning mobility particle sizing has been used for a long time to follow the evolution of soot particle size distribution function in flames and other reactors [55-58, 111, 123]. The technique maps the evolution of the size distribution of nascent soot particles and particles as small as 1.6 nm can be detected [124, 125]. These data are now modeled by many groups [70, 75, 108] with particular emphasis on the sensitivity of the PSDF to the respective model parameters, e.g., the collision efficiency [75] and particle rounding due to sintering and surface reactions [108].

In general, the probe sampling technique utilizes a tubular probe crossing the flame. A gas sample from the flame zone is continuously drawn through a pin hole and delivered to a scanning mobility sizer by a carrier gas for particle sizing in the DMA and counting in the Condensation Particle Counter (CPC). The technique is simple to use, but it also has several limitations and requires some care in experimentation and data interpretation [26].

To minimize the problem of probe perturbation in mobility measurements, a burner-stabilized stagnation flame technique was proposed some time ago [53]. In this technique, a previously developed sampling probe is combined with a water-cooled circular plate such that the probe simultaneously acts as a flow stagnation surface and as sampler for subsequent online mobility sizing. The technique allows for a fairly rigorous definition of the boundary condition of the flame and reduces ambiguity in experiment and model comparisons.

Lindstedt and Waldheim [126] examined soot PSDFs in a BSS ethylene flame computationally, using a sectional model coupled with detailed gas-phase chemistry. Comparison with the

experimental data of Abid et al. [53] allowed them to propose a set of collision efficiencies among the nucleating species. In paragraph 5.4, these BSS flame data are studied to test and examine the soot model developed in this work. Meanwhile, the BSS flame technique is used to obtain new experimental data on soot PSDFs in propylene flames, as shown in paragraph 6.1.

Nonetheless, another issue of the mobility technique is that the particle size sampled is the mobility size, which can deviate from the true size even for a sphere [26, 127]. However, the full extent of deviation of nascent soot from spherical shape has only recently been realized. Helium-ion microscopy techniques and other related studies of nascent soot have increased the understanding of how the morphology of nascent soot evolves from the earliest growth stages and these studies suggest that the spherical assumption for nascent soot is no longer valid [103, 116].

A separate diagnostic is necessary to measure the soot mass because the mobility only gives an indirect measure of particle size. To measure particle mass, tandem measurements that involve preselecting particles with a DMA are carried out on atmospheric aerosols, engine exhaust or well-characterized laboratory aerosols [128].

The utility of this technique was first demonstrated using the Aerosol Particle Mass analyzer (APM) [129] to measure the mass of mobility-classified particles in a SMPS system enables first-principles, *in situ* measurements of mass distributions and mass concentrations of particles smaller than about 0.5 μm mobility diameter. It has recently been refined with the introduction of the centrifugal particle mass analyzer [130], in which particles are subject to an electrostatic force and an additional acceleration due to rotational motion. In the CPMA, the balance between the electrostatic force and the opposing radial acceleration allows for particle mass to be classified without any assumptions about the particle shape and morphology. The mass-mobility relationship has been measured for flame [131] and diesel soot [132], but this relationship has not been evaluated for flame soot in the nascent stage. Therefore, paragraph 5.4.4 presents the interpretation of the measured mobility diameter of nascent soot from a premixed BSS ethylene flame, evaluated by measuring the particle mass in tandem with mobility measurements.

Moreover, the fractal dimension or the effective density of soot aggregates can be determined with this tandem technique, as discussed in [133, 134].

2.3.3 Optical techniques

Another group of very promising methods for soot diagnostic are the optical techniques. Optical methods for soot particles are non-intrusive, allowing for material to be probed in a flame and with minimal perturbation, which is decidedly an advantage over for instance extractive techniques. These *in situ* soot optical diagnostics remain invaluable tools, indeed their most attractive application concerns turbulent flames and engines [135]. Here the discussion is focused on their application to laminar flames.

Soot volume fraction can be determined by light extinction or by Laser Induced Incandescence (LII). Soot morphology knowledge can be determined partly by LII and Elastic Light Scattering (ELS) [135]. LII permits to measure the primary particle diameter, while ELS is the most sensitive to aggregate size and can provide information on aggregate size (e.g. radius of gyration, R_g) only if the volume fraction is known. Therefore, a renewed interest in ELS in combination with other diagnostics, such as LII, is currently growing for the instantaneous and synchronous determination of soot volume fraction and morphology.

Optical exploration has also led to new insight into soot inception. Lately, a high-sensitivity two-color LII setup was used to probe the nascent soot particles in low-sooting premixed ethylene/air flames at atmospheric pressure [136]. Interestingly, it was shown that flame conditions near the sooting threshold exist for which the LII decay-time is the same for all heights above burner (HAB), suggesting little or no soot growth. These flames were called nucleation flames and are thought to be very interesting systems for studies of the nucleation step. Particle sizes inferred using the LII model indicate diameters as low as ~1–1.5 nm at low flame positions and similar sizes were found all along the nucleation flames. The results from the evaluation are shown in Figure 2.7.

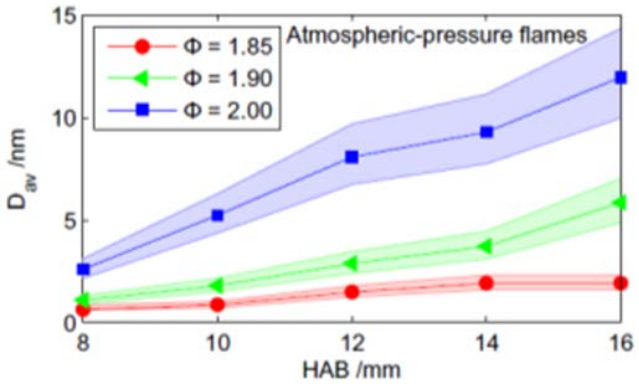

Figure 2.7 Evaluated average primary particle diameters, D_{av}, as function of HAB for atmospheric flames. [136]

It is worth to note that the inferred soot particle size increases with equivalence ratio at a specific flame position and the soot particles appears to grow more rapidly as a function of height above burner for increasing equivalence ratio. It should be noted that there is a high degree of uncertainty in the presented values. The shaded regions in Figure 2.7 visualize the variation in evaluated size when varying both the *E(m)* and the α_T with ±20%.

Despite the various improvements, the ultimate accuracy of the soot diagnostic methods such as LII, light extinction and ELS relies on the knowledge of the soot optical properties, which may vary as a function of soot age in flames. For example, Small Angle X-ray Scattering (SAXS) and Small Angle Neutron Scattering (SANS) techniques have been utilized because of the advantage they have over light extinction and scattering techniques in that they do not require a precise knowledge of the complex refractive index of soot material in data interpretation [26].

2.4 Applications of soot theory

The knowledge gained through the longstanding interest in soot formation may be used and carried over to flame synthesis of functional nanomaterials for clean and renewable energy applications [26].

Actually, combustion as a method of material synthesis is well-known. For instance, titania, which is the white pigment in paints, and silica, used for fiber optics applications, are produced almost exclusively by flame processes [137]. In recent years, new flame-synthesized materials, such as nanoparticles and thin films, are emerging rapidly, with applications in catalysis [138], dye sensitized solar cells [139] and biomedical devices [140].

The flame process holds the key to inexpensive manufacturing of energy conversion materials for use in photovoltaics, rechargeable batteries, and combustion pollutant sensing. As an example, a flame method for producing nanophase titania crystals and mesoporous titania (TiO_2) thin films for dye sensitized solar cells and chemical sensing of gaseous air pollutants was recently proposed in [141]. The flame synthesis technique utilizes well-controlled laboratory flames and particle characterization techniques, both of which were realized through studies into soot formation.

Beyond their common origin in flames, flame soot formation and functional nanomaterial synthesis by flames share many common characteristics. Both involve the formation of condensed-phase materials from gases starting with vapor-phase nucleation, followed by mass and size growth through coalescence, coagulation, surface reactions and condensation of vapor species, and finally by aggregation into fractal structures, all of which occur over very short periods of time, typically a few milliseconds.

Similar diagnostic and computational tools are employed to study the formation of both condensed-phase materials and the long history of studies into soot formation research has yielded many useful insights into nanomaterial synthesis [26]. Some examples are present in [142, 143].

3. Gas-phase kinetic model

The detailed gas-phase kinetic model [144] adopted here consists of about 200 species and 6300 reactions. It describes the high-temperature pyrolysis and oxidation of a wide range of hydrocarbons. This mechanism was developed with a modular and hierarchical approach and using extensively the lumping rules, in order to be able to analyze in a flexible way also the extension towards heavier PAHs species up soot particles. An extensive discussion on chemical lumping procedures adopted in pyrolysis and combustion systems is already reported elsewhere [145]. As discussed in paragraph 2.1.2, many isomers of aromatic compounds are formed with increasing the molecular mass. Therefore, the lumping procedure applied to species and reactions, allowed to account for the behavior of groups of isomers with only one pseudo-species, real or fictitious, and to reduce the number of chemical species and kinetic parameters. Kinetic and thermodynamic properties are obtained from an average of the isomers constituting the lumped compound, thus reducing the computational cost and considering the possible use of this mechanism for multidimensional applications, as described in the work of Stagni et al. [146]. The POLIMI gas-phase model includes the formation of PAHs from benzene to PAHs larger than pyrene (e.g., 9,10-dimethyltetraphene and corannulene). The isomers of heavy PAHs are lumped in a single equivalent species, as in the case of $C_{14}H_{10}$ or $C_{16}H_{10}$. The same lumping technique is adopted to define the BIN species in the soot kinetic model. Thermochemical data for most species were obtained from the CHEMKIN thermodynamic database [147, 148]. For those species whose thermodynamic data are not available in the literature, the group additivity method [149] was used to estimate these properties. To predict soot formation, it has been necessary to couple the detailed gas-phase mechanism with a soot model, which will be described in Chapter 4. Finally, after coupling gas-phase kinetics with the soot kinetic model, numerical simulations of reactors and premixed flames were performed using the updated version of OpenSMOKE code [150].

In this paragraph the refinement and validation of the gas-phase model over a wide range of conditions for the pyrolysis and oxidation of benzene [151] and the pyrolysis of acetylene [152] are presented. Successively, the predicted PAH formation and depletion is tested against experimental

data in premixed ethylene flames and the refined gas-phase kinetic model is coupled with a new version of the method of moments, recently developed in the University of Freiberg [105].

3.1 Benzene pyrolysis and oxidation

Benzene is the first aromatic compound, a relevant intermediate of several combustion processes and also a key precursor to soot formation. Aromatic species are present in significant amounts in liquid fuels such as gasoline, diesel, kerosene, and jet fuels. They are used as anti-knock additives and improve resistance to auto-ignition, thus enhancing the octane number of the fuels. Real and commercial liquid fuels are complex and variable mixtures of several hydrocarbon species. Therefore, both in numerical simulations and in the experimental investigation of combustion processes, the complex real fuels are often simplified and represented by surrogates, in which aromatics are key components [153]. As a result, the proper kinetic understanding of the primary steps in the chemistry of aromatic species is also crucial to the kinetic modeling of surrogate mixtures. Since the pioneering work of Brezinsky [154], the pyrolysis and oxidation reactions of benzene and alkyl aromatics have been widely debated and an extensive range of experimental data is now available in the literature.

The goal of this work was to further validate the general and detailed POLIMI kinetic mechanism [144] using the complete set of experimental data of benzene pyrolysis, oxidation and combustion. The refined kinetics of benzene oxidation will lay the basis not only for the extension of the scheme towards heavier aromatic fuels, but also for a better kinetic understanding of the successive growing processes of PAH and soot. The initial benzene conversion proceeds mainly through H-abstraction from benzene (C_6H_6) to form the phenyl radical (C_6H_5), followed by C_6H_5 oxidation to form the phenoxy radical (C_6H_5O). In addition to this, benzene may be oxidized directly with the oxygen atom to form phenol (C_6H_5OH), phenoxy, or CO and cyclopentadienyl radical (C_5H_5). At high temperatures, the phenoxy radical quickly decomposes to form CO and cyclopentadienyl, while at low temperatures recombination reactions of these radicals have a significant effect on the chemistry of benzene decomposition. Even from these simple features, it is clear that a hierarchical and modular approach to the chemistry of benzene and aromatics first demands a proper description of the pyrolysis and oxidation of cyclopentadiene and the C_5H_5

radical, as well as of phenol and the C_6H_5O radical. Reaction flux and sensitivity analyses of different reacting systems, herein successively presented and discussed, show the crucial role of specific reactions and interactions amongst phenyl, phenoxy and cyclopentadienyl radicals.

Figure 3.1 shows an axonometric view of all the reviewed experimental conditions.

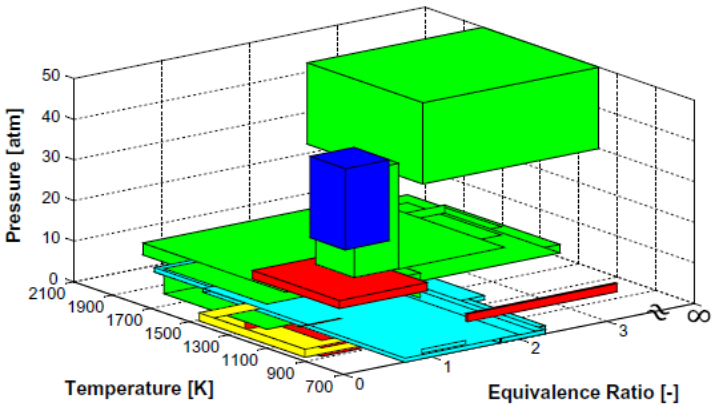

Figure 3.1 Axonometric view of the analyzed experimental conditions as function of temperature, pressure and equivalence ratio. The different colors refer to different reactors and conditions (red: jet stirred reactor, yellow: plug flow reactor, green: shock tube, blue: rapid compression machine, cyan: flame conditions). [151]

The focus of the analysis of benzene kinetics was on high pressure pyrolysis experiments, ignition delay times in shock tubes, premixed flames as well as low temperature reactions with recombination and propagation reactions of cyclopentadienyl and phenoxy radicals playing a significant role. Collecting and reviewing this large amount of new experiments relating to benzene pyrolysis and oxidation allowed both to analyze them by using and refining the POLIMI detailed kinetic mechanism and thereby to identify sensitive and crucial portions of the mechanism itself. As a result, the kinetic model may also become a useful tool in comparing and unifying different sets of experimental measurements.

The detailed study of the comparisons between model predictions and experimental data is thoroughly described in the work of Saggese et al. [151], while herein a comprehensive discussion of some representative experimental data performed at different operating conditions is carried out in such a way to point out the main kinetic findings and results. Mainly three different conditions are explored and discussed, namely benzene oxidation in lean and rich conditions in the Princeton flow reactor, high pressure partial oxidation in a jet stirred reactor and high temperature combustion in premixed laminar flames. Moreover, a comparative analysis of the flux analysis of these

conditions allows to derive a final comment on the overall benzene oxidation mechanism in the different reacting systems. Finally, an example of pyrolysis conditions in a shock tube experiment is analyzed and discussed using the POLIMI kinetic model.

Aromatic hydrocarbon pyrolysis and oxidation were extensively studied in the Princeton flow reactor at temperatures up to 1200 K and all this activity was critically reviewed by Brezinsky [154]. Parallel to the H-abstraction reactions to form phenyl radical, benzene oxidation mainly proceeds via O• and OH• radical addition to the ring to produce phenol and the phenoxy radical. Furthermore, with low O• and H• radical concentrations, the reaction of the phenyl radical with molecular oxygen is a significant source of phenoxy radicals. Subsequent C_6H_5O pyrolysis leads to CO and cyclopentadienyl radical. Successive O• attack on C_5H_5 leads to ring opening and C_4H_5 formation. Both the phenyl radical addition to O_2 and the reaction of phenoxy radical with an O• atom lead to benzoquinone (OC_6H_4O) formation. Both these reactions are fuel-specific sensitive reactions in the laminar flame speed of benzene and aromatic species. In this refined kinetic model, the two benzoquinone isomers are lumped into a single equivalent species.

Figure 3.2 shows the profiles of benzene and major products of the atmospheric oxidation of benzene at Φ = 0.76 and Φ = 1.36 and ~1100 K in the Princeton plug flow reactor [155].

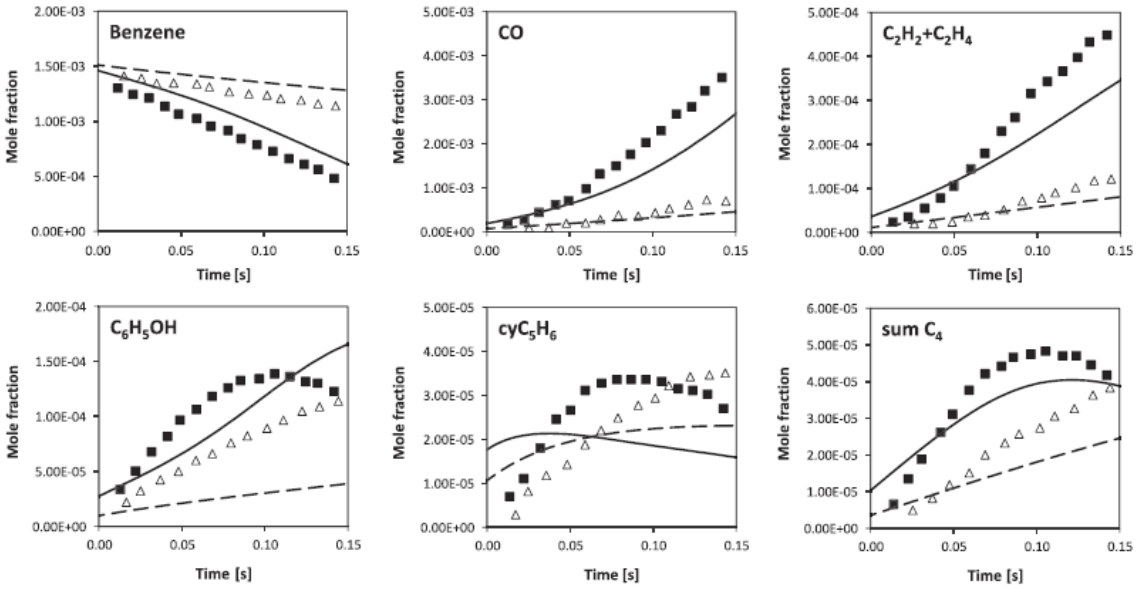

Figure 3.2 Profiles of benzene and main products from the oxidation of benzene at ~1100 K in the Princeton plug flow reactor [155]. Experimental data (Φ = 0.76: squares, Φ = 1.36: triangles), model predictions (solid and dashed lines).

The experiments are conveniently modeled as an isobaric and adiabatic plug flow reactor only after the initial mixing zone and the experimental data are shifted by 30 ms. Figure 3.3 shows the main reaction paths in benzene oxidation at Φ = 1.36 and benzene conversion of 15%. The thickness of the arrows reflects the relative importance of the different reaction paths.

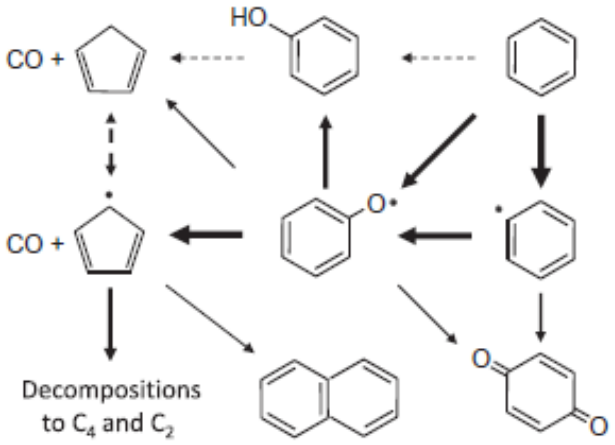

Figure 3.3 Main reaction paths in benzene oxidation in the Princeton flow reactor. The thickness of the arrows reflects the relative significance of the different reaction paths at Φ = 1.36 and 15% of benzene conversion.

The important role played by the cyclopentadienyl radical, both with the oxidation and decomposition reactions to form CO and C2 and C4 species, and with the recombination reaction to form naphthalene is quite clear. The model properly reflects the relative amount of main products even though a systematic under prediction of overall benzene reactivity is observed. The predicted conversion agrees better with similar benzene oxidation data, reported in [156].

The kinetic model is also tested against the high pressure data of benzene partial oxidation and combustion of Marchal et al. [157] obtained in a jet stirred reactor. These data refer to 10atm, residence time of 0.7s, a wide range of temperatures (900-1200K) and equivalence ratios (0.5-1.5). As can be seen from Figure 3.4, the model overpredicts benzene conversion, but is still able to reproduce the pressure and stoichiometry effects and the main trends of the experimental data.

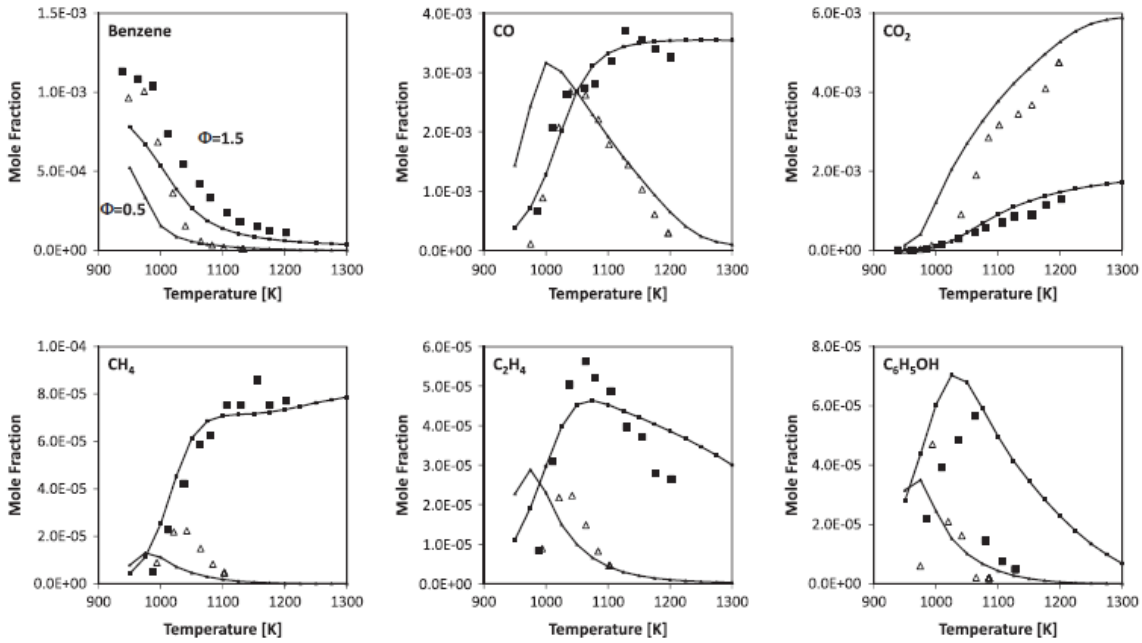

Figure 3.4 Benzene oxidation in a jet-stirred reactor at Φ = 0.5 (triangles) and Φ = 1.5 (squares), at 10 atm and 0.7 s [157]. Comparisons between experimental (symbols) and predicted (lines with small symbols) mole fractions.

Figure 3.5 shows the main reaction paths in benzene oxidation at 1000 K, Φ = 1.5, and benzene conversion of 50%.

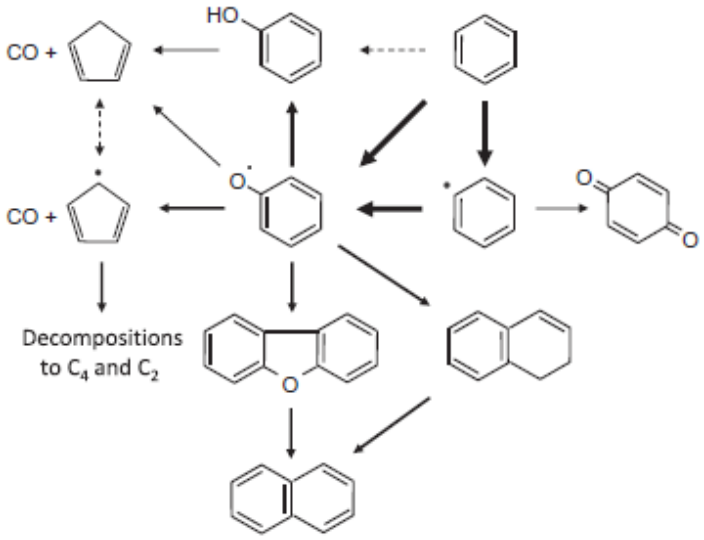

Figure 3.5 Major reaction paths of benzene oxidation in a jet-stirred reactor at 10 atm and 1000 K. The thickness of the arrows reflects the relative significance of the different reaction paths at Φ = 1.5 and 50% of benzene conversion.

At this high pressure and intermediate temperature, the important role played by the recombination reactions of phenoxy radicals forming heavier species is quite clear. The recombination of phenoxy radicals with H_2O elimination and dibenzofuran formation is considered, as well as a parallel lumped recombination reaction with the intermediate formation of dialin

($C_{10}H_{10}$). Both benzofuran and dialin are thus responsible for naphthalene formation. The high temperature CH_4 formation in rich conditions (Figure 3.4) is mainly due to ethylene and vinyl radical oxidation to form ketene which adds H• atoms and decomposes with methyl formation.

The combustion chemistry of benzene is further studied in the high temperature conditions typical of premixed laminar flames. Similar rich and low-pressure benzene flames (Φ = 1.78-2; P = 25-40 mbar) have been studied by many different groups using different experimental techniques [158-161]. These experimental data have been very useful not only in further validating and improving the kinetic model, but also in evaluating possible uncertainties and discrepancies related to experimental measurements. The thorough comparisons among all experimental data and model predictions are shown in the work of Saggese et al. [151], while herein the focus will be on the benzene kinetics in flames using only the data of Bittner and Howard [158] as an example to support the discussion. Bittner and Howard [158] studied a near-sooting rich premixed benzene flame at Φ=1.8 using Molecular Beam Mass Spectrometry (MBMS). The flame was operating at a total pressure of 26.7 mbar with initial mixture concentration of 13.5% C_6H_6, 56.5% O_2, and 30% Ar. Figure 3.6 reports the comparisons of predicted and experimental profiles of the major species up to heavier PAHs formed in this laminar premixed benzene flame.

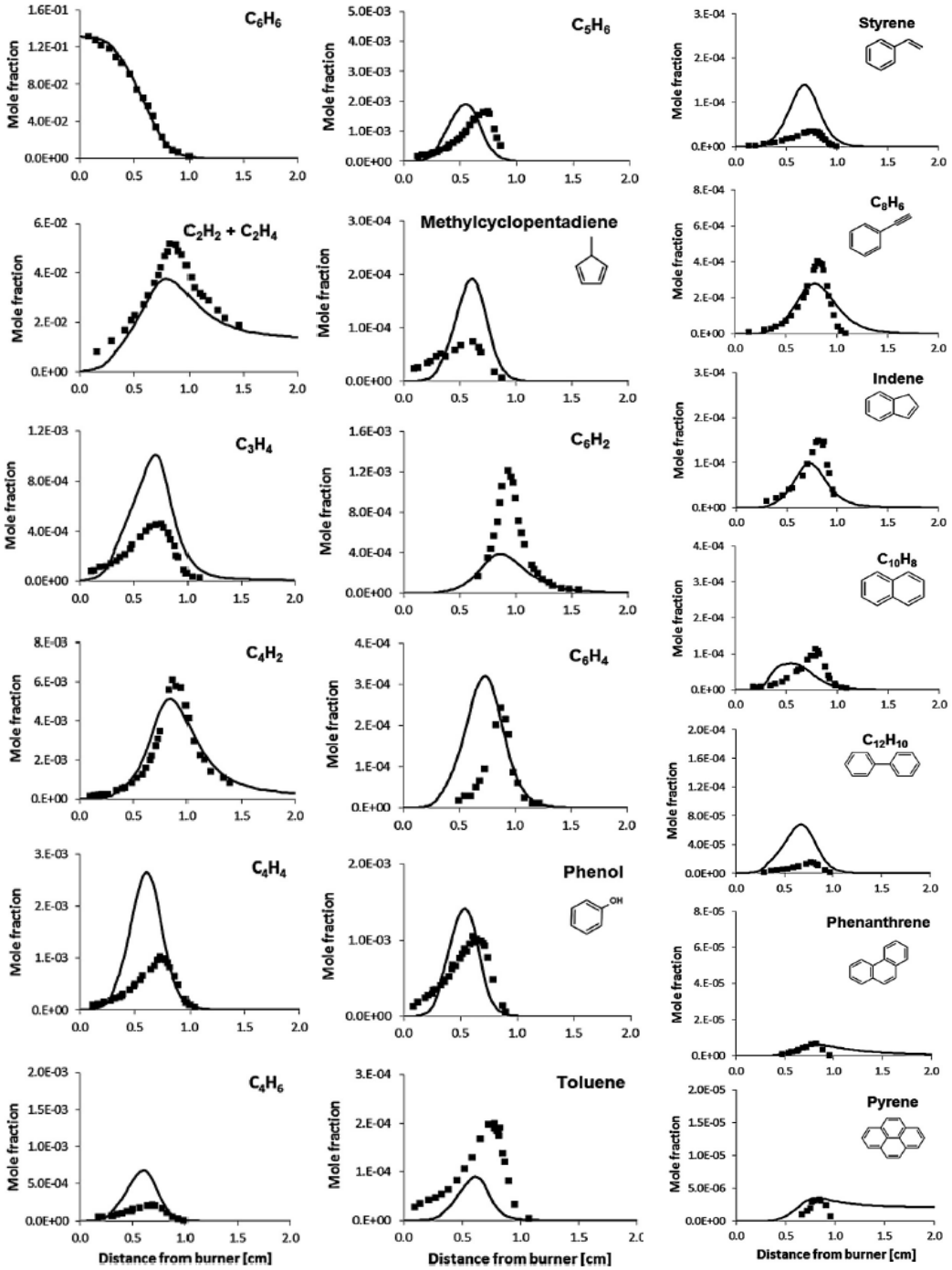

Figure 3.6 Profiles of major species up to heavier PAHs of benzene combustion in a low-pressure and rich flame [158]. Experimental data: symbols. Model predictions: lines.

The model predictions agree reasonably well with the experiments and the following main considerations can be derived from the analysis of Figure 3.6:

- Model deviations of C2 and C3 species are within the experimental uncertainties. Note that C_3H_4 is the sum of allene and propyne and model predictions also agree fairly well with the relative amount of the two isomers.

- C_4H_6 is overpredicted in comparison with these data. Butadiene is then decomposed mainly producing C2 and C4 species.
- C_4H_2 is the most abundant C4 species and is well predicted by the model. Diacetylene mainly derives from the decomposition of *o*-C_6H_4.
- Cyclopentadiene is well predicted, as well as the lower concentrations of methylcyclopentadiene.
- At high temperatures and flame conditions, the H-abstraction reactions on the phenyl radical promoted by OH•, H• and O• radicals account for only a small amount of total phenyl depletion. These reactions justify the formation of C_6H_4, with the successive dehydrogenation reactions to form C_6H_3 and then the more stable C_6H_2, which is relatively important with mole fractions up to 10^{-3}.
- The mole fraction of phenol, which mainly derives from the very important H recombination reaction of the phenoxy radical, is slightly overpredicted.
- The predicted formation of heavier aromatics, such as toluene, styrene and phenyl-acetylene is reasonable and consistent compared to the experimental uncertainties, while naphthalene and indene are underpredicted.

To better understand the meaning of the comparisons, Figure 3.7 reports the rate of production analysis (ROPA) of the analyzed flame.

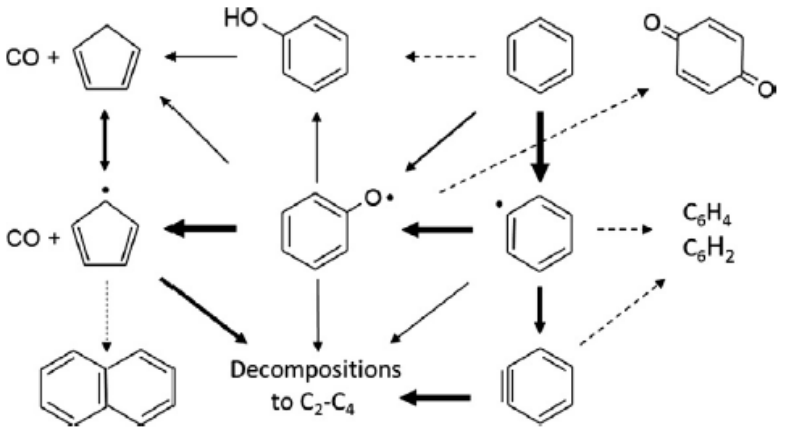

Figure 3.7 Main reaction pathways in the rich and low-pressure flame. The thickness of the arrows reflects the relative significance of the different reaction paths.

At high temperatures and in rich conditions, the most favored decomposition path for benzene is phenyl radical formation with the latter oxidized to form the phenoxy radical. Once again, the

phenoxy radical can mostly decompose to cyclopentadiene and CO and partly recombine with H• atoms to form phenol.

The comparative analysis of Figure 3.3, Figure 3.5 and Figure 3.7, which show the main reaction paths of benzene decomposition, provides a better description of the overall benzene oxidation mechanism in the different reacting systems. The addition reaction of O• atoms to benzene to form phenoxy radicals always competes with the H-abstraction reactions, because it is difficult to remove H• atoms from the aromatic ring. H• and OH• are the major H-abstracting radicals and the relative prevailing role of H• is mainly seen in flame conditions, due to its back diffusion. The H-abstraction reaction of O• atoms accounts for less than 10% of the total H-abstraction reactions on benzene, and is also of limited importance with respect to the O• addition to form phenoxy. Phenyl radical addition to O_2 to form phenoxy radical always prevails with respect to benzoquinone formation. Nonetheless, the reactions involving benzoquinone formation are sensitive reactions in premixed laminar flame speed computations. Thus, benzene decomposition mostly moves through the successive reactions of the phenoxy radical which assumes a central role in the overall oxidation mechanism. In the high or intermediate temperatures of benzene oxidation in the flames (Figure 3.7) or in the flow reactor (Figure 3.3), the phenoxy radical mainly decomposes to form cyclopentadienyl radical. The recombination reaction with H• to form phenol is less significant. Decomposition reactions of the phenoxy radical with the breaking of the aromatic ring to form C2-C4 species play a marginal role, also in flame conditions. At high temperatures, the C_5H_5 radical mainly decomposes to form C4 and lower species. The main reaction paths of benzene decomposition from Figure 3.5 show that, at high pressure and lower temperatures, phenoxy radical decomposition is less important and recombination reaction to form dibenzofuran plays an increasingly important role. A similar consideration also applies to C_5H_5 radicals and to their recombination reaction.

Regarding benzene pyrolysis, Figure 3.8 shows the comparison between model predictions and experimental data obtained in a study of the thermal decomposition of benzene [162]. This analysis was performed behind reflected shocks, in a pressurized driver single-pulse shock tube, in the temperature range 1400-2000K and contact times of ~2 ms.

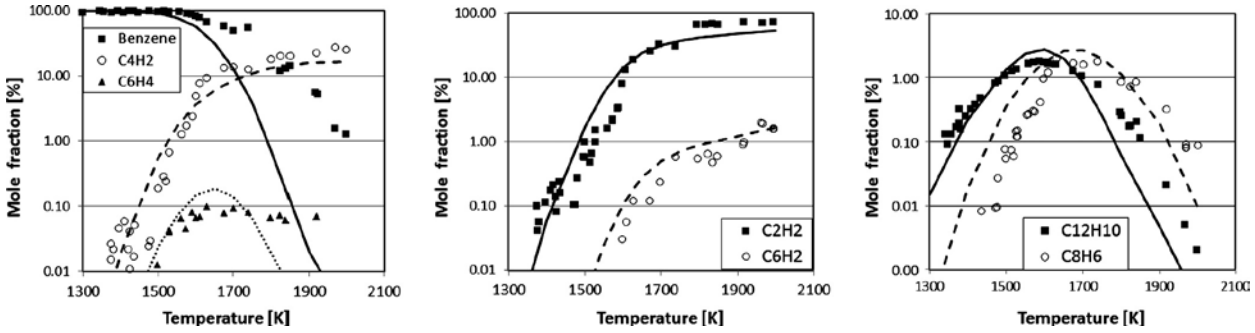

Figure 3.8 High temperature pyrolysis of benzene [162]. Experimental data (symbols) and predicted mole percent (lines) as a function of temperature.

As shown in Figure 3.8, temperature strongly affects benzene pyrolysis. At lower temperatures, recombination reactions are favored and a significant amount of biphenyl is formed. Increasing the temperature, phenyl radical can also break the aromatic ring and form C2 and C4species. At high temperatures, the acetylene addition on the aromatic ring forms PAHs through the typical HACA mechanism, starting from phenyl-acetylene. At very high temperatures (T > 1800 K), the aromatic ring decomposition starts to compete and prevails on PAHs formation. This pyrolysis mechanism explains the well-known bell shaped temperature dependence of the soot volume fraction and confirms the importance of benzene as intermediate in soot formation.

In conclusion, the discussion of the chosen representative conditions of benzene combustion has shown the major findings of the systematic and hierarchical revision of the POLIMI kinetic mechanism, that is carried out by moving from pyrolysis experiments to partial oxidation and combustion in very lean conditions and by a detailed and comparative flux analysis on the different systems. A wide range of temperatures and pressures are analyzed and the predictions of a general kinetic model are compared with a large set of experimental measurements coming from different sources. In this way a more reliable validation of the kinetic scheme is performed and the possible use of the kinetic scheme as a tool for unifying measurements and indicating areas of major experimental uncertainties is shown.

3.2 Acetylene pyrolysis

Diffusion flames, rich combustion and pyrolysis conditions represent the most favored reacting systems in which soot formation occurs. All these conditions also highlight the key role of acetylene, besides benzene, as an important precursor to PAHs and soot nucleation and formation through the HACA mechanism. Therefore acetylene pyrolysis kinetics is reviewed and refined in the POLIMI detailed kinetic mechanism [144] over a wide range of conditions, especially from 900 to 2500 K [152]. The revised reactions and their kinetic constants are shown in **Figure 3.9**.

reactions	$k = AT^n \exp(-E_a/RT)^a$	A	n	E_a
	Acetylene Reactions			
1	$C_2H_2 + C_2H_2 \leftrightarrow C_4H_4$	1.5×10^9	0	37 400
2	$C_2H_2 + C_2H_2 \leftrightarrow C_4H_2 + H_2$	1.0×10^{13}	0	68 200
3	$C_4H_4 \leftrightarrow C_4H_2 + H_2$	3.5×10^{11}	0	66 000
4	$C_2H_2 + C_2H_2 \leftrightarrow C_4H_3 + H$	2.0×10^{13}	0	81 500
5	$C_4H_4 \leftrightarrow C_4H_3 + H$	3.682×10^{19}	−1	116 282
6	$C_2H_3 + C_2H \leftrightarrow C_2H_2 + C_2H_2$	3.3×10^9	0	−1 980
7	$H + C_2H_2 + M \leftrightarrow C_2H_3 + M$	$k_\infty = 5.9 \times 10^9$	0	2 770
8	$C_2H_2 + H \leftrightarrow C_2H + H_2$	5.7×10^5	1.9	30 259
9	$C_2H + C_2H_2 \leftrightarrow C_4H_3$	1.5×10^{10}	0	0
10	$C_2H + C_4H_2 \leftrightarrow C_6H_2 + H$	7.5×10^9	0	0
11	$C_2H + C_6H_2 \leftrightarrow C_8H_2 + H$	5.0×10^9	0	0
12	$C_2H_2 + C_4H_4 \rightarrow C_6H_6$	6.0×10^9	0	37 400
13	$C_2H_2 + C_2H_3 \leftrightarrow C_4H_4 + H$	8.0×10^8	0	5 000
14	$C_2H_2 + C_4H_5 \leftrightarrow C_6H_6 + H$	5.0×10^8	0	5 000
15	$C_2H_2 + C_6H_5 \leftrightarrow C_8H_6 + H$	2.0×10^9	0	8 000
16	$C_2H_2 + C_8H_5 \rightarrow C_{10}H_7$	1.0×10^9	0	5 000
	Vinylacetylene and Diacetylene Reactions			
17	$C_4H_4 \leftrightarrow C_2H + C_2H_3$	1.0×10^{16}	0	105 000
18	$C_4H_4 + C_4H_4 \leftrightarrow C_4H_3 + C_4H_5$	5.0×10^{13}	0	81 500
19	$C_4H_4 + C_4H_4 \rightarrow C_8H_8$	1.2×10^{10}	0	37 400
20	$C_4H_4 + C_4H_4 \rightarrow C_8H_6 + H_2$	1.0×10^{11}	0	44 000
21	$C_4H_4 + C_4H_4 \rightarrow C_6H_6 + C_2H_2$	2.5×10^{11}	0	44 000
22	$C_4H_5 \leftrightarrow H + C_4H_4$	5.0×10^{12}	0	44 000
23	$H + C_4H_4 \leftrightarrow C_2H_4 + C_2H$	2.0×10^{10}	0	2 000
24	$H + C_4H_3 \leftrightarrow C_4H_2 + H_2$	1.0×10^{11}	0	0
25	$H + C_4H_2 \leftrightarrow C_4H_3$	2.5×10^{11}	0	3 016
26	$C_6H_3 + C_2H \leftrightarrow C_4H_2 + C_4H_2$	5.5×10^9	0	0
27	$C_4H_2 + C_4H_2 \leftrightarrow C_6H_2 + C_2H_2$	2.0×10^{13}	0	54 000
28	$C_4H_2 + C_4H_2 \leftrightarrow C_8H_2 + H_2$	2.5×10^{11}	0	44 000
29	$C_4H_2 + C_6H_2 \leftrightarrow C_8H_2 + C_2H_2$	6.0×10^{12}	0	44 000
30	$C_4H_2 + C_2H_2 \leftrightarrow C_6H_2 + H_2$	1.0×10^{13}	0	68 125
31	$C_2H_2 + C_6H_2 \leftrightarrow C_8H_2 + H_2$	5.0×10^{10}	0	44 000

[a]Units are: mole, L, s, K, and cal. [b]Adjusted to maintain the similarities and analogies among similar reactions.

Figure 3.9 Major reactions of Acetylene, Vinylacetylene, and Diacetylene Pyrolysis.

This study of Saggese et al. [152] moves from the analysis of data involving primary decomposition of acetylene and its first intermediates (C_4H_4 and C_4H_2) with negligible soot formation, to more

severe conditions of temperature, time and pressure, that permit to study successive addition and condensation reactions to form heavy PAHs and soot. As schematically shown in Figure 3.10, the pyrolysis mechanism of acetylene conversion first moves through successive addition and condensation reactions.

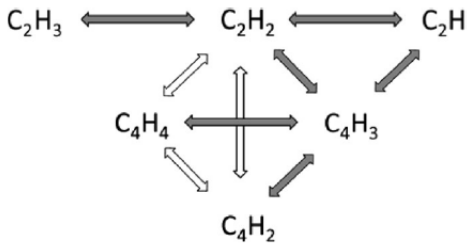

Figure 3.10 Acetylene pyrolysis: major radicals (filled arrows) and molecular paths (empty arrows).

Vinylacetylene (C_4H_4) and diacetylene (C_4H_2), together with C_2H•, C_2H_3•, and C_4H_3• radicals, are the first intermediates. This mechanism is indeed characterized by a competition between molecular and radical reaction paths. As discussed by Kiefer and Von Drasek [163], the core mechanism of acetylene pyrolysis relies on five major reaction steps, reported in Figure 3.9 as:

R1) $C_2H_2 + C_2H_2 \leftrightarrow C_4H_4$

R2) $C_2H_2 + C_2H_2 \leftrightarrow C_4H_2 + H_2$

R3) $C_4H_4 \leftrightarrow C_4H_2 + H_2$

R4) $C_2H_2 + C_2H_2 \leftrightarrow C_4H_3\bullet + H\bullet$

R5) $C_4H_4 \leftrightarrow C_4H_3\bullet + H\bullet$

Successive molecular polymerization reactions explain the formation of heavier species, whereas secondary radical processes allow the acetylene pyrolysis mechanism to complete. According to the kinetic analysis of Kiefer and Von Drasek [163], acetylene pyrolysis follows a molecular polymerization path at temperatures lower than 1100 K and chain radical reactions at temperatures higher than 1800 K, where H• and C_2H• drive the polymerization path to form polyynes. Vinylacetylene, benzene, and phenyl-acetylene are the major products of a second order molecular path. At high temperatures, the acetylene pyrolysis becomes of lower order and C_4H_2 together with C_6H_2 are the more stable intermediates, with only minor traces of C_3H_4 and butadiene. Because of the high activation energies of the radical chain initiation reactions R4 and R5, the high temperature mechanism is mainly a free radical process.

Figure 3.11 shows the comparison of predictions of the revised POLIMI mechanism and the experimental data of the neon-diluted pyrolysis of 3.2% of acetylene at 0.3-0.5 atm [164], in terms of acetylene conversion and diacetylene and triacetylene formation.

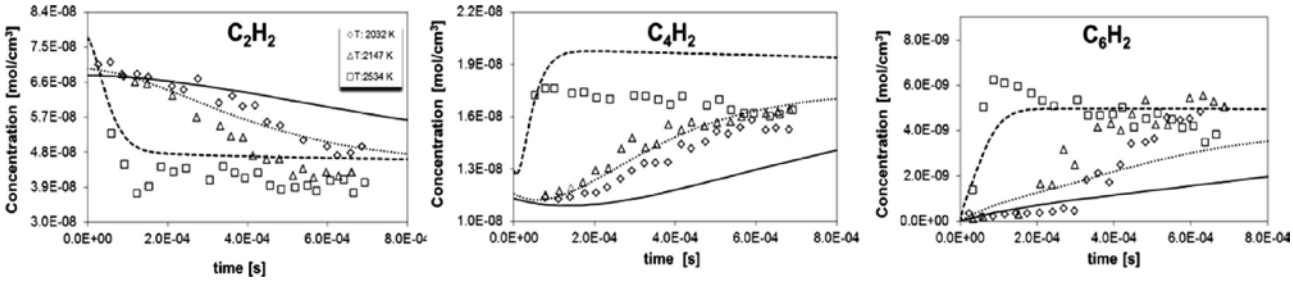

Figure 3.11 Low-pressure shock tube pyrolysis of acetylene at 2032-2147 and 2534 K [164]. Comparisons of experimental (symbols) and predicted results (lines: solid, T=2032 K; dotted, T=2147 K; and dashed, T=2534 K).

Chain radical reactions prevail in these conditions, and the molecular paths account for less than 20% of acetylene decomposition at 2032 K. Despite the low pressure and the limited reaction times, the formation of heavier species, lower than 5% in terms of carbon selectivity at 2032 K, becomes higher than 40% at 2534 K.

At temperatures lower than 1200 K, the molecular reaction path is the prevailing one, and reaction R1 is the major one responsible for acetylene conversion. In these conditions, the successive addition reaction of C_2H_2 on vinylacetylene forms the first aromatic ring of benzene. At higher temperatures of the shock tube experiments, the chain radical mechanism prevails, together with the HACA mechanism to form aromatics and PAHs. As will be better discussed later, the mechanism below 1500 K is still the subject of sharp controversy and is influenced by the impurities of the feed. Manufacturers often specify acetylene to be only 99.6% pure, containing up to 30 000 ppm of acetone. For this reason, the acetylene feed is usually passed through a dry acetone cold trap packed with glass beads to remove acetone contamination to less than 100-150 ppm of acetone. Colket et al. [165] discussed the role of these acetone impurities in the feed in explaining the low temperature chain radical process.

In order to explore acetylene pyrolysis at lower temperatures and in more severe conditions, the recent data of Sánchez et al. [166, 167] are investigated with the refined POLIMI kinetic model. Acetylene pyrolysis is studied in a quartz flow reactor of 4.5 cm inside diameter and 80 cm in

length, placed inside an electric furnace. The reactor inlet and outlet can be cooled by means of an air flow that allows the control of temperature inside the reactor. Additionally, the reactor outlet is mobile and, thus, can be adjusted to vary the residence time. Temperature inside the reactor has been measured with a ceramic S thermocouple, so the temperature profile data are available and are used in the calculations. The outlet of the reactor was linked to a quartz filter for soot collection and a resin trap for capturing the PAH in the gas phase. Thus, suitable methods were used to analyze light gases, PAH, and soot [167]. These data are interesting because of the very severe conditions tested and relative low temperatures, as well as the accurate details on intermediate PAHs, and also because these experiments are carried out under sooting conditions. Figure 3.12 and Figure 3.13 compare the experimental data and model predictions for two different series of pyrolysis experiments with different C_2H_2 concentration and residence times (10000 ppm and 1.5 ± 0.3 s; 30000 ppm and 3.8 ± 1 s) as a function of the reaction temperatures.

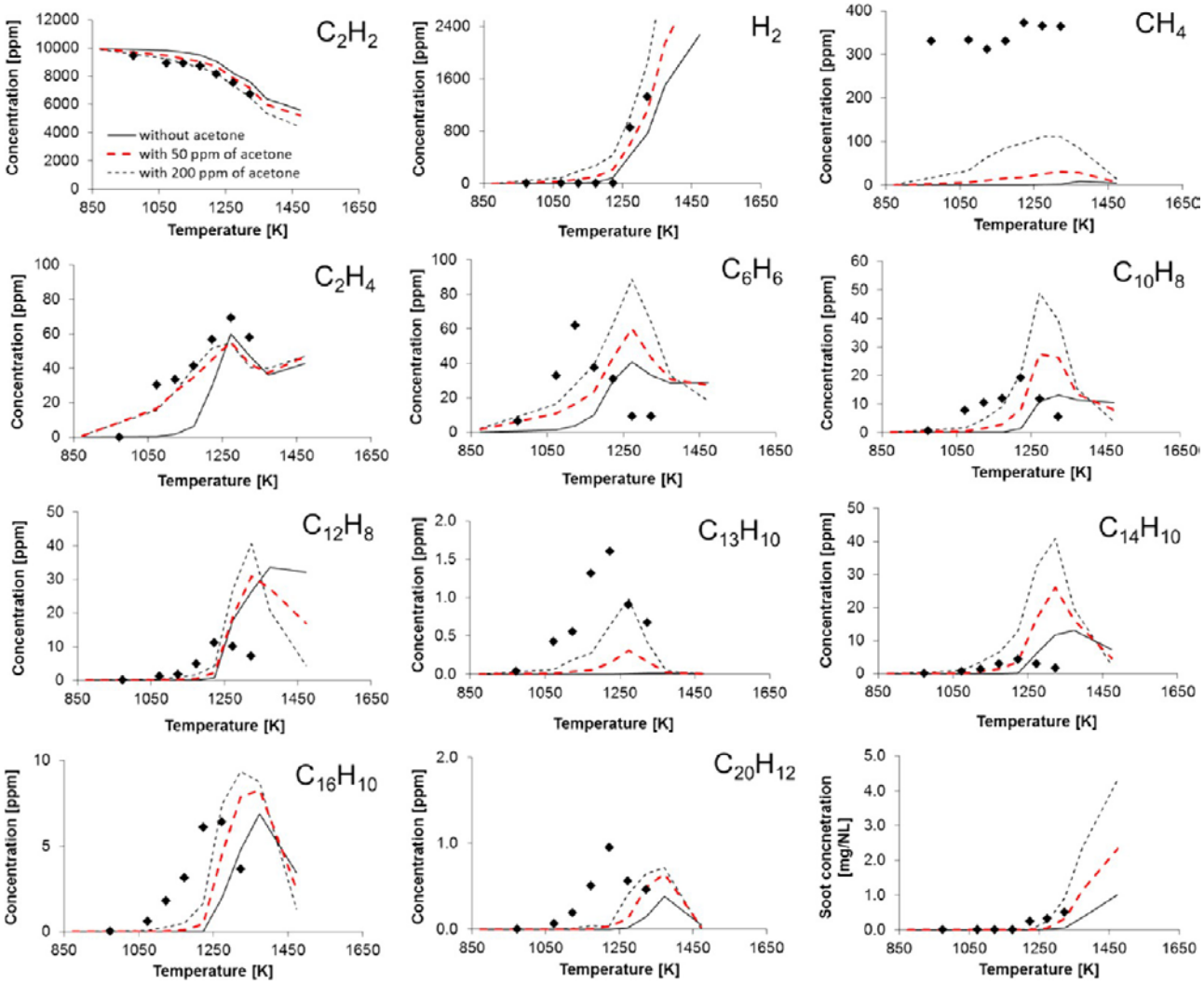

Figure 3.12 Nitrogen-diluted pyrolysis of 10000 ppm of acetylene in a flow reactor at atmospheric pressure [166, 167] without acetone (solid line) and with 50 ppm (red dashed line) and 200 ppm of acetone (black dashed line). Comparisons of experimental (symbols) and predicted (lines) results at 1.5 ± 0.3 s.

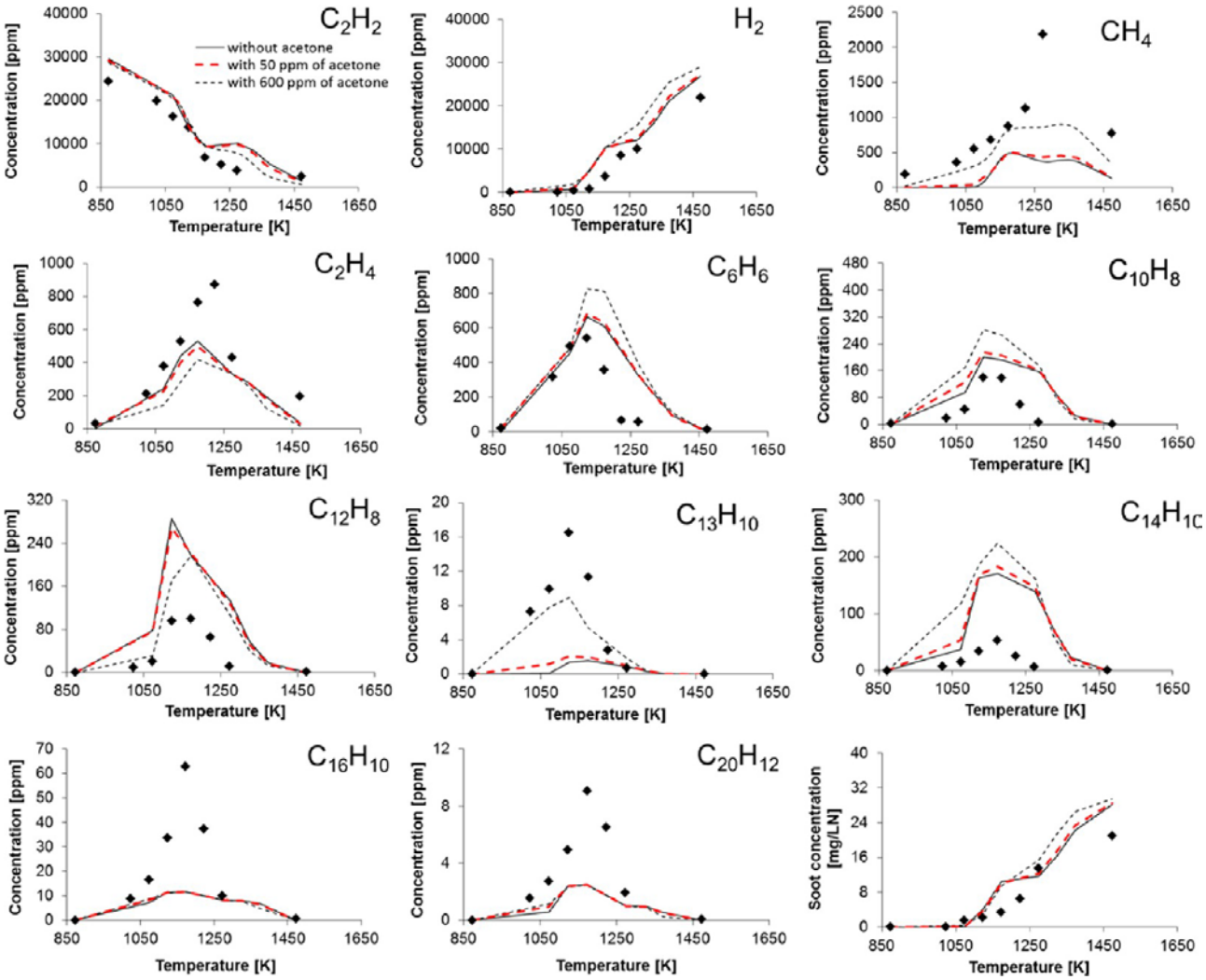

Figure 3.13 Nitrogen-diluted pyrolysis of 30000 ppm of acetylene in a flow reactor at atmospheric pressure [166, 167] without acetone (solid line) and with 50 ppm (red dashed line) and 600 ppm of acetone (black dashed line). Comparisons of experimental (symbols) and predicted (lines) results at 3.8 ± 1 s.

The experiments are carried out with reaction temperatures between 873 and 1473 K and large amount of soot is formed, mainly at the highest temperatures. No appreciable acetone is present in the acetylene feed, and the possible traces are expected to be limited to a few parts per million. Feed analysis during some experiments confirmed that acetone was measured up to 50 ppm only when the bottle was about to be finished. Nevertheless, following the kinetic study of Colket et al. [30] and only to analyze the possible acetone effect, the model predictions in Figure 3.12 and Figure 3.13 are reported both without acetone in the feed and with 50 ppm of acetone. To further stress this effect, 200 ppm of acetone in the case of 10000 ppm of acetylene and 600 ppm in the case of 30000 ppm of acetylene are also considered.

The model predictions show that the influence of acetone concentration is not significantly important. Molecular reaction paths of acetylene conversion are the dominant ones in these conditions. In agreement with the experiments, the carbon selectivity towards soot is lower than 10% in the first series of experiments (Figure 3.12) and becomes higher than 70% at the highest severity conditions of Figure 3.13. The conversion of acetylene is generally well predicted together with the formation of the main final products, hydrogen and soot. The experimental benzene peak at ~1070 K is well represented by the model at longer residence time and higher initial acetylene concentration, while at shorter residence time and lower initial acetylene concentration the model shows a later benzene peak at ~1250 K due to the slower acetylene conversion. In the latter case the model does not agree with the benzene experimental profile, that seems to be not coherent with the measured acetylene conversion. The predicted profiles of heavier PAH, such as $C_{14}H_{10}$ and $C_{16}H_{10}$, are considered lumped species in the POLIMI kinetic model and compared with the correct sum of the respective measured isomers. Moreover, the predicted $C_{20}H_{12}$ is lumped between the first two pseudo-species BINs. These two pseudo-species (BIN_{1A} and BIN_{1B}) belong to the soot model, as explained in Chapter 4. The soot model is coupled with the refined gas-phase mechanism and a preliminary satisfactory comparison of predicted and measured soot profile in this flow reactor is shown in Figure 3.12 and Figure 3.13. According to the kinetic model, the impurity of acetone seems to justify a higher reactivity at low temperatures and a larger formation of methane and fluorene because of the increased methyl radical concentration. Acetone enhances benzene formation and PAHs odd growth pathways. In fact, the rate of production analysis and sensitivity analysis of acetylene pyrolysis show that the first ring is formed not only through the molecular reaction between acetylene and vinylacetylene, but also through C3 pathways, such as propargyl recombination and toluene decomposition. Propargyl radical is mainly formed by propyne, which derives again from the methyl attack on acetylene, increased in quantity by acetone presence. The benzyl radical, which then evolves into toluene, is formed by the propargyl radical and the acetylene addition on cyclopentadienyl radical. The general agreement is fair, though $C_{14}H_{10}$ is overpredicted. This fact, mainly if further supported by different experimental data, seems to indicate that the reaction path to form heavier species from phenanthrene could be increased. Moreover, the dimerization of the heavy PAHs, such as pyrene and the first pseudo-species BINs,

can be considered of lower importance, in line with the fact that the collision efficiency decreases reducing the mass of colliding particles, as also suggested by Sabbah et al. [168]. It is important to note that these experiments are particularly challenging, both from the experimental and from the modeling point of view, because of the severe conditions tested and the great amount of soot formed.

3.3 PAH formation in ethylene premixed flames

The prediction of PAH formation and depletion is explored with the refined gas-phase model not only in the case of benzene combustion or acetylene pyrolysis, but also more carefully in laminar premixed ethylene flames.

As previously mentioned, the refined kinetic scheme is based on a detailed description of the C1-C4 chemistry, which has been extensively validated in comparison with a large amount of experimental data [144]. It includes detailed models of the formation and disappearance of first aromatic rings (benzene (A1-C_6H_6) and toluene (A1-C_7H_8), in particular) and of PAHs, which are known to be precursors of soot. The formation of the first aromatic ring has been carefully validated in recent studies, as shown in the previous paragraphs 3.1 and 3.2. Special focus is also put on the first ring formation by the resonantly stabilized radicals such as propargyl (C_3H_3) and cyclopentadienyl (C_5H_5) [37]. The growth rates of larger PAH species are modeled using the well-known HACA mechanism. Moreover, the typical chemical reaction pathways of PAH growth, like the stabilized radical mechanisms, are included, even though they are of lower importance in the case of ethylene flames. The main consumption reactions of aromatics and PAHs are H-abstraction reactions by H• and OH• radicals. The capability of the model to reproduce PAH formation and disappearance is of paramount importance for the prediction of soot formation. The model used in this analysis is adapted to further connect it to a method of moments [105]. Hence, A4-$C_{16}H_{10}$ is set to be the heaviest component of the gas phase and thus accounts for other heavier PAHs.

An argon-diluted C_2H_4/O_2 flame with an equivalence ratio of 3.06 experimentally studied by Castaldi et al. [169] is chosen to examine this kinetic gas-phase model. Several measured PAH species profiles are available, which were sampled using an online gas chromatograph/mass spectrometer analysis technique. Figure 3.14 shows the comparison between the measured and the simulated mole fraction profiles for the major species as well as the PAHs.

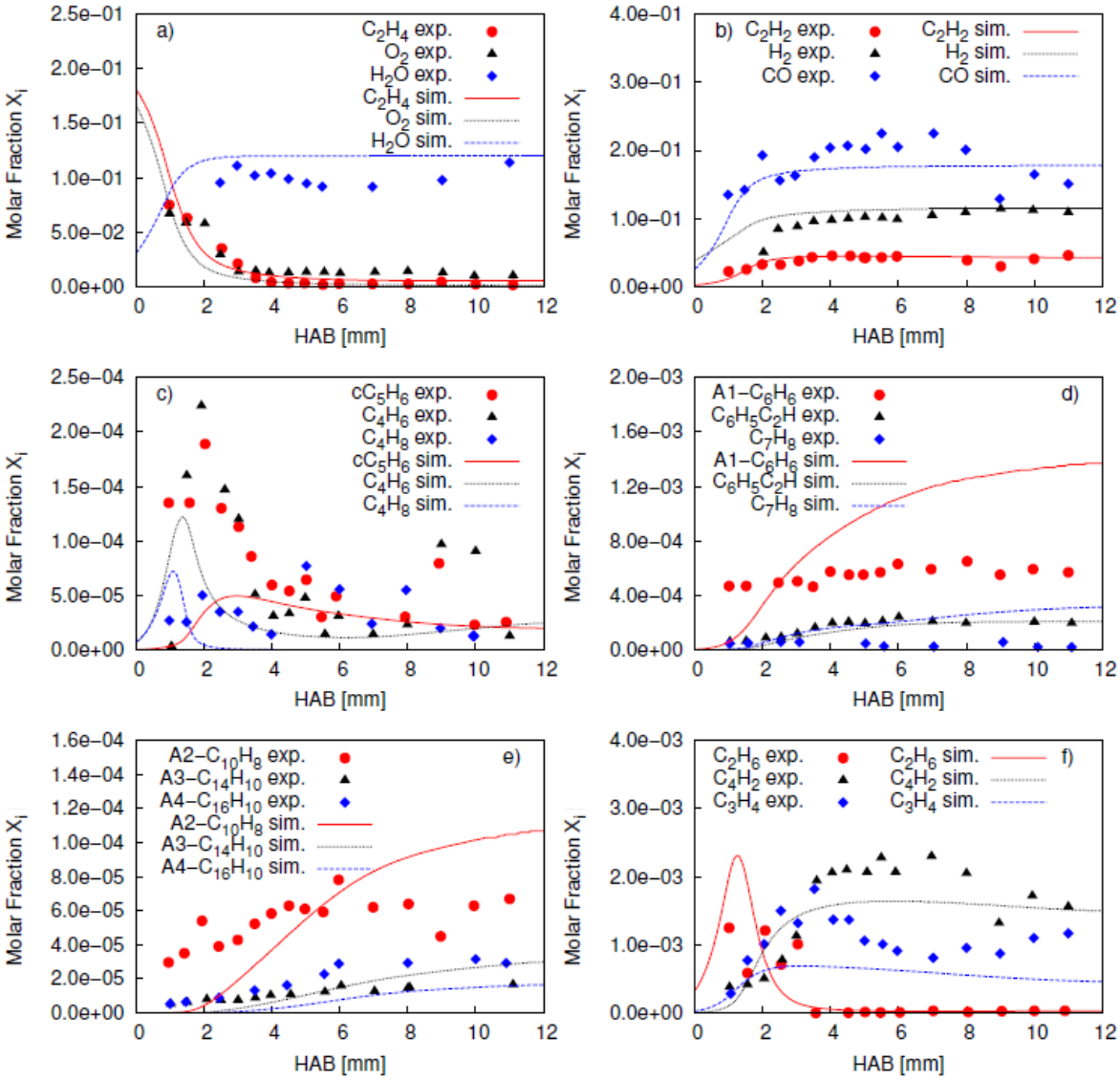

Figure 3.14 Comparison between experimental and calculated mole fraction profiles for major species and PAHs in a premixed $C_2H_4/O_2/Ar$ flame with Φ=3.06 [169]. a) C_2H_4, O_2, H_2O. b) C_2H_2, H_2, CO. c) cC_5H_6, C_4H_6, C_4H_8. d) A1-C_6H_6, $C_6H_5C_2H$, C_7H_8. e) A2-$C_{10}H_8$, A3-$C_{14}H_{10}$, A4-$C_{16}H_{10}$. f) C_2H_6, C_4H_2, C_3H_4.

As the significant heat losses are difficult to estimate in premixed burner-stabilized flames, the temperature profile measured is used as an input in the numerical simulations. Thereby, this profile is increased by 100 K in the post-flame zone to better reproduce the post-flame values of several important stable species, such as C_2H_2, H_2 and CO. This correction is expected to be within the experimental uncertainty range of temperature measurements in sooting flame conditions, as the flame temperature measured could be affected by the soot deposition on the thermocouple [121, 170].

Taking into account the fact that species measurements in sooting flames are difficult and therefore yield to uncertainties, the comparison between the model predictions and the measurements is quite satisfactory. This applies not only for the general flame structure and the major gaseous products, but also for the intermediate species and aromatic compounds with 1-4 rings. The major deviation refers to toluene. Part of the toluene overestimation is related to the benzene overestimation. This error is not present in the case of the laminar flow reactor (Figure 3.15), where the agreement between the model and the experimental data is better. Moreover, toluene predictions are generally quite satisfactory in other comparisons, where the presence of large or systematic deviations cannot be observed [37, 151]. One of the main purposes of the mechanism is to describe the A4-$C_{16}H_{10}$ profile, which directly influences the successive soot formation. As mentioned, A4-$C_{16}H_{10}$ is mainly built by HACA reactions, where phenyl-acetylene ($C_6H_5C_2H$) is a key intermediate. As shown in panel d of Figure 3.14, the model is able to represent the measured $C_6H_5C_2H$ trend very well. Consequently, the kinetic model is also able to predict the measured A4-$C_{16}H_{10}$ profile reasonably well.

Moreover, in order to discuss the kinetic model's ability to predict the effect of methane (CH_4) addition on the formation of soot precursors, the laminar flow reactor experiments of Roesler et al. [171] are also modeled. This involves studying CH_4/C_2H_4 mixtures in a laminar flow reactor at 1430 K. Initially, the fuel consists of pure C_2H_4. Then, CH_4 is gradually added to the system, maintaining the total carbon content (3 mole-%) and a C/O ratio of about 2, corresponding to an equivalence ratio of between 6 or 7 due to the added H_2 in the presence of CH_4. Therefore, the comparison between the model and experiments regarding the effect of CH_4 addition is shown in Figure 3.15.

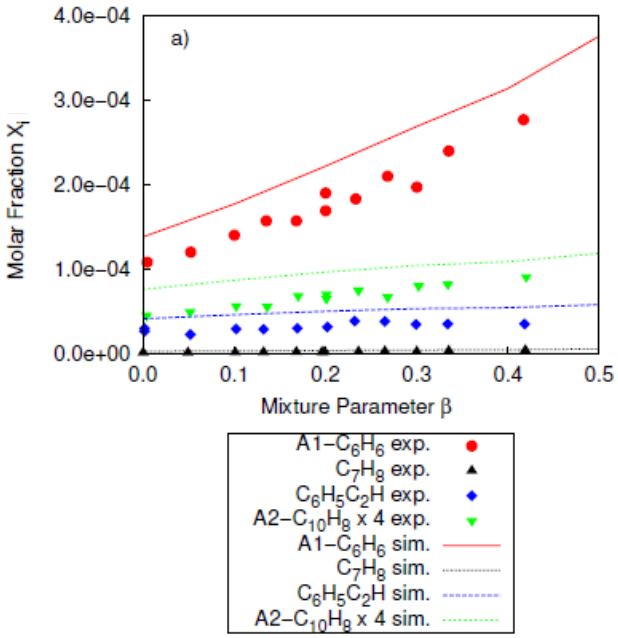

Figure 3.15 Comparison between experimental and modeling results of mole fractions of A1-C_6H_6, C_7H_8, $C_6H_5C_2H$ and A2-$C_{10}H_8$ (times 4) in a laminar flow reactor for the combustion of C_2H_4 and C_2H_4/CH_4 mixtures at T=1425 K as a function of the mixture parameter β [171].

The simulation results for premixed mixtures in a flow reactor are reported as a function of a mixture parameter β, representing the fraction of fuel carbon injected as methane [172]:

$$\beta = \frac{X_{CH_4}}{X_{C_2H_4}+X_{CH_4}} \tag{3.1}$$

where X_i is the mole fraction of species *i*.

In this case, the model also correctly predicts the experimental trends, especially the significant increase in benzene when CH_4 is added to the system.

4. Soot kinetic model

The soot kinetic model presented herein, is developed using a discrete sectional approach, similar to the one used by Sirignano et al. [75] and discussed in paragraph 2.2.2.

Nevertheless, there are many differences in respect to the advanced multi-sectional method, that are carefully described in this chapter. Briefly, this model is made up of 20 sections of pseudo-species instead of 25. These classes are different not only in term of mass and hydrogenation, but also in terms of shape. Aggregates are included in the model, considering their collision diameter that influences the kinetics.

4.1 Pseudo-species BINs

Aerosol dynamics of soot nucleation and mass/size growth are treated using a discrete sectional approach. Heavy PAHs and particle sizes are discretized in 20 classes of pseudo-species with an increasing molecular mass; specifically, the mass doubles from one class to another. Each class is represented by a combination of lumped pseudo-species or BINs, each with an assigned number of carbon and hydrogen atoms, as summarized in Table 4.1.

Heavy PAHs						
BIN_i	nC	Mass [amu]	Diameter [nm]	H/C A	H/C B	H/C C
BIN_1	20	~ 250	0.81	0.8	0.5	0.4
BIN_2	40	~ 500	1.02	0.8	0.5	0.4
BIN_3	80	~ 1000	1.28	0.75	0.5	0.4
BIN_4	160	~ 2000	1.62	0.75	0.5	0.4
Soot particles						
BIN_i	nC	Mass [amu]	Diameter [nm]	H/C A	H/C B	H/C C
BIN_5	320	~ $4 \cdot 10^3$	2.04	0.7	0.5	0.32
BIN_6	640	~ $8 \cdot 10^3$	2.57	0.65	0.5	0.30
BIN_7	1250	~ $1.55 \cdot 10^4$	3.21	0.6	0.5	0.30
BIN_8	2500	~ $3 \cdot 10^4$	4.04	0.6	0.5	0.30
BIN_9	$5 \cdot 10^3$	~ $6 \cdot 10^4$	5.09	0.55	0.45	0.30
BIN_{10}	10^4	~ $1.2 \cdot 10^5$	6.40	0.5	0.40	0.25
BIN_{11}	$2 \cdot 10^4$	~ $2.45 \cdot 10^5$	8.05	0.45	0.35	0.25
BIN_{12}	$4 \cdot 10^4$	~ $4.9 \cdot 10^5$	10.14	0.45	0.30	0.2
Soot aggregates						
BIN_i	nC	Mass [amu]	Collision diameter [nm]	N_p	H/C A	H/C B
BIN_{13}	$8 \cdot 10^4$	~ $9.7 \cdot 10^5$	13.27	2	0.40	0.20
BIN_{14}	$1.6 \cdot 10^5$	~ $1.95 \cdot 10^6$	19.50	4	0.40	0.15
BIN_{15}	$3.2 \cdot 10^5$	~ $3.9 \cdot 10^6$	28.63	8	0.35	0.10
BIN_{16}	$6.4 \cdot 10^5$	~ $7.8 \cdot 10^6$	41.98	16	0.35	0.10
BIN_{17}	$1.25 \cdot 10^6$	~ $1.51 \cdot 10^7$	60.89	32	0.30	0.08
BIN_{18}	$2.5 \cdot 10^6$	~ $3.02 \cdot 10^7$	89.49	64	0.30	0.05
BIN_{19}	$5 \cdot 10^6$	~ $6.02 \cdot 10^7$	131.53	128	0.25	0.05
BIN_{20}	10^7	~ $1.21 \cdot 10^8$	193.32	256	0.25	0.05

Table 4.1 Classes of lumped pseudo-species or BINs (Heavy PAHs, Soot particles and Soot aggregates) and their properties: mass, equivalent spherical diameter and H/C ratio for particles and also collision diameter and number of primary particles for each aggregate (N_p).

PAHs larger than 20 C atoms constitute the first four classes of BINs, each of which is composed of three subclasses with different H/C ratios. The first soot particles are assumed to be clusters of 320 C atoms, i.e. BIN_5. This threshold is also consistent with the observation of heavy PAHs extracted from flame-generated soot [111, 124, 125, 173] and with the particle sizes recently measured with laser-induced incandescence in low-sooting premixed flames [136]. Spherical soot particles are assumed between BIN_5 and BIN_{12}, with density equal to 1.5 g/cm^3 [134]. BIN_{12} is considered the primary particle with an equivalent spherical diameter (d_p) of ~10 nm [75, 174]. BINs with larger mass, up to BIN_{20}, represent soot aggregates and are composed by N_p primary particles calculated to satisfy their overall mass. Soot aggregates are described as mass fractals, with a fractal dimension (D_f) of 1.8, according to the recent values for premixed ethylene flames [116]

and for very rich sooting flames [175]. To calculate the collision diameter (d_c), it is first necessary to derive the radius of gyration (R_g) from this relationship:

$$N_p = k_f \cdot \left({}^{2R_g}/_{d_p} \right)^{D_f} \qquad \text{with} \quad k_f = \left(1 + {}^{2}/_{D_f}\right)^{{}^{D_f}/_{2}} \tag{4.1}$$

where k_f is derived from the empirical correlation of Köylü et al. [176]. Thus, the collision diameter becomes [177]:

$$d_c = \sqrt{{}^{5}/_{3}} \cdot 2R_g = \sqrt{{}^{5}/_{3}} \cdot d_p \cdot \left({}^{N_p}/_{k_f} \right)^{{}^{1}/_{D_f}} \tag{4.2}$$

For each of the 52 $BIN_{i,j}$ the corresponding surface radical $BIN_{i,j}$• is also considered. These 104 lumped species are involved in successive sooting process moving from the heavy PAHs of the gas phase kinetic model.

Several subclasses of H/C ratios [178] allow to describe the dehydrogenation and aging processes occurring in the growth and maturation of soot particles and aggregates. Hydrogenation decreases with an increase in molecular mass [179], due to the higher number of condensed rings, thus influencing soot properties. As shown in Figure 4.1 and reported in Table 4.1, three H/C ratios are considered up to BIN_{12}, while only two hydrogenation levels are assumed for heavier BINs. Therefore, two indexes are used to define the pseudo-species $BIN_{i,j}$, where *i=1,..20* refers to the number of C atoms and *j* to the two or three hydrogenation levels.

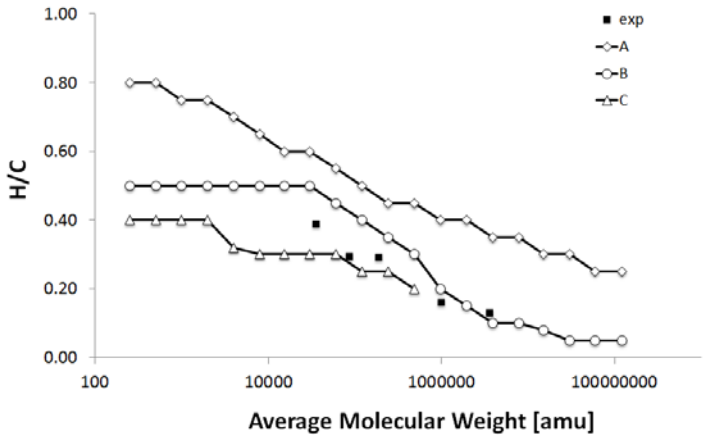

Figure 4.1 Comparison between the assumed H/C ratios of different BINs (lines with small symbols) and experimental data (symbols) [179] as function of particle mass.

In order to test the reliability of the assumed H/C ratio, Figure 4.2 shows a comparison between model prediction and recent experimental data of the H/C ratio of soot measured in a rich premixed ethylene flame (Φ = 2.4; C/O = 0.8; v_0 = 4 cm/s) as function of HAB [121, 180, 181].

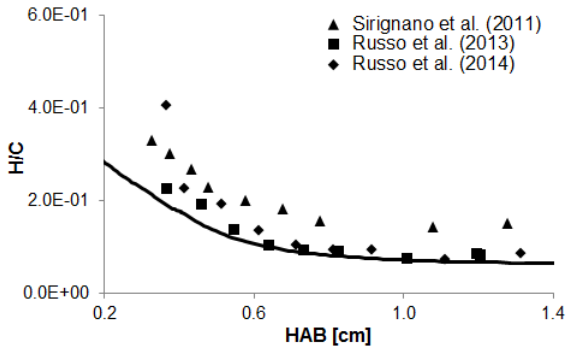

Figure 4.2 Comparison of predicted (line) and experimental (symbols) H/C ratio of soot formed in a rich premixed ethylene flame (Φ=2.4; C/O=0.8; v_0=4 cm/s) at atmospheric pressure [121, 180, 181].

Even if slightly underpredicted at lower HAB, the experimental trend of H/C ratio is well modeled and reasonable, because it is inside the experimental uncertainties and shows a progressive decrease at larger HAB. A more detailed discussion about the prediction of this flame, including its structure, main products and soot, is reported in paragraph 5.3.

Soot has been generally considered to be constituted of high molecular weight PAH possibly linked by aliphatic bridges, especially at early stages of soot mass and size growth [26]. The assumed hydrogenation levels allow to reproduce the core-shell structure and describe the possible alkylation of nascent soot particle before they start to graphitize. Despite the prevalent disordered

character, soot nanostructures show some degree of crystalline order, typically in the form of short-order stacked graphene layers or onion-like structure or partially graphitic order (longer range parallelity of layers) [20]. Indeed, from 'lattice fringe analysis' of HRTEM images, emerged that the BSU (basic structural unit) in both nascent and mature soot formed in different laminar premixed flames is constituted by 2-3 stacked layers (fringes) of nanometric size [21, 22, 121]. Therefore, the building block of the layer may be assumed as a pericondensed structure, considered here as the coronene's one. In order to reach the experimentally measured layer size, a continuous growth of the layer around the coronene structure is defined progressively symmetric and circular. The final layer structure can be divided in six 60° symmetric slices. Figure 4.3 schematically shows the 60° slice view of the layer's growing structure, formed through the successive addition of N_c circles of benzene rings around coronene.

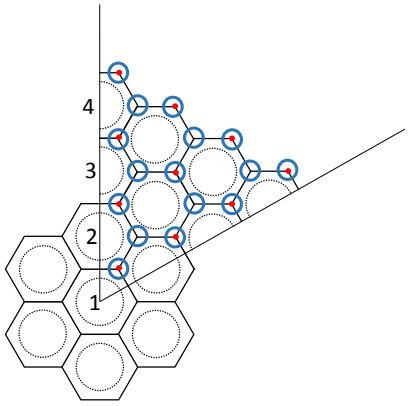

Figure 4.3 Schematic 60° slice view of the growing layer around the building block structure, considered as coronene. The number of added circles of benzene rings, N_c, are marked, as well as the C atoms (open blue circles) and H atoms (red dots) for the considered layer's slice.

For each N_c in the considered slice, it is possible to observe that the number of C (nC) and H (nH) atoms are:

$$nC_{Nc} = 2 \cdot N_c - 1 \quad (4.3)$$

$$nH_{Nc} = N_c \quad (4.4)$$

Therefore, the total number of added C and H atoms for the considered slice are:

$$nC_{slice} = N_c^2 \quad (4.5)$$

$$nH_{slice} = N_c \quad (4.6)$$

The final layer structure is assumed built around coronene adding 5 circles of benzene rings; hence composed by 150 C atoms and 30 H atoms with H/C ratio of 0.2 and with a mean diameter of ~2 nm. As experimentally measured, two or three layers are considered forming the BSU inside the growing soot particle and many of them constitute heavier particles as shown in Figure 4.4.

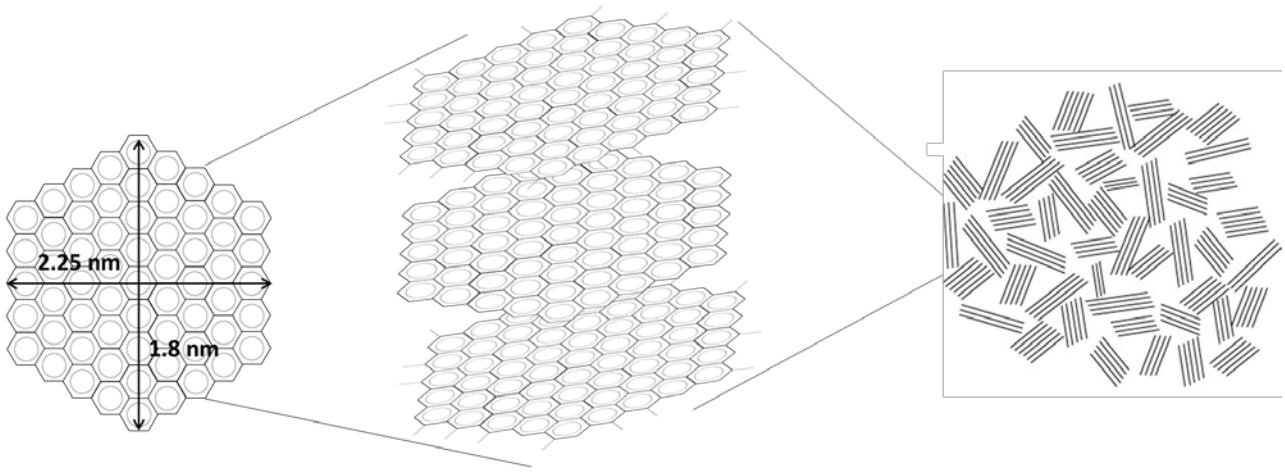

Figure 4.4 Schematic representation of a soot particle, constituted by pericondensed and alkylated layers that are stacked together forming the BSU.

Indeed, the first particle of soot considered in this soot model as BIN_5 and with an equivalent spherical diameter of ~2 nm, may be constituted by two layers, each made up of 61 benzene rings. These two layers have an H/C ratio of 0.2 as previously mentioned, but BIN_5 has three different hydrogenation levels: 0.7 for BIN_{5A}, 0.5 for BIN_{5B} and 0.32 for BIN_{5C}. Therefore, it is possible to account for these higher hydrogenation levels assuming that these layers have methyl groups attached to their external carbon atoms. To calculate the number of methyl groups (n_{met}) for each BIN_5 species the following equation is solved:

$$\frac{H}{C} = \frac{nH+2\cdot n_{met}}{nC+n_{met}} \qquad (4.7)$$

with H/C being the hydrogenation level of the species, nH the number of H atoms of the layer and nC the number of C atoms of the layer.

In this case, BIN_{5B} is assumed made up of 2 layers with 30 methyl groups. BIN_{5A} is a soot particle with 58 methyl groups. It can be considered as a pericondensed species not only with

external methyl groups but also with some alkyl bond among its layers. BIN_{5C} is instead more aromatic, with less methyl groups (11). To account for the more graphitization of the dehydrogenated species, C-C bonds among the different layers could be considered.

The same procedure is applied for heavier BINs and Figure 4.5 shows the assumed number of methylations as function of the BIN species and their different hydrogenation levels.

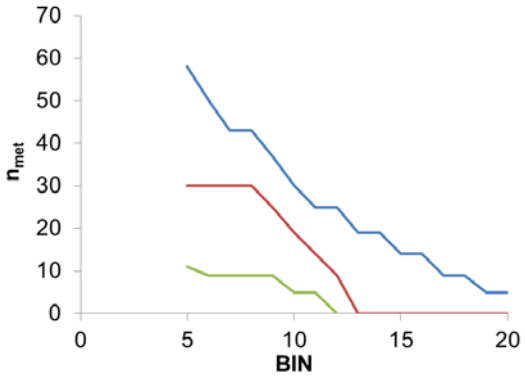

Figure 4.5 Number of methyl groups for $BIN_{i;A}$ (blue line), $BIN_{i;B}$ (red line) and $BIN_{i;C}$ (green line).

Successively it is possible to estimate the aromatic hydrogen content as the H atoms of the layers constituting the particles and the aliphatic hydrogen content as the H atoms of the methyl groups. Figure 4.6 shows the preliminary comparison between the experimental and theoretical ratio between aliphatic and aromatic H atoms in the premixed ethylene flame studied by Russo et al. [180] as a function of height above the burner.

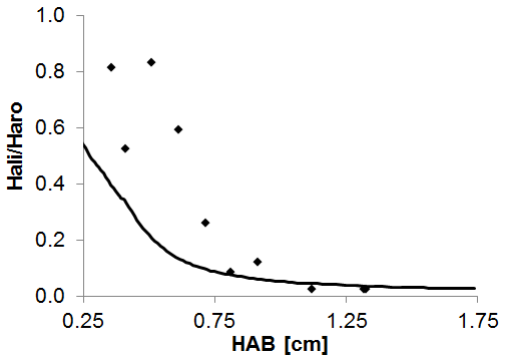

Figure 4.6 Comparison between theoretical (line) and experimental (symbols) ratio between aliphatic and aromatic H atoms in a rich premixed ethylene flame as function of HAB [180].

In the inception region the predicted H_{ali}/H_{aro} ratio is lower than experiments, while further from the burner the model predicts that no more methylations are present in soot particles, as

experimentally observed. The higher aliphatic content in nascent soot shown in these measurements at lower HAB is in line with the work of Cain et al. [44]. In this study, they developed a methodology for characterizing the surface composition of nascent soot particles produced in a premixed, burner-stabilized flame, sampled by a cascade impactor, and analyzed using micro-FTIR spectroscopy. An in-depth investigation was conducted to examine the changes in soot surface-bound functional groups with flame temperature, particle size and sampling position; for this purpose a set of four canonical ethylene–oxygen–argon flames at an equivalence ratio of 2.07 were studied. Large amounts of aliphatic C–H groups were observed with concentrations ranging from 1 to 30 times that of aromatic C–H. The amount of aliphatic C–H relative to aromatic C–H remained approximately constant with respect to particle sizes, but this size insensitivity may be the result of particle coagulation and aggregation during particle sampling and collection [44]. These findings were confirmed later [182], observing the increase of the aliphatic-to-aromatic C‑H ratio with an increase in flame temperature. The observations suggested that the aliphatic components are in the form of alkyl, alkenyl side chains or cross linkages covalently bound to aromatic units in the soot material.

4.2 Thermodynamics

Thermochemical properties of the pseudo-species BINs are based on the group additivity (GA) method [149]. These pseudo-species are considered constituted by different functional groups that are shown in the works of Stein et al. [183], Benson et al. [184] and Cohen and Benson [185] and herein the same nomenclature is maintained. Four functional groups are identified for PCAH: the C-H group in benzene [group A, CB-(H)] and three groups associated with carbon atoms located at the border of two or three fused rings, CBF, are distinguished. The first CBF group [group B, CBF-(CB)2(CBF)] may be recognized as the unsubstituted carbon in naphthalene and anthracene and inherently contains 1,5 H,H repulsion energy. The simplest illustration of the second CBF group [group C, CBF-(CB)(CBF)2] is found in phenanthrene; each of these groups contains half of the 1,6 H,H repulsion energy. The third CBF group [group C, CBF-(CBF)3] is identical with a carbon atom present in a layer of graphite, free of interplanar interactions; each of the two interior carbons in pyrene are members of this group. The groups E, F and G are instead characteristics of non-completely condensed aromatic oligomers and are found in substituted aromatics and radicals. Group E [CB-C] denotes a five-membered ring, such as in acenaphthalene. Group F [C-CB(H)3] connects the aromatic rings in biphenyl. Groups G [CB-CB] belongs to substituted aromatics, such as in the phenyl radical. Table 4.2 shows the additivity values corresponding to each group at 298 K and for ΔH_f, S and C_p in the temperature range of 300-1000 K, that are derived from literature.

Groups		ΔH_f (kcal/mol)	S (cal/molK)	C_p cal /molK					
				300 K	400 K	500 K	600 K	800 K	1000 K
CB-(H)	A	3.3	11.53	3.24	4.44	5.46	6.3	7.54	8.41
CBF-(CB)2(CBF)	B	4.8	-5	2.99	3.66	4.22	4.64	5.23	5.55
CBF-(CB)(CBF)2	C	3.7	-5	2.99	3.66	4.22	4.64	5.23	5.55
CBF-(CBF)3	D	1.45	1.82	2.08	2.85	3.5	4.03	4.75	5.14
CB-C	E	5.51	-7.69	2.67	3.14	3.68	4.15	4.96	5.44
C-CB(H)3	F	-10	30.41	6.19	7.84	9.4	10.79	13.02	14.77
CB-CB	G	4.96	-8.64	3.33	4.22	4.89	5.27	5.76	5.95

Table 4.2 Functional groups considered in the GA method used to calculate BINs thermodynamic properties [183].

As previously mentioned, BINs species are divided in different hydrogenation classes, defined by the H/C ratios, which mainly span from 0.05 to 0.8 and are shown in Table 4.1. Knowing the H/C ratio allows to determine the amount of C atoms involved in each group. Hence, it is assumed

that the number of groups for BINs with a ratio H/C ~ 0.05 to 0.6 is calculated considering different hypothesis, namely:

- The lower BINs hydrogenation suggests a pericondensed structure. This kind of structure, i.e. pyrene, shows a lower H/C ratio and a higher number of fused carbons. Hence, the contribution of the H atoms in these species corresponds to the one of the C-H group in benzene (group A). Figure 4.7 shows them in the case of pyrene.

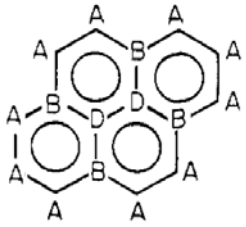

group A=[CB-(H)]=10

group B=[CBF-(CB)2CBF]=4

group D=[CBF-(CBF)3]=2

Figure 4.7 Example of the groups identified in pyrene.

- The pericondensed species (PCAH) include also bonded carbon atoms, classified as group B or C. Taking into account some different PCAH species, such as Benzo[a]Pyrene as shown in Figure 4.8, it is observed that groups B+C are usually half of the group A.

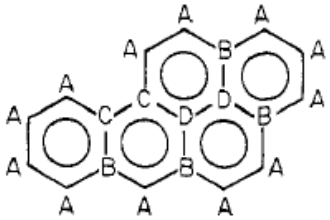

group A=[CB-(H)]=12

group B=[CBF-(CB)2CBF]=4

group C=[CBF-(CB)(CBF)2]=2

group D=[CBF-(CBF)3]=2

Figure 4.8 Example of the groups identified in Benzo[a]Pyrene.

This rule is applied for all cases where H/C ≤ 0.6. The additivity values of group B and C are very similar, but it is found that group B is more frequent (~80%) compared to group C.

Finally, the number of groups is defined by the following equations:

group A = number of H atoms

groups (B+C) = 0.5·(group A)

group B = groups (B+C)·0.78

group C = groups (B+C)·0.22

- The group D is defined as the number of carbon atoms present in the species minus the rest of the groups:

group D = number of C atoms - (group A) – (group B) – (group C)

- The more hydrogenation of some BINs with H/C ~ 0.8 suggests a structure ortho-fused (e.g. chrysene) or aromatic molecules linked with aliphatic chains. For instance, an aromatic structure with six-member rings, linked each other by σ bonds, and including the presence of methyl groups is considered for the case of BIN_{2A}, BIN_{3A}, BIN_{4A} and BIN_{5A} as it is shown in the Figure 4.9 for BIN_{2A}.

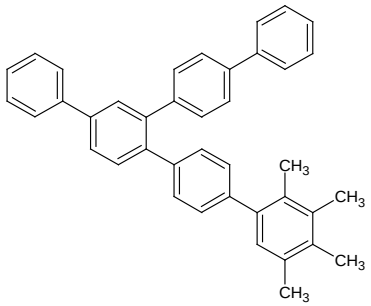

group A = 22

group E = 4

group F = 4

group G = 10

Figure 4.9 Example of the groups identified in BIN_{2A}.

- It is worth to be mentioned that due to the higher hydrogenation of the BINs, groups E, F and G are included in the GA evaluation. In this case, the distribution for each group follows a fixed rule. The contribution of the groups E and F corresponds to the number of methyl groups assumed to be present in each BIN. Group A is almost half of the number of carbons in the molecule, the groups B, C and D are zero for all cases and group G was considered as the

number of carbons in the molecule minus the contribution of the groups A, E and F. For instance BIN_{1A} is assumed as 1,11-dimethyltetraphene, which is shown in Figure 4.10.

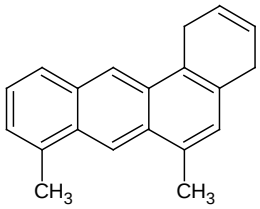

group A=10

groups (B+C)=6

group E=2

group F=2

Figure 4.10 Example of the groups identified in BIN_{1A}.

Using the previous listed assumptions, a group distribution for each BIN is assumed. Successively, seven polynomial coefficients for two different temperature ranges (low T: <1000 K; high T: >1000 K) which fit the specific heat (C_p), enthalpy and entropy as function of temperature [186] are calculated, in order to obtain the BINs thermodynamic properties. The expressions for the properties are:

$$\frac{c_p}{R} = a_1 + a_2 T + a_3 T^2 + a_4 T^3 + a_5 T^4$$

$$\frac{H^0}{RT} = a_1 + \frac{a_2}{2} T + \frac{a_3}{3} T^2 + \frac{a_4}{4} T^3 + \frac{a_5}{5} T^4 + \frac{a_6}{T}$$

$$\frac{S^0}{R} = a_1 \ln T + a_2 T + \frac{a_3}{2} T^2 + \frac{a_4}{3} T^3 + \frac{a_5}{4} T^4 + a_7$$

Five coefficients are estimated through a polynomial regression on the C_p values reported in Table 4.2 as function of the temperature. In order to take into account also the high temperature, the value of C_p at 3000 K was fixed about 25% more than the C_p at 1000 K, as for the C_p(3000 K)/C_p(1000 K) ratio for pyrene. The sixth and seventh parameters are obtained solving respectively the enthalpy and entropy expressions listed previously, at 298 K and using the data of ΔH_f and S in

Table 4.2. Therefore, 7 coefficients for each group are established for the low and high temperature ranges and they are shown in

Table **4.3**.

Group	a_1	a_2	a_3	a_4	a_5	a_6	a_7
A	-5.54E-01	8.91E-03	-5.03E-06	1.51E-09	-2.01E-13	1.47E+03	6.52E+00
B	3.52E-01	4.88E-03	-3.52E-06	1.01E-09	-1.51E-13	2.12E+03	-5.82E+00
C	3.52E-01	4.88E-03	-3.52E-06	1.01E-09	-1.51E-13	1.57E+03	-5.82E+00
D	-3.84E-01	5.99E-03	-4.03E-06	1.51E-09	-1.51E-13	6.11E+02	1.49E+00
E	8.66E-02	4.98E-03	-3.52E-06	1.01E-09	-1.51E-13	2.56E+03	-5.68E+00
F	5.90E-02	1.16E-02	-5.03E-06	1.01E-09	-2.01E-14	-5.52E+03	1.17E+01
G	-1.93E-01	8.45E-03	-1.01E-05	3.02E-09	-4.03E-13	2.26E+03	-5.34E+00

Table 4.3 Fitting coefficient for high and low temperature ranges for each group considered in the GA analysis of the BINs.

These coefficients are used to estimate the 7 fitting coefficients for each BIN. For instance, an example of the calculation of the coefficient $\mathbf{a_1}$ for BIN_{ij} is shown below:

$$a_1(BIN_{ij}) = \sum_{k=A}^{G}\left(a_{1k} * (number\ of\ group\ k\ in\ BIN_{ij})\right) \quad (4.8)$$

where $a_1(BIN_{ij})$ corresponds to the first fitting coefficient for BIN_{ij}. a_{1k} refers to the coefficient 1 for each group (k = A..G) of

Table 4.3 and is multiplied by the number of each group assumed to be present in BIN_{ij}. The specific heat and entropy of radical species is considered the same of molecular ones, while the enthalpy of formation of radicals is increased of 60000 cal/mol, as in the case of pyrene, phenanthrene and naphthalene radicals in respect of their relative molecules. This means that only the sixth coefficient is modified both for low and high temperature range.

It is noteworthy to found that the proper estimation of these properties has an important role especially in the most severe operating conditions, as verified in the kinetic modeling study of acetylene pyrolysis [152].

4.3 Kinetics

This soot mechanism is constituted of different families of reaction classes. Namely, the following six reaction classes are considered:

1. HACA Mechanism
2. Soot inception
3. Surface growth
4. Dehydrogenation reactions
5. Particle coalescence and aggregation
6. Oxidation

Analogy and similarity rules were employed to describe the surface reaction kinetics of soot using known kinetic rates of gas-phase species. Table 4.4 schematically describes the kinetic parameters of the different reaction classes, with several reference gas-phase reactions.

Reactions and their classes	$k = A\,T^n \exp(-E/RT)$[a] A	n	E	Refs.	Reference Reaction
1. HACA mechanism					
1a. H-abstraction					
$H + BIN_i \rightarrow H_2 + BIN_i\bullet$	$5.4\cdot10^5$	2	10.5	[187, 188]	$H + BIN_5 \rightarrow H_2 + BIN_5\bullet$
1b. Acetylene addition					
$C_2H_2 + BIN_i\bullet \rightarrow$ *products*	$1.0\cdot10^9$	0	5	[25, 66]	$C_2H_2 + C_{10}H_7 \rightarrow C_{12}H_9\bullet$
2. Soot inception ($i,n < 5$)					
$BIN_i\bullet + BIN_n\bullet \rightarrow$ *products*	$1.0\cdot10^9$	0	6*	[37, 189]	$C_5H_5\bullet+C_5H_5\bullet \rightarrow C_{10}H_8+2H\bullet$
$BIN_i + BIN_n\bullet \rightarrow$ *products*	$1.0\cdot10^9$	0	8*	[37]	$C_6H_5\bullet+C_8H_6 \rightarrow C_{14}H_{10}+H\bullet$
$BIN_i + BIN_n \rightarrow$ *products*	$1.0\cdot10^6$	0.5	0	[190]	$C_{16}H_{10}+C_{16}H_{10} \rightarrow$ products
3. Surface growth					
3a. Small RR• addition					
$RR\bullet + BIN_i \rightarrow$ *products*	$2.0\cdot10^9$	0	19*	[37]	$C_3H_3\bullet+C_6H_6 \rightarrow C_9H_8+ H\bullet$
$RR\bullet + BIN_i\bullet \rightarrow$ *products*	$2.5\cdot10^9$	0	3*	[37]	$C_3H_3\bullet+C_6H_5\bullet \rightarrow C_9H_8$
3b. PAH condensation					
$i \geq 5$					
$PAH\bullet + BIN_i\bullet \rightarrow$ *products*	$5.0\cdot10^{11}$	0.5	0	This work	see text
$PAH\bullet + BIN_i \rightarrow$ *products*					
$i < 5$ and $n \geq 5$					
$BIN_i\bullet + BIN_n\bullet \rightarrow$ *products*	$3.0\cdot10^{11}$	0.5	0	This work	see text
$BIN_i + BIN_n\bullet \rightarrow$ *products*					
4. Dehydrogenation reactions					
4a. Dehydrogenation					
$BIN_i\bullet \rightarrow H\bullet + BIN_i$	$1.0\cdot10^{11}$	0	12	[85]	$C_{13}H_{11}\bullet \rightarrow C_{13}H_{10} + H\bullet$
$BIN_i \rightarrow H_2 + BIN_i$	$1.0\cdot10^8$	0	32	[40]	$C_{13}H_{12} \rightarrow C_{13}H_{10}+H_2$
4b. Demethylation (for H/C > 0.3)					
$H\bullet + BIN_i \rightarrow CH_3\bullet +$ *products*	$1.2\cdot10^{10}$	0	5	[191]	$C_{11}H_{10} + H\bullet \rightarrow C_{10}H_8 + CH_3\bullet$
4c. C-H fission/recombination					
$BIN_i \rightarrow H\bullet + BIN_i\bullet$	$1.5\cdot10^{17}$	0	114	[151]	$C_6H_6 \rightarrow C_6H_5\bullet + H\bullet$
$H\bullet + BIN_i\bullet \rightarrow BIN_i$	$1.0\cdot10^{11}$	0	0	[151]	$C_6H_5\bullet+H\bullet \rightarrow C_6H_6$
5. Particle coalescence and aggregation					
5a. Particle coalescence ($5 \leq i,n < 13$)					
$BIN_i + BIN_n \rightarrow$ *products*	$2.0\cdot10^{11}$	0.5	0	This work	see text
5b. Particle coalescence on aggregates ($5 \leq i < 13$ and $n \geq 13$)					
$BIN_i + BIN_n \rightarrow$ *products*	$1.5\cdot10^{11}$	0.5	0	This work	see text
5c. Particle aggregation ($i,n \geq 13$)					
$BIN_i + BIN_n \rightarrow$ *products*	$1.5\cdot10^{11}$	0.5	0	This work	see text
6. Oxidation					
6a. Oxidation with OH•					
$OH\bullet + BIN_i \rightarrow$ *products* $+ CH_2CO$	$1.0\cdot10^{10}$	0	10	[25]	$OH\bullet+C_{16}H_{10} \rightarrow C_{14}H_9\bullet+CH_2CO$
$OH\bullet+BIN_i \rightarrow$ *products* $+CO+CH_3\bullet$	$1.0\cdot10^{10}$	0	4	[85]	$OH\bullet+C_{11}H_{10} \rightarrow C_9H_8+CO+CH_3\bullet$
$OH\bullet+BIN_i\bullet \rightarrow$ *products* $+CO+H\bullet$	$2.0\cdot10^{11}$	0	0	[85]	$OH\bullet+C_{10}H_7\bullet \rightarrow C_9H_7\bullet+CO+H\bullet$
$OH\bullet + BIN_i \rightarrow$ *products* $+ HCO\bullet$	$3.0\cdot10^9$	0.5	10.6	[190]	$OH\bullet+C_{10}H_8 \rightarrow C_9H_8+HCO\bullet$
6b. Oxidation with O•					
$O\bullet + BIN_i \rightarrow$ *products* $+ HCCO\bullet$	$2.0\cdot10^{10}$	0	4	[25]	$O\bullet+C_{16}H_{10} \rightarrow C_{14}H_9\bullet+HCCO\bullet$
$O\bullet + BIN_i\bullet \rightarrow$ *products* $+ CO$	$5.0\cdot10^{10}$	0	0	[85]	$O\bullet+C_{10}H_7\bullet \rightarrow C_9H_7\bullet + CO$
6c. Oxidation with O_2					
$O_2+BIN_i\bullet \rightarrow$ *products* $+CO+HCO\bullet$	$2.1\cdot10^9$	0	7.4	[25]	$O_2+C_{10}H_7\bullet \rightarrow C_8H_6\bullet+CO+HCO\bullet$
$O_2 + BIN_i\bullet \rightarrow$ *products* $+O\bullet +CO$	$2.6\cdot10^{10}$	0	6.12	[85]	$O_2+C_{10}H_7\bullet \rightarrow C_9H_7\bullet+O\bullet+CO$
$O_2 + BIN_i\bullet \rightarrow$ *products* $+ 2CO$	$4.2\cdot10^8$	0.5	8	[190]	$O_2+C_{16}H_9\bullet \rightarrow C_{14}H_9\bullet+2CO$

[a]Units are mol, L, s, K and kcal. *see text.

RR• = $C_3H_3\bullet$, *i*-$C_4H_3\bullet$ *i*-$C_4H_5\bullet$, and $C_5H_5\bullet$ (cyclopentadienyl). PAH• = parent radicals of C_6H_6, C_7H_8, $C_6H_5C_2H$, $C_6H_5C_2H_3$, xylene, ethylbenzene, indene, $C_{10}H_8$, $C_{10}H_7CH_3$, $C_{12}H_8$, $C_{12}H_{10}$, fluorine, diphenylmethane, $C_{14}H_{10}$, $C_{14}H_{14}$, $C_{16}H_{10}$.

Table 4.4 Reaction classes in soot kinetic model and their reference kinetics.

An automatic mechanism generator (SootGEN) was developed and used to build the complete soot kinetic mechanism [85].

4.3.1 HACA mechanism

HACA mechanism (H-abstraction reactions and acetylene additions) mostly contributes not only to soot inception but also to the soot growth [46, 52]. H-abstraction reactions by H• (and OH•) radicals form surface radicals BIN•. Due to the analogy of PAH and BIN aromatic sites, rate parameters of these reactions depend on number and type of H atoms [187, 188, 192]. Reaction Class 1a of Table 4.4 refers to H-abstraction reactions and an example is the following H-abstraction reaction on naphthalene by H• radicals:

$$H\bullet + C_{10}H_8 \rightarrow C_{10}H_7\bullet + H_2 \qquad (R1)$$

The successive acetylene addition completes the HACA mechanism. The reference reaction is the acetylene addition on naphthyl radical [25, 66], with reference kinetic parameters $1.0 \cdot 10^9 \cdot \exp(-5000/RT)$ [l/(mol s)]:

$$C_2H_2 + C_{10}H_7\bullet \rightarrow C_{12}H_9 \qquad (R2)$$

As a matter of flexibility of the soot kinetic model, two reaction paths to form BIN• and (BIN+H•) are considered. The reference kinetic parameters of acetylene addition to heavy PAHs, soot particles and soot aggregates are modified according to different assumptions.

For heavy PAHs the kinetic constants vary depending on their H/C. The activation energy is always 5 kcal/mol, while the frequency factors decrease from $1.4 \cdot 10^9$, to $1.2 \cdot 10^9$ and $1.0 \cdot 10^9$ l/(mol s), respectively for $BIN_{i;A}\bullet$, $BIN_{i;B}\bullet$, and $BIN_{i;C}\bullet$. These values are consistent with the reference gas phase kinetic parameters of HACA mechanism [46, 52], as shown in Table 4.4.

For soot particles (BIN_5-BIN_{12}) and soot aggregates (BIN_{13}-BIN_{20}) the frequency factor is obtained by rescaling the reference one, shown in Table 4.4, taking into account the nature of the surface, both in terms of particle aggregation and hydrogenation level. The surface area is directly derived from the diameter (d) for particles; whereas in case of aggregates is obtained by considering the surfaces of all the primary particles. Thus, there are two different scaling factors for soot particles and aggregates:

Soot particles: $$A/A_{ref} = 1 + \frac{d^2 \cdot H/C}{d_{ref}^2} \quad (4.9)$$

Soot aggregates: $$A/A_{ref} = 1 + \frac{n_P \cdot d_p^2 \cdot H/C}{d_{ref}^2} \quad (4.10)$$

where d_{ref} is the reference diameter at soot inception, i.e. ~ 1.91 nm, that is the average value of BIN_5. For a better understanding of these dependences, the frequency factors for the different BINs are shown in Figure 4.11.

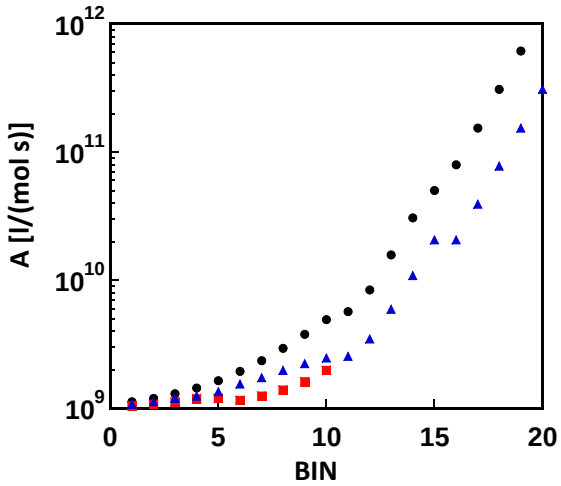

Figure 4.11 Frequency factor of HACA mechanism for $BIN_{i;A}$ (black symbols), $BIN_{i;B}$ (blue symbols) and $BIN_{i;C}$ (red symbols).

4.3.2 Soot inception

As already mentioned, the first BINs (*i=1,..4*) are considered as gas-phase PAHs. PAH-PAH interactions contribute in forming heavier PAHs and a first three-dimensional soot nuclei, up to soot inception [38, 46], here assumed as the formation of BIN_5. All radical-radical, radical-molecule, and molecule-molecule reactions, involving the first BIN until BIN_5, are considered in this reaction class representing soot nucleation. Reference kinetic parameters refer to analogous gas phase reactions. Cyclopentadiene and cyclopentadienyl radical, as well as benzene and phenyl radicals are the typical reference gas phase species. According to the self-recombination reaction of cyclopentadienyl radicals [37, 189]:

$C_5H_5\bullet + C_5H_5\bullet \rightarrow C_{10}H_8 + 2H\bullet$ (R3)

the reference kinetic parameters for the recombination of two resonantly stabilized radicals is assumed as $1.0 \cdot 10^9 \cdot \exp(-6000/RT)$ l/(mol s). This activation energy is required to overcome the

relative stability of the resonant radicals. Therefore, it becomes 3 kcal/mol if only one recombining radical is resonant, and zero when two non-resonant radicals are recombining. Furthermore, the reference reaction for radical molecule interaction is:

$C_6H_5\bullet + C_8H_6 \rightarrow C_{14}H_{10} + H\bullet$ (R4)

with the kinetic parameters $1 \cdot 10^9 \cdot \exp(-8000/RT)$ l/(mol s) [37]. The activation energy becomes 19 kcal/mol for resonantly stabilized radicals.

Finally, the reference reaction for molecule-molecule interactions, from pyrene up to BIN_4 [62, 193], is $1.0 \cdot 10^6 \cdot T^{0.5}$ l/(mol s) [190]:

$C_{16}H_{10} + C_{16}H_{10} \rightarrow C_{32}H_{20} \rightarrow 0.4\,[BIN_1] + 0.6\,[BIN_2]$

$0.4[BIN_1]+0.6[BIN_2] \rightarrow 0.1667BIN_{1,1}+0.2333BIN_{1,2}+0.25BIN_{2,1}+0.35BIN_{2,2}$ (R5)

Stoichiometric coefficients of the four BINs nearest to the addition product $C_{32}H_{20}$ are derived using a linear interpolation (lever rule) and respecting first the C and then the H atomic balances. As already mentioned, all the interactions among BINs up to BIN_4 and heavy gas phase PAHs with their parent radicals are considered in this reaction class. For sake of simplicity, the stoichiometry of reaction products, as well as the *j* index of BINs, are omitted in Table 4.4.

According to chemical kinetics and aerosol dynamics theory [194], frequency factors are scaled with respect to the reference values (A/A_{ref}) accounting for the change in collision frequency ($C_f/C_{f,ref}$) due to the different molecular weights of the reactants:

$$A = A_{ref} \cdot {C_f}/{C_{f,ref}} \quad \text{with} \quad C_f = \sigma^2 \sqrt{\frac{8\pi k_B T}{\mu_r}} \quad \text{l/(mol s)} \qquad (4.11)$$

where k_B is the Boltzmann constant, T is the temperature, μ_r is the reduced mass, σ is the mean collision diameter.

4.3.3 Surface growth

Together with HACA Mechanism, small resonantly-stabilized radicals, like propargyl ($C_3H_3\bullet$), ethylnyl-1-vinyl ($CH{\equiv}C{-}C\bullet{=}CH_2$ or *i*-$C_4H_3\bullet$), 1,3-butadien-2-yl ($CH_2{=}C\bullet{-}CH{=}CH_2$ or *i*-$C_4H_5\bullet$) and cyclopentadienyl ($C_5H_5\bullet$), further contribute to the soot growth, through addition reactions to

BIN• and BIN. These resonant radicals are referred as RR• in Table 4.4. Their additions to C_6H_5• or C_6H_6 are considered as reference reactions, as shown for propargyl radicals:

C_3H_3• +C_6H_5•→ C_9H_8 +H• (R6)

C_3H_3•+C_6H_6→C_9H_8+H• (R7)

The kinetic parameters specific for each radical are derived from reference values, again accounting for the change of the collision frequency ($C_f/C_{f,ref}$), due to the increase of the mean collision diameter of the BIN particles and aggregates.

The same addition reactions on soot particles and aggregates are also extended to the heavier gas phase PAH radicals. Their kinetic parameters, slightly varying for lighter and heavier PAH radicals, are derived from the asymptotic values of the reference addition reactions on BIN_{20}, reported in Table 4.4. In agreement with experimental evidences [195], the reference kinetic parameters are multiplied by a collision efficiency (γ), function of the collision diameter (σ):

$$k = A_{ref} \cdot T^{0.5} \cdot \gamma(\sigma) = A_{ref} \cdot T^{0.5} \cdot \frac{100+\sigma^{6.5}}{10^5+\sigma^{6.5}} \quad (4.12)$$

Figure 4.12 shows a comparison of the proposed correlation with the experimental collision efficiency reported by D'Alessio et al. [195].

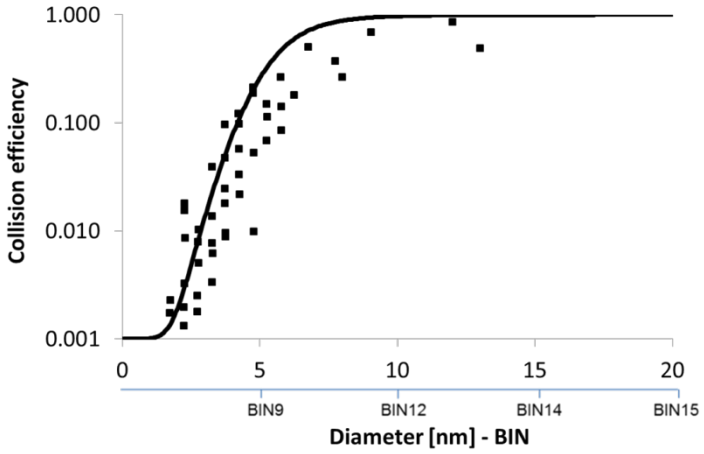

Figure 4.12 Collision efficiency for heavy PAH radical condensation on soot particles or aggregates (line) compared to experimental data (symbols) [195].

Our collision efficiency is slightly higher than the experimental one, but lower than the one suggested by Raj et al. [196], also for this reason a sensitivity analysis on this parameter will be shown in the next paragraphs.

4.3.4 Dehydrogenation reactions

Heavy PAHs and soot particles can undergo dehydrogenation following both molecular and radical pathways. As discussed before, two or three hydrogenation levels are considered for the different BINs. Higher is the severity of the reacting system, higher is the progressive dehydrogenation of PAH and soot particles, up to the less hydrogenated ones.

The reference reaction for radical dehydrogenation is the fluorene formation from the benzyl-2-phenyl radical [85] :

$C_{13}H_{11}\bullet \rightarrow C_{13}H_{10} + H\bullet$ (R8)

The reaction of di-phenyl-methane to give fluorene [40] is the reference dehydrogenation reaction of BIN molecules:

$C_6H_5CH_2C_6H_5 \rightarrow C_{13}H_{10} + H_2$ (R9)

The frequency factor of these molecular dehydrogenation reactions accounts for reactant hydrogenation level.

H addition reactions on heavy species and successive de-methylation, also called ipso-addition reaction, further favor dehydrogenation. Again, the kinetic parameters are taken from the similar reactions of light aromatics [191]:

$CH_3C_{10}H_7 + H\bullet \rightarrow C_{10}H_8 + CH_3\bullet$ (R10)

The reference kinetic constant is scaled on the basis of the reactant H/C ratio, while BINs with H/C ratio lower than 0.3 cannot undergo this reaction path.

At very high temperatures, surface radicals can be generated also from C-H fission and kinetic parameters are derived from the reference reaction [151]

$C_6H_6 \rightarrow C_6H_5\bullet + H\bullet$ (R11)

Again the frequency factor is adjusted accounting for the reactant hydrogenation level.

4.3.5 Particle coalescence and aggregation

Particle coalescence and aggregation are very important reaction steps to properly account for the time evolution of particle size distribution [75, 197]. Soot kinetic mechanism includes both these processes.

Particle coalescence involves all the interactions among soot particles (BIN_5-BIN_{12}), and soot particles and aggregates (BIN_{13}-BIN_{20}). Particle aggregation involves only all the interactions among soot aggregates. It is important to observe that after soot inception, i.e. for species heavier than BIN_4, kinetic parameters are similar for radicals and molecules. For this reason, Table 4.4 only refers to BIN, without distinguishing it from the parent radical BIN•.

An asymptotic reference frequency factor of $2 \cdot 10^{11}$ l/(mol s) is assumed for the coalescence among soot particles. Figure 4.13 shows that the collision efficiency adopted in this case is higher than the previous one.

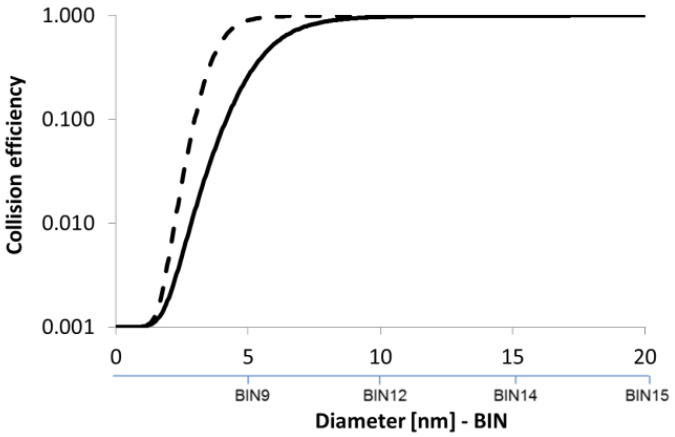

Figure 4.13 Comparison between the collision efficiency of PAH radical condensation on soot particles or aggregates (solid line) and the collision efficiency for particle-particle coalescence (dashed line).

A slightly lower reference value ($1.5 \cdot 10^{11}$ l/(mol s)) is assumed for coalescence of soot particles and aggregates and aggregation. These kinetic parameters fairly agree with the ones proposed by Sirignano et al. [75].

4.3.6 Oxidation

While the complexity of the kinetics of soot inception and growth is well evident from the previous discussions, the successive soot oxidation processes are highly correlated to soot formation

and are even less defined. In fact, soot oxidation rates strongly depend on its structure, aging, and morphology [23].

In order to maintain a large flexibility of the overall kinetic model, several oxidation reactions are considered:

- OH• oxidation of BINs molecules and radicals
- O• oxidation of BINs molecules and radicals
- O_2 oxidation of BINs radicals

Again, the kinetic parameters are derived from similar gas-phase reactions of aromatic species. Rate parameters of the reference reactions of OH• oxidation are derived from the works of Wang and Frenklach [25]:

$OH\bullet + C_{16}H_{10} \rightarrow C_{14}H_9\bullet + CH_2CO$ $k=1\cdot10^{10}\cdot\exp(-10000/RT)$ l/(mol s) (R12)

Moreover, in agreement with Granata et al. [85], OH• interactions to form CO and CH_3• or H• radical are considered:

$OH\bullet + C_{11}H_{10} \rightarrow C_9H_8 + CO + CH_3\bullet$ $k=1.0\cdot10^{10}\cdot\exp(-4000/RT)$ l/(mol s) (R13)

$OH\bullet + C_{10}H_7\bullet \rightarrow C_9H_7\bullet + CO + H\bullet$ $k=2.0\cdot10^{11}$ l/(mol s) (R14)

Finally, the similar reaction of OH proposed by D'Anna and Kent [190] is included,

$OH\bullet + C_{10}H_8 \rightarrow C_9H_8 + HCO\bullet$ $k=3.0\cdot10^{9}\cdot T^{0.5}\cdot\exp(-10600/RT)$ l/(mol s) (R15)

Frequency factors are always dependent on the soot particle or aggregate diameter.

The reference reactions of O• radical oxidation are taken from Wang and Frenklach [25] and Granata et al. [85]:

$O\bullet + C_{16}H_{10} \rightarrow C_{14}H_9\bullet + HCCO\bullet$ $k=2.0\cdot10^{10}\cdot\exp(-4000/RT)$ l/(mol s) (R16)

$O\bullet + C_{10}H_7\bullet \rightarrow C_9H_7\bullet + CO$ $k=5.0\cdot10^{10}$ l/(mol s) (R17)

Moreover, reference O_2 oxidation reactions of BINs radicals to form HCO• and CO [25] and O• and CO [85] are considered:

$O_2 + C_{10}H_7\bullet \rightarrow C_8H_6\bullet + CO + HCO\bullet$ $k=2.1\cdot10^{9}\cdot\exp(-7400/RT)$ l/(mol s) (R18)

$O_2 + C_{10}H_7\bullet \rightarrow C_9H_7\bullet + O\bullet + CO$ $k=2.6\cdot10^{10}\cdot\exp(-6120/RT)$ l/(mol s) (R19)

Furthermore, O_2 oxidation reaction proposed by D'Anna and Kent [190]with the release of two CO is taken into account:

$O_2 + C_{16}H_9\bullet \rightarrow C_{14}H_9\bullet + 2CO$ $k=4.2\cdot10^{8}\cdot T^{0.5}\cdot\exp(-8000/RT)$ l/(mol s) (R20)

Among all these oxidation reactions, OH• radicals play the dominant role, followed by O_2 reactions. Finally, HO_2• oxidation reactions, derived from the reaction of HO_2• with indenyl radical [198], proved to be practically negligible, in the analyzed conditions.

4.3.7 Oxidation-induced fragmentation

The oxidation-induced fragmentation, considered as a process in which the soot clusters or aggregates BIN_i break forming particles of the two previous classes (BIN_{i-1} and BIN_{i-2}), with the kinetics proposed by Sirignano et al. [75] is also considered and its implementation can be explained as follows.

As previously defined, two indexes are used to define the pseudo-species $BIN_{i,j}$, where *i=1,..20* refers to the number of C atoms and *j* to the hydrogenation levels. Figure 4.14 shows for instance the fragmentation of $BIN_{i,B}$.

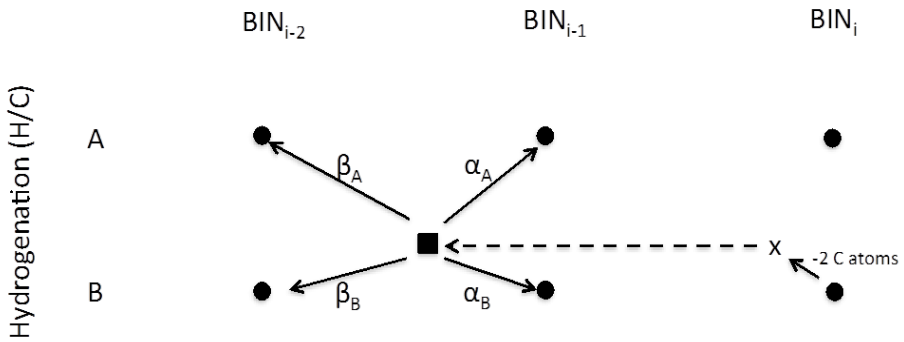

Figure 4.14 Schematic representation of $BIN_{i,B}$ fragmentation induced by O_2 oxidation and the successive splitting of the product "x" among the 4 adjacent BIN pseudo-species (Case 1).

Every black square represents an aggregate BIN_{ij}. Following the loss of two carbon atoms due to oxygen, the resulting fictitious product will have a higher H/C ratio and is graphically represented by the "x" mark. The product "x" is then shifted in the region among four BINs of the previous classes (BIN_{i-1} and BIN_{i-2}) and its carbon and hydrogen atoms are split among them. This is similar to the splitting process of a product of a reaction involving BINs, among the 4 adjacent BINs pseudo-species, as explained for (R5) and in [84].

Several cases with slightly different reactions have to be distinguished in order to respect the stoichiometry. Actually, in the fragmentation process, the H/C ratio of the species that is going to break increases, because of the loss of two carbon atoms. Hence, depending on the H/C ratio of the adjacent classes and the species undergoing the reaction, the stoichiometry and the products are slightly different. Firstly, a first distinction has to be made between $BIN_{i,B}$ (with lower hydrogenation) reactions in Table 4.5 and $BIN_{i,A}$ reactions in Table 4.6.

$BIN_{i,B}$ molecules	
1	if $(H/(C_i\text{-}2))_{i,B} \geq (H/C)_{i\text{-}1,B}$ and $(H/(C_i\text{-}2))_{i,B} \geq (H/C)_{i\text{-}2,B}$ $BIN_{i,B} \rightarrow 2CO + \alpha_A\ BIN_{i\text{-}1,A} + \alpha_B\ BIN_{i\text{-}1,B} + \beta_A\ BIN_{i\text{-}2,A} + \beta_B\ BIN_{i\text{-}2,B}$
$\alpha_B = \dfrac{\left(\frac{H}{C}\right)_{BIN_{i-1}A} - \frac{H_{BIN_i}}{C_{BIN_i}-2}}{\left(\frac{H}{C}\right)_{BIN_{i-1}A} - \left(\frac{H}{C}\right)_{BIN_{i-1}B}}$ $\alpha_A = 1 - \alpha_B = 1 - \dfrac{\left(\frac{H}{C}\right)_{BIN_{i-1}A} - \frac{H_{BIN_i}}{C_{BIN_i}-2}}{\left(\frac{H}{C}\right)_{BIN_{i-1}A} - \left(\frac{H}{C}\right)_{BIN_{i-1}B}}$ $\beta_B = \dfrac{(H_{BIN_i} - \alpha_A \cdot H_{BIN_{i-1}A} - \alpha_B \cdot H_{BIN_{i-1}B}) \cdot C_{BIN_{i-2}} - (C_{BIN_i} - 2 - C_{BIN_{i-1}}) \cdot H_{BIN_{i-2}A}}{C_{BIN_{i-2}} \cdot (H_{BIN_{i-2}B} - H_{BIN_{i-2}A})}$ $\beta_A = \dfrac{C_{BIN_i} - 2 - C_{BIN_{i-1}}}{C_{BIN_{i-2}}} - \beta_B$	
2	if $(H/(C_i\text{-}2))_{i,B} = (H/C)_{i\text{-}1,B}$ and $(H/(C_i\text{-}2))_{i,B} < (H/C)_{i\text{-}2,B}$ $BIN_{i,B} \rightarrow 2CO + \alpha_A\ BIN_{i\text{-}1,A} + \alpha_B\ BIN_{i\text{-}1,B}$
$\alpha_B = \dfrac{\frac{C_{BIN_i}-2}{C_{BIN_{i-1}}} \cdot H_{BIN_{i-1}A} - H_{BIN_i}}{H_{BIN_{i-1}A} - H_{BIN_{i-1}B}}$ $\alpha_A = \dfrac{C_{BIN_i}-2}{C_{BIN_{i-1}}} - \alpha_B$	
3	else (all other cases) $BIN_{i,B} \rightarrow 2CO + BIN_{i\text{-}1,B} + \beta_B\ BIN_{i\text{-}2,B} + \gamma\ CSOLID$
$\beta_B = \dfrac{H_{BIN_i} - H_{BIN_{i-1}B}}{H_{BIN_{i-2}B}}$ $\gamma = C_{BIN_i} - 2 - C_{BIN_{i-1}} - \beta_B \cdot C_{BIN_{i-2}}$	
$BIN_{i,BJ}$ radicals	
4	if $(H/(C_i\text{-}2))_{i,BJ} \geq (H/C)_{i\text{-}1,BJ}$ and $(H/(C_i\text{-}2))_{i,BJ} \geq (H/C)_{i\text{-}2,BJ}$ $BIN_{i,BJ} \rightarrow 2CO + \alpha_A\ BIN_{i\text{-}1,AJ} + \alpha_B\ BIN_{i\text{-}1,BJ} + \beta_B\ BIN_{i\text{-}2,B}$
$\alpha_B = \dfrac{H_{BIN_{i-1}AJ} - H_{BIN_iJ} + \frac{C_{BIN_i}-2-C_{BIN_{i-1}}}{C_{BIN_{i-2}}} \cdot H_{BIN_{i-2}B}}{H_{BIN_{i-1}AJ} - H_{BIN_{i-1}BJ}}$ $\alpha_A = 1 - \alpha_B$ $\beta_B = \dfrac{C_{BIN_i} - 2 - C_{BIN_{i-1}}}{C_{BIN_{i-2}}}$	
5	if $(H/(C_i\text{-}2))_{i,BJ} < (H/C)_{i\text{-}1,BJ}$ or $(H/(C_i\text{-}2))_{i,BJ} < (H/C)_{i\text{-}2,B}$ $BIN_{i,B} \rightarrow 2CO + BIN_{i\text{-}1,BJ} + \beta_B\ BIN_{i\text{-}1,B} + \gamma\ CSOLID$
$\beta_B = \dfrac{H_{BIN_iJ} - H_{BIN_{i-1}BJ}}{H_{BIN_{i-2}B}}$ $\gamma = C_{BIN_i} - 2 - C_{BIN_{i-1}} - \beta_B \cdot C_{BIN_{i-2}}$	

Table 4.5 Oxidation-induced fragmentation reactions for $BIN_{i,B}$ species. The letter "J" after the *j* index indicates a radical species.

$BIN_{i,A}$ molecules	
6	if $(H_i - H_{i-1,A})/(C_i - 2 - C_{i-1}) \leq (H/C)_{i-1,B}$ $BIN_{i,A} \rightarrow 2CO + BIN_{i-1,A} + \beta_A\ BIN_{i-2,A} + \beta_B\ BIN_{i-2,B}$
$\beta_B = \frac{H_{BIN_i} - H_{BIN_{i-1}A} - \frac{H_{BIN_{i-2}A}}{C_{BIN_{i-2}}} \cdot (C_{BIN_i} - 2 - C_{BIN_{i-1}})}{H_{BIN_{i-1}B} - H_{BIN_{i-1}A}}$ $\beta_A = \frac{C_{BIN_i} - 2 - C_{BIN_{i-1}}}{C_{BIN_{i-2}}} - \beta_B$	
7	if $(H_i - H_{i-1,A})/(C_i - 2 - C_{i-1}) > (H/C)_{i-1,B}$ $BIN_{i,A} \rightarrow 2CO + BIN_{i-1,A} + \beta_A\ BIN_{i-2,A} + \gamma\ BIN_{i-n}$
$\beta_A = \frac{(H_{BIN_i} - H_{BIN_{i-1}}) \cdot C_{BIN_{i-n}} + (2 + C_{BIN_{i-1}} - C_{BIN_i}) \cdot H_{BIN_{i-n}}}{H_{BIN_{i-2}} \cdot C_{BIN_{i-n}} - C_{BIN_{i-2}} \cdot H_{BIN_{i-n}}}$ $\gamma = \frac{C_{BIN_i} - 2 - C_{BIN_{i-1}} - \beta_A \cdot C_{BIN_{i-2}}}{C_{BIN_{i-n}}}$	

Table 4.6 Oxidation-induced fragmentation reactions for $BIN_{i,A}$ species.

Case 1 of oxidation-induced fragmentation for $BIN_{i,B}$ species is represented in Figure 4.14 and involves the formation of the "x" product with higher H/C ratio than the one of previous classes (BIN_{i-1} and BIN_{i-2}). The four stoichiometric coefficients of the products are found solving C and H atom balances (2 equations), under the hypothesis that every molecule is split in only one molecule of the immediately lower BIN class (BIN_{i-1}) and the rest of C atoms forms BINs molecules of two lower classes (1 equation) and on the basis of a lever rule that can be used as far as $(H/C)_{i,B} = (H/C)_{i-1,B} = (H/C)_{i-2,B}$ (1 equation).

Case 2 regards the formation of the "x" product with the same H/C ratio of the lower BIN class (BIN_{i-1}). As shown in Figure 4.15, the product is splitted only between BINs of the immediately lower class.

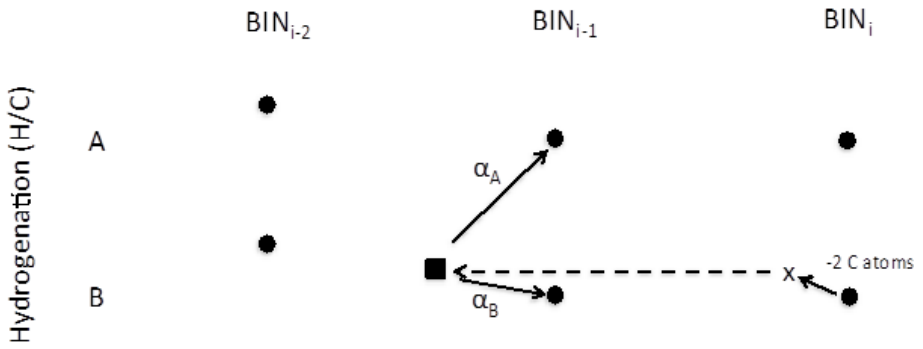

Figure 4.15 Schematic representation of $BIN_{i,B}$ fragmentation induced by O_2 oxidation and the successive splitting of the product "x" (Case 2).

Case 3 regards all the other conditions, such as the formation of the "x" product with a lower H/C than the hydrogenation of $BIN_{i,B}$, as shown in Figure 4.16.

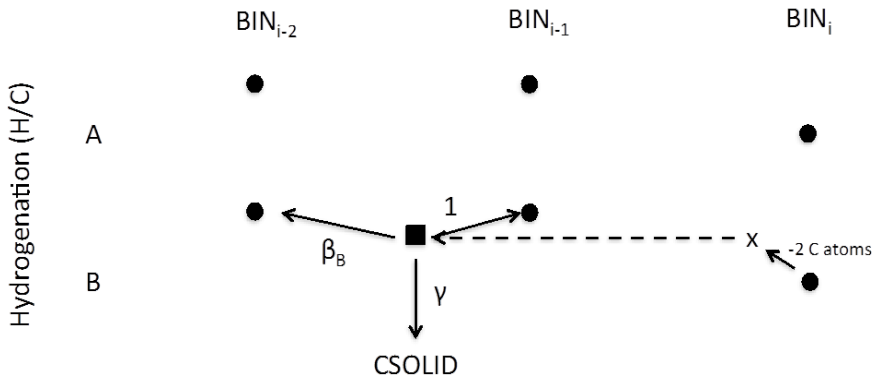

Figure 4.16 Schematic representation of $BIN_{i,B}$ fragmentation induced by O_2 oxidation and the successive splitting of the product "x" (Case 3).

In this case, it is necessary to consider a very dehydrogenated species that is called CSOLID and is the graphitized BIN with only C atoms, which are the same of the last BIN class.

Case 4 and 5 regard the reactions of BIN radical species, defined with the letter "J" after the j index ($BIN_{i,BJ}$). These reactions are similar to molecules' ones, but it is necessary to modify the stoichiometry in such a way that only one radical ($BIN_{i-1,J}$) is formed. Hence, the radical formed is the BIN_{i-1}, while BIN_{i-2} are the corresponding molecules with the same H/C ratio.

Table 4.6 summarizes the main reactions of $BIN_{i,A}$ molecules. Case 6 involves the "x" product more hydrogenated of the immediately lower class, but still more dehydrogenated of the BIN_{i-2} species. Case 7 represents instead the case in which the hydrogenation of the product "x" is also higher than BIN_{i-2} species. A new BIN class has to be introduced (BIN_{i-n}), as shown Figure 4.17, for which $(H/C)_{i-n,A} > (H/C)_{i-2,A}$.

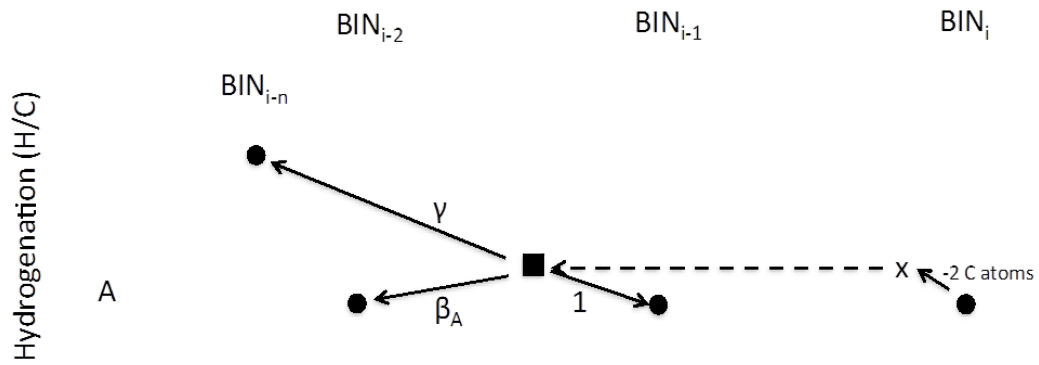

Figure 4.17 Schematic representation of $BIN_{i,A}$ fragmentation induced by O_2 oxidation and the successive splitting of the product "x" (Case 7).

For $BIN_{i,AJ}$ radical species, the reactions are exactly the same as for the molecules. The only difference is that the reactant and the product BIN_{i-1} are radicals.

Nevertheless, the effect of these oxidation-induced fragmentation reactions resulted negligible in the conditions of the premixed BSS ethylene flame, described in paragraph 5.4.

5. Laminar premixed ethylene flames

In this paragraph, the capability of the model to predict soot formation is tested against different laminar premixed ethylene flames, that are listed as some of the target flames of the International Sooting Flame workshop (ISF) [199].

The effect of the equivalence ratio is discussed thanks to the comparisons between predictions and experiments of three atmospheric flames measured in the University of Michigan and in the Pennsylvania State University [200, 201].

The model is also examined against different pressures and equivalence ratios of premixed ethylene flames explored at the German Aerospace Center (DLR) [202].

Finally different temperature conditions are investigated by means of comparison with the experimental data collected by the University of Naples [50, 121, 180, 181, 203, 204].

As the significant heat losses are difficult to estimate in premixed burner-stabilized flames, the temperature profile suggested on the ISF website [198] is used as input in the numerical simulations.

5.1 The effect of equivalence ratio

Two groups studied soot formation in laminar premixed ethylene/air flames at atmospheric pressure in respect of variations of the equivalence ratio [200, 201]. The flames are produced by a 6 cm diameter water-cooled porous-plate laminar premixed flat-flame burner at atmospheric pressure (McKenna model). The reactant mixture at the burner exit is surrounded by an annular nitrogen flow to eliminate peripheral diffusion. The burner is cooled using water at room temperature with a flow rate sufficiently high. The flame is stabilized using a 125 mm diameter circular aluminum plate with a 30 mm hole in the center that is mounted 32 mm above the burner surface.

Temperatures are measured through 2 different techniques, namely:

- using multiline emission measurements (effectively 2-color pyrometry measurements) within the soot-containing regions of the flame [200]. Even though, the experimental uncertainties are estimated below 50 K, these measurements are larger than the adiabatic flame temperatures (by 200 or 300 K) and should not be used.

- using a spectral line reversal technique (769.9 nm emission line of potassium) in regions where substantial absorption of the radiation by soot particles is observed. Temperature is determined using two-color pyrometry [201].

Concentrations of major gas species are measured by isokinetic sampling and gas chromatography, with experimental errors below 15% for mole fractions greater than 0.5% [200].

Soot volume fractions are measured using 3 different techniques, namely:

- Laser-extinction measurements at 632.8 nm. Refractive indices from Dalzell and Sarofim. The experimental uncertainties of these measurements (95% confidence) are estimated to be less than 10% for f_v > 0.1 ppm, increasing inversely proportional to f_v for smaller soot volume fractions. [200]
- Isokinetic sampling from the flames followed by measurement of the gas and soot volumes in the samples (gravimetric method with an assumed soot density of ρ =1850 kg/m^3). The gravimetric soot volume fraction has experimental uncertainty (95% confidence) less than 15%. [200]
- Laser-extinction measurements at 524.5 nm. Refractive indices from Dalzell and Sarofim. [201]

Table 5.1 shows the characteristics of the three flames.

	C/O ratio	**Equivalence ratio Φ**	**Cold gas velocity [cm/s]**	**C_2H_4 mole fraction**	**O_2 mole fraction**	**N_2 mole fraction**
Flame 1	0.78	2.34	6.8	0.14	0.18	0.68
Flame 2	0.88	2.64	6.8	0.156	0.177	0.667
Flame 3	0.98	2.94	5.3	0.17	0.174	0.656

Table 5.1 Inlet characteristics of the Target flames 2.

The profiles of the major species at different C/O ratio are shown in Figure 5.1.

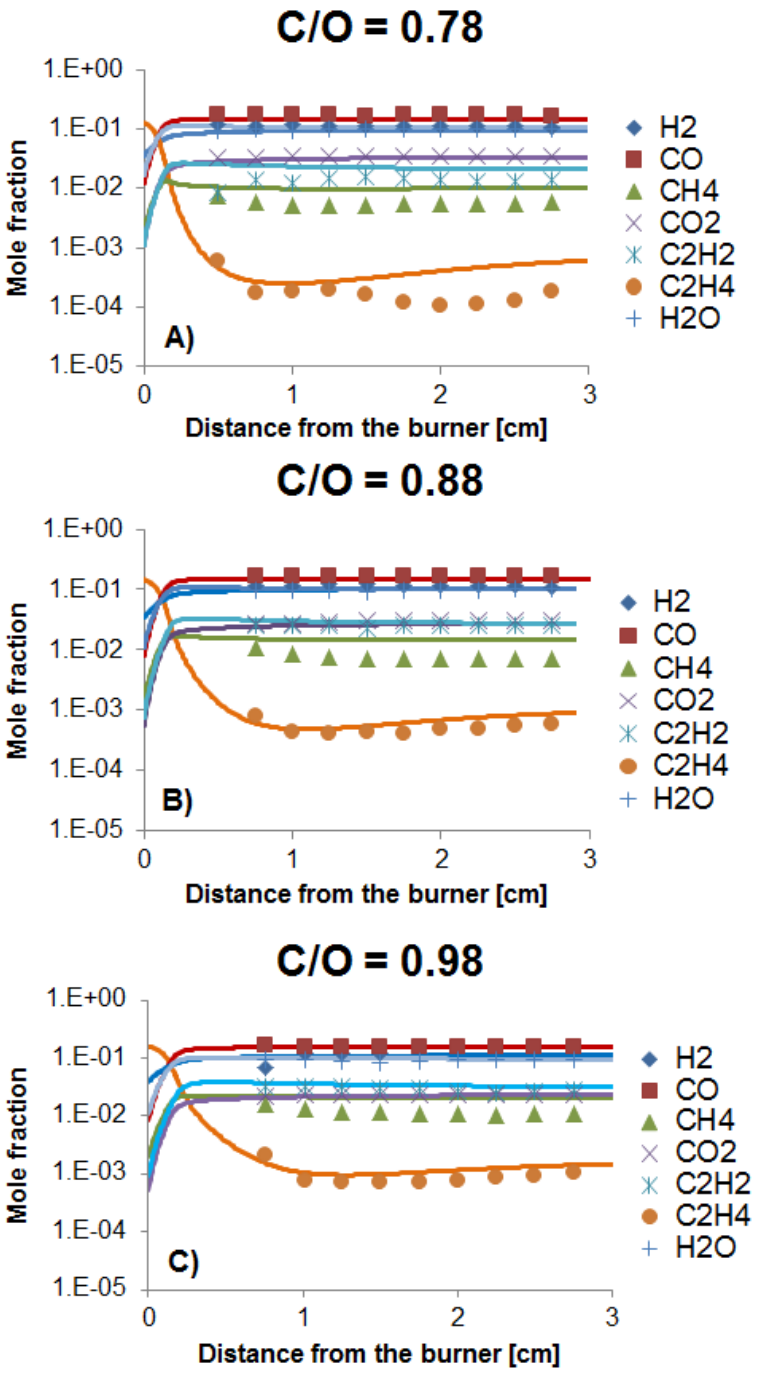

Figure 5.1 Comparison between the experimental measurements (symbols) [200] and simulation results (solid lines) for the major gas species as function of distance from the burner. Panel A) C/O = 0.78; Panel B) C/O = 0.88; Panel C) C/O = 0.98.

The experimental data are presented in a logarithmic scale; therefore it is difficult to make a precise comparison. However, there is a good agreement between the model and the measured values. Ethylene is consumed more slowly in the richer environment, since oxygen is consumed faster (even though the experimental oxygen profiles are not shown in the paper). CO_2 and H_2O concentration decreases in richer flames, because the ideal reaction is penalized.

The predicted and measured soot volume fraction for each flame is presented in Figure 5.2.

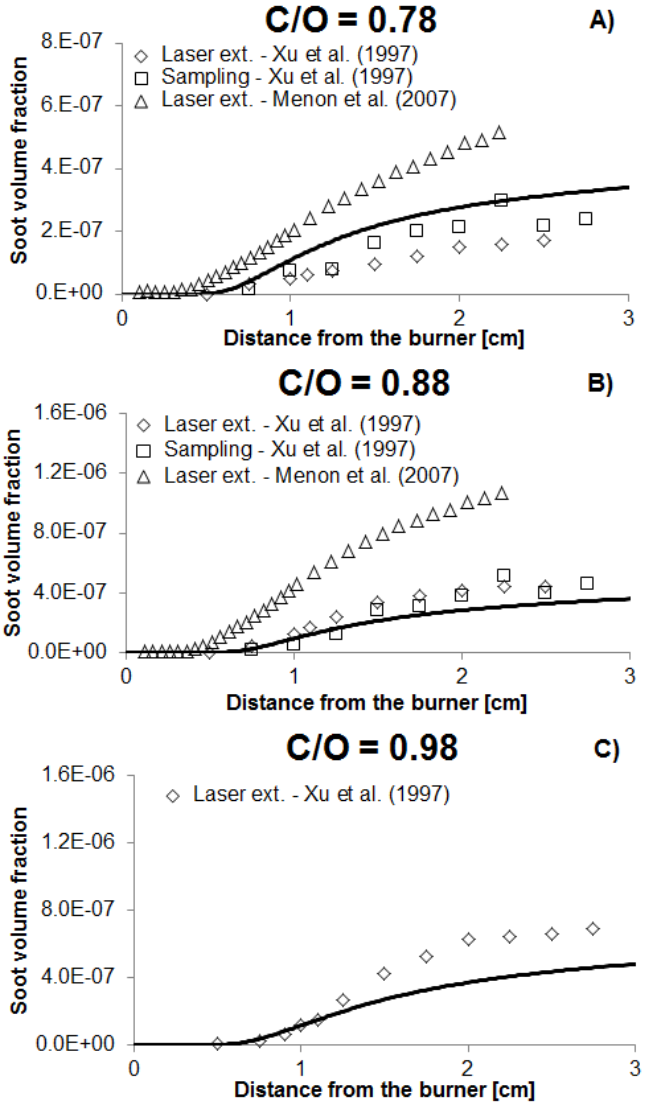

Figure 5.2 Comparison between the experimental measurements (symbols) [200, 201] and simulation results (solid lines) for soot volume fraction as a function of the distance from the burner. Panel A) C/O = 0.78; Panel B) C/O = 0.88; Panel C) C/O = 0.98.

At higher C/O ratios of course the soot volume fraction is higher, because the pyrolytic pathway is fostered. The model predicts well the point of soot inception inside the experimental uncertainties, but slightly underestimates the experimental data in richer conditions. No data on number density or PSDFs are available, hence it is hard to analyze the possible causes of the overestimation.

5.2 The effect of pressure

Tsurikov et al. [202] conducted an experimental investigation into soot formation in laminar premixed ethylene flames at atmospheric and elevated pressures (1-5 bar) and with different equivalence ratios, as shown in Table 5.2.

Fuel	Φ	Pressure [bar]	Inlet mass flow rate [kg/s]	Maximum temperature [K]	Maximum experimental soot f_v
C_2H_4	2.3	1	1.2e-4	1734	0.5
	2.5	1	1.2e-4	1671	0.6
	2.3	3	2.6e-4	1732	1.7
	2.5	3	2.6e-4	1710	4
	2.05	5	3.2e-4	1724	1.7
	2.4	5	3.2e-4	1738	10

Table 5.2 Inlet conditions and summary of the characteristics of the laminar premixed ethylene flames (Target flames 4). Φ is the equivalence ratio and f_v the soot volume fraction.

The central, sooting flame (ethylene/air) is stabilized above a water-cooled sintered bronze matrix. This flame is surrounded by a non-sooting "shielding flame" of methane/air (Φ =1.68). The flames are surrounded by an air coflow. The diameters of the central matrix, shielding matrix, and coflow duct are 41.3 mm, 61.3 mm, and 150 mm, respectively. This dual-flame burner is enclosed in a pressure housing.

Soot volume fraction measurements are obtained using LII coupled with a quasi-simultaneous absorption measurement for calibration. Temperature measurements are obtained with shifted vibrational coherent anti-Stokes Raman scattering, which yields well-resolved, accurate temperature measurements in sooting and non-sooting environments. The experimental errors are within 30% for soot volume fraction and 3% for the temperature.

The results of the soot formed in premixed ethylene flames at different pressures and equivalence ratios are presented in Figure 5.3.

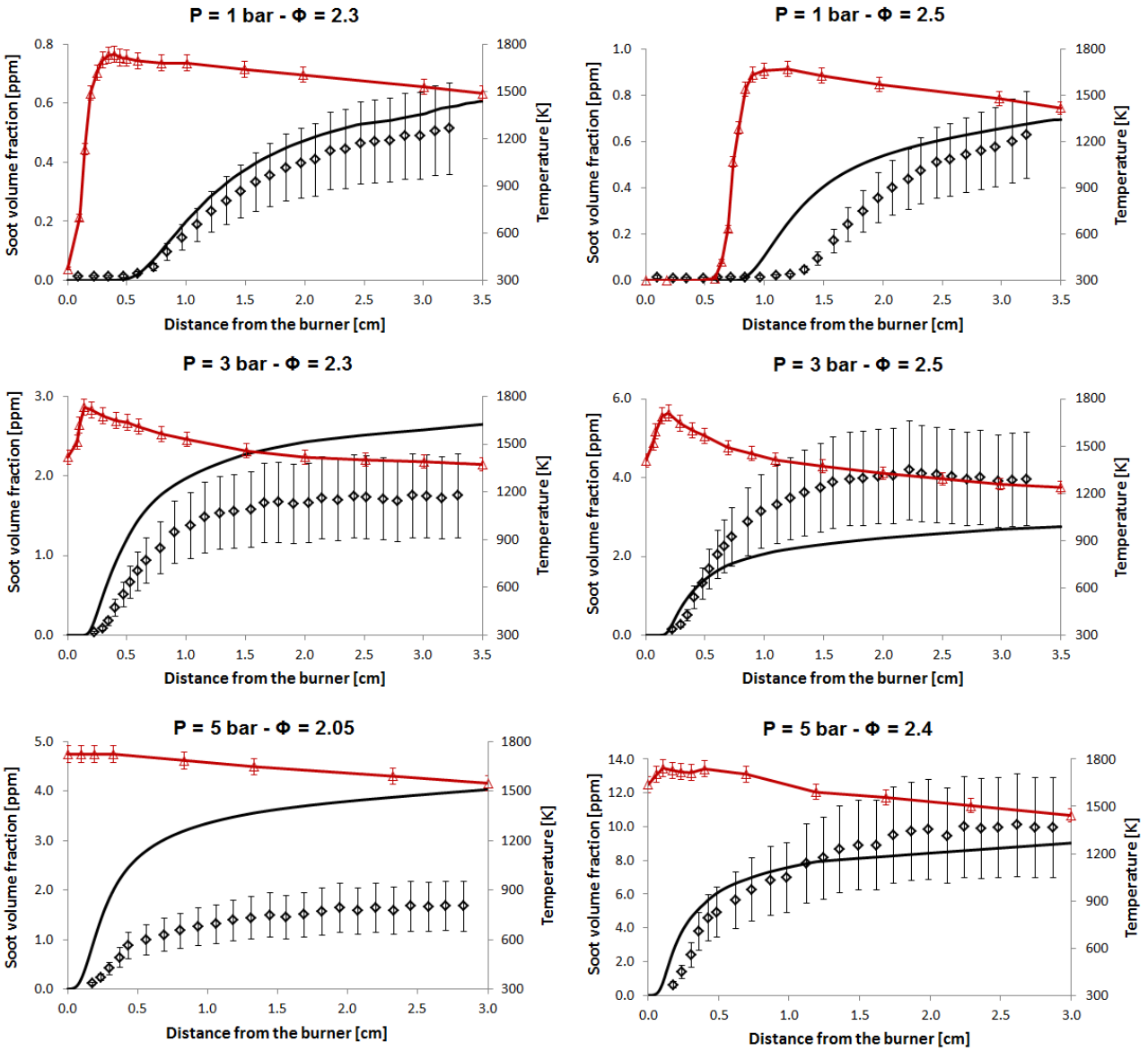

Figure 5.3 Comparison between the experimental (diamonds) [202] and the computed (black line) soot volume fraction profiles along the flame axes. Soot volume fraction refer to the primary axis; while the respective experimental temperature profile imposed in each simulation (red line with triangles) refer to the secondary axis.

The model manages to predict the soot volume fractions quite well at different pressures and equivalence ratios. The temperature peaks in the main reaction zone; at higher heights above the burner it decreases because of radiative losses from soot particles.

Soot starts to form further downstream with respect to the main reaction zone, after the sequential growth processes have occurred. The soot volume fraction increases with pressure and its formation starts closer to the burner surface. Surface growth, nucleation and coagulation reactions are indeed enhanced at higher pressure, fostering the pathway that leads to soot. The earlier soot formation, instead, is related to the shift of the main reaction zone towards the burner surface

because, as experimentally observed, the flame itself moves closer to the burner since it is not possible to lift it at high pressure. Moreover, the rate of production analysis of the ethylene flame at 1 bar and Φ = 2.3 is performed, focusing mainly on the pathways leading to soot formation, and presented in Figure 5.4.

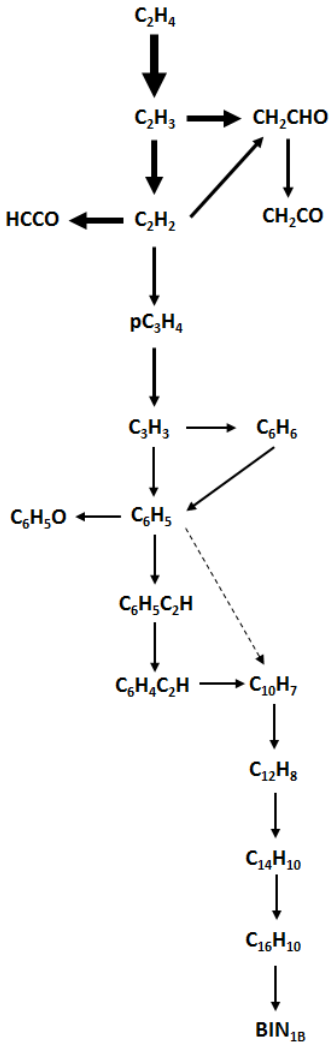

Figure 5.4 Pathways from fuel to BIN_{1B} for ethylene flame at 1 bar and Φ = 2.3. The thickness of the arrows reflects the relative significance of the different reaction pathways.

After the formation of the propargyl radical (C_3H_3), the central step is the production of phenyl radical. It afterwards grows to phenylacetylene, naphthalene and heavier PAHs. The importance of the HACA mechanism is evident since the most important steps involve an even PAHs growth. Soot production is very sensitive with respect to pressure because growth reactions like condensation and coagulation involve a decrease of the moles' number; therefore they are favored

by a pressure increase (at least in the pressure-range of interest). The profiles of the main species and some soot precursors along the flame axis from our simulations of the conditions in [202] are compared for two different pressures and similar equivalence ratio in Figure 5.5.

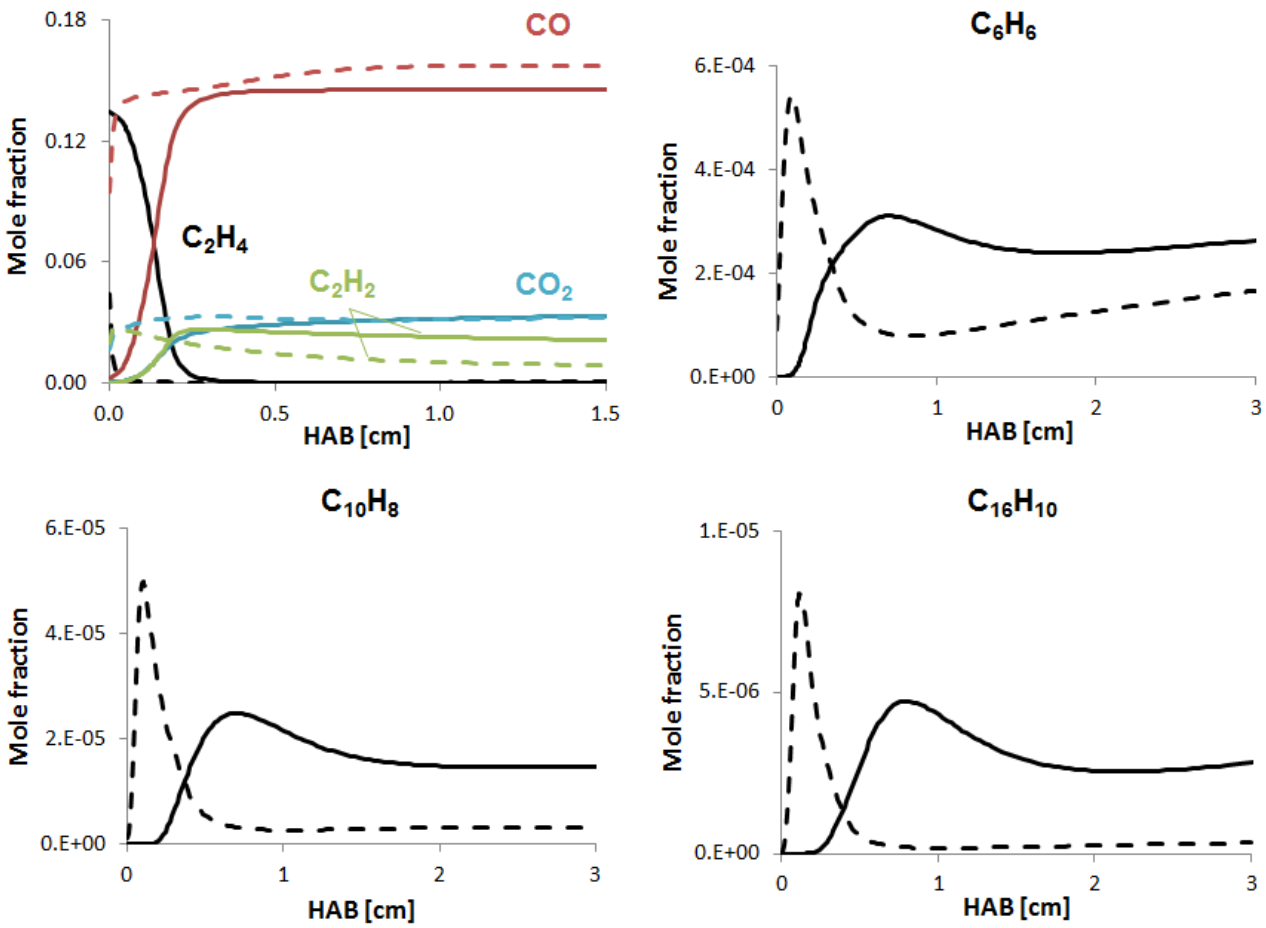

Figure 5.5 Profiles of the main species (C_2H_4, CO, CO_2, C_2H_2) and soot precursors (C_6H_6, $C_{10}H_8$, $C_{16}H_{10}$) along the flame axis for the premixed ethylene flames at 1 bar and Φ = 2.3 (solid line) and 5 bar and Φ = 2.4 (dashed line).

These flames have similar stoichiometric conditions and also similar peak temperature (around 1730 K, see Table 5.2), therefore the effect of pressure is clear and can be studied independently. As pressure increases, the flame thickness becomes narrower with maximum temperature shifted to lower HAB (see Figure 5.3). Therefore, the chemistry evolution occurs closer to the burner as shown by the ethylene profile in Figure 5.5. All species at 5 bar are formed nearer to the burner in respect to lower pressures, with a peak at ~0.1 cm, and their depletion towards heavier species ends within the first centimeter above the burner.

Figure 5.6 and Figure 5.7 show the comparison of benzene rate of production analysis at 1 bar and at 5 bar, respectively. The numbers on the left column identify the reaction number inside the kinetic scheme. The right column presents the values of the global rate of reaction, proportional to the bars' length. The negative values indicate reactions that lead to depletion of the considered species (identified by blue bars), the positive ones those in which the species is produced (identified by red bars).

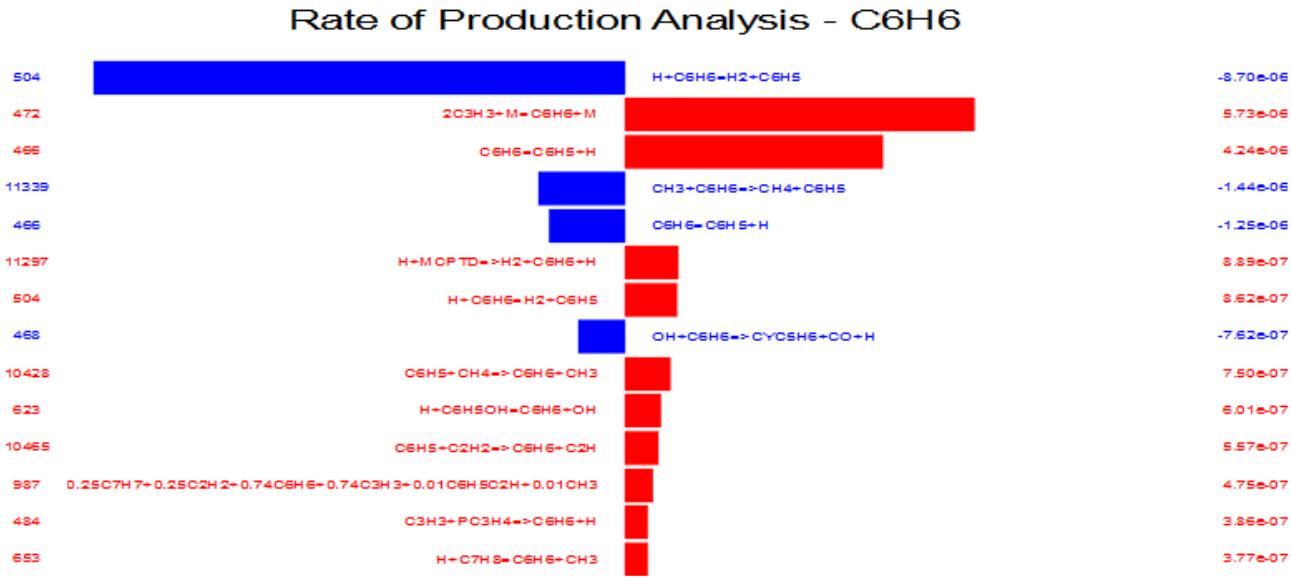

Figure 5.6 ROPA of benzene for the ethylene flame at 1 bar and Φ = 2.3.

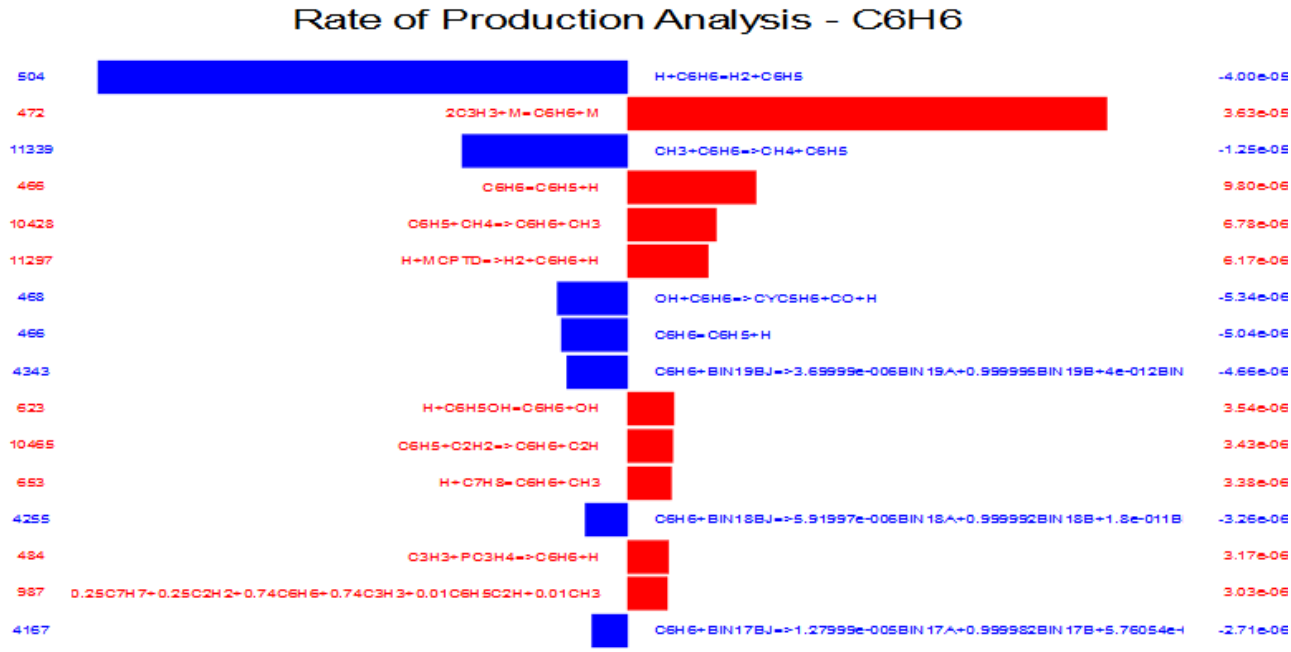

Figure 5.7 ROPA of benzene for the ethylene flame at 5 bar and Φ = 2.4.

The reactions involved are not drastically different, but the pathways leading to benzene condensation on BIN species (reactions' numbers: 4167, 4255 and 4343 in Figure 5.7) grow in importance at higher pressures, as mentioned before.

5.3 The effect of temperature

The research group of the University of Naples [50, 121, 180, 181, 203, 204] studied the temperature dependence of soot in fuel-rich, atmospheric, premixed C_2H_4/O_2 flames. To analyze such behavior three different flames were set up, all with the same equivalence ratio but different cold-gas velocities, which means different temperatures. The flames were stabilized on a water-cooled, sintered-bronze McKenna burner (diameter = 6 cm) surrounded by a shroud of nitrogen. The temperature was measured with a thermocouple following a fast insertion procedure to prevent soot from depositing and affecting the measurements. The uncertainty of the measured temperatures was estimated to be as high as 100 K. Soot, condensable species (CS), and gaseous combustion products were isokinetically sampled along the flame axis by using a stainless-steel water-cooled probe. On-line gas chromatography was used to analyze the light hydrocarbons. Soot and CS were collected on a teflon filter and in a cold trap and extracted by dichloromethane (DCM) to separate the DCM-soluble material (condensed species) from the insoluble solid carbonaceous material (soot). The amount of soot was then determined gravimetrically. Table 5.3 shows the characteristics of the three flames.

	Equivalence ratio Φ	C_2H_4 mole fraction	O_2 mole fraction	Cold gas velocity [cm/s]	Maximum Temperature [K]	Pressure [atm]
Flame 1	2.4	0.444	0.556	2	1520	1
Flame 2	2.4	0.444	0.556	4	1715	1
Flame 3	2.4	0.444	0.556	6	1820	1

Table 5.3 Inlet conditions of the Target flames 5.

In the simulation of each flame, to account for the probe perturbation, the computed profiles are shifted of ~0.15 cm, in order to match the 50% of ethylene conversion. Figure 5.8 shows the

profiles of ethylene, acetylene, benzene and heavier PAHs along the flame axis for the three different flames (Red symbols and lines: Flame 1; Black: Flame 2; Blue: Flame 3).

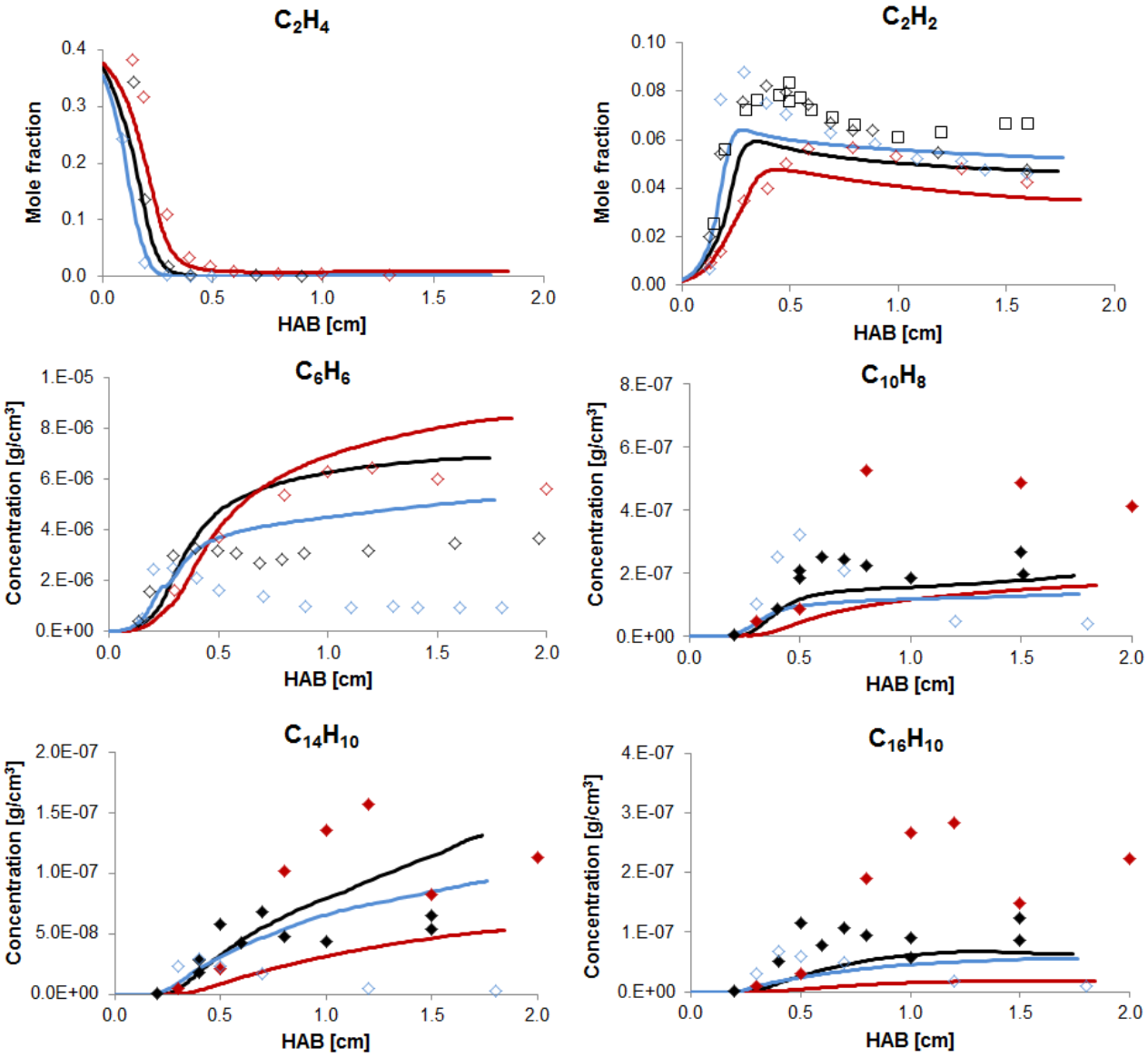

Figure 5.8 Comparison between experimental measurements (symbols) and computed profiles (solid lines) of ethylene, acetylene, benzene, naphthalene, phenanthrene and pyrene in the three flames. Red symbols and lines: Flame 1; black: Flame 2; blue: Flame 3. Open diamonds: Ciajolo et al. (1996) [203]; filled diamonds: Ciajolo et al. (2001) [50]; squares: Apicella et al. (2002) [204].

As the cold-gas velocity increases, the maximum temperature, located around the flame front, rises, increasing the burning velocity and hence shortening the main reaction zone. Actually, the fuel is consumed closer to the burner surface, all the species profiles shift and ethylene conversion increases.

Acetylene peaks after the fuel is consumed and then levels off, as seen in Figure 5.8. Even though the model underpredicts acetylene concentration in the main reaction zone, the relative trend of acetylene concentration among the three flames is well represented and further from the burner the computed concentrations of the two flames at higher temperature match the experimental data. Probably in the flame with the lowest cold-gas velocity the temperature is too low to activate the reactions that lead to acetylene production. The comparison of the C_2H_2 rates of production at the lowest temperature (Figure 5.9) and the highest (Figure 5.10) shows that the reactions involved are not drastically different. In Figure 5.9 and Figure 5.10, the numbers on the left column identify the reaction number inside the kinetic scheme. The right column presents the values of the global rate of reaction, proportional to the bars' length. The negative values indicate reactions that lead to depletion of the considered species (identified by blue bars), the positive ones those in which the species is produced (identified by red bars).

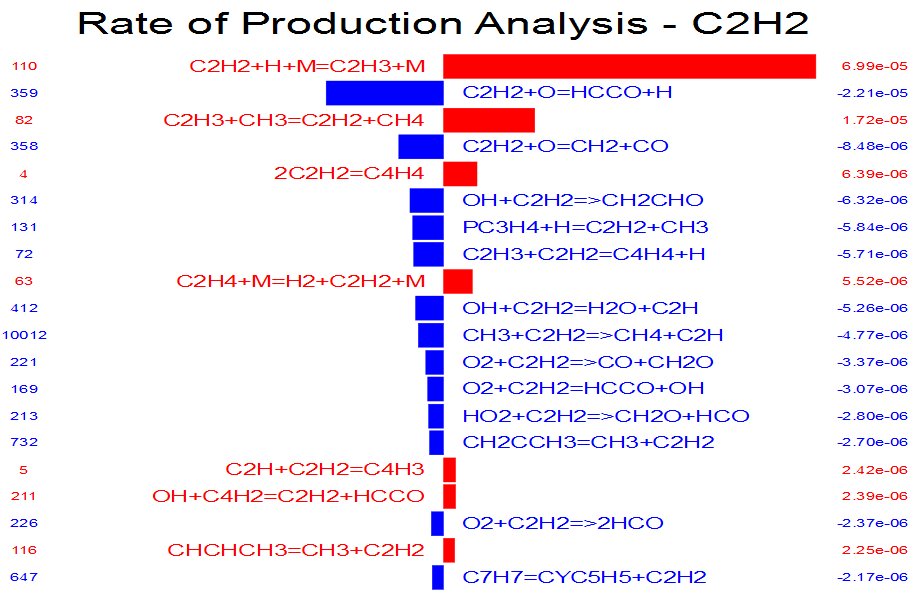

Figure 5.9 ROPA of acetylene for Flame 1.

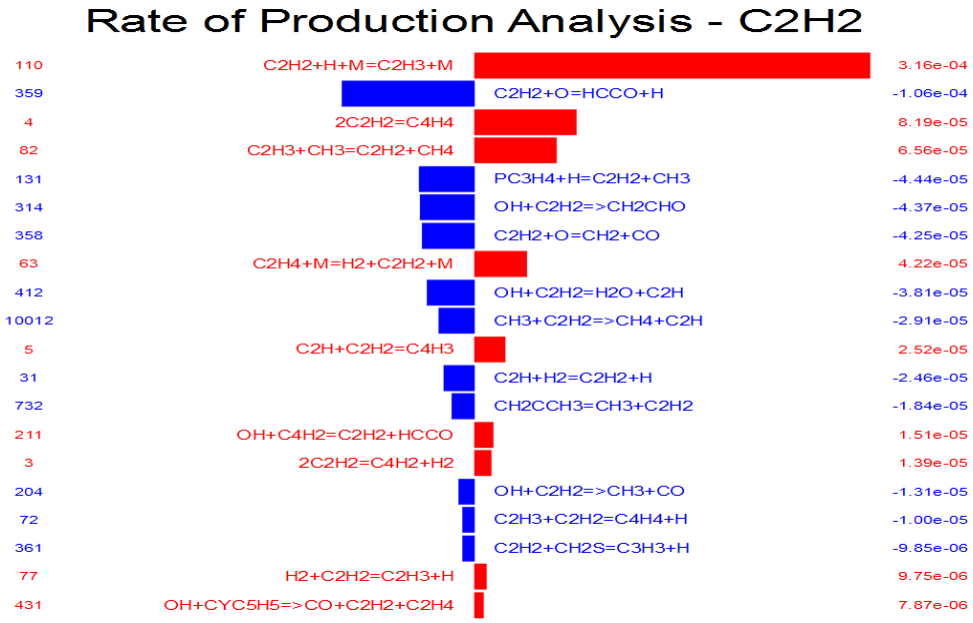

Figure 5.10 ROPA of acetylene for Flame 3.

The pathway is analogous, but the main reactions leading to acetylene formation at high temperature lose importance at low temperature with respect to acetylene consumption pathways, as for instance reactions 358, 72, 221…. In Figure 5.8, the model overpredicts benzene concentration in Flames 2 and 3, while agrees well with the data measured in Flame 1. The profiles of heavy PAHs, such as $C_{10}H_8$, $C_{14}H_{10}$ and $C_{16}H_{10}$, in Flame 2 and Flame 3 are inside the experimental uncertainties, while in Flame 1 are underpredicted. Therefore, soot concentration (Figure 5.11) is

fairly well predicted and inside the experimental uncertainty in Flame 2 and Flame 3, while clearly underpredicted in Flame 1.

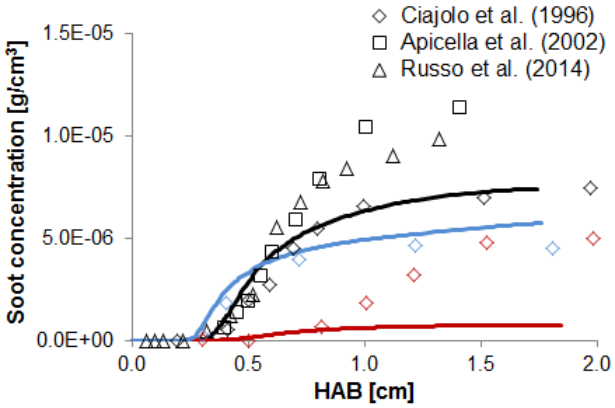

Figure 5.11 Comparison between experimental measurements (symbols) and computed profiles (lines) of soot concentration in the three flames along the flame axis. Red diamonds and lines: Flame 1; black: Flame 2; blue: Flame 3. Diamonds: Ciajolo et al. (1996) [203]; squares: Apicella et al. (2002) [204]; triangles: Russo et al. (2014) [180].

For Flame 1, as expected considering that the acetylene plays a fundamental role in the growth process of PAHs and soot, the model does not predict a reasonable soot concentration because the temperature is too low to activate the pathways that lead to its production. On the other hand, soot inception in Flame 2 and 3 is reasonably caught by the model, as could be deduced also from the observation of the PAHs that are the main soot precursors.

Investigating the soot temperature dependence, we can observe that the soot mass fraction presents a maximum with respect to temperature. At low temperatures soot formation process is not activated, while at high temperature and in pyrolytic conditions particles break up to produce acetylene, which is more stable. Figure 5.12 shows the measured and computed maximum soot concentrations as a function of the maximum flame temperature.

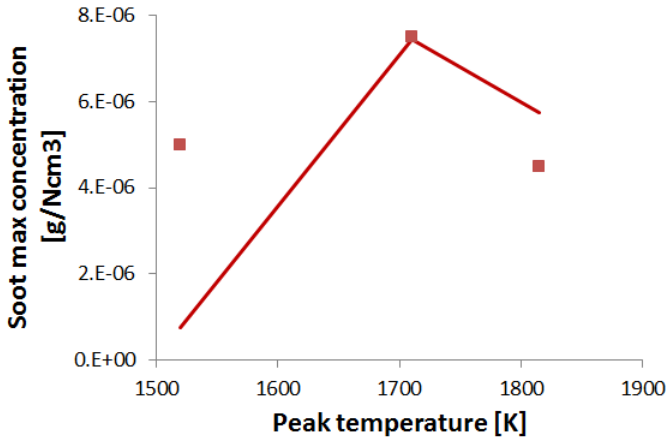

Figure 5.12 Comparison between experimental (symbols) and computed (line) maximum soot concentration as function of maximum flame temperature.

The soot bell attains the experimental and computed maximum at 1700 K. However, in the rising side of the bell the model is slower than experimentally observed.

In conclusion, an improvement of the precision of temperature measurements and more data of the evolution of heavier PAH species along the flame axis, thereby reducing experimental uncertainties, seem to be required to better examine and discuss model predictions.

5.4 Burner-stabilized stagnation ethylene flame

In this paragraph, the discussion focuses mainly on the analysis of the burner-stabilized stagnation ethylene flame, that is described in the work of Abid et al. [53], listed as target flame in the ISF website and chosen as main case study to examine and refine the soot kinetic model.

In particular, traditionally soot sampling in laminar premixed flames has been done by means of a probe [54, 58]. Soot particles are isokinetically sampled along the flame axis by means of a probe positioned horizontally with an orifice on the center axis. The main issue with this technique lies in the intrusiveness of the probe. Indeed, the probe cools down the surroundings [53, 205], affecting the kinetics, and introduces a local flow stagnation, thus modifying the flow field and altering particles residence times with respect to those in a free flame.

However, usually in modeling studies the system is simulated as a free flame, since the boundary conditions are not well defined. The given experimental temperature profile is measured without the presence of the probe and anyway it is not possible to reproduce the fluid dynamics around a cylinder in cross flow with a 1D simulation. The intrusiveness of the sampling system and its cooling effect on the upstream flow are roughly taken into account by shifting the computed results along the flame axis [206]. Hence, comparisons between experimental measurements and modeling results are only approximated. Recently, there has been a lot of effort to quantify the probe effects on the flame structure by means of 2D modeling [205, 207]. Of course, a direct numerical simulation can give very detailed information about the system, the fluid dynamics and the changes in reactivity, but it is computationally demanding.

Therefore to minimize the problem of probe perturbation in mobility measurements, Abid et al. [53] proposed the BSS flame configuration, in which the sampling probe is embedded in a water-cooled circular plate positioned above the flame that acts as a flow stagnation surface (Figure 5.13). This technique allows for a rigorous description of the perturbation brought to the flame by the sampling system, through well-defined boundary conditions.

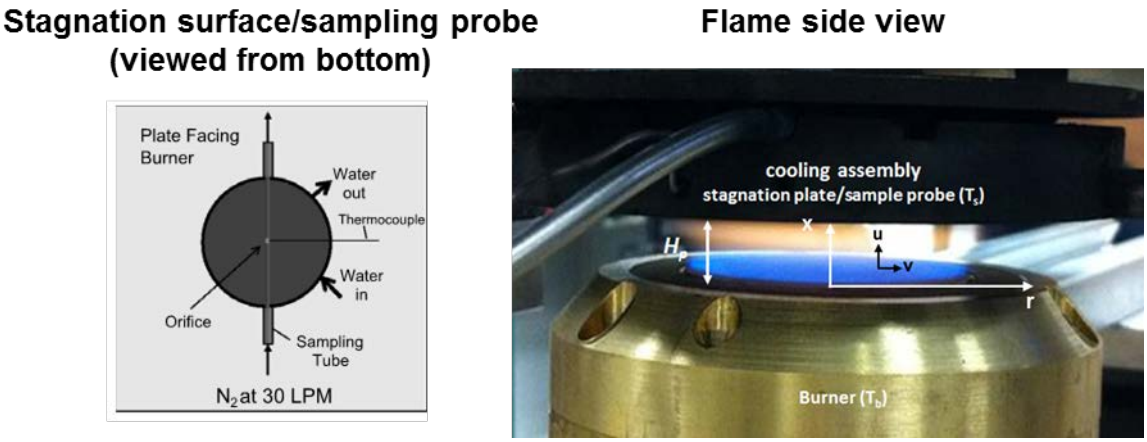

Figure 5.13 Schematic representation of the burner-stabilized stagnation (BSS) flame configuration. Left panel: water-cooled stagnation surface with the embedded sampling probe as seen from the bottom up of the burner exit. Right panel: flame picture and illustration of the main characteristics of the system. x and r are the axial and radial coordinates, respectively. u is the axial velocity and v the radial one.

It is important to notice that each sampling position gives a different flame, because the temperature and velocity profiles change with the distance between the stagnation plane and the burner. Therefore, it is not possible anymore to obtain a profile of soot properties along the axis with a single simulation, but it becomes necessary instead to run various simulations for each of the considered separation distances between the burner and the stagnation plane (H_p). This leads to an increase in the computational cost, which is well counterbalanced by higher accuracy in describing the flame conditions.

5.4.1 Numerical method

For a complete description of the system, the kinetic scheme must be coupled with a fluid dynamic model able to follow its physical evolution by means of transport equations. Specifically, this configuration can be simulated as a counterflow flame with zero velocity and diffusivity (except for soot) on the side corresponding to the stagnation plane. The temperature on the stagnation surface is fixed, since in the real setup the plate is water-cooled (Figure 5.13).

The counterflow diffusion flame to which the BSS configuration is assimilated consists of two concentric, circular nozzles directed towards each other. The resulting geometry is axisymmetric, thus the governing equations should depend on time, the axial and the radial position. However,

even exploiting the symmetry of the system around the axis, a two-dimensional model would be computationally very demanding when coupled to a detailed kinetic scheme.

Since the spacing between the nozzles is far smaller than their diameter, it is possible to assume that the radial velocity varies linearly in the radial direction and to express fluid properties as functions of the axial distance only [208]. Since the interest is to describe the evolution of the system along the axis (where the sampling is made), it becomes possible to model it as one-dimensional.

The numerical solution of the counterflow flame is obtained by solving the steady conservation equations of mass, momentum, energy and species concentrations [209]:

$$\frac{\partial \rho}{\partial t} = 2\left(G - \frac{\partial F}{\partial x}\right) \tag{5.1}$$

$$\frac{\partial}{\partial x}\left[\mu \frac{\partial}{\partial x}\left(\frac{G}{\rho}\right)\right] - 2\frac{\partial}{\partial x}\left(\frac{FG}{\rho}\right) + \frac{3}{\rho}G^2 + H = 0 \tag{5.2}$$

$$\rho \hat{C}_P \left[\frac{\partial T}{\partial t} + \frac{2F}{\rho}\frac{\partial T}{\partial x}\right] = \frac{\partial}{\partial x}\left[\lambda \frac{\partial T}{\partial x}\right] - \rho \sum_{k=1}^{N_S} \hat{C}_{P,k}\omega_k V_k \frac{\partial T}{\partial x} + \dot{Q} - \sum_{k=1}^{N_S} \widehat{H}_k \dot{\Omega}_k \tag{5.3}$$

$$\rho \left[\frac{\partial \omega_k}{\partial t} + \frac{2F}{\rho}\frac{\partial \omega_k}{\partial x}\right] = -\frac{\partial}{\partial x}(\rho \omega_k V_k) + \dot{\Omega}_k \qquad k = 1 \dots N_s \tag{5.4}$$

where F and G are two functions defined for convenience:

$$F(x) = \frac{\rho u}{2} \tag{5.5}$$

$$G(x) = -\frac{\rho v}{r} \tag{5.6}$$

and H is an eigenvalue of the resulting system.

In the equations above: x is the axial coordinate; r the radial coordinate; u and v the axial and radial velocities respectively; ρ is the density; P the pressure; μ the gas mixture dynamic viscosity; λ the thermal conductivity; C_p the specific heat; $C_{p,k}$ the specific heat of species k; M_k the molecular weight; ω_k the mass fraction; $\dot{Q}$ is the radiative heat flux; $\widehat{H_k}$ is the specific enthalpy for species k; V_k the mass diffusion velocity and $\dot{\Omega}_k$ the molar production rate of species k. The mass diffusion velocity V_k for species k is calculated as the sum of three contributions: Fick's, Soret's and thermophoretic diffusion.

The thermophoretic velocity is expressed as [210]:

$$\vec{V}_k^{(Th)} = -0.538\,\nu\,\frac{\nabla T}{T} \tag{5.7}$$

where ν is the gas mixture kinematic viscosity.

The detailed derivation of the conservation equations used in this configuration is presented in Appendix A, with an explanations of the different terms contributing to diffusivity and a brief overview on the radiative heat losses.

The boundary conditions are critical to describe the system near the stagnation plane surface, where the sampling is made. At the inlet (I) (Figure 5.13) the boundary conditions are the same as those for a normal counterflow flame:

$$Inlet\ (x=0)\begin{cases} F = \frac{\rho_I u_I}{2} \\ G = 0 \\ T = T_I \\ \rho u \omega_k + \rho \omega_k V_k = (\rho u \omega_k)_I \end{cases} \tag{5.8}$$

while at the stagnation plane (SP):

$$Stagnation\ plane\ (x=L)\begin{cases} F = 0 \\ G = 0 \\ T = T_{SP} \\ \rho u \omega_k + \rho \omega_k V_k = 0 & for\ gaseous\ species \\ \rho u \omega_k + \rho \omega_k V_k = \rho \omega_k V_k^{(Th)} & for\ particles \end{cases} \tag{5.9}$$

It is worth noticing that normally the nominal flux at the nozzles is equal to the sum of the convective and the diffusive fluxes, so that if gradients exist at the boundary, these conditions allow for diffusion into the inlet, resulting in a more accurate description. At the stagnation plane, the nominal flux on the air side is zero, hence for gaseous species the sum of the convective and the diffusive terms is zero too. For soot particles, instead, the total flux at the oxidizer boundary is not zero, because soot, due to the thermophoretic force, deposits on the stagnation wall.

After coupling gas-phase kinetics with the soot kinetic model, the 1D numerical simulations of the BSS flame are carried out using a modified version of OpenSMOKE code [150]. The code, used

for the pseudo one-dimensional formulation of counterflow reacting jets [211], is adapted to the burner-stabilized stagnation flame configuration just discussed.

5.4.2 Comparison between model predictions and experimental data

The BSS flame data of Abid et al. [53] are chosen as the case study for investigating the sectional soot kinetic mechanism. In that study, soot was generated in a 16.3% ethylene–23.7% oxygen–argon flame (equivalence ratio $\Phi = 2.07$) stabilized on a water-cooled flat flame burner at atmospheric pressure. The cold gas velocity is 8 cm/s (STP), which is identical to C3 Flame reported earlier [212]. The soot was sampled in situ along the centerline of the flame at the stagnation surface, which also defines the downstream boundary condition of the flame. The diluted soot sample was analyzed for its size distribution for particle diameters $D_p > 2.4$ nm by a Scanning Mobility Particle Sizer as a function of the separation distance H_p between the burner and the stagnation surface. Global soot properties, including the volume fraction and number density of particles with $D_p > 2.4$ nm, were obtained from the detailed PSDF data.

The same flame conditions have been recently revised by Wang and coworkers [213] and the results are shown in comparison with Abid data [53]. Flame C3 is characterized within the BSS flame configuration at 3 different facilities and across 4 burners of varying size and origin. The measured PSDFs currently observed at the 3 facilities show close agreement, while the PSDF reported previously by Abid et al. [53] shows a slower onset of soot nucleation in comparison to the current measurements [213] probably due to the aged porous plate, as shown later (Figure 5.19). However, the new temperature measurements [213] are consistent with Abid's ones [53] (Figure 5.14). The reason of this agreement could be that the Abid's temperature measurement [53] was taken before the PSDF was measured; therefore it is feasible that some change occurred in the burner or facility after the axial temperature profiles were measured. A better explanation of the aging problem will be given in Appendix B.

Figure 5.14 shows the comparison between experimental and computed flame temperature for different positions of the stagnation surface with respect to the burner.

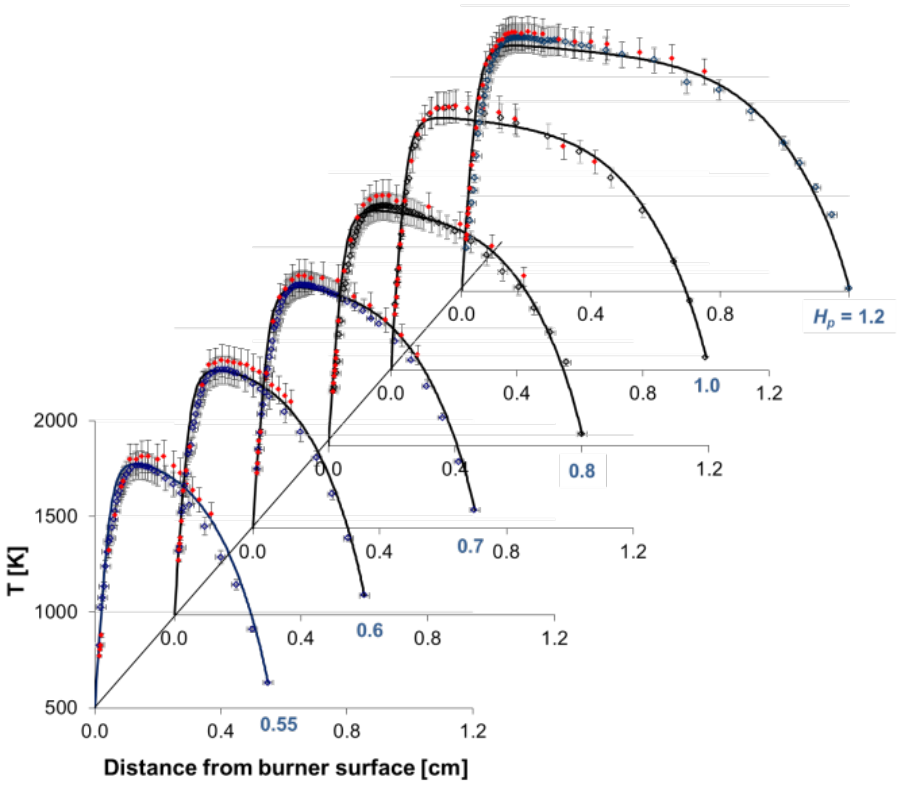

Figure 5.14 Temperature profiles of the BSS ethylene flame at different H_p. Blue symbols: experimental data of Abid et al. [53]; Red symbols: new experimental data [213]; lines: model predictions.

The cooling effect of the stagnation plane is evident; the temperature does not decrease slowly as in a free flame, but it cools down quickly to the value measured on the water-cooled plate. However, the maximum temperature is around 1830 K for all of the positions, therefore the flames are still comparable. The temperature profile has been computed taking into account gas and soot radiation [214, 215], even if soot radiation effect is negligible since the flame is lightly sooty. The model describes the temperature profile within the experimental error.

To better analyze the flame structure, a simulation of a BSS flame at a given burner-to-stagnation surface separation (H_p = 1.0 cm) is carried out including and excluding the Soret effect from the model. Figure 5.15 shows the predicted flame structure and the influence of the Soret effect on the main species' profiles.

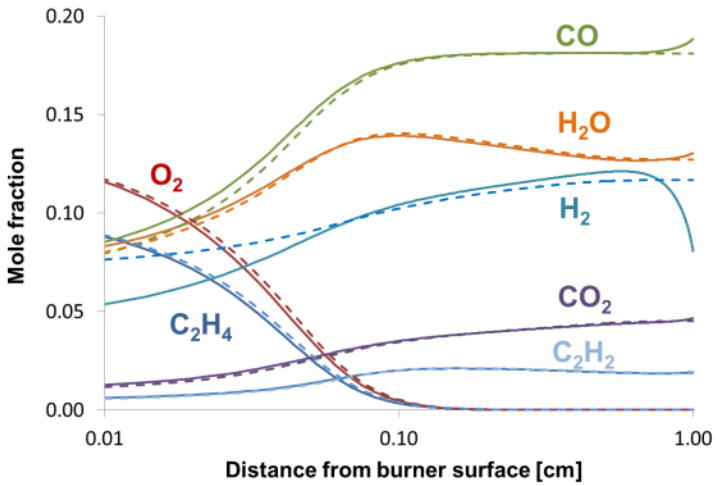

Figure 5.15 BSS ethylene flame structure at H_p = 1 cm with (solid lines) and without (dashed lines) Soret effect.

The influence on the main species is observed at the steep temperature gradient, in the vicinity of the stagnation surface. As expected, the Soret effect on hydrogen has consequences on the PAH production and this is shown in Figure 5.16.

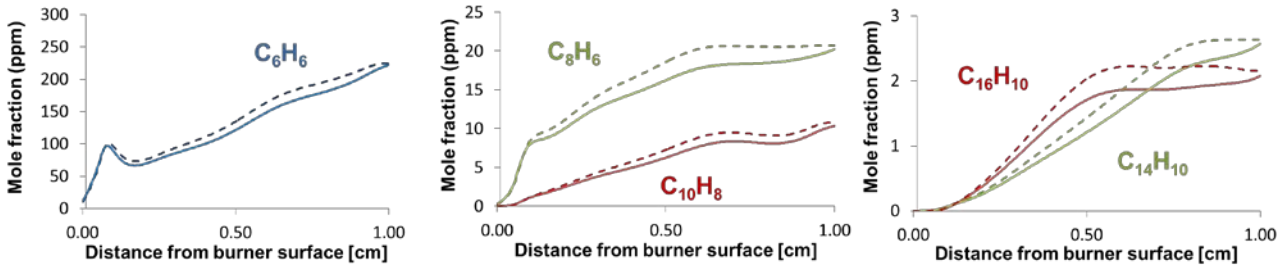

Figure 5.16 Heavy PAHs profiles in BSS ethylene flame at H_p =1 cm with (solid lines) and without (dashed lines) Soret effect.

PAHs profiles along the flame axis are affected by that and soot evolution cannot be predicted properly without considering this effect. In these flame conditions, the modifications of the heavier species' profiles due to the Soret effect are about 10% in the vicinity of the stagnation surface. It is worth noticing the benzene peak in the pre-flame region, that is probably due to a different mechanism than the one in the post-flame region, activated after all the fuel consumption.

Thermophoresis is a phenomenon wherein small particles, such as soot particles, suspended in a gas characterized by a temperature gradient ∇T, drift in the direction opposite to that of ∇T. It can be seen as a particular case of the Soret effect acting on aerosols and in fact it affects mostly bigger

particles, such as BIN_{20}. The influence of Soret effect and thermophoresis on heavier pseudo-species BINs is shown in Figure 5.17.

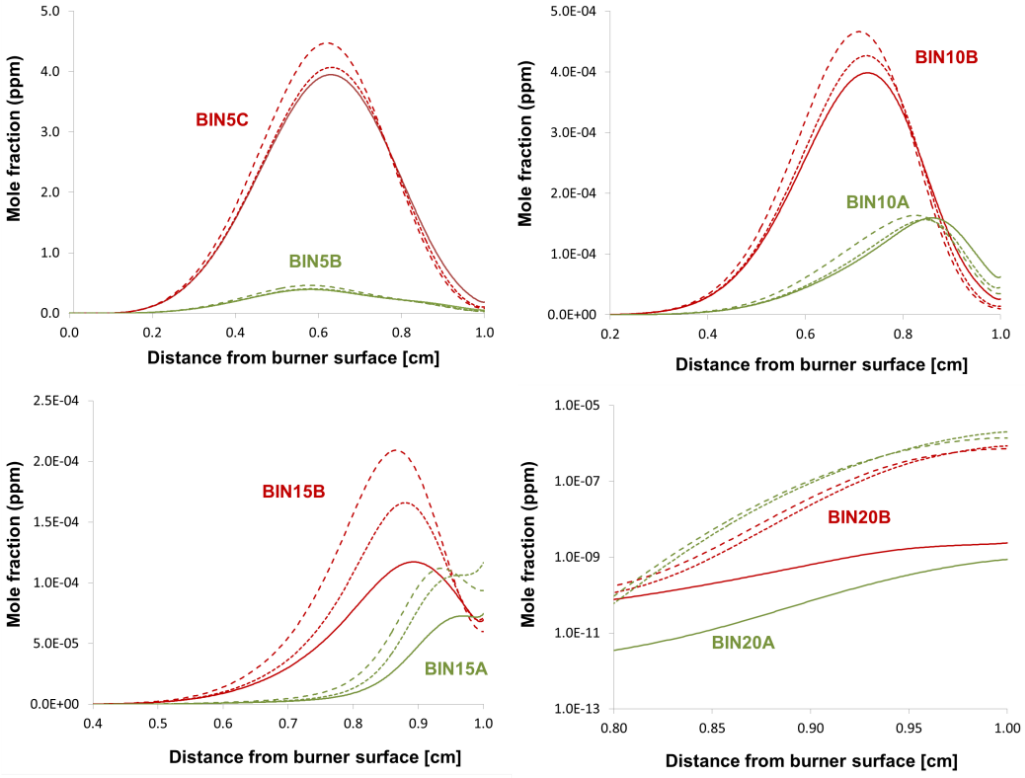

Figure 5.17 Particle and aggregate profiles in BSS ethylene flame with Soret and Thermophoretic effect (solid lines), without only Thermophoretic effect (dotted lines) and without both Soret and Thermophoretic effect (dashed lines).

Not considering Thermophoretic effect causes an overestimation of the bigger particles near the stagnation surface because the particle lifetime becomes artificially long as flow stagnation occurs.

The comparisons between the model predictions and old [53] and new experimental data [213] of soot volume fraction f_v and number density N are shown in Figure 5.18 for different values of H_p.

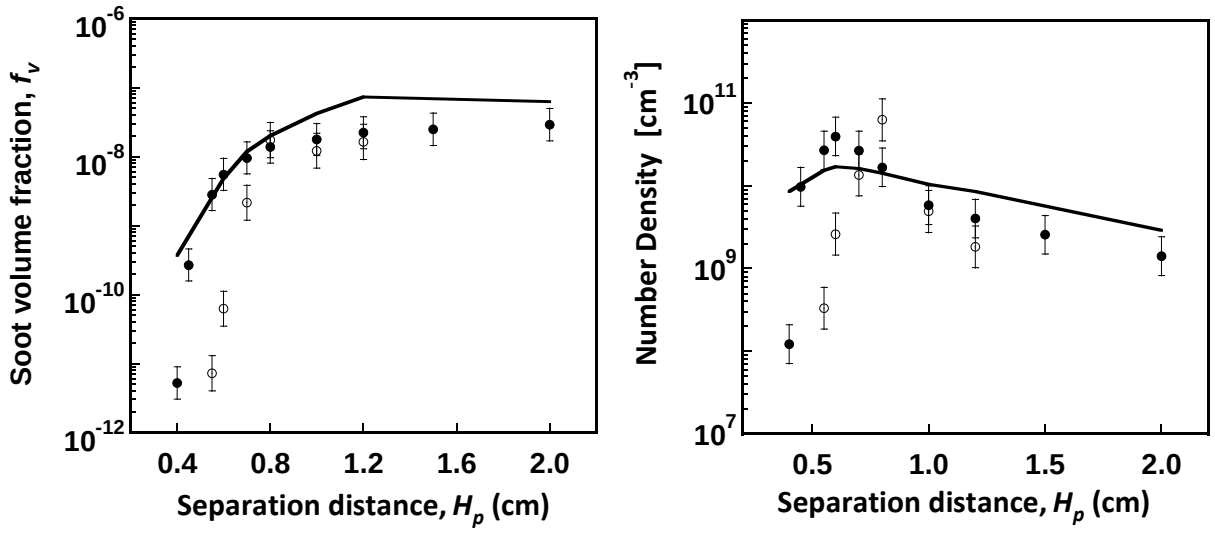

Figure 5.18 Soot volume fraction and number density from the BSS ethylene flame as a function of the separation distance. Open symbols: experimental data of Abid et.al. [53]; Black symbols: new experimental data [213]; Lines: model predictions.

The number density is calculated in the model by taking into account the 2.4 nm cut-off of the experiments. The predicted profiles of f_v- and N-vs.-H_p are closer to the new data, but they show a slight overprediction of the experimental values, especially for larger burner-stagnation surface separations. The comparison between model and experimentally measured PSDFs from soot nucleation stages to a later stage of mass/size growth is shown in Figure 5.19 for several H_p.

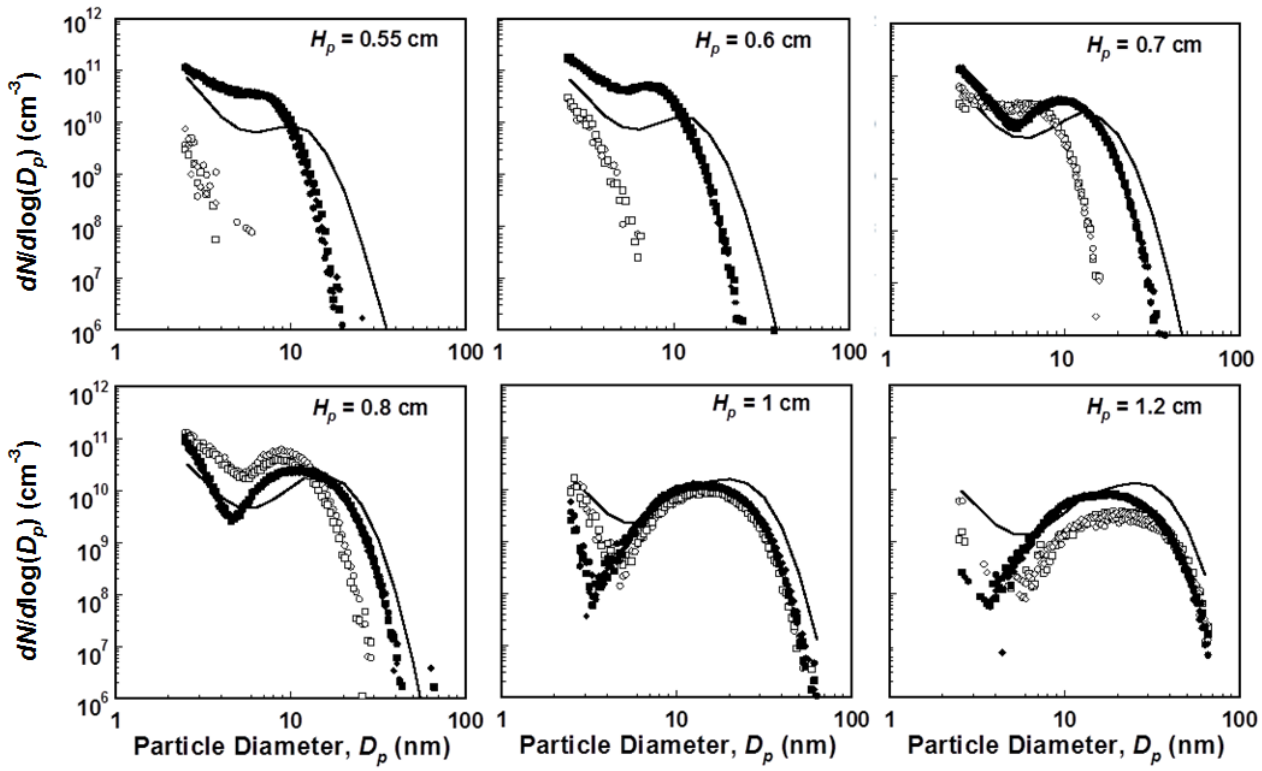

Figure 5.19 Soot PSDFs in BSS ethylene flame as a function of the burner-stagnation surface separations. Open symbols: experimental data of Abid et.al. [53]; Black symbols: new experimental data [213]; Lines: model predictions.

As previously mentioned, the earlier measurements of Flame C3 reported by Abid et al. [53] are not in agreement with the current experimental data [213]. A significant difference occurs at the observed onset of soot nucleation. The burst of nucleation sized particles is observed at H_p = 0.4 cm in the current work [213] while this was observed at H_p = 0.55 cm in the earlier work [53]. However, the final volume fraction and number density are the same in both studies. Later nucleation with the same final volume fraction may indicate that the flame studied in Abid et al. [53] could be actually colder than expected during the PSDF measurements. The reason may be that the porous plug ages with ongoing burner use. This aging can result in contraction of the plug pores and circumference. The axial temperature measurements may not have been subject to aging as indicated by the acceptable agreement between both measurements in Figure 5.14, because they were carried out before the PSDF measurements.

It can be also observed that the model predicts the overall progression of the PSDFs very well: a burst of nuclei enters into the detectable size window at H_p = 0.55 cm; a shoulder appears at a larger separation, which evolves into a lognormal type of the PSDF eventually. For H_p = 1.2 cm,

the predicted PSDF shows a tail on the small size side along with a lognormal-like PSDF on the large size site, both are in close agreement with the experimental PSDF. The major contribution to soot volume fraction comes from larger particles, hence it is useful to analyze the model predictions for soot concentration jointly to the right tail of the PSDFs. As discussed above, the volume fraction is slightly overestimated at larger burner-to-stagnation surface separations and this is observed in the PSDF as an overprediction of the larger particle sizes.

The number density instead is mainly determined by the smaller particles, thus it is related to the first mode of the PSDF. The nucleation mode is indeed overestimated at larger distances, apart from the data at 0.7 cm and 0.8 cm above the burner.

5.4.3 Model uncertainties: sensitivity analysis

A brute-force sensitivity analysis of the different kinetic model parameters is carried out in order to understand their influence in predicting the global and detailed soot behavior. Hence the sensitivity analysis on such a detailed kinetic scheme would be more effective if performed on a group of similar reactions, here identified as Reaction Classes, than on a single reaction.

The global and detailed soot features are analyzed for two burner-to-stagnation surface separations, H_p = 0.55 cm and H_p = 1.0 cm, which correspond to nucleation and agglomeration stages, respectively. In order to understand each contribution independently, the sensitivity analysis is first carried out to the reference kinetic parameters of different reaction classes involved in soot evolution and then separately to the kinetics of particle-particle coalescence, particle-aggregate coalescence and aggregation.

Particularly, in this work the focus is on reactions that are significant for soot growth, coalescence and aggregation, while the effect of oxidation reactions is not considered in the sensitivity analysis. This decision is made because in this flame conditions oxidation reaction don’t have an important role as in non-premixed combustion systems, such as diffusion flames.

As listed in Table 5.4, four computational test cases are made in addition to the Base case calculation.

		Case no.			
Reaction class	**no.**	**I**	**II**	**III**	**IV**
Acetylene addition	1b	$k_{C_2H_2}$·10	-	-	-
PAH condensation	3b	-	k_{PAH}·10	-	-
Small RR• addition	3a	-	-	k_{RR}·10	-
Coalescence and aggregation	5a-c	-	-	-	k_{coag}·10

Table 5.4 Sensitivity cases on the different reaction classes.

Cases II and III increase respectively the contributions of PAH condensation and the direct reactions of propargyl (C_3H_3•) and cyclopentadienyl (C_5H_5•) radicals on BINs; while Case IV increases both coalescence and aggregation reference kinetics. Finally the results of these computational cases are compared to an augmented contribution of acetylene surface reactions (Case I). The sensitivity analysis on soot volume fraction and number density of the BSS ethylene flame is shown in Figure 5.20.

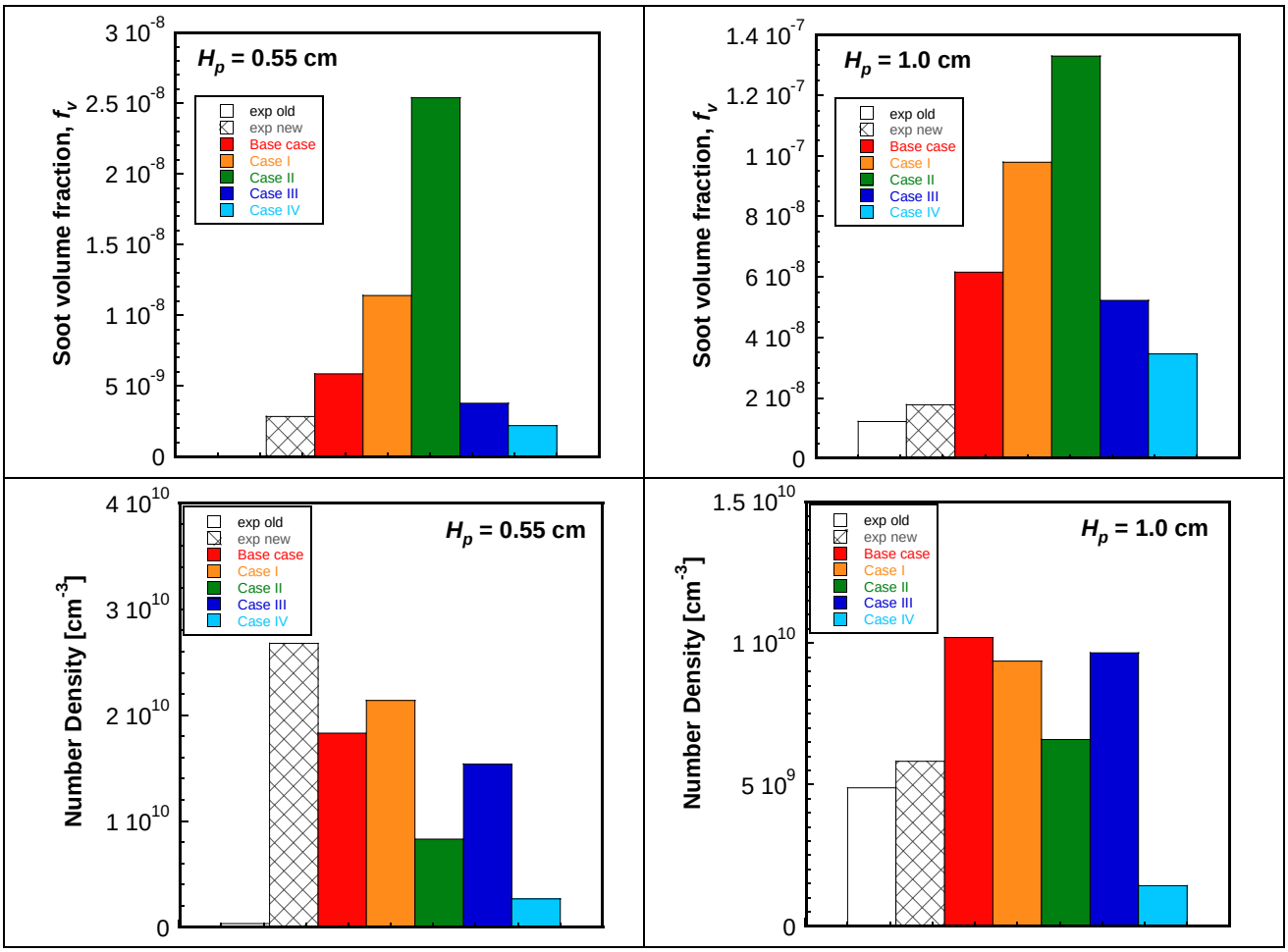

Figure 5.20 Sensitivity analysis of predicted soot volume fraction and soot number density to the different reaction classes at H_p =0.55 cm and H_p =1.0 cm.

It is evident that the small resonantly stabilized radicals (C_3H_3• and C_5H_5•) do not contribute to the soot volume fraction appreciably for this ethylene flame. Their effect is mainly evident in the pre-flame region. The increase of the surface reaction rate constant of C_2H_2 (Case I) augments the soot volume fraction at both separation distances, while the effect of the increased PAH condensation kinetics (Case II) enhances soot formation almost fivefold at H_p = 0.55 cm and twofold at H_p = 1.0 cm, because of broadening the agglomeration mode. On the contrary, Case IV halves the soot volume fraction at both separation distances, due to the decrease of the surface area per volume due to coagulation. Regarding the number density, Case II reduces it at both separation distances because it enhances the reactivity of small particles. Moreover, a larger number density reduction is caused by the increase of particle coalescence and aggregation (Case IV).

The sensitivity analysis described above also applies to the PSDF and these effects are shown in Figure 5.21.

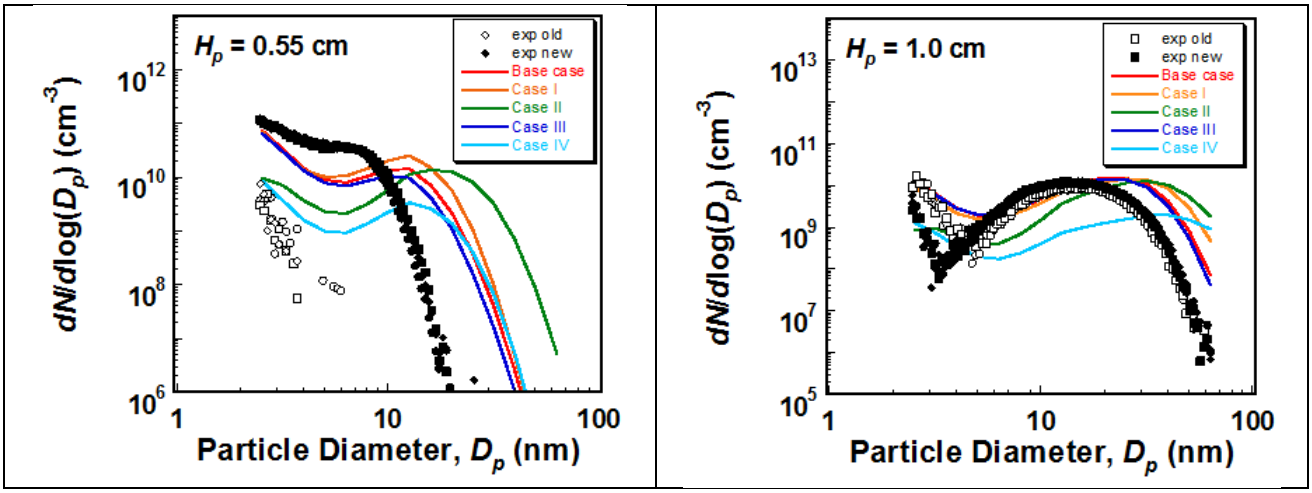

Figure 5.21 Sensitivity analysis of the soot PSDFs in the BSS ethylene flame to the different reaction classes at H_p = 0.55 cm and H_p = 1.0 cm. Symbols: experimental data; lines: model predictions.

As discussed previously for the sensitivity on number density, Cases II and IV cause a decrement of the nucleation mode of almost one order of magnitude and accordingly the trough of the distribution is moving downward, without any changes in the slope of the nucleation mode. The trough corresponds to pseudo-species BIN with equivalent spherical diameter of about 7 nm, while the experimental data show a trough around 5 nm. While Case II shifts the agglomeration mode to bigger particles, Case IV lowers it due to the enhancement not only of coalescence kinetics but also of aggregation kinetics.

In order to investigate independently coalescence and aggregation processes, a sensitivity analysis on the different kinetics of Reaction Classes 5a, 5b and 5c is performed and the different cases are shown in Table 5.5. In particular, three cases are studied. Firstly, the particle-particle coalescence between particles kinetics has been modified (Case V) by increasing its pre-exponential factor to $5.5 \cdot 10^{11}$ l/(mol s). Secondly, the pre-exponential factor of the kinetics of particle coalescence on aggregates is augmented to $5 \cdot 10^{11}$ l/(mol s) (Case VI). Finally, the kinetics of the aggregation process has been lowered to $5 \cdot 10^{10}$ l/(mol s) (Case VII).

		Case no.		
Reaction class	**no.**	**V**	**VI**	**VII**
Particle coalescence	5a	$A_{5a}=5.5\cdot10^{11}$ l/(mol s)	-	-
Particle coalescence on aggregates	5b	-	$A_{5b}=5\cdot10^{11}$ l/(mol s)	-
Particle aggregation	5c	-	-	$A_{5c}=5\cdot10^{10}$ l/(mol s)

Table 5.5 Sensitivity cases on coalescence and aggregation kinetics.

Figure 5.22 and Figure 5.23 shows the results of the sensitivity analysis for global soot properties and its PSDF, respectively.

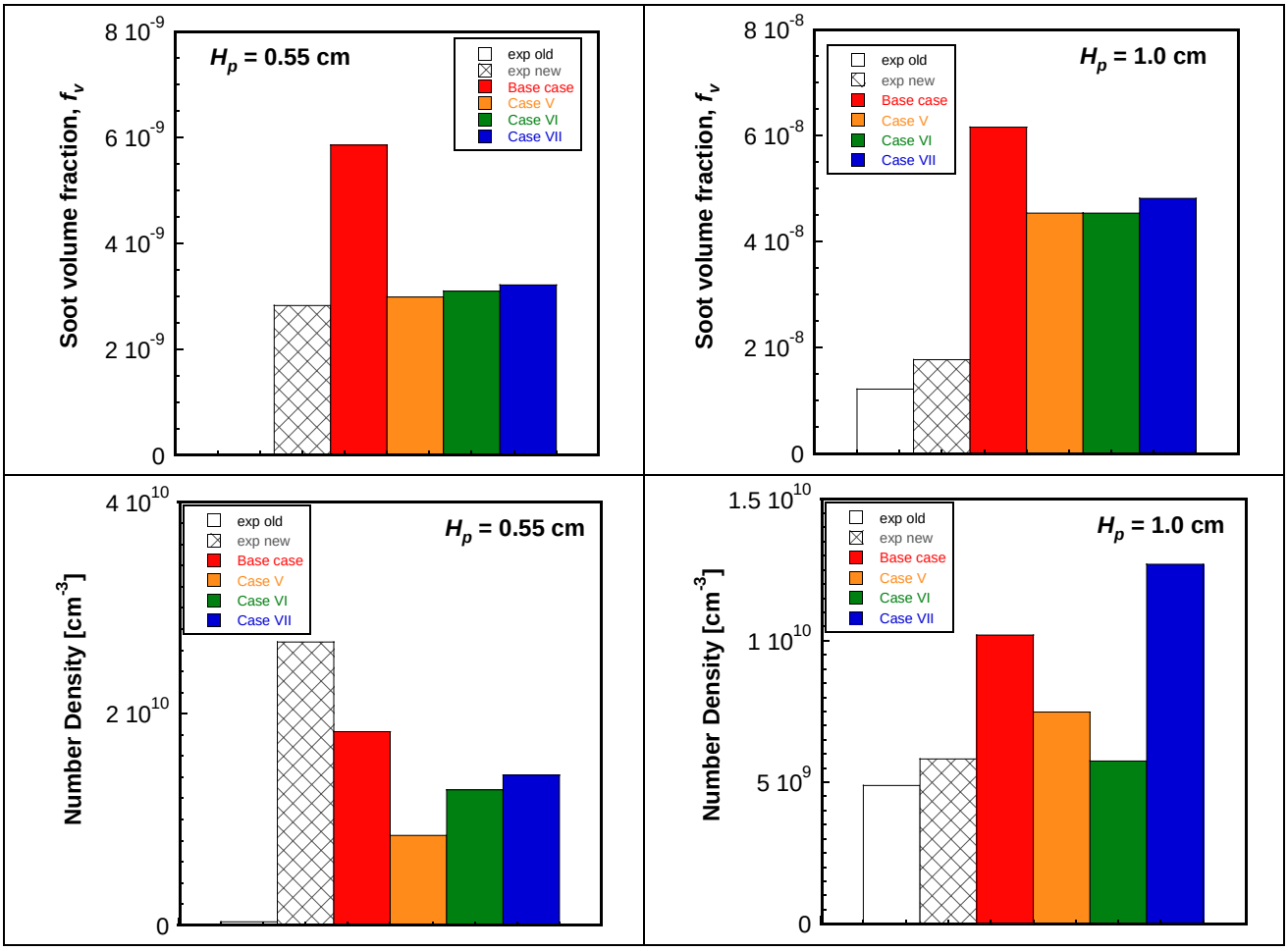

Figure 5.22 Sensitivity analysis of predicted soot volume fraction and soot number density to the coalescence and aggregation kinetics at H_p=0.55 cm and H_p=1.0 cm.

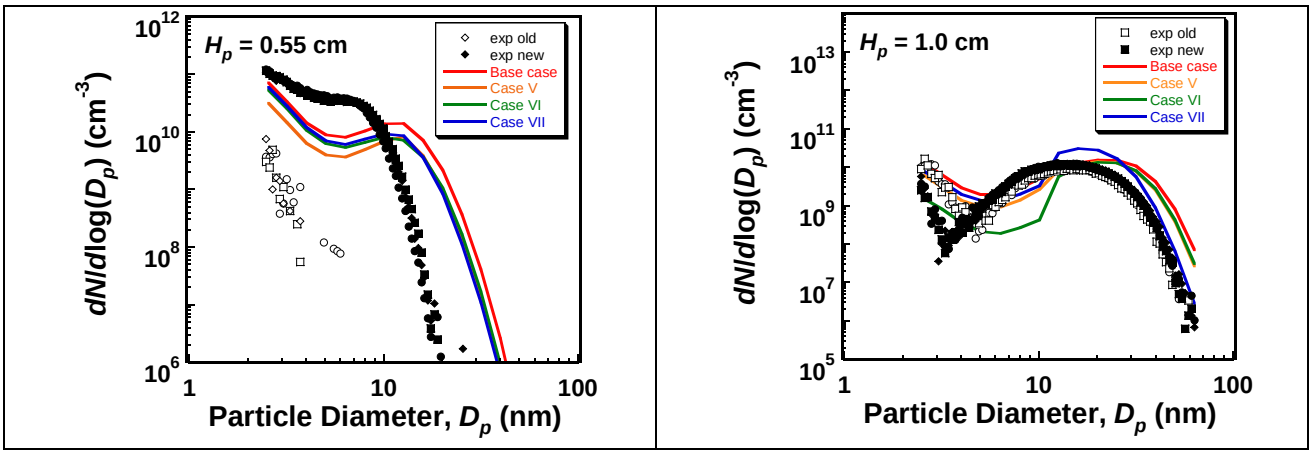

Figure 5.23 Sensitivity analysis of the soot PSDFs in the BSS ethylene flame to the coalescence and aggregation kinetics at H_p=0.55 cm and H_p=1.0 cm. Symbols: experimental data; lines: model predictions.

For both H_p, increasing coalescence kinetics or decreasing agglomeration kinetics lowers soot volume fraction. The enhancement of particle-particle coalescence promotes the reactivity of smaller particles mostly at lower H_p, where particle coalescence on aggregates and aggregation are negligible. On the other hand, the effect of increasing Reaction Class 5b or lowering Reaction Class 5c is evident for higher H_p. In particular enhancing particle coalescence on aggregates lowers the height of the trough and moves it towards larger particles. On the contrary, the reduction of the aggregation kinetics causes an accumulation of particles slightly heavier than BIN_{12}.

5.4.4 Experimental uncertainties: interpretation of mobility measurements

To better understand the limits of the mobility measurements mentioned in the paragraph 2.3.2, the mass of nascent soot from the previously studied BSS ethylene flame is also measured by a Cambustion Centrifugal Particle Mass Analyzer (CPMA) at University of California, Riverside. Aerosol particles with a known charge distribution are subjected to a rotational flow in the CPMA such that the particles are accelerated outward. An electrostatic force is then applied in a direction which opposes the acceleration of the particles so that the radial velocity and radial drag force vanish. In this way, the particles can be classified by the particle mass-to-charge ratio without any assumptions about the particle shape or morphology. In this study [213], the mass classification of the CPMA is calibrated with an aerosol composed of polystyrene latex nanoparticles of known diameter and density. Specifically, Figure 5.24 shows the setup for tandem mass and mobility

measurements, that consists in a coupling of the Centrifugal Particle Mass Analyzer (CPMA) and the SMPS system (DMA and CPC) in cascade.

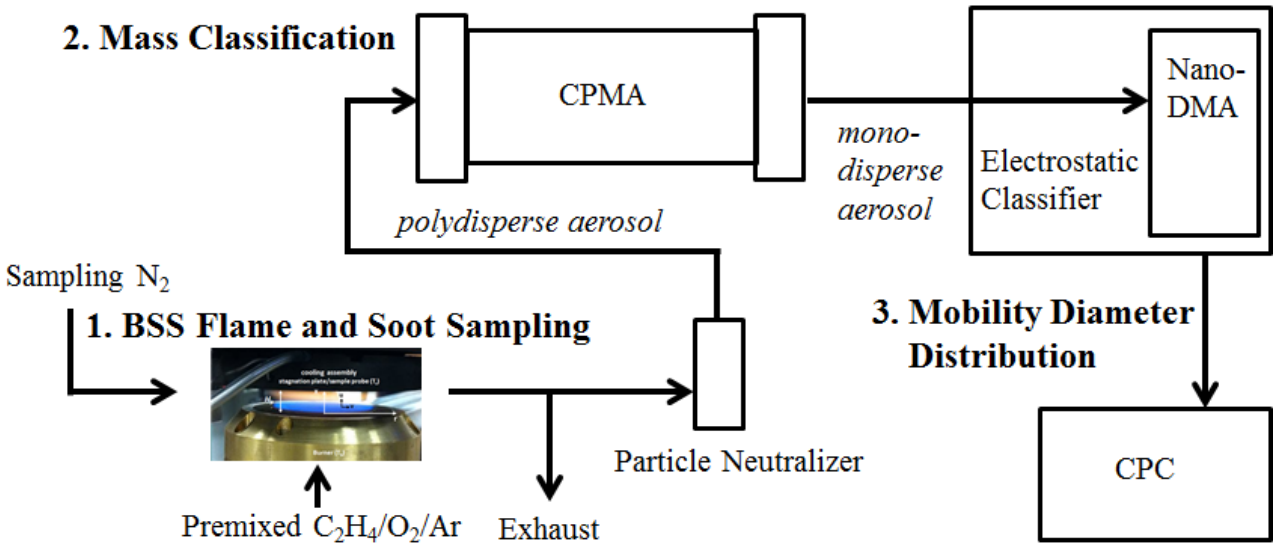

Figure 5.24 Experimental setup for the tandem mass and mobility measurements of nascent soot particles formed in the BSS ethylene flame [213].

Soot particles and aggregates have been sampled at H_p = 0.8 and 1.2 cm using a previously established dilution technique. The diluted flame sample is sent downstream for analysis at a flowrate of 1.5 L/min and the rest of the sample is sent to the exhaust. A known charge distribution is then applied to the soot sample by a particle neutralizer before being introduced into the CPMA. The rotational speed and voltage are then set in the CPMA to classify the polydisperse aerosol by a chosen mass. For each mass classification, the monodisperse aerosol is sent to the electrostatic classifier where the voltage is scanned (TSI model 3085 Nano-DMA, 10:1.5 Sheath-to-sample flow, 50 s up-scan, 10 s down-scan) to measure the mobility diameters in the range of 2.5-79 nm. A mobility diameter distribution corresponding to each mass classification is then obtained by counting the particles in a TSI model 3776 CPC. Mobility diameter distributions are measured for CPMA classified masses ranging from 2-113 attograms.

This tandem configuration allows for the mobility diameter and number density corresponding to each mass classification of nascent soot to be measured, in order to quantify the deviation from spherical shape. Therefore, soot mass distribution and mobility size distribution are simultaneously obtained. As shown in Figure 5.25, the reliability of this tandem technique is verified by the close

agreement between the obtained mobility size distribution [213] and the PSDF of Abid et al. [53] previously presented.

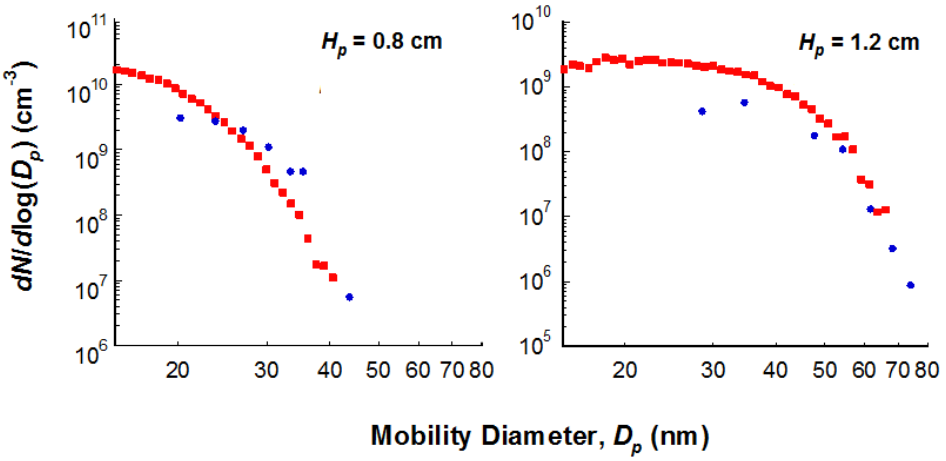

Figure 5.25 Comparisons of PSDFs measured by Wang and coworkers (red squares) and the ones obtained with the tandem CPMA-DMA technique (blue circles) at H_p = 0.8 and 1.2 cm.

To understand how the spherical assumption affects the mobility measurements, the CPMA measured mass is compared to the mobility mass (m_m) calculated using the mobility diameter (D_m), the spherical assumption and a constant density (ρ_{soot}) of 1.5 g/cm^3:

$$m_m = \pi \cdot \rho_{soot} \cdot D_m^3/6 \qquad (5.11)$$

The result of the comparison is shown in Figure 5.26.

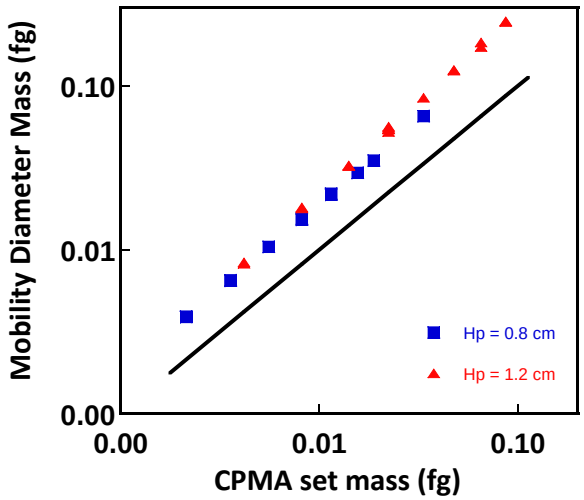

Figure 5.26 Comparison between CPMA measured mass (line) and the calculated mobility diameter mass (symbols) at two different H_p. Blue squares: H_p = 0.8; Red triangles: H_p = 1.2.

The mobility spherical mass (m_m) does not agree with the CPMA measured mass (m) which indicates that nascent soot cannot be assumed to be spherical. Specifically, the calculated mobility mass is greater than the CPMA mass by about a factor of 3. The current observation is in line with recent findings that soot formed in these slightly sooty BSS ethylene flames has irregular shapes at nucleation stages [116]. According to these results, it leads to an overprediction by about 60% of the real mass of soot particles. To highlight and confirm this result, Figure 5.27 reports the mass distributions measured using the CPMA and the ones calculated using mobility diameter and the spherical assumption.

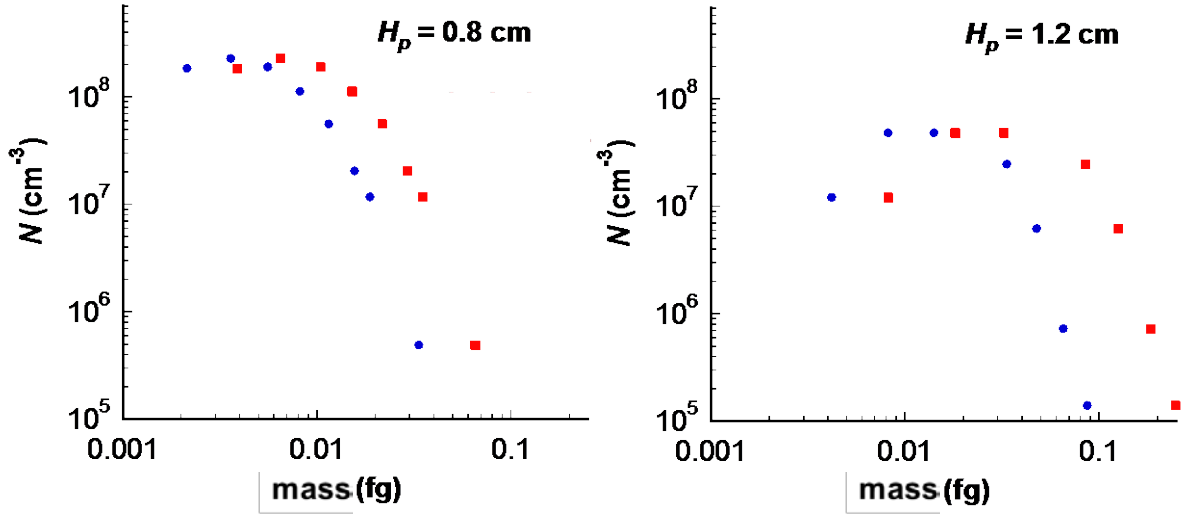

Figure 5.27 Comparisons between CPMA measured mass distributions (blue circles) and the calculated mobility diameter mass distributions (red squares) at two different H_p.

The mobility mass distributions are clearly shifted towards heavier particles. Therefore, in order to match the real soot mass, mobility diameter has to be corrected. Hence, our observations suggest that care must be taken in modeling studies. The spherical-particle assumption alone could yield an error in the computed particle size by as much as a factor of $3^{1/3}$ in model and experimental PSDF comparison.

Another way to correct the mobility measurements is to consider aggregates instead of spheres. Nevertheless in this case it is necessary to assume a primary particle diameter. It was recently observed through LII measurements that the primary particle diameter in rich premixed ethylene flames at low and atmospheric pressure varies as function of the height above the burner [136]. Specifically, it increases in the range 5-15 nm for atmospheric and rich flames, confirming the

primary particle polydispersity. Along the flame axis soot is forming and growing, hence increasing its mass. Therefore it could be deduced that the primary particle diameter increases also as function of mass. Following these considerations, Figure 5.28 shows on the left panel the assumed mean primary particle diameter as a function of mass and on the right panel again the CPMA measured mass compared to the mass calculated under spherical particle assumption and the one obtained with TSI aggregate analysis software [216], that considers the aggregate shape.

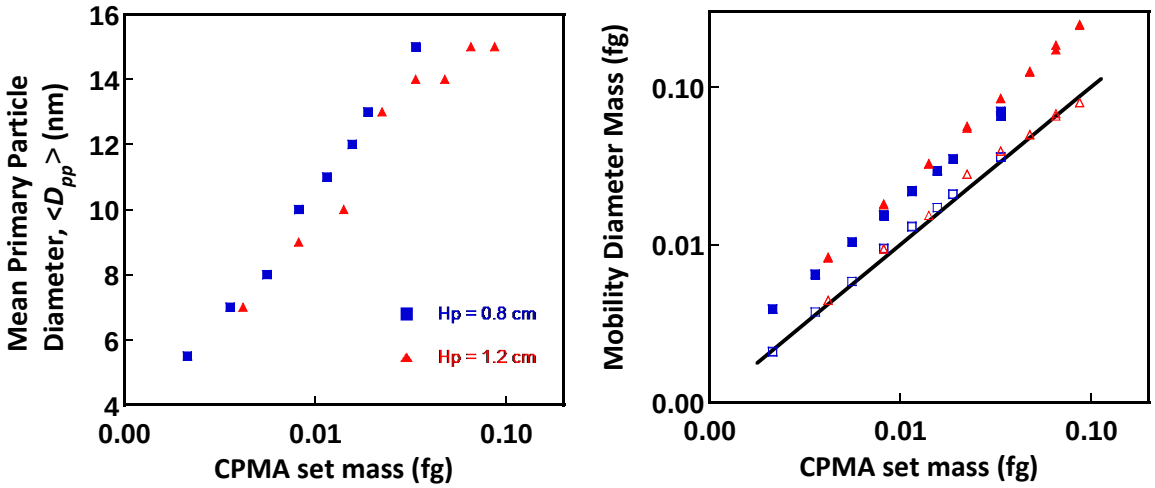

Figure 5.28 Left panel: Assumed mean primary particle diameter as function of mass. Right panel: Comparison between CPMA measured mass (line), the calculated mass under spherical assumption (filled symbols) and the mass obtained considering polydisperse aggregate (open symbols) at two different H_p. Blue squares: H_p = 0.8 cm; Red triangles: H_p = 1.2 cm.

It can be observed that assuming a primary particle diameter that increases as function of mass in the range 5-15 nm allows to correctly estimate the real mass of the particles and match these CPMA measurements. To be confirmed as a general finding, this estimated primary particle polydispersity has to be examined against more experimental data.

However, the aggregate analysis applied herein [216] assumes that the soot particles have an open structure with the entire particle surface being subject to collisions by the surrounding gas. Well-aged soot with large mobility diameters are known to follow this behavior, but the morphology of the nascent soot studied here may correspond to more closed structures. If some surface area of the particle is not exposed to collisions than the drag force cannot be estimated by a spherical chain with fractal dimension less than 2 and the TSI aggregate analysis software cannot be used to account for particle aggregation.

Figure 5.29 shows a plot of m_m/m versus the mobility diameter for both burner-to-stagnation surface separations sampled and assuming ρ_{soot} = 1.5 g/cm^3. The deviation of the m_m/m value from unity reflects the deviation from the spherical shape.

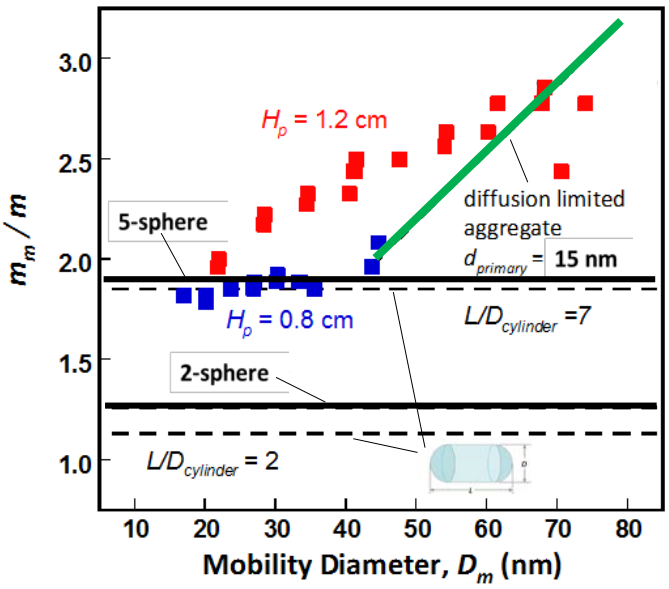

Figure 5.29 Measured mass ratio (symbols) as a function of mobility diameter compared to mass ratios for rounded cylinders, spherical chains and a diffusion limited aggregate (dashed lines).

For the two H_p values probed, the "older" particles (H_p = 1.2 cm) clearly have greater deviations from the sphericity than the "younger" particles (H_p = 0.8 cm), as one would expect. That is, older particles are more aggregated than the younger ones. Three idealized shape models were considered and they are superimposed with the data in the same figure. These models are:

1) a cylinder with spherical caps (or a prolated spheroid) of overall length L and diameter D (the black and dashed horizontal lines);
2) a chain of n-spherical particles (the black and solid horizontal lines);
3) diffusion-limited aggregates (DLA, the green solid line).

The mobility diameter may be determined for models 1 and 2 using expressions of the drag force in the rigid body limit [217], averaged over orientations following Chan and Dahneke [218]. The prolated spheroidal model has been used in earlier kinetic studies of nascent soot oxidation [76].

For model 3, we note that large carbon aggregates have been shown to follow a scaling law where the number of primary particles increases with aggregate cross section as follows [219, 220]:

$$n_p = k_a \left[\frac{A_a}{A_p} \right]^{D_a} \tag{5.12}$$

where n_p is the number of primary particles, k_a is a constant, A_a is the cross-section area of the aggregate, A_p is the cross-section of the primary particle and D_a is the exponent. In the free molecule regime, the mobility diameter D_m is a measure of the collision cross-section and thus it is related to the total particle cross-section as:

$$D_m = \left(\frac{4}{\pi} A_a \right)^{1/2} \tag{5.13}$$

The values of k_a and D_a are taken from Eggersdorfer and Pratsinis [221] for the two morphological models accordingly, assuming that the geometric standard deviation of the primary particle size distribution is 1.44.

From Fig. 15, it may be seen that the morphology of the particles at H_p = 0.8 cm can be explained satisfactorily with either a 5-sphere chain model or by a prolated spheroid with L/D = 7. The morphology of particles sampled at H_p = 1.2 cm are consistent with the DLA model of 10-15 nm in the primary particle diameter. However, a further interpretation of the data presented herein is hampered by the uncertainty in the mass density of the nascent soot material. Nevertheless, the finding of the current study supports and, to an extent, further quantifies the results of microscopy analyses of Schenk et al. [116]: even at an early state of growth, nascent soot exhibits structural and geometrical inhomogeneity, and it deviates from sphericity at almost all sizes.

6. Fuel dependency on soot formation

In this paragraph fuel dependency on soot formation is explored experimentally and numerically focusing the attention mainly on premixed C3 and C6 flames.

The time resolved formation of nascent soot from the onset of nucleation to later growth stages was examined experimentally for BSS flames of ethylene/propene and pure propene at Stanford University. Specifically, the evolution of the detailed particle size distribution was compared among ethylene, ethylene/propene and pure propene flames at a carbon-to-oxygen ratio of 0.69 and maximum flame temperature of 1800 K. Under these constraints, the overall sooting process was considered comparable as highlighted by similar time resolved bimodal PSDF. Afterwards, a preliminary comparison of these data with model predictions is presented.

Finally, C6 premixed laminar flames of cyclohexane and benzene studied by different groups [222-225] under similar fuel-rich and temperature conditions are herein numerically analyzed and discussed in relation to the different pathways leading to soot.

6.1 BSS propylene flames

Nascent soot formation in premixed ethylene flames have been examined extensively over the past two decades. In contrast, very few studies have been performed for measuring soot formed in propene flames [202, 226]. Tsurikov et al. [202] investigated the global sooting behavior in laminar premixed propene flames at different pressures (1-5 bar) and equivalence ratios as previously discussed for ethylene. Propene flames were found to be narrow, more lifted and slightly less stable than the ethylene flames, as observed for the flames considered in the experimental investigation herein described. Moreover, the maximum soot levels were observed to increase with pressure and equivalence ratio. On the other hand, Lamprecht et al. [226] studied several laminar, flat, premixed flames at atmospheric pressure burning methane, propane, ethylene and propene with oxygen at different C/O ratios. The flames stabilized in a McKenna burner (McKenna Products) were examined using Dynamic Light Scattering (DLS) to determine the particle size. In addition, the measurements of the local flame temperature and of the absorption at each measurement location were performed in order to derive the particle number density and soot volume fraction. The comparison between different fuels' sooting behavior was presented showing the DLS potential.

Accordingly, the aim of the experimental work described below was to explore the influence of the fuel structure on the detailed sooting behavior and in particular for the first time to have an insight in the soot formation process from the onset of nucleation to later growth stages in premixed BSS flames burning propene at ambient pressure. Then an analysis and discussion of these data with the soot model previously described was carried out.

6.1.1 Experimental setup and results

The evolution of the detailed PSDFs was compared among the previously described BSS ethylene flame (Flame C3) and the measured ethylene/propene (Flame J2) and pure propene flames (Flame J1 and J3), as summarized in Table 6.1.

Flame No.	Mole fractions[a]			C/O	Φ	Velocity,[b] v_0 (cm/s)	T_{max} (K)
	C_3H_6	C_2H_4	O_2				
C3	0	0.163	0.2370	0.69	2.07	8.00	1816 ± 76
J1	0.1071	0	0.2332	0.69	2.07	4.15	1809 ± 86
J2	0.0422	0.0987	0.2345	0.69	2.07	5.69	1811 ± 87
J3	0.1190	0	0.2773	0.64	1.93	6.02	1954 ± 92

a. The balance gas is argon *b*. STP cold gas velocity (300 K)

Table 6.1 Summary of the stoichiometry and inlet conditions of the laminar premixed BSS flames. Φ is the equivalence ratio.

These flames are studied at C/O=0.69 and maximum flame temperature of about 1800 K. Under these constraints, the overall soot formation process was comparable as highlighted by similar time resolved bimodal PSDF. J1 and J2 flames were studied for the sake of comparison with C3 flame, while J3 flame was investigated for having an insight of the nucleation stage in propene flames.

The experiments were carried out using an in-house water-cooled flat flame burner, which had an outlet diameter of 5 cm and was operated in the BSS configuration. A sheath of nitrogen shielded the flame to prevent radial entrainment and diffusion of oxygen from ambient air. Propene was injected into the fuel line directly mixed with oxygen and argon. The mass flow rates of propene,

oxygen, argon and nitrogen were measured by critical orifices and calibrated by a bubble displacement.

Particle size distributions were determined with a TSI 3080 SMPS (Electrostatic Classifier 3085 and UCPC 3080, AIM Software V.8.1) using a sample dilution technique developed earlier and improved over time [53]. The sample gas entered the probe through an orifice and was immediately diluted with a cold nitrogen flow to prevent particle losses. The dilution range and calibration were used before and care was taken to avoid diffusion losses, condensation of higher-molecular weight hydrocarbons, and probe-induced particle-particle coagulation during dilution. Limitations of the Cunningham slip correction caused particles below 10 nm to be overestimated by mobility measurements and thus a nanoparticle transport theory was used for small particles to obtain more accurate particles sizes [127].

The gas temperature profiles were measured with a Y_2O_3/BeO coated type-S thermocouple with radiation correction using a procedure discussed earlier [212]. The experimentally measured temperature profiles were radiation corrected. The inlet temperature was extrapolated from the measured temperature profile immediately adjacent to the burner surface. The temperature variation was roughly linear with respect to the distance and the probe temperature was measured with a type K thermocouple embedded on the stagnation surface. Being in the same condition of the C3 flame, J1 and J2 flames had lower cold gas velocities than the flow rates of C3 and J3 flames in order to match the 1800 K flame temperature constraint and to have a more stable flame.

Because local temperature is the dominant parameter which governs the soot chemistry, the predicted and measured temperature profiles of J3 flame are shown at a series of burner-to-stagnation surface separation distances in Figure 6.1.

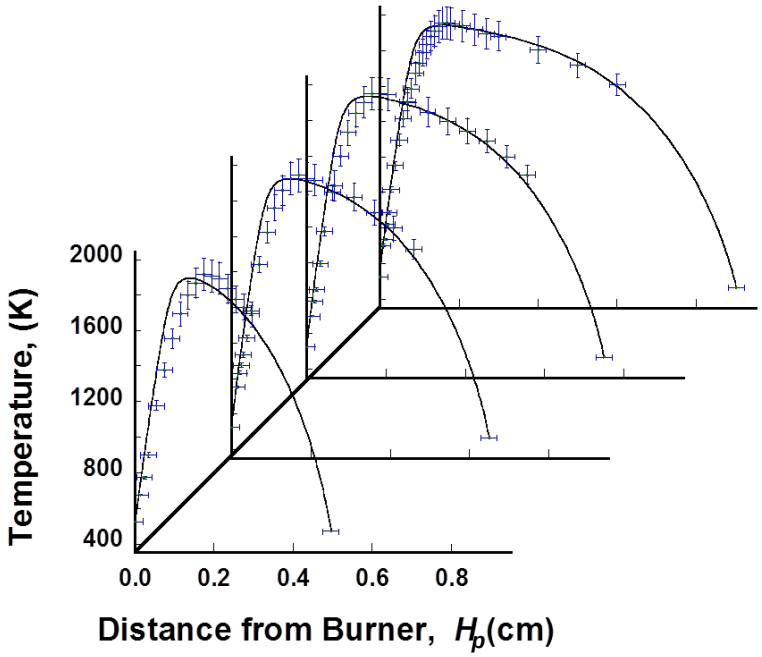

Figure 6.1 Temperature profiles for J3 flame at different H_p (symbols: experiments; solid lines: model predictions).

The modeled temperature profiles take into account the radiation correction in order to show the degree to which the stagnation probe causes heat loss. The boundary condition imposed in the simulation software gives rise to a different flame at each sampling distance, as discussed in paragraph 5.4.1. However, the inlet and probe temperature are the only required to model the flame for the given flow rate and sampling distance. The agreement between the radiation corrected measurements and the simulated temperatures is within the thermocouple position uncertainty (±0.3 cm) and the temperature measurement uncertainty (±70 K around the peak temperature region). The temperature profiles for the other flames studied were similar at a series of sampling distances. A fairly good agreement between them was observed, even if the model seems to be quicker in the temperature rise in the pre-flame region with respect to the experimental evidence.

Soot nucleation is therefore measured in J3 flame under controlled conditions, as shown in Figure 6.2.

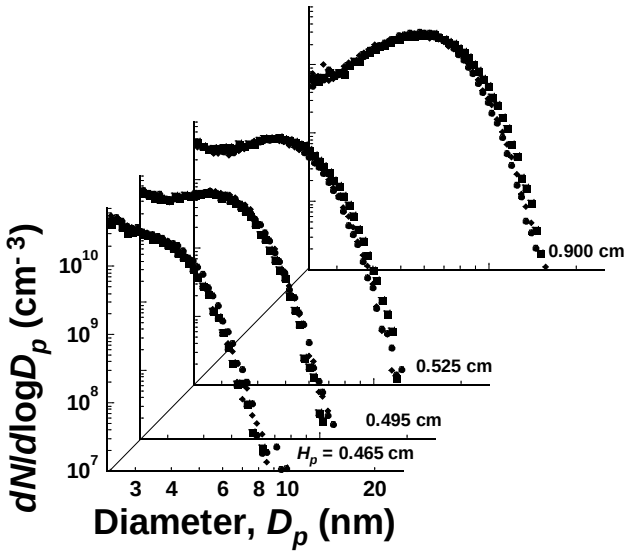

Figure 6.2 Measured PSDFs (symbols) for ethylene flames expressed as a function of the particle diameter.

The onset of nucleation was sampled H_p = 0.465 cm, where already a hint of the agglomeration mode is evident. Being the flame unstable as stretching it, this is the lowest burner-to-stagnation surface distance that was possible to sample. At 0.9 cm the agglomeration mode was fully developed without anymore a visible nucleation mode.

The effective residence time of soot particles was defined as the time interval for the particle to traverse from the calculated location of the peak flame temperature to the location of the stagnation probe. It was calculated from the axial convective velocity and particle thermophoretic velocity for each burner-to-probe separations. Therefore, the global and detailed sooting behavior of different flames are herein compared in terms of residence time of the soot particles along the flame and not in terms of separation distance between the burner and the stagnation surface.

To compare the sooting behavior of ethylene C3 flame and propene flames, two different flames are studied: J1 and J2 flames. J1 is a pure propene flame and J2 is a mixture of 70% ethylene and 30% propylene. As in J1 flame the residence times of particles along the flame corresponding to different H_p are higher than C3 flame's ones, the propene percentage in the mixture of flame J2 is chosen to have similar particle residence times to C3 flame and to have a stable flame in which it is evident the effect of propene. Therefore, Figure 6.3 shows the detailed sooting behavior of J2 flame compared to the one of C3 flame at comparable particle residence time *t*.

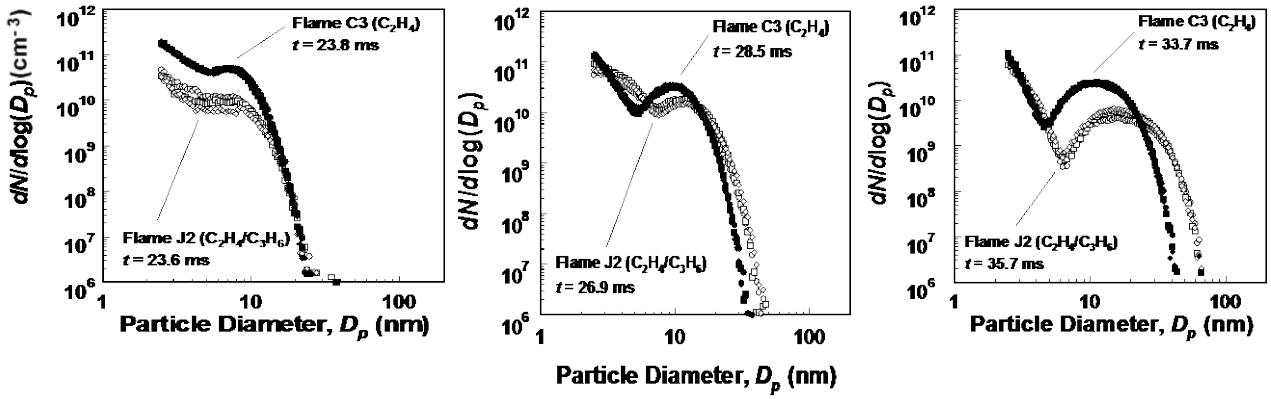

Figure 6.3 Comparisons between PSDFs of J2 flame (open symbols) and the corresponding ones of C3 flame (black symbols) during the evolution in the particle residence time along the flame.

Comparison of the PSDFs shows the similar PSDF development in C3 and J2 flames, especially at small residence times. At larger residence times the nucleation is still persistent in J2 with respect to C3 flames, as well as the formation of bigger particles is enhanced.

Therefore, Figure 6.4 shows the comparison between flame C3 and flame J1 at comparable residence times in order to stress the fuel dependence of soot in the later stages of growth.

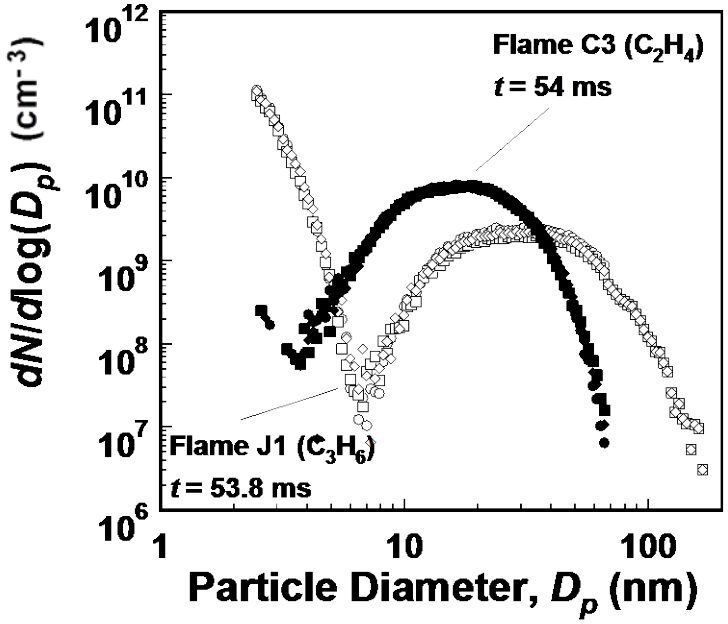

Figure 6.4 Comparison between PSDF of J1 flame (open symbols) and the corresponding one of C3 flame (black symbols) at comparable residence times.

The persistence of nucleation is still evident in the case also of pure propene as the aggregates' growth, that is favored in propene then in ethylene flames.

6.1.2 Comparison between measurements and model predictions

The competing kinetic processes leading to the nucleation of soot are linked to the underlying gas phase chemistry in a manner that is not completely understood. The formation of aromatic precursors is an important rate-limiting step and the onset of soot nucleation may be tied to the fuel specific chemistry leading to aromatic formation.

Therefore the BSS propene flame J1 is studied using the detailed kinetic mechanism previously described and the prediction of the flame structure is shown in Figure 6.5.

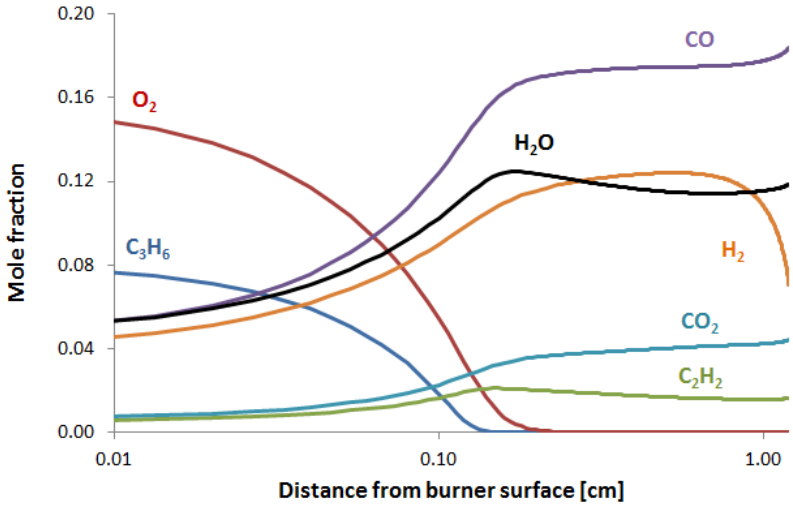

Figure 6.5 Computed BSS propene flame structure at H_p = 1.2 cm.

As already mentioned for the BSS ethylene flame, the influence of the Soret effect on the main species is observed at the steep temperature gradient, that is in the vicinity of the stagnation surface. The evolution of the main species is similar to the ethylene's one in similar conditions. Hence a rate of production analysis of the J1 flame is carried out for H_p = 1.2 cm, in order to gain more insights in the chemical pathway leading to soot, as shown in Figure 6.6. The thickness of the arrows reflects the relative significance of the different reaction pathways.

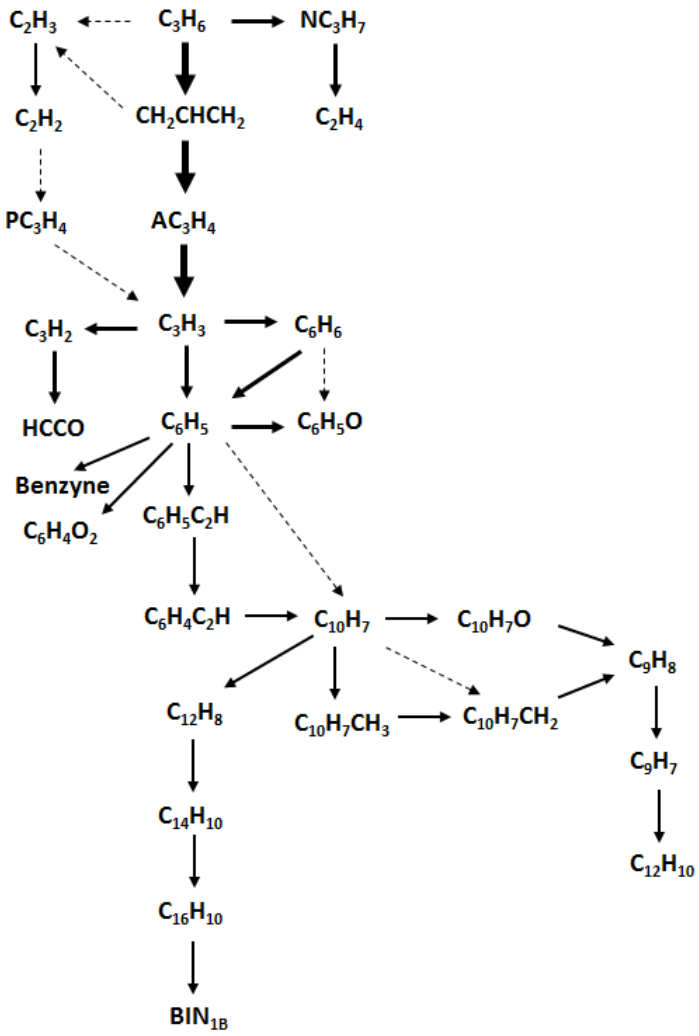

Figure 6.6 Pathways from fuel to soot precursors for J1 flame at H_p = 1.2 cm.

Propene undergoes mainly H-abstraction reactions producing allene and successively the propargyl radical (C_3H_3). Ethylene instead forms the propargyl radical passing through acetylene formation by vinyl radical decomposition and its reaction with methyl radical to form propyne. Propyne afterwards through H-abstraction reaction forms C_3H_3. After the formation of C_3H_3, both ethylene and propene flames form phenyl radical. This afterwards grows to phenylacetylene, naphthalene and heavier PAHs. In the propene flame, the presence of small resonant-stabilized radicals favors the major formation of some other PAHs, such as indene. A comparison of the small resonant radicals and major PAH species in BSS ethylene and propene flames with the stagnation plate located at 1 cm from the burner surface are presented in Figure 6.7.

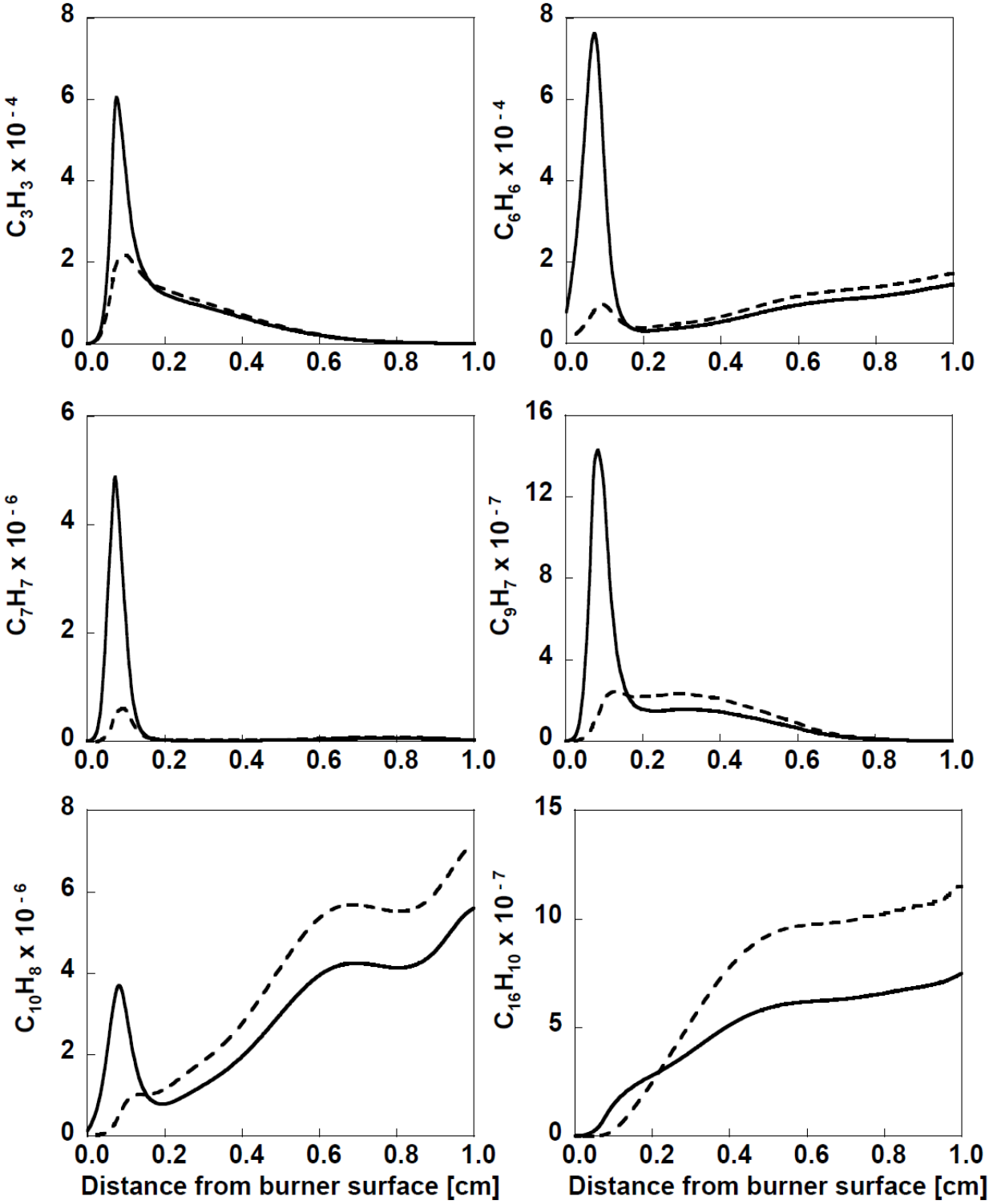

Figure 6.7 Computed profiles of mole fractions of small resonant-stabilized radicals and major PAHs species in BSS ethylene (flame C3; dashed lines) and BSS propene (flame J1; solid lines) flames at H_p = 1.0 cm.

From the simulations it is evident that in the propene flame resonant stabilized radicals are produced in greater concentrations than in the ethylene flame, but these species are produced mainly in the preheat zone and are oxidized quite extensively in the flame. Although the amount of

PAHs near the burner surface of the propene flames is higher than that in ethylene flames, based on the current reaction model, the PAH concentrations in the ethylene flame are higher than in the propene flame in the post flame regions where soot nucleates and grows. Hence, the larger concentration of the resonantly stabilized species in the preheat zone bears little consequences in the PAH production in the post flame region. The higher PAH concentration computed for the ethylene flame is the result of higher acetylene and H atom concentrations than for the propene flame.

Figure 6.8 represents the computed mass fractions for different BIN classes (BIN_1, BIN_5, BIN_{10}, BIN_{15} and BIN_{20}), both in their molecular and radical form summing all the differently hydrogenated species, in both BSS ethylene (solid lines) and propene flames (dashed lines) at H_p = 1.2 cm.

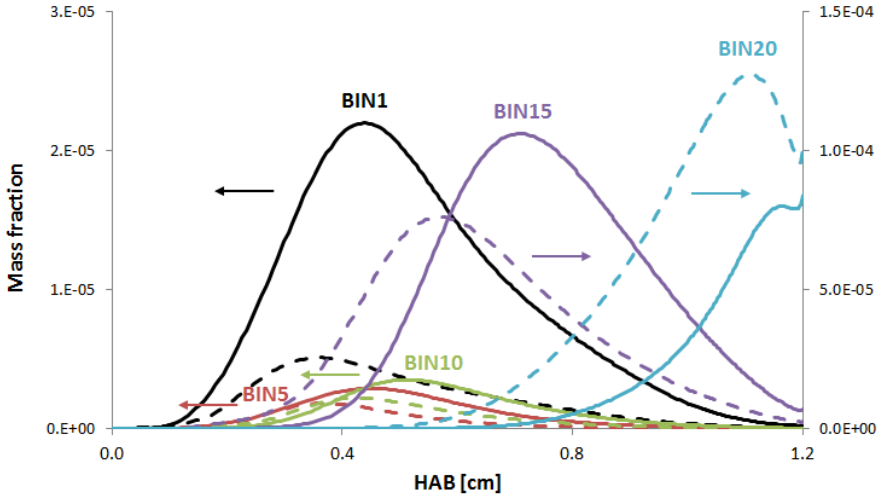

Figure 6.8 Computed mass fractions of BIN_1, BIN_5, BIN_{10}, BIN_{15} and BIN_{20} formed in BSS ethylene flame (solid lines) and in BSS propene flame (dashed lines) at H_p = 1.2 cm. These classes are the sum of the radical and molecular form of the BINs. BIN_{15} and BIN_{20} refer to the secondary axis. All the other species refer to the primary axis.

Heavier species show peaks at progressively higher height above the burner. Lighter species, in fact, undergo a growing process and become larger particles that then evolve in forming aggregates. The larger PAHs and soot particles (BIN_1, BIN_5, BIN_{10}) formed in ethylene and propene flames peak almost at the same distance from the burner, but in the ethylene flame their quantity is greater. Instead the aggregates (BIN_{15}, BIN_{20}) in propene flame form earlier than the aggregates in ethylene flame and also their mass fraction progressively becomes bigger than the ethylene's one.

Figure 6.9 reports the comparison between the measured and predicted global sooting behavior of the three flames in terms of soot volume fraction and number density in function of the residence time *t* along the flame.

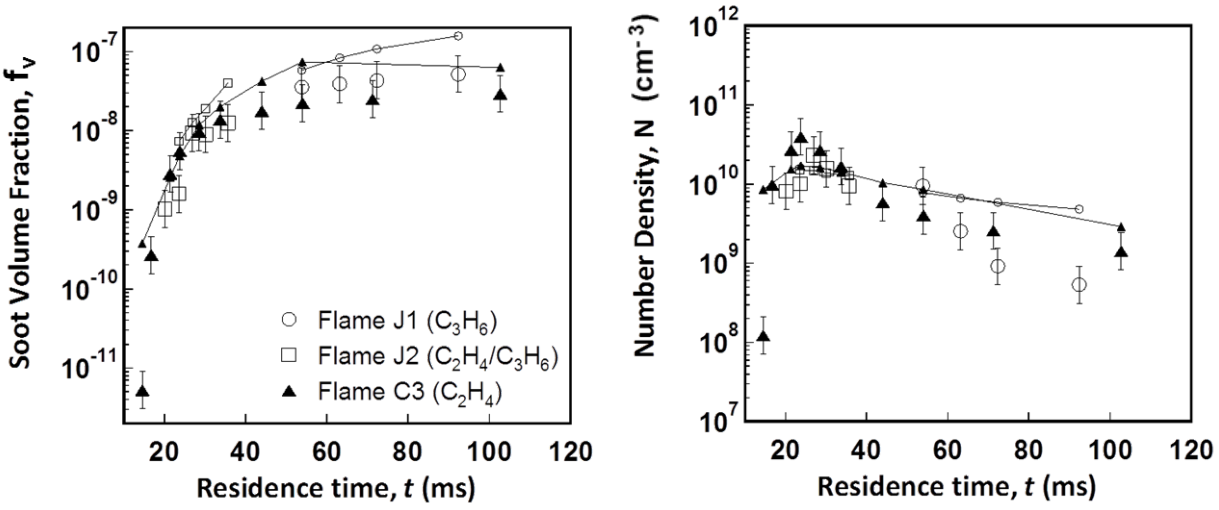

Figure 6.9 Measured (symbols) and predicted (lines with small symbols) soot volume fraction (left panel) and total number density (right panel) of the three studied flames. J1 flame (open circles), J2 flame (open squares) and C3 (black triangles) as function of the particle residence time *t* along the flame.

The results show that final soot volume fraction has a weak dependency on the structure of the parent fuel, as shown by the comparison of the previously studied ethylene flame (Flame C3) and the current propene flames. Moreover, at larger residence times the two fuels form the same soot quantity and they have similar soot evolution. The model predictions agree with the experimental data as increasing the residence time, even though the overprediction of the model for both soot volume fraction and number density in pure propene flames (J1 flames) is evident. Figure 6.10 shows the measured and computed PSDFs for J1 flame.

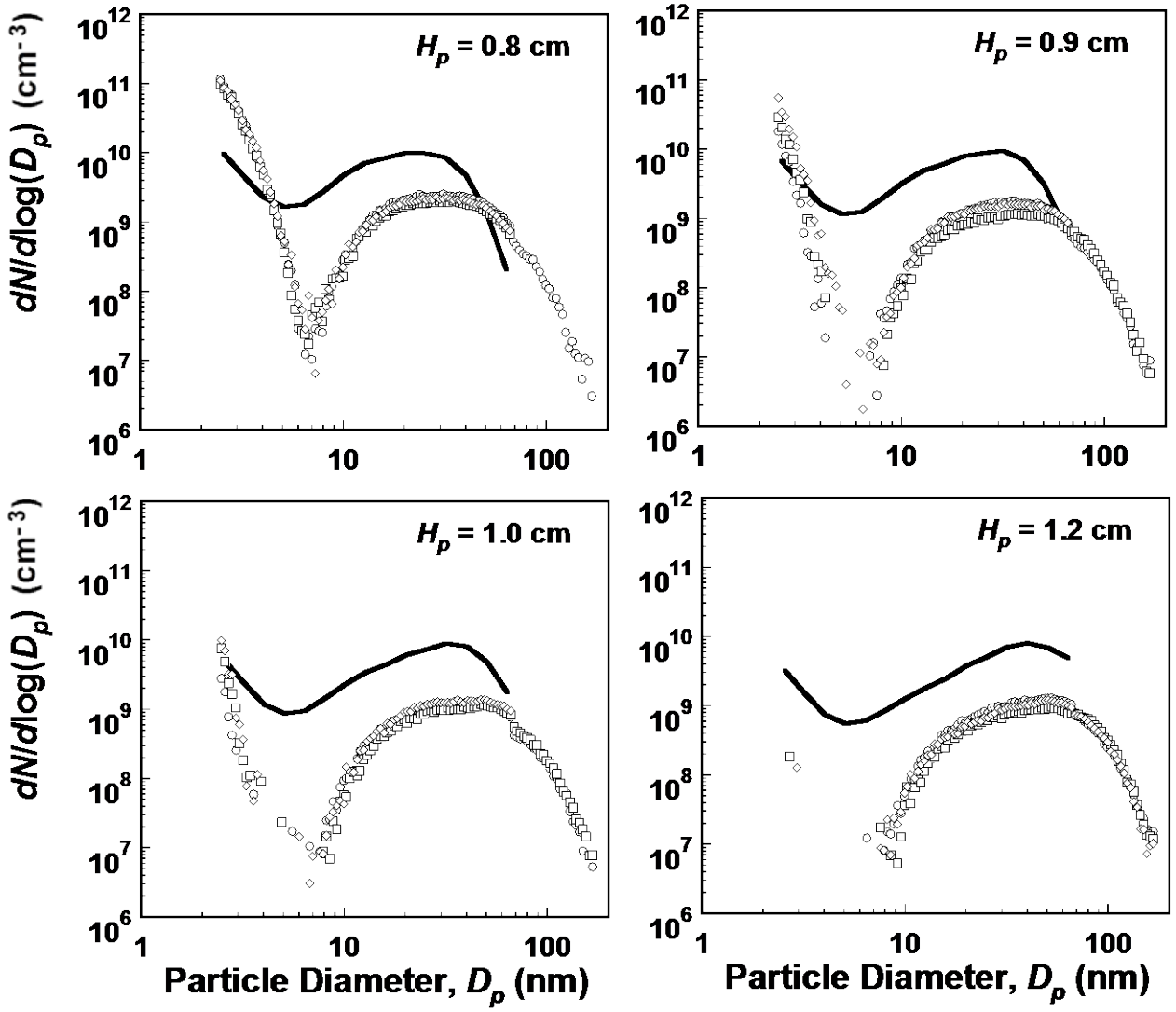

Figure 6.10 Measured (symbols) and predicted (lines) PSDFs of J1 flames at different H_p.

The trough of the distribution is significantly deeper than experimental observations and also the agglomeration mode is overpredicted by the model, showing a rapid aggregate formation. As shown before in the sensitivity analysis, increasing coalescence and aggregation kinetics would lower the number density of particles and favor formation of bigger aggregates. However, these results show also that the soot model need still to be improved to be able to reproduce these new data taken in a pure propene flame. However, the measured global and detailed behavior of J2 flame (mixture of ethylene and propene) is better caught by the model and Figure 6.11 shows the satisfactory comparisons of their experimental and predicted PSDFs.

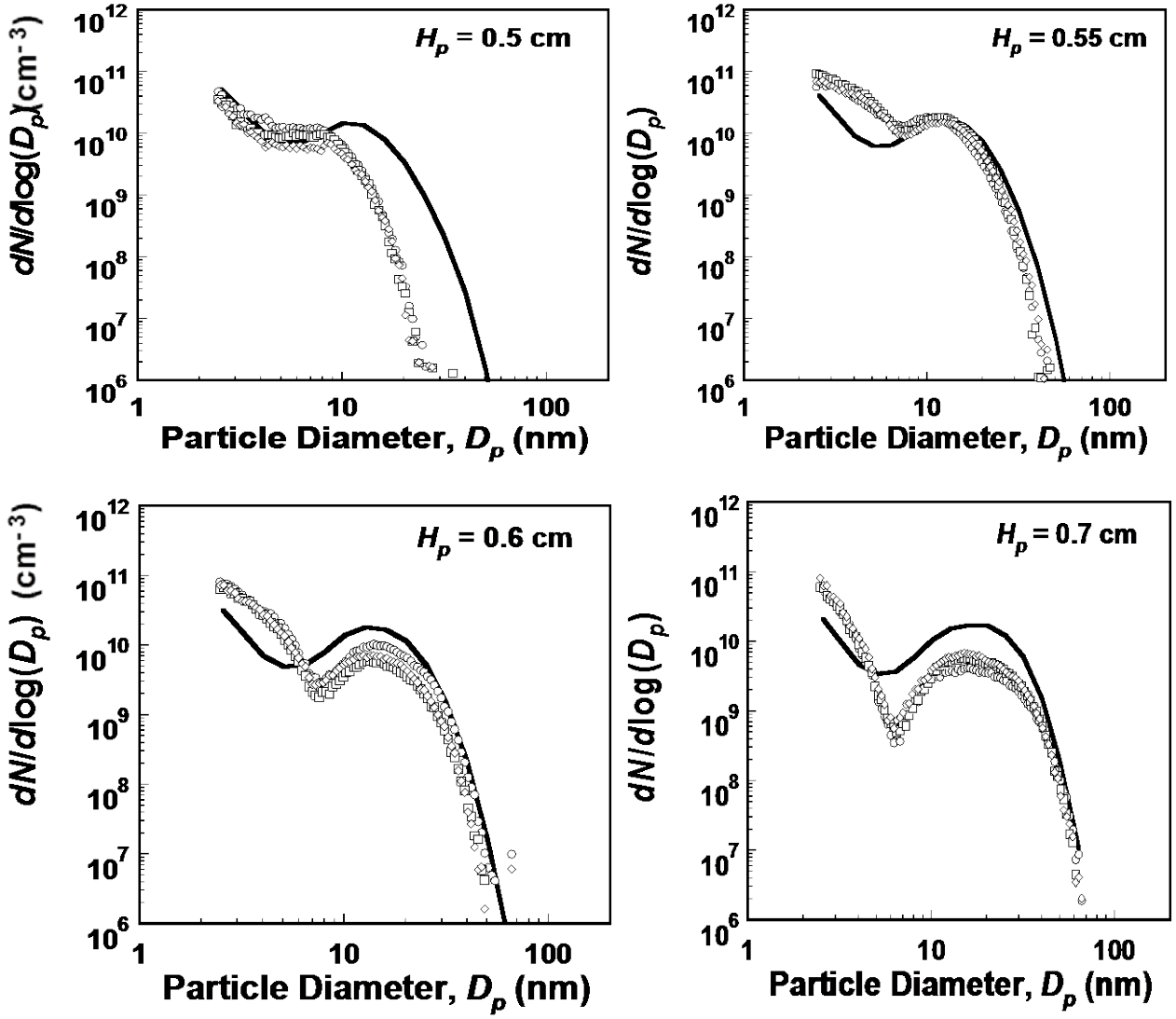

Figure 6.11 Measured (symbols) and predicted (lines) PSDFs of J2 flames at different H_p.

6.2 C6 cyclic hydrocarbon flames

Aromatics and cycloalkanes play an important role in practical fuel chemistry due to their relevant presence in liquid transportation fuels [227]. Therefore the study of their combustion kinetics results very important especially at high temperatures, similar to engine conditions.

Because of the subtle differences in the fuel structures between cyclic C6 hydrocarbons, different pathways to aromatics and hence different rates to aromatic growth are expected. The fuel structure difference can impact the nucleation rate of soot and its subsequent mass and size growth, and such effect remains mostly un-explored for premixed flames.

In the last years, benzene and cyclohexane atmospheric, laminar premixed flames were studied experimentally on a commercial water-cooled sintered bronze burner in order to understand the influence of the peak temperature of the flame [223, 225], the influence of stoichiometry and fuel structure [224] on benzene and soot formation.

Moreover, recent data on soot growth in premixed C6 hydrocarbons flames in Burner Stabilized Stagnation (BSS) conditions [222] came out with details on the evolution of the detailed soot particle size distribution function (PSDF). Similar data of n-heptane and toluene flames have been also recently modeled considering the BSS configuration and a soot chemistry model [228].

6.2.1 Premixed benzene and cyclohexane flames

The soot concentration is measured in laminar premixed benzene and cyclohexane flames, whose stoichiometric and operating conditions are reported in the Table 6.2. These flames have fixed carbon-to-oxygen ratio of 0.77 and maximum flame temperature of ~1730 K, in order to isolate these parameters from the fuel structure effect.

Fuel	Φ	x_{FUEL}	x_{O2}	x_{N2}	C/O	v_0 [cm/s]	T_{max} [K]	P [atm]
Cyclohexane [224]	2.3	0.124	0.482	0.394	0.77	4	1722	1
Benzene [223]	1.9	0.049	0.19	0.761	0.77	4	1742	1
Benzene [225]	1.98	0.057	0.216	0.727	~0.8	3	1720	1

Table 6.2 Summary of the laminar premixed flame conditions.

The flames are stabilized at atmospheric-pressure on a commercial water-cooled sintered bronze burner (McKenna Products Inc., USA).

Combustion products are isokinetically sampled along the flame axis by means of a water-cooled stainless-steel probe vertically inserted in the flames.

Flame temperature is measured with a fast-response thermocouple (silica-coated 25 μm Pt/Pt-13%Rh with a bead of ~50 μm) by using a fast-response procedure (insertion time of about 100 ms). A fast-insertion procedure is used to avoid massive soot deposition on the thermocouple bead. Temperatures are corrected for radiative losses. To account for probe effects the mole fraction profiles are shifted 2 mm upstream relative to the unperturbed temperature profiles. The uncertainty of the measured temperatures is estimated to be as high as 100 K.

Light hydrocarbons (C1–C6) and stable gases (O_2, CO_2, CO, H_2, N_2) are analyzed using on-line gas chromatography with a flame ionization detector (GC-FID) and a thermal conductivity detector, respectively. The uncertainties of these measurements are estimated to be less than 30%.

Total particulate, which includes solid and tarry materials collected on the probe wall, on a Teflon filter (porosity 0.5 μm from Fluoropore Whatman) and in an ice-cooled trap placed along the sampling line, is extracted by dichloromethane to separate the species soluble in DCM, from the insoluble solid carbonaceous material (soot). Soot is dried and weighed for the determining of its concentration in the sampled gases.

Comparisons between experimental data and model predictions of benzene and cyclohexane flame structures are shown in

Figure **6.12**.

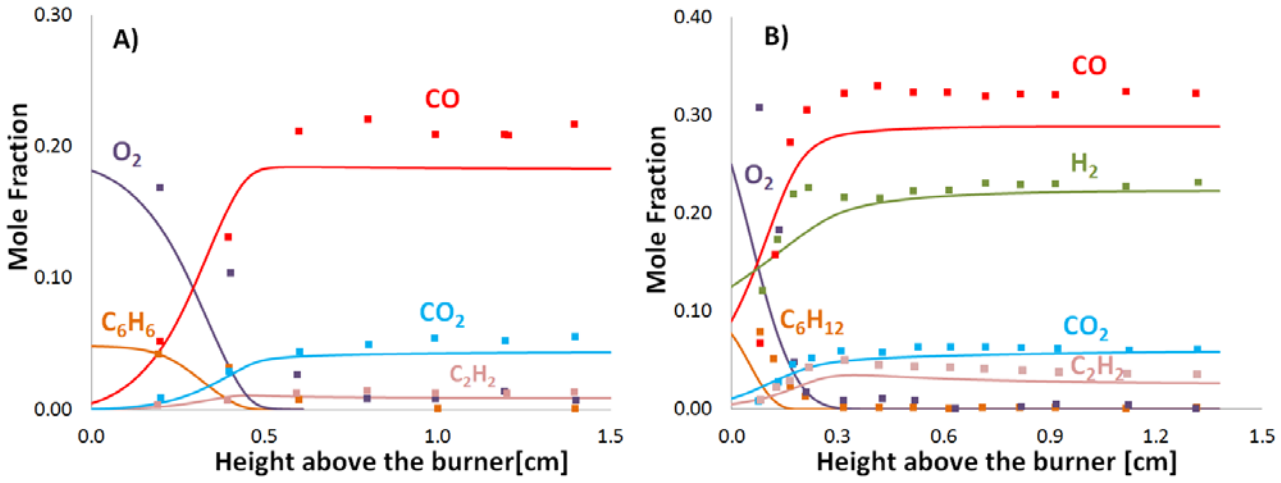

Figure 6.12 Benzene [223] (panel A) and cyclohexane [224] (panel B) flame structures. Experimental data: symbols. Model predictions: solid lines.

The model predicts fairly well the reactivity of the two flames. In particular, in Figure 6.13 is reported the comparison between the measured and predicted benzene concentration in the cyclohexane flame (left panel) and the its rate of production analysis (right panel), as key precursor to soot formation.

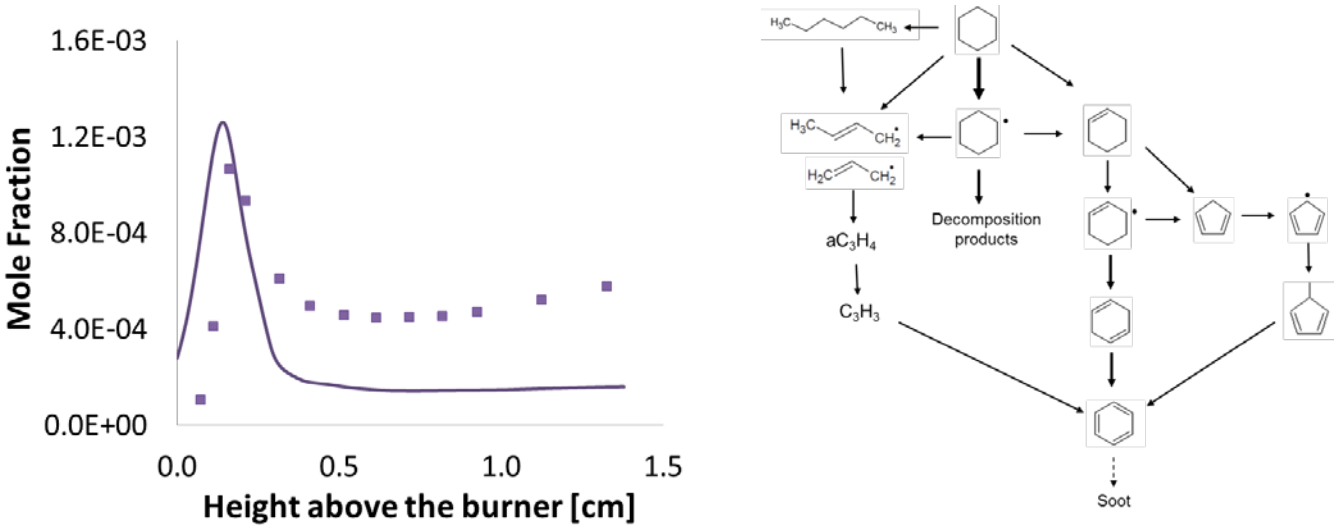

Figure 6.13 Measured (symbols) and predicted (line) benzene mole fraction (left panel) and its ROPA (right panel) in the cyclohexane flame.

The peak of benzene is well predicted by the model and it is mainly formed by the dehydrogenation of cyclohexadiene.

The analysis of the pathways leading to soot from the benzene formed in this cyclohexane flame are shown in Figure 6.14.

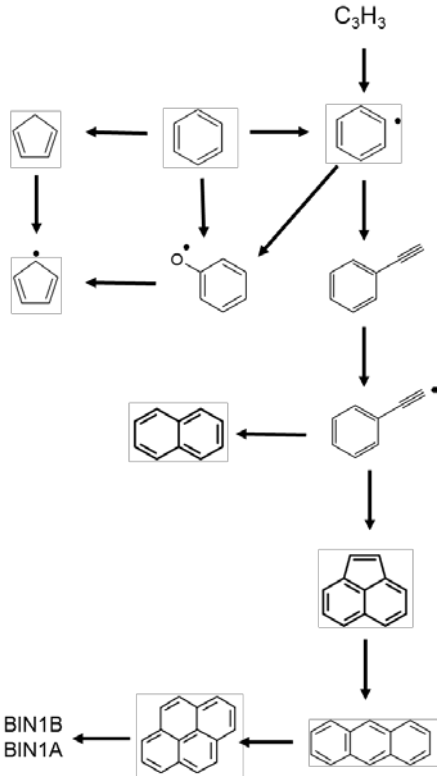

Figure 6.14 ROPA of benzene depletion and soot formation in the cyclohexane flame.

The main step involves the formation of phenylacetylene, that successively leads to the formation of heavier PAHs, precursors of soot. It is noteworthy that in more lean conditions phenoxy radicals starts to play an important role.

Finally, in Figure 6.15 the predicted and measured soot concentration in the three studied flames are reported.

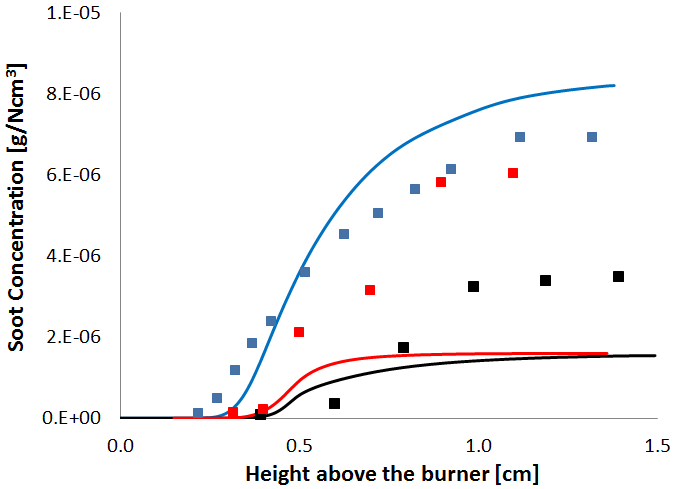

Figure 6.15 Soot concentration in all the three flames as function of height above the burner. Experimental data: symbols. Model predictions: solid lines. Blue: cyclohexane flame; Red: benzene flame [225]; Black: benzene flame [223].

The model reasonably predicts the soot formed in the cyclohexane flame, with a soot inception that starts at 0.4 cm and a plateau at higher heights above the burner.

However, in the benzene flames the soot is underpredicted by the model, even though inception seems to be fairly caught within experimental uncertainties.

Sooting tendency of aromatics is higher than that of cycloalkanes. The larger soot formation in cyclohexane flame is due to the higher fuel concentration.

It is also worth to notice that the local temperature is the dominant parameter which governs the soot chemistry and, because of the difficulties in its measurement, there are great experimental uncertainties on the temperature profile.

6.2.2 BSS benzene and cyclohexane flames

Recently, the time resolved formation of nascent soot from the onset of nucleation to later growth stages is examined by Camacho et al. [222] for premixed burner stabilized stagnation (BSS) flames of C_6 hydrocarbons, namely *n*-hexane, *n*-hexene, 2-methylpentane, cyclohexane and benzene. BSS flame approach coupled with mobility sizing is employed to probe nascent soot formation.

Herein the analysis will focus on the flames that are summarized in Table 6.3.

Fuel	Φ	x_{FUEL}	x_{O2}	x_{Ar}	C/O	v_0[a] [cm/s]	T_{max} [K]	P [atm]
Cyclohexane	2.07	0.0748	0.325	0.6002	0.69	4.87	~1800	1
Benzene	1.72	0.0748	0.325	0.6002	0.69	3.41	~1800	1

[a] STP cold gas velocity

Table 6.3 Summary of the premixed BSS flame conditions.

These flames are studied at a fixed carbon-to-oxygen ratio of 0.69 and maximum flame temperature of 1800 K. Under this constraint, the overall sooting process is comparable as evidenced by similar time resolved bimodal PSDF. The adiabatic flame temperature for benzene is much greater than the other flame because the equivalence ratio is closer to unity. Thus the cold gas velocity of the benzene flame is lower than the flow rate of the cyclohexane one, to match the 1800 K flame temperature constraint.

The gas temperature profiles are measured with a Y_2O_3/BeO coated type-S thermocouple with radiation correction using a procedure discussed earlier for BSS propene flames.

The flat flame burner is 5 cm in diameter and is uncooled because of potential condensation of the fuel in the porous material. A sheath of nitrogen shields the flame to prevent radial entrainment and diffusion of oxygen from ambient air.

The C_6 hydrocarbon fuels, supplied by Sigma-Aldridge (ACS Reagent grade, 99% purity), are injected into the fuel line and vaporized in a manner similar to a previous study of dodecane BSS flames [229]. Particle size distributions are determined with a TSI 3080 SMPS (Electrostatic Classifier 3085 and UCPC 3080, AIM Software V.8.1) using a sample dilution technique developed earlier and improved over time, as showed for propene flames.

These BSS benzene and cyclohexane flames are simulated and discussed using the previously described kinetic model of soot formation.

Figure 6.16 shows the comparisons between the experimental and predicted soot volume fraction and number density for BSS benzene and cyclohexane flames at different burner-stagnation plate distances H_p.

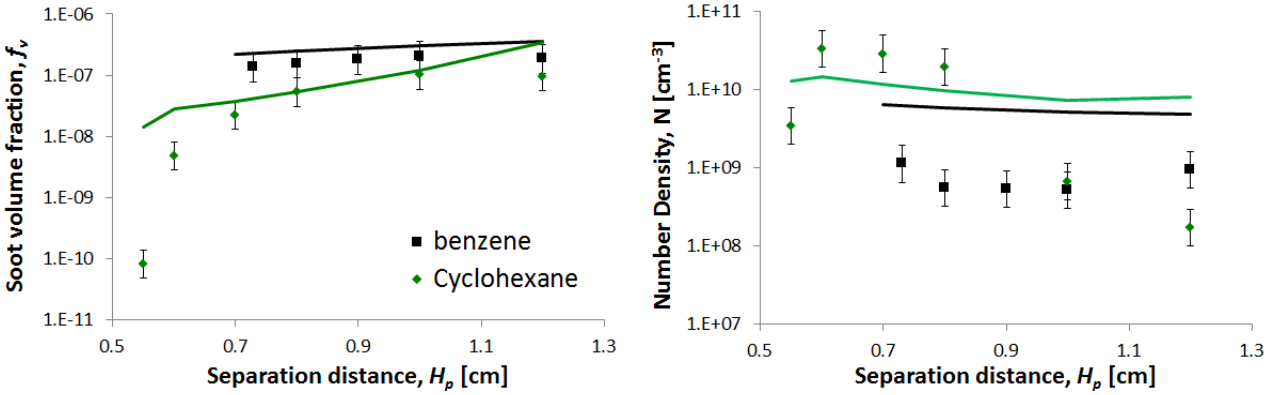

Figure 6.16 Measured and predicted soot volume fraction (left panel) and number density (right panel) in benzene and cyclohexane BSS flames at different separation distances H_p [222]. Experimental data: symbols. Model predictions: solid lines. Green: cyclohexane flame; Black: benzene flame.

Experimentally, only the nucleation in the cyclohexane flame is probed, while benzene flame is too sooty and not possible to stretch at H_p lower than 0.7 because resulted unstable.

In these conditions, the soot volume fraction formed in the benzene flame is greater than the one formed in the cyclohexane flame and the model well predicts this behavior. The evolution of both

soot volume fraction is similar to experimental observations, while the number density is overpredicted for benzene flames and for cyclohexane flames only at larger separation distances as following shown by the detailed sooting behavior predicted by the model.

Figure 6.17 and Figure 6.18 report the measured and computed PSDF of BSS cyclohexane and benzene flames, respectively. Both are shown for two significant H_p to show the soot evolution inside the flame.

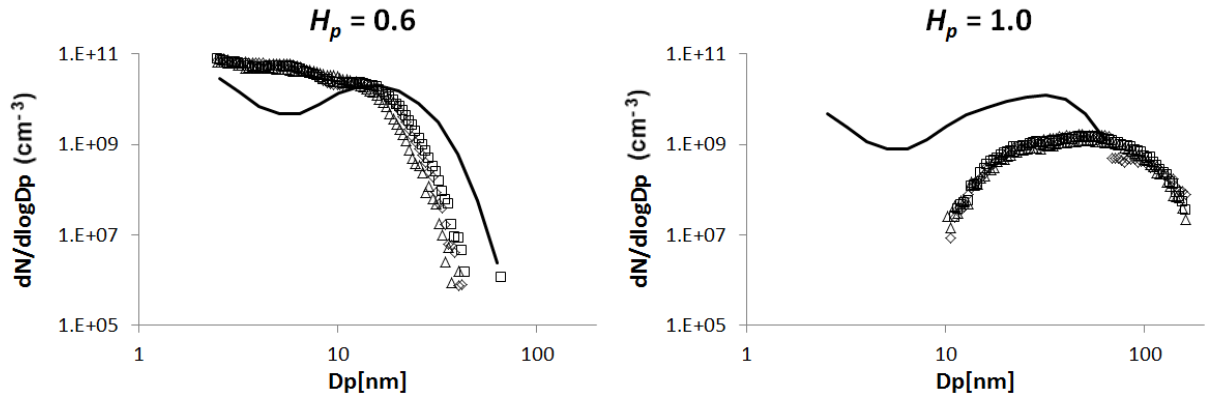

Figure 6.17 Measured (symbols) and predicted (lines) PSDFs of cyclohexane flames at different H_p.

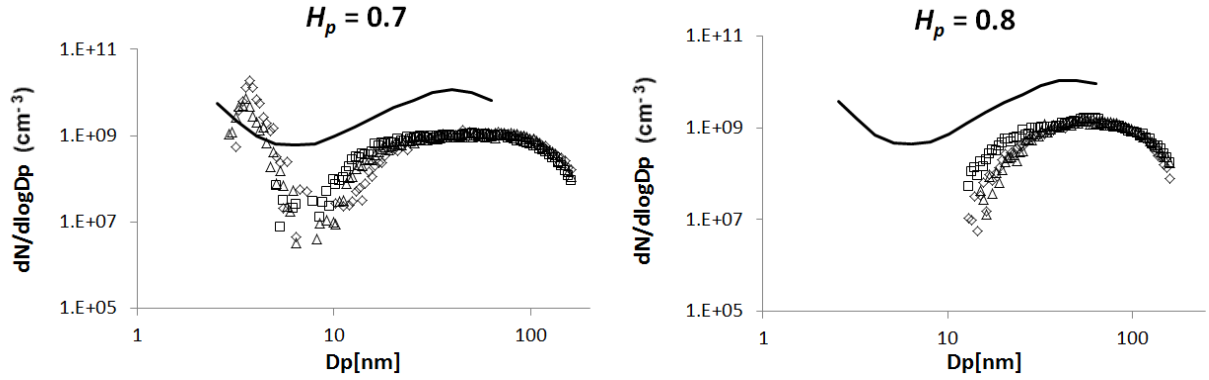

Figure 6.18 Measured (symbols) and predicted (lines) PSDFs of benzene flames at different H_p.

Experimentally, it is observed not only a fastest onset of soot nucleation in flames of cyclic hydrocarbon fuels in respect to linear C6 hydrocarbons but also a faster disappearance of nucleation-size particles.

In the cyclohexane flame, the progression of the PSDFs is clear: already at H_p = 0.6 cm a hint of the agglomeration mode appears, which evolves into a lognormal type of the PSDF eventually. In the benzene flame, only agglomeration was possible to probe and its evolution shows the

progressive disappearance of the tail of the small size particles. In this case, the model is not able to predict the disappearance of the soot nucleation and the agglomeration mode is related to smaller particles than the observed ones. As for propene, increasing coalescence and aggregation kinetics would lower the number density of particles and favor formation of bigger aggregates. Moreover, the model still has to be improved to better represent soot formation from these parent fuels. A thorough experimental analysis of the gas phase species, with also the heavier PAHs, along the flame axis could help to move forward and gain a better kinetic understanding of this system.

The formation of acetylene, propargyl radical and benzene is numerically analyzed to gain insight into the impact of fuel structure within the C_6 hydrocarbon fuels. The computed species profiles are shown in Figure 6.19 as a function of distance between the burner and the stagnation plate for both flames. The profiles are characterized by the two distinct regions which come before and after the thin reaction zone (flame zone).

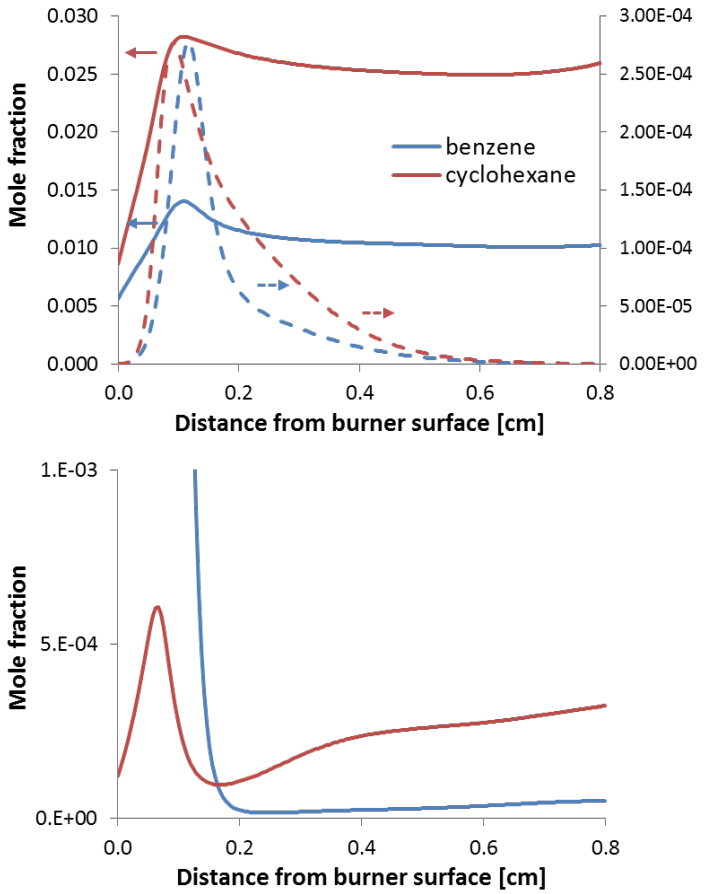

Figure 6.19 Mole fraction profile of acetylene (top panel-solid lines), propargyl radical (top panel-dashed lines) and benzene (bottom panel-solid lines) computed at H_p = 0.8 cm for each of the fuels studied. Red lines: cyclohexane flame; Blue lines: benzene flame. Acetylene refers to the primary axis, while propargyl radical refers to the secondary axis.

The onset of nucleation is fastest in the cyclohexane flame and the pre-flame peak of benzene production shown in Figure 6.19 may influence this detailed sooting behavior. The prediction of benzene at the peak temperature allows for a possible pathway to soot which starts in the pre-flame region. It is well established that local flame temperature and acetylene production in the post flame are the main factors controlling soot precursor formation thus the parent fuel structure is only of secondary importance. In this case, the fuel structure of cyclohexane has a primary impact in a manner not conventionally considered.

The formation of the first aromatic ring does not depend only on acetylene and propargyl radical production. This is possible in fuels that have structures close to the benzene ring such as cyclohexane. The reaction rates of benzene formation are analyzed numerically and three prominent pathways are summarized in Figure 6.20 as function of the distance from the burner.

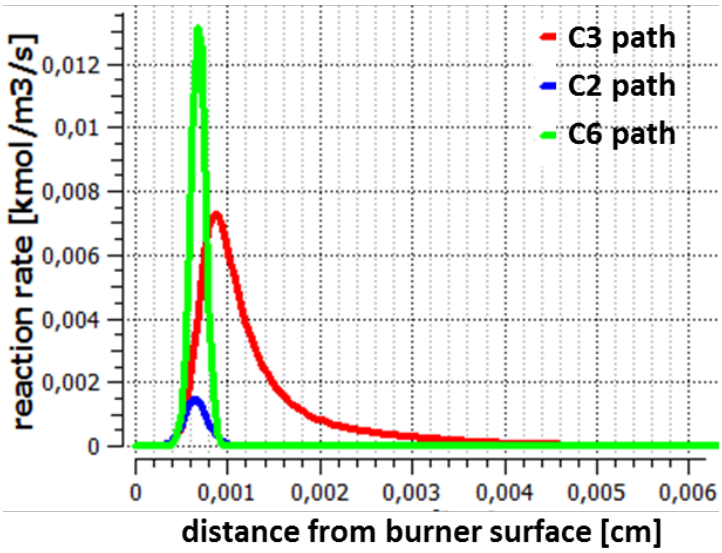

Figure 6.20 Reaction rate profiles computed for propargyl recombination (C3 path - red line), butynyl + acetylene (C2 path - blue line) and dehydrogenation (C6 path- green line) steps to benzene formation in the BSS cyclohexane flame.

Propargyl recombination (C3 path), Butynyl + Acetylene (C2 path), and dehydrogenation (C6 path) are the most dominant pathways to benzene for the studied cyclohexane flame. The C3 path is the common pathway to form benzene for many fuels, such as ethylene and propene. However, the rate of the C6 path, that only exists in cyclohexane flames, is predicted to be significant in the pre-flame region, along with the C2 path. These paths, which are specific to the cyclohexane flames, may provide a pathway for soot formation which begins in the pre-flame region. If stable aromatics

survive the flame, this early benzene production may influence the onset of soot nucleation in cyclohexane flames.

The relatively early start and early end to nucleation in the benzene flames can be understood under similar arguments. The existence of high concentrations of benzene in the pre-flame region, shown in Figure 6.19, contributes to the overall volume of soot and to the early formation of nucleation sized particles.

On the other hand, the PSDF of benzene shows that the nucleation size particles stop forming earlier than the aliphatic fuels and this behavior may also be tied to the detailed species profile of soot precursors.

For the given *C/O* ratio, the benzene flame has a much lower equivalence ratio than the other fuels. This relatively low excess fuel in the benzene flame causes much lower amounts of soot precursors such as acetylene and benzene to form in the post-flame region. The limited formation of precursors may hinder nucleation of soot in the post-flame region of the benzene flame.

7. Conclusions and Outlooks

Soot formation is a persistent problem in all of the processes involving combustion. It has detrimental effects on environment, health and energy efficiency of the devices, therefore it is necessary to improve the understanding of the processes involved in its formation in order to correlate the operating conditions with emission characteristics.

This thesis work originates from this need, and through modeling and experimental activity some steps forward in the comprehension of some phenomena have been moved. However, further studies have to be done to improve the model and to experimentally improve mobility measurements in accounting polydisperse aggregates and describe soot morphology and chemical composition.

7.1 Modeling activity

The comparison with experimental data, very important for the tuning process, provided useful information for the model.

The refinement of the gas phase kinetics of the soot precursors allowed to better characterize the steps towards the formation of the first soot nuclei.

Moreover, the comparison with the experimental data from the BSS ethylene flame shows that the updated model, with aggregates and new kinetic rules, is able to predict the temperature within the experimental error and also the soot volume fraction in agreement with the measurements. It can also reproduce the bimodal distribution found experimentally, which is important to characterize the formation of the smallest particles, particularly dangerous for human health. The number density is slightly overpredicted, due to an overestimation of the particles involved in the nucleation step.

A further and preliminary analysis of model capability has been performed against BSS propylene flame data and cyclic C6 hydrocarbon flames.

Overall, this thesis work presented a promising pathway to systematically construct a more complete model for the entire chemical reaction process from fuel to soot, which has shown many features that can reasonably well predict experimental results from different sources. It is clear that more work must be done, but if so, systematical approaches like shown here should be favored.

In particular, a sensitivity analysis on the fractal dimension should be performed as function of number of particles, as recently theoretically emerged [230]. Actually, as discussed in paragraph 5.4.4, the morphology of nascent soot is not well defined and experiments shows that is different from the well-aged soot particles. Nascent soot aggregates have a more closed structure, leading to a fractal dimension greater than 1.8.

A deeper study of soot oxidation should be carried out in diffusion flames and in specific systems such as reactors and coupled burners that are created with the specific task to study the reactions of O_2 and OH• with soot particles and aggregates.

Nowadays biofuels, such as alcohols, methyl esters, acyclic and cyclic ethers, are mostly used as additives to petroleum fuels. Therefore, their combustion should also be analyzed trying to understand the influence of their chemical composition ($C_xH_yO_z$) on soot formation process. As a matter of fact, a lumped kinetic model for the combustion and pyrolysis of heavy methyl-esters, usual components of biodiesel fuels, was developed and included in the POLIMI gas-phase mechanism [231].

Finally, to explore soot formation in more complex fluid dynamic systems, a smart reduction of the soot kinetic model is needed. An example of the reduction of this soot mechanism and its use for simulating a turbulent flame has been recently carried out in collaboration with the Centre of Turbulence Combustion at Stanford [232].

7.2 Experimental activity

Mobility measurements have been performed in BSS ethylene and propene flames, sampling soot and measuring its volume fraction and size distributions. The limit of this experimental technique is that it retains the spherical assumption of the soot particles, while they are found with irregular shapes also at nucleation stages [116]. Therefore, a critical analysis of these experiments has to be performed, as discussed in paragraph 5.4.4. A step forward could be describe aggregate polydispersity in the mobility measurements or measure mass distributions, that are not affected by the shape assumption.

Moreover, not only the morphology but also the chemical composition of soot particles should be studied experimentally to better characterize their reactivity with the environment.

References

1. BP London 2014, *BP Energy Outlook 2035*, at http://www.bp.com.

2. T.C. Bond; E. Bhardwaj; R. Dong; R. Jogani; S. Jung; C. Roden; D.G. Streets; N.M. Trautmann, *Global Biogeochemical Cycles* 21 (2007).

3. T.C. Bond; S.J. Doherty; D.W. Fahey; P.M. Forster; T. Berntsen; B.J. DeAngelo; M.G. Flanner; S. Ghan; B. Kärcher; D. Koch; S. Kinne; Y. Kondo; P.K. Quinn; M.C. Sarofim; M.G. Schultz; M. Schulz; C. Venkataraman; H. Zhang; S. Zhang; N. Bellouin; S.K. Guttikunda; P.K. Hopke; M.Z. Jacobson; J.W. Kaiser; Z. Klimont; U. Lohmann; J.P. Schwarz; D. Shindell; T. Storelvmo; S.G. Warren; C.S. Zender, *Journal of Geophysical Research: Atmospheres* 118 (2013) 5380-5552.

4. Exxon Mobil 2012, *The Outlook for Energy: A View to 2040*, at http://www.exxonmobil.com.

5. B. Frank; M.E. Schuster; R. Schlögl; D.S. Su, *Angewandte Chemie International Edition* 52 (2013) 2673-2677.

6. D.R. Tree; K.I. Svensson, *Progress in Energy and Combustion Science* 33 (2007) 272-309.

7. A.K. Agarwal, *Progress in Energy and Combustion Science* 33 (2007) 233-271.

8. G.W. Huber; S. Iborra; A. Corma, *Chemical Reviews* 106 (2006) 4044-4098.

9. Y. Román-Leshkov; C.J. Barrett; Z.Y. Liu; J.A. Dumesic, *Nature* 447 (2007) 982-985.

10. K. Yehliu; R.L. Vander Wal; O. Armas; A.L. Boehman, *Combustion and Flame* 159 (2012) 3597-3606.

11. A.L. Boehman; J. Song; M. Alam, *Energy & Fuels* 19 (2005) 1857-1864.

12. K. Yamamoto; K. Yamauchi, *Proceedings of the Combustion Institute* 34 (2013) 3083-3090.

13. M.A. Cole; R.J. Elliott; K. Shimamoto, *Journal of Environmental Economics and Management* 50 (2005) 121-143.

14. R.M. Harrison; H.M. ApSimon; H. Beck; L. Devell; M. Dickerson; J.A. Garland; G. Graziani; P. Gudiksen; W.A. McKay; U.C. Mishra; K.W. Nicholson; F.B. Smith; C.S. Shapiro, SCOPE 50 - Radioecology after Chernobyl, Chapter 3, Atmospheric Pathways. http://www.scopenvironment.org/downloadpubs/scope50/chapter03.html. January 2015.

15. World Health Organization. Hazard Prevention and Control in the Work Environment: Airborne Dust. http://www.who.int/occupational_health/publications/en/. January 2015.

16. PM emission health relevance. http://hussgroup.com/cdc/en/infocenter/PM.php. (checked: 01/2015).

17. N.A.H. Janssen; M.E. Gerlofs-Nijland; T. Lanki; R.O. Salonen; F. Cassee; G. Hoek; P. Fischer; B. Brunekreef; M. Krzyzanowski, *Health effects of black carbon*, Copenaghen: WHO Regional Office for Europe, 2012.

18. M. Krzyzanowski; B. Kuna-Dibbert; J. Schneider, *Health effects of transport-related air pollution*, Copenaghen: WHO Regional Office Europe, 2005.

19. M. Wentzel; H. Gorzawski; K.-H. Naumann; H. Saathoff; S. Weinbruch, *Journal of Aerosol Science* 34 (2003) 1347-1370.

20. R.L. Vander Wal; A.J. Tomasek, *Combustion and Flame* 136 (2004) 129-140.

21. M. Alfè; B. Apicella; R. Barbella; J.N. Rouzaud; a. Tregrossi; a. Ciajolo, *Proceedings of the Combustion Institute* 32 (2009) 697-704.

22. B. Apicella; P. Pré; M. Alfè; A. Ciajolo; V. Gargiulo; C. Russo; A. Tregrossi; D. Deldique; J. Rouzaud, *Proceedings of the Combustion Institute* 35 (2014) 1895-1902.

23. R.L. Vander Wal; A.J. Tomasek, *Combustion and Flame* 134 (2003) 1-9.

24. R.L. Vander Wal; C.J. Mueller, *Energy & Fuels* 20 (2006) 2364-2369.

25. H. Wang; M. Frenklach, *Combustion and Flame* 110 (1997) 173-221.

26. H. Wang, *Proceedings of the Combustion Institute* 33 (2011) 41-67.

27. M. Frenklach; H. Wang in: *Detailed mechanism and modeling of soot particle formation*, Soot Formation in Combustion, 1994; Springer; pp 165-192.

28. M. Frenklach; D.W. Clary; W.C. Gardiner Jr; S.E. Stein in: *Detailed kinetic modeling of soot formation in shock-tube pyrolysis of acetylene*, Symposium (International) on Combustion, 1985; Elsevier; pp 887-901.

29. J. Cole; J. Bittner; J. Longwell; J. Howard, *Combustion and Flame* 56 (1984) 51-70.

30. M.B. Colket III in: *The pyrolysis of acetylene and vinylacetylene in a single-pulse shock tube*, Symposium (International) on Combustion, 1988; Elsevier; pp 851-864.

31. J.A. Miller; C.F. Melius, *Combustion and Flame* 91 (1992) 21-39.

32. A. Fahr; S. Stein in: *Reactions of vinyl and phenyl radicals with ethyne, ethene and benzene*, Symposium (International) on Combustion, 1989; Elsevier; pp 1023-1029.

33. C.F. Melius; M.E. Colvin; N.M. Marinov; W.J. Pit; S.M. Senkan in: *Reaction mechanisms in aromatic hydrocarbon formation involving the C_5H_5 cyclopentadienyl moiety*, Symposium (International) on Combustion, 1996; Elsevier; pp 685-692.

34. N. Marinov; W. Pitz; C. Westbrook; M. Castaldi; S. Senkan, *Combustion Science and Technology* 116 (1996) 211-287.

35. A. D'Anna; A. Violi in: *A kinetic model for the formation of aromatic hydrocarbons in premixed laminar flames*, Symposium (International) on Combustion, 1998; Elsevier; pp 425-433.

36. D. Wang; A. Violi; D.H. Kim; J.A. Mullholland, *The Journal of Physical Chemistry A* 110 (2006) 4719-4725.

37. M.R. Djokic; K.M. Van Geem; C. Cavallotti; A. Frassoldati; E. Ranzi; G.B. Marin, *Combustion and Flame* 161 (2014) 2739-2751.

38. H. Richter; J. Howard, *Progress in Energy and Combustion Science* 26 (2000) 565-608.

39. A. D'Anna, *Energy & Fuels* 22 (2008) 1610-1619.

40. M. Colket; D. Seery in: *Reaction mechanisms for toluene pyrolysis*, Symposium (International) on Combustion, 1994; Elsevier; pp 883-891.

41. K. Hemelsoet; V. Van Speybroeck; K.M. Van Geem; G.B. Marin; M. Waroquier, *Molecular Simulation* 34 (2008) 193-199.

42. V. Kislov; A. Mebel; J. Aguilera-Iparraguirre; W. Green, *The Journal of Physical Chemistry A* 116 (2012) 4176-4191.

43. V. Van Speybroeck; M.F. Reyniers; G.B. Marin; M. Waroquier, *ChemPhysChem* 3 (2002) 863-870.

44. J.P. Cain; P.L. Gassman; H. Wang; A. Laskin, *Physical Chemistry Chemical Physics* 12 (2010) 5206-5218.

45. Q.-L. Zhang; S. O'Brien; J. Heath; Y. Liu; R. Curl; H. Kroto; R. Smalley, *The Journal of Physical Chemistry* 90 (1986) 525-528.

46. M. Frenklach; H. Wang in: *Detailed modeling of soot particle nucleation and growth*, Symposium (International) on Combustion, 1991; Elsevier; pp 1559-1566.

47. J.H. Miller in: *The kinetics of polynuclear aromatic hydrocarbon agglomeration in flames*, Symposium (International) on Combustion, 1991; Elsevier; pp 91-98.

48. J.D. Herdman; J.H. Miller, *The Journal of Physical Chemistry A* 112 (2008) 6249-6256.

49. H. Richter; T.G. Benish; O.A. Mazyar; W.H. Green; J.B. Howard, *Proceedings of the Combustion Institute* 28 (2000) 2609-2618.

50. A. Ciajolo; A. Tregrossi; R. Barbella; R. Ragucci; B. Apicella; M. De Joannon, *Combustion and Flame* 125 (2001) 1225-1229.

51. A. Violi; A. Kubota; T. Truong; W. Pitz; C. Westbrook; A. Sarofim, *Proceedings of the Combustion Institute* 29 (2002) 2343-2349.

52. M. Frenklach, *Physical Chemistry Chemical Physics* 4 (2002) 2028-2037.

53. A.D. Abid; J. Camacho; D.A. Sheen; H. Wang, *Combustion and Flame* 156 (2009) 1862-1870.

54. A. De Filippo; L. Sgro; G. Lanzuolo; A. D'Alessio, *Combustion and Flame* 156 (2009) 1744-1754.

55. S.L. Manzello; D.B. Lenhert; A. Yozgatligil; M.T. Donovan; G.W. Mulholland; M.R. Zachariah; W. Tsang, *Proceedings of the Combustion Institute* 31 (2007) 675-683.

56. M.M. Maricq; S.J. Harris; J.J. Szente, *Combustion and Flame* 132 (2003) 328-342.

57. B. Öktem; M.P. Tolocka; B. Zhao; H. Wang; M.V. Johnston, *Combustion and Flame* 142 (2005) 364-373.

58. B. Zhao; Z. Yang; M.V. Johnston; H. Wang; A.S. Wexler; M. Balthasar; M. Kraft, *Combustion and Flame* 133 (2003) 173-188.

59. C.A. Schuetz; M. Frenklach, *Proceedings of the Combustion Institute* 29 (2002) 2307-2314.

60. C. Allouis; B. Apicella; R. Barbella; F. Beretta; A. Ciajolo; A. Tregrossi, *Chemosphere* 51 (2003) 1097-1102.

61. D. Koley; E. Arunan; S. Ramakrishnan, *Journal of Computational Chemistry* 33 (2012) 1762-1772.

62. H.-B. Zhang; X. You; H. Wang; C.K. Law, *The Journal of Physical Chemistry A* 118 (2014) 1287-1292.

63. H. Retcofsky; J. Stark; R. Friedel, *Analytical Chemistry* 40 (1968) 1699-1704.

64. S. Yan; E.G. Eddings; A.B. Palotas; R.J. Pugmire; A.F. Sarofim, *Energy & Fuels* 19 (2005) 2408-2415.

65. T. Ishiguro; Y. Takatori; K. Akihama, *Combustion and Flame* 108 (1997) 231-234.

66. J. Appel; H. Bockhorn; M. Frenklach, *Combustion and Flame* 121 (2000) 122-136.

67. M. Smoluchowski, *Zeitschrift für Physikalische Chemie* 92 (1917) 129-168.

68. K. Homann, *Combustion and Flame* 11 (1967) 265-287.

69. J. Howard; B. Wersborg; G. Williams in: *Coagulation of carbon particles in premixed flames*, Faraday Symposia of the Chemical Society, 1973; Royal Society of Chemistry; pp 109-119.

70. A. D'Anna; M. Sirignano; J. Kent, *Combustion and Flame* 157 (2010) 2106-2115.

71. B. Stanmore; J. Brilhac; P. Gilot, *Carbon* 39 (2001) 2247-2268.

72. M. Mueller; G. Blanquart; H. Pitsch, *Proceedings of the Combustion Institute* 33 (2011) 667-674.

73. R. Vierbaum; P. Roth, *Proceedings of the Combustion Institute* 29 (2002) 2423-2429.

74. C.A. Echavarria; I.C. Jaramillo; A.F. Sarofim; J.S. Lighty, *Proceedings of the Combustion Institute* 33 (2011) 659-666.

75. M. Sirignano; J. Kent; A. D'Anna, *Energy & Fuels* 27 (2013) 2303-2315.

76. J. Camacho; Y. Tao; H. Wang, *Proceedings of the Combustion Institute* 35 (2014) 1887-1894.

77. I.C. Jaramillo; C.K. Gaddam; R.L. Vander Wal; C.-H. Huang; J.D. Levinthal; J.S. Lighty, *Combustion and Flame* 161 (2014) 2951-2965.

78. A. D'Anna, *Proceedings of the Combustion Institute* 32 (2009) 593-613.

79. H. Bockhorn, *Soot Formation in Combustion*, Springer-Verlag, Berlin, 1994.

80. H. Bockhorn; A. D'Anna; A. Sarofim; H. Wang, *Combustion Generated Fine Carbonaceous Particles*, KIT Scientific Publishing, Karlsruhe, Germany, 2009.

81. G. Blanquart; H. Pitsch in: *A joint volume-surface-hydrogen multi-variate model for soot formation*, Combustion Generated Fine Carbonaceous Particles, 2009; pp 437-463.

82. M. Frenklach; S.J. Harris, *Journal of Colloid and Interface Science* 118 (1987) 252-261.

83. G. Blanquart; H. Pitsch, *Combustion and Flame* 156 (2009) 1614-1626.

84. S. Granata; F. Cambianica; S. Zinesi; T. Faravelli; E. Ranzi in: *Detailed kinetics of PAH and soot formation in combustion processes: analogies and similarities in reaction classes*, Proceedings of the European Combustion Meeting, 2005.

85. H. Richter; S. Granata; W.H. Green; J.B. Howard, *Proceedings of the Combustion Institute* 30 (2005) 1397-1405.

86. R. Hall; M. Smooke; M. Colket, *Physical and Chemical Aspects of Combustion: A Tribute to Irvin Glassman* (1997) 189-230.

87. M. Smooke; C. McEnally; L. Pfefferle; R. Hall; M. Colket, *Combustion and Flame* 117 (1999) 117-139.

88. C.J. Pope; J.B. Howard, *Aerosol Science and Technology* 27 (1997) 73-94.

89. M. Balthasar; M. Kraft, *Combustion and Flame* 133 (2003) 289-298.

90. J. Singh; M. Balthasar; M. Kraft; W. Wagner, *Proceedings of the Combustion Institute* 30 (2005) 1457-1465.

91. M. Celnik; R. Patterson; M. Kraft; W. Wagner, *Combustion and Flame* 148 (2007) 158-176.

92. M. Goodson; M. Kraft, *Journal of Computational Physics* 183 (2002) 210-232.

93. M. Sander; R.I. Patterson; A. Braumann; A. Raj; M. Kraft, *Proceedings of the Combustion Institute* 33 (2011) 675-683.

94. A. Violi; S. Izvekov, *Proceedings of the Combustion Institute* 31 (2007) 529-537.

95. D.L. Marchisio; R.O. Fox, *Computational models for polydisperse particulate and multiphase systems*, Cambridge University Press, 2013.

96. M. Frenklach, *Chemical Engineering Science* 57 (2002) 2229-2239.

97. R. McGraw, *Aerosol Science and Technology* 27 (1997) 255-265.

98. C. Yuan; F. Laurent; R. Fox, *Journal of Aerosol Science* 51 (2012) 1-23.

99. A. Cuoci; A. Frassoldati; T. Faravelli; E. Ranzi, *Environmental Engineering Science* 25 (2008) 1407-1422.

100. D.L. Marchisio; A.A. Barresi, *Chemical Engineering Science* 64 (2009) 294-303.

101. D.L. Marchisio; R.O. Fox, *Journal of Aerosol Science* 36 (2005) 43-73.

102. M. Mueller; G. Blanquart; H. Pitsch, *Combustion and Flame* 156 (2009) 1143-1155.

103. M. Schenk; S. Lieb; H. Vieker; A. Beyer; A. Gölzhäuser; H. Wang; K. Kohse-Höinghaus, *ChemPhysChem* 14 (2013) 3248-3254.

104. C. Yuan; R.O. Fox, *Journal of Computational Physics* 230 (2011) 8216-8246.

105. S. Salenbauch; A. Cuoci; A. Frassoldati; C. Saggese; T. Faravelli; C. Hasse, *Combustion and Flame* (2015), *accepted*.

106. Q. Zhang. *Detailed modeling of soot formation/oxidation in laminar coflow diffusion flames*. PhD Thesis, University of Toronto, 2009.

107. A. Violi; A. Venkatnathan, *The Journal of Chemical Physics* 125 (2006) 054302.

108. D. Chen; Z. Zainuddin; E. Yapp; J. Akroyd; S. Mosbach; M. Kraft, *Proceedings of the Combustion Institute* 34 (2013) 1827-1835.

109. A. Ciajolo; M. Alfè; B. Apicella; R. Barbella; A. Tregrossi, *Chemical Engineering Transactions* 17 (2009) 99-104.

110. A.D. Eisner; D.E. Rosner, *Combustion and Flame* 61 (1985) 153-166.

111. L. Sgro; A. Barone; M. Commodo; A. D'Alessio; A. De Filippo; G. Lanzuolo; P. Minutolo, *Proceedings of the Combustion Institute* 32 (2009) 689-696.

112. C. Arnal; M. Alfè; V. Gargiulo; A. Ciajolo; M. Alzueta; Á. Millera; R. Bilbao in: *Characterization of Soot*, Cleaner Combustion, 2013; Springer London; pp 333-362.

113. R.L. Vander Wal; V.M. Bryg; C.-H. Huang, *Combustion and Flame* 161 (2014) 602-611.

114. P.J. Goodhew; J. Humphreys; R. Beanland, *Electron microscopy and analysis*, CRC Press, 2000.

115. P.J. Eaton; P. West, *Atomic force microscopy*, Oxford University Press, 2010.

116. M. Schenk; S. Lieb; H. Vieker; A. Beyer; A. Gölzhäuser; H. Wang; K. Kohse-Höinghaus, *Proceedings of the Combustion Institute* 35 (2014) 1879-1886.

117. C. Jäger; T. Henning; R. Schlögl; O. Spillecke, *Journal of Non-Crystalline Solids* 258 (1999) 161-179.

118. J.-N. Rouzaud; C. Clinard, *Fuel Processing Technology* 77 (2002) 229-235.

119. P. Toth; Á. Palotás; J. Lighty; C. Echavarria, *Fuel* 99 (2012) 1-8.

120. P. Toth; A.B. Palotas; E.G. Eddings; R.T. Whitaker; J.S. Lighty, *Combustion and Flame* 160 (2013) 909-919.

121. C. Russo; M. Alfè; J.-N. Rouzaud; F. Stanzione; A. Tregrossi; A. Ciajolo, *Proceedings of the Combustion Institute* 34 (2013) 1885-1892.

122. A. Santamaria; N. Yang; E. Eddings; F. Mondragon, *Combustion and Flame* 157 (2010) 33-42.

123. C.A. Echavarria; A.F. Sarofim; J.S. Lighty; A. D'Anna, *Proceedings of the Combustion Institute* 32 (2009) 705-711.

124. L. Sgro; A. De Filippo; G. Lanzuolo; A. D'Alessio, *Proceedings of the Combustion Institute* 31 (2007) 631-638.

125. A. Abid; E. Tolmachoff; D. Phares; H. Wang; Y. Liu; A. Laskin, *Proceedings of the Combustion Institute* 32 (2009) 681-688.

126. R.P. Lindstedt; B.B.O. Waldheim, *Proceedings of the Combustion Institute* 34 (2013) 1861-1868.

127. Z. Li; H. Wang, *Physical Review E* 68 (2003) 061206.

128. K. Park; D. Dutcher; M. Emery; J. Pagels; H. Sakurai; J. Scheckman; S. Qian; M. Stolzenburg; X. Wang; J. Yang, *Aerosol Science and Technology* 42 (2008) 801-816.

129. K. Ehara; C. Hagwood; K.J. Coakley, *Journal of Aerosol Science* 27 (1996) 217-234.

130. J. Olfert; N. Collings, *Journal of Aerosol Science* 36 (2005) 1338-1352.

131. R. Ghazi; H. Tjong; A. Soewono; S.N. Rogak; J.S. Olfert, *Aerosol Science and Technology* 47 (2013) 395-405.

132. D.C. Quiros; S. Hu; S. Hu; E.S. Lee; S. Sardar; X. Wang; J.S. Olfert; H.S. Jung; Y. Zhu; T. Huai, *Journal of Aerosol Science* (2015), DOI: 10.1016/j.jaerosci.2014.12.004i.

133. K. Park; F. Cao; D.B. Kittelson; P.H. McMurry, *Environmental Science & Technology* 37 (2003) 577-583.

134. M.M. Maricq; X. Ning, *Journal of Aerosol Science* 35 (2004) 1251-1274.

135. P. Desgroux; X. Mercier; K.A. Thomson, *Proceedings of the Combustion Institute* 34 (2013) 1713-1738.

136. H. Bladh; N.-E. Olofsson; T. Mouton; J. Simonsson; X. Mercier; A. Faccinetto; P.-E. Bengtsson; P. Desgroux, *Proceedings of the Combustion Institute* 35 (2014) 1843-1850.

137. G.D. Ulrich, *Chemical & Engineering News Archive* 62 (1984) 22-29.

138. R. Strobel; S.E. Pratsinis, *Journal of Materials Chemistry* 17 (2007) 4743-4756.

139. Y. Chen; M. Hsu; Y. Cai, *Journal of Alloys and Compounds* 490 (2010) 493-498.

140. W. Kong; J. Shan; Y. Ju, *Materials Letters* 64 (2010) 688-691.

141. E.D. Tolmachoff; A.D. Abid; D.J. Phares; C.S. Campbell; H. Wang, *Proceedings of the Combustion Institute* 32 (2009) 1839-1845.

142. S. Shekar; A.J. Smith; W.J. Menz; M. Sander; M. Kraft, *Journal of Aerosol Science* 44 (2012) 83-98.

143. R.H. West; M.S. Celnik; O.R. Inderwildi; M. Kraft; G.J.O. Beran; W.H. Green, *Industrial & Engineering Chemistry Research* 46 (2007) 6147-6156.

144. E. Ranzi; A. Frassoldati; R. Grana; A. Cuoci; T. Faravelli; A.P. Kelley; C.K. Law, *Progress in Energy and Combustion Science* 38 (2012) 468-501.

145. E. Ranzi; M. Dente; A. Goldaniga; G. Bozzano; T. Faravelli, *Progress in Energy and Combustion Science* 27 (2001) 99-139.

146. A. Stagni; A. Cuoci; A. Frassoldati; T. Faravelli; E. Ranzi, *Industrial & Engineering Chemistry Research* 53 (2013) 9004-9016.

147. A. Burcat; B. Ruscic, *Third millenium ideal gas and condensed phase thermochemical database for combustion with updates from active thermochemical tables*, Argonne National Laboratory, Argonne, IL, 2005.

148. R. Kee; F. Rupley; J. Miller, *Technical Report SAND89-8009 (CHEMKIN-II)*, Sandia National Laboratories, Livermore, CA, 1989.

149. S.W. Benson, *Thermochemical kinetics*, 1976.

150. A. Cuoci; A. Frassoldati; T. Faravelli; E. Ranzi, *Computer Physics Communications* (2015), DOI: 10.1016/j.cpc.2015.02.014.

151. C. Saggese; A. Frassoldati; A. Cuoci; T. Faravelli; E. Ranzi, *Combustion and Flame* 160 (2013) 1168-1190.

152. C. Saggese; N.E. Sánchez; A. Frassoldati; A. Cuoci; T. Faravelli; M.U. Alzueta; E. Ranzi, *Energy & Fuels* 28 (2014) 1489-1501.

153. A. Violi; S. Yan; E. Eddings; A. Sarofim; S. Granata; T. Faravelli; E. Ranzi, *Combustion Science and Technology* 174 (2002) 399-417.

154. K. Brezinsky, *Progress in Energy and Combustion Science* 12 (1986) 1-24.

155. A.B. Lovell; K. Brezinsky; I. Glassman, *Symposium (International) on Combustion* 22 (1989) 1063-1074.

156. C. Venkat; K. Brezinsky; I. Glassman, *Symposium (International) on Combustion* 19 (1982) 143-152.

157. A. Marchal; M. Cathonnet; P. Dagaut; M. Reuillon; M. Audinet; G. Belot; J.-F. Béziau, Proceedings of the Joint Meeting of the French and German Sections of the Combustion Institute, Mulhouse, October 1995, pp 11–13.

158. J. Bittner; J. Howard in: *Composition profiles and reaction mechanisms in a near-sooting premixed benzene/oxygen/argon flame*, Symposium (International) on Combustion, 1981; Elsevier; pp 1105-1116.

159. F. Defoeux; V. Dias; C. Renard; P. Van Tiggelen; J. Vandooren, *Proceedings of the Combustion Institute* 30 (2005) 1407-1415.

160. B. Yang; Y. Li; L. Wei; C. Huang; J. Wang; Z. Tian; R. Yang; L. Sheng; Y. Zhang; F. Qi, *Proceedings of the Combustion Institute* 31 (2007) 555-563.

161. V. Detilleux; J. Vandooren, *Combustion, Explosion, and Shock Waves* 45 (2009) 392-403.

162. A. Laskin; A. Lifshit in: *Thermal decomposition of benzene. Single-pulse shock-tube investigation*, Symposium (International) on Combustion, 1996; Elsevier; pp 669-675.

163. J.H. Kiefer; W.A. Von Drasek, *International Journal of Chemical Kinetics* 22 (1990) 747-786.

164. C. Wu; H. Singh; R. Kern, *International Journal of Chemical Kinetics* 19 (1987) 975-996.

165. M. Colket III; D. Seery; H. Palmer, *Combustion and Flame* 75 (1989) 343-366.

166. N. Sánchez; A. Callejas; A. Millera; R. Bilbao; M. Alzueta, *Energy* 43 (2012) 30-36.

167. N.E. Sánchez; Á. Millera; R. Bilbao; M.U. Alzueta, *Journal of Analytical and Applied Pyrolysis* 103 (2013) 126-133.

168. H. Sabbah; L. Biennier; S.J. Klippenstein; I.R. Sims; B.R. Rowe, *The Journal of Physical Chemistry Letters* 1 (2010) 2962-2967.

169. M.J. Castaldi; N.M. Marinov; C.F. Melius; J. Huang; S.M. Senkan; W.J. Pit; C.K. Westbrook in: *Experimental and modeling investigation of aromatic and polycyclic aromatic hydrocarbon formation in a premixed ethylene flame*, Symposium (International) on Combustion, 1996; Elsevier; pp 693-702.

170. A. Cuoci; A. Frassoldati; T. Faravelli; H. Jin; Y. Wang; K. Zhang; P. Glarborg; F. Qi, *Proceedings of the Combustion Institute* 34 (2013) 1811-1818.

171. J. Roesler; S. Martinot; C. McEnally; L. Pfefferle; J.-L. Delfau; C. Vovelle, *Combustion and Flame* 134 (2003) 249-260.

172. A. Cuoci; A. Frassoldati; T. Faravelli; E. Ranzi, *Combustion and Flame* 160 (2013) 870-886.

173. A.L. Lafleur; K. Taghizadeh; J.B. Howard; J.F. Anacleto; M.A. Quilliam, *Journal of the American Society for Mass Spectrometry* 7 (1996) 276-286.

174. B. Zhao; K. Uchikawa; H. Wang, *Proceedings of the Combustion Institute* 31 (2007) 851-860.

175. M.M. Maricq, *Journal of Aerosol Science* 38 (2007) 141-156.

176. Ü.Ö. Köylü; C. McEnally; D. Rosner; L. Pfefferle, *Combustion and Flame* 110 (1997) 494-507.

177. R.I.A. Patterson; M. Kraft, *Combustion and Flame* 151 (2007) 160-172.

178. A. Goldaniga; L. Zappella; T. Faravelli; M. Dente; E. Ranzi in: *Reaction Classes and Lumping Criteria for the Extension of Detailed Kinetic Schemes to Heavy PAH*, Open meeting on Combustion - XXIII Event of the Italian Section of the Combustion Institute, Ischia (Italy), May 2000.

179. K.H. Homann; H.G. Wagner in: *Some new aspects of the mechanism of carbon formation in premixed flames*, Symposium (International) on Combustion, 1967; Elsevier; pp 371-379.

180. C. Russo; A. Tregrossi; A. Ciajolo, *Proceedings of the Combustion Institute* 35 (2014) 1803-1809.

181. M. Sirignano; M. Alfè; A. Tregrossi; A. Ciajolo; A. D'Anna, *Proceedings of the Combustion Institute* 33 (2011) 633-640.

182. J.P. Cain; J. Camacho; D.J. Phares; H. Wang; A. Laskin, *Proceedings of the Combustion Institute* 33 (2011) 533-540.

183. S. Stein; D. Golden; S.W. Benson, *The Journal of Physical Chemistry* 81 (1977) 314-317.

184. S.W. Benson; F. Cruickshank; D. Golden; G.R. Haugen; H. O'neal; A. Rodgers; R. Shaw; R. Walsh, *Chemical Reviews* 69 (1969) 279-324.

185. N. Cohen; S. Benson, *Chemical Reviews* 93 (1993) 2419-2438.

186. E.R. Ritter; J.W. Bozzelli, *International Journal of Chemical Kinetics* 23 (1991) 767-778.

187. E. Ranzi; M. Dente; T. Faravelli; G. Pennati, *Combustion Science and Technology* 95 (1993) 1-50.

188. A. Violi; T.N. Truong; A.F. Sarofim, *The Journal of Physical Chemistry A* 108 (2004) 4846-4852.

189. C. Cavallotti; D. Polino, *Proceedings of the Combustion Institute* 34 (2013) 557-564.

190. A. D'Anna; J. Kent, *Combustion and Flame* 144 (2006) 249-260.

191. J. Emdee; K. Brezinsky; I. Glassman, *The Journal of Physical Chemistry* 96 (1992) 2151-2161.

192. A. Goel; J.B. Howard, *Carbon* 41 (2003) 1949-1954.

193. M. Rapacioli; F. Calvo; F. Spiegelman; C. Joblin; D. Wales, *The Journal of Physical Chemistry A* 109 (2005) 2487-2497.

194. N.A. Fuks, *The mechanics of aerosols*, Dover Publications, 1964.

195. A. D'Alessio; A. Barone; R. Cau; A. D'Anna; P. Minutolo, *Proceedings of the Combustion Institute* 30 (2005) 2595-2603.

196. A. Raj; M. Sander; V. Janardhanan; M. Kraft, *Combustion and Flame* 157 (2010) 523-534.

197. M. Sander; R.H. West; M.S. Celnik; M. Kraft, *Aerosol Science and Technology* 43 (2009) 978-989.

198. N. Marinov; W. Pitz; C. Westbrook; A. Lutz; A. Vincitore; S. Senkan in: *Chemical kinetic modeling of a methane opposed-flow diffusion flame and comparison to experiments*, Symposium (International) on Combustion, 1998; Elsevier; pp 605-613.

199. International Sooting Flame (ISF) Workshop. http://www.adelaide.edu.au/cet/isfworkshop/data-sets/laminar/. (checked: 08/2014).

200. F. Xu; P. Sunderland; G. Faeth, *Combustion and Flame* 108 (1997) 471-493.

201. A.V. Menon; S.-Y. Lee; M.J. Linevsky; T.A. Litzinger; R.J. Santoro, *Proceedings of the Combustion Institute* 31 (2007) 593-601.

202. M. Tsurikov; K.P. Geigle; V. Krüger; Y. Schneider-Kühnle; W. Stricker; R. Lückerath; R. Hadef; M. Aigner, *Combustion Science and Technology* 177 (2005) 1835-1862.

203. A. Ciajolo; A. D'anna; R. Barbella; A. Tregrossi; A. Violi in: *The effect of temperature on soot inception in premixed ethylene flames*, Symposium (International) on Combustion, 1996; Elsevier; pp 2327-2333.

204. B. Apicella; R. Barbella; A. Ciajolo; A. Tregrossi, *Combustion Science and Technology* 174 (2002) 309-324.

205. V. Gururajan; F.N. Egolfopoulos; K. Kohse-Höinghaus, *Proceedings of the Combustion Institute* 35 (2015) 821-829.

206. N. Hansen; T.A. Cool; P.R. Westmoreland; K. Kohse-Höinghaus, *Progress in Energy and Combustion Science* 35 (2009) 168-191.

207. U. Struckmeier; P. Oßwald; T. Kasper; L. Böhling; M. Heusing; M. Köhler; A. Brockhinke; K. Kohse-Höinghaus, *Zeitschrift für Physikalische Chemie* 223 (2009) 503-537.

208. A. Cuoci; A. Frassoldati; T. Faravelli; E. Ranzi, *Combustion Science and Technology* 180 (2008) 767-784.

209. R.J. Kee; J.A. Miller; G.H. Evans; G. Dixon-Lewis in: *A computational model of the structure and extinction of strained, opposed flow, premixed methane-air flames*, Symposium (International) on Combustion, 1989; Elsevier; pp 1479-1494.

210. A. Gomez; D. Rosner, *Combustion Science and Technology* 89 (1993) 335-362.

211. M. Smooke; I. Puri; K. Seshadri in: *A comparison between numerical calculations and experimental measurements of the structure of a counterflow diffusion flame burning diluted methane in diluted air*, Symposium (International) on Combustion, 1988; Elsevier; pp 1783-1792.

212. A.D. Abid; N. Heinz; E.D. Tolmachoff; D.J. Phares; C.S. Campbell; H. Wang, *Combustion and Flame* 154 (2008) 775-788.

213. J. Camacho; C. Liu; C. Gu; H. Lin; Z. Huang; Q. Tang; X. You; C. Saggese; Y. Li; H. Jung; L. Deng; I. Wlokas; H. Wang, *Combustion and Flame* (2015).

214. W.L. Grosshandler, *RADCAL: A narrow-band model for radiation calculations in a combustion environment*, National Institute of Standards and Technology Gaithersburg, MD, 1993.

215. S. Sazhin, *An approximation for the absorption coefficient of soot in a radiating gas,* 1994.

216. TSI Incorporated. Aerosol Instrument Manager® Software for Scanning Mobility Particle Sizer™ (SMPS™) Spectrometer. http://www.tsi.com/.

217. B.E. Dahneke, *Journal of Aerosol Science* 4 (1973) 139-145.

218. P. Chan; B. Dahneke, *Journal of Applied Physics* 52 (1981) 3106-3110.

219. A.I. Medalia, *Journal of Colloid and Interface Science* 24 (1967) 393-404.

220. P. Meakin, *Advances in Colloid and Interface Science* 28 (1987) 249-331.

221. M. Eggersdorfer; S. Pratsinis, *Aerosol Science and Technology* 46 (2012) 347-353.

222. J. Camacho; H. Wang in: *Size Evolution of Soot Formed in Premixed C6 Hydrocarbon Flames*, Western States of the Combustion Institute Spring Meeting, Caltech, Pasadena, CA, March 24-25, 2014.

223. A. Tregrossi; A. Ciajolo; R. Barbella, *Combustion and Flame* 117 (1999) 553-561.

224. A. Ciajolo; A. Tregrossi; M. Mallardo; T. Faravelli; E. Ranzi, *Proceedings of the Combustion Institute* 32 (2009) 585-591.

225. C. Russo; F. Stanzione; A. Tregrossi; M. Alfè; A. Ciajolo, *Combustion and Flame* 159 (2012) 2233-2242.

226. A. Lamprecht; W. Eimer; K. Kohse-Höinghaus, *Combustion and Flame* 118 (1999) 140-150.

227. H.R. Zhang; E.G. Eddings; A.F. Sarofim, *Proceedings of the Combustion Institute* 31 (2007) 401-409.

228. K.V. Puduppakkam; A.U. Modak; C.V. Naik; J. Camacho; H. Wang; E. Meeks in: *A Soot Chemistry Model that Captures Fuel Effects*, ASME Turbo Expo 2014: Turbine Technical Conference and Exposition, Germany, June 16-20, 2014.

229. A.D. Abid; J. Camacho; D.A. Sheen; H. Wang, *Energy & Fuels* 23 (2009) 4286-4294.

230. E. Goudeli; M.L. Eggersdorfer; S.E. Pratsinis, *Langmuir* 31 (2015) 1320-1327.

231. C. Saggese; A. Frassoldati; A. Cuoci; T. Faravelli; E. Ranzi, *Proceedings of the Combustion Institute* 34 (2013) 427-434.

232. B. Franzelli; A. Cuoci; A. Stagni; C. Saggese; A. Frassoldati; T. Faravelli; M. Ihme in: *Accounting for strain-rate effect in soot modeling of turbulent flames*, 15th International Conference on Numerical Combustion, Avignon (France), April 19-22, 2015.

233. A. Cuoci. *Pollutant formation in turbulent reactive flows: interactions between chemistry and turbulence*. PhD Thesis, Politecnico di Milano 2008.

234. Columbia University. Conservation Equations. http://www.ldeo.columbia.edu/~mspieg/mmm/Conserveq.pdf. January 2015.

235. R.B. Bird; W.E. Stewart; E.N. Lightfoot, *Transport phenomena*, John Wiley & Sons, 2007.

236. T. Poinsot; D. Veynante, *Theoretical and Numerical Combustion*. (2005).

237. L. Talbot; R. Cheng; R. Schefer; D. Willis, *Journal of Fluid Mechanics* 101 (1980) 737-758.

238. T. Smith; Z. Shen; J. Friedman, *Journal of Heat Transfer* 104 (1982) 602-608.

Appendix A

Herein, the detailed derivation of the conservation equations used in the counterflow flame configuration is presented as adapted from [233], with an explanations of the different terms contributing to diffusivity and a brief overview on the radiative heat losses.

1. Conservation equations

Global conservation equations express the existing relation between incoming and outcoming fluxes of a given physical quantity, its generated and depleted amount and the cumulated one; they are written for a generic volume unit of the system.

The primitive and general form of these equations, referred to the time unit, is the following:

$$\begin{pmatrix} Cumulated\ amount \\ in\ the\ volume \\ in\ the\ time\ unit \end{pmatrix} = \begin{pmatrix} Resulting\ fluxes\ in\ the\ domain \\ through\ the\ boundary\ surface \\ by\ convection\ and\ diffusion \end{pmatrix} + \begin{pmatrix} total\ generated\ amount \\ inside\ the\ volume\ in\ the \\ time\ unit \end{pmatrix}$$

That, translated in a mathematical form becomes:

$$\frac{d}{dt}\int_V \phi\, dV = -\int_S \boldsymbol{Fl}\, d\boldsymbol{S} - \int_S \phi \boldsymbol{V}\, d\boldsymbol{S} + \int_V R\, dV$$

where d**S** is the vector normal to a small patch on the surface S and points outwards by convention, ϕ is a generic quantity (units of the quantity per unit volume) that can change within this volume.

Fl is the flux of ϕ in the absence of fluid transport, ϕ**V** is the transport flux (quantity per unit volume per unit time) and R is a source or sink of ϕ.

The negative signs in front of the surface integrals are present because a positive outward flux corresponds to a negative rate of change of the integral on the left [234].

Applying Gauss' theorem the surface integrals in the previous equation can be replaced:

$$-\int_S Fl\, d\boldsymbol{S} - \int_S \phi \boldsymbol{V}\, d\boldsymbol{S} = \int_V \nabla\,(\boldsymbol{Fl} + \phi \boldsymbol{V}) dV$$

Because V is of arbitrary shape and size and the surface and volume are fixed in an inertial frame then the above equation becomes:

$$\frac{\partial \phi}{\partial t} + \nabla\,(\boldsymbol{Fl} + \phi \boldsymbol{V}) - R = 0$$

The general concept can be applied to the fundamental balances, referring to the specific quantities for each balance.

Due to the axisymmetric geometry it is more convenient to write the conservation equations of mass, momentum, species and energy in cylindrical coordinates.

Conservation of mass

The principle of mass conservation states that the quantity of mass is conserved over time. To derive conservation of mass we just substitute ϕ = ρ (density), **Fl** = 0 (mass flux can only change due to transport) and R = 0 (mass cannot be created or destroyed) in the generic equation and the resulting equation is:

$$\frac{\partial \rho}{\partial x} + \nabla(\rho \boldsymbol{V}) = 0$$

This equation is often referred to as “the continuity equation”.

In cylindrical coordinates:

$$\frac{\partial \rho}{\partial t} + \frac{\partial}{\partial x}(\rho u) + \frac{1}{r}\frac{\partial}{\partial r}(r\, \rho v) = 0$$

where r is the radial coordinate and v is the radial velocity (Figure 5.13).

From the hypotheses that u and ρ depend on x only, it is possible to obtain:

$$\frac{1}{r}\frac{\partial}{\partial r}(r\, v) = 2f(x)$$

Integrating:

$$v = f(x)\, r$$

$$\frac{\partial v}{\partial r} = f(x) = \frac{v}{r}$$

Thus the radial velocity is a linear function of the radius with a coefficient that depends on the axial coordinate (x). Substituting in the continuity equation:

$$\frac{\partial \rho}{\partial t} + \frac{\partial}{\partial x}(\rho u) + 2\rho\frac{v}{r} = 0$$

Two functions are defined for convenience:

$$F(x) = \frac{\rho u}{2}$$

$$G(x) = -\frac{\rho v}{r}$$

So that the continuity equation becomes:

$$\frac{\partial \rho}{\partial t} = 2\left(G - \frac{\partial F}{\partial x}\right)$$

Conservation of momentum

Momentum is a vector field. In general momentum is m**V**, therefore the amount of momentum per unit volume is ϕ = ρ**V**. There are two kind of forces that can change the momentum: the stress that acts on the surface of the volume with local force **f** = **σ** d**S** that can also be thought as a flux of force **Fl** = **-σ** (the negative sign ensures that if the net force on the volume points in, the momentum increases) and the body forces, such as gravity, which act like a source of momentum; thus R = ρ**g**, where **g** is the net acceleration.

The equation for the momentum conservation becomes then:

$$\frac{\partial \rho \boldsymbol{V}}{\partial t} + \nabla\,(\rho \boldsymbol{V}\boldsymbol{V}) = -\nabla\, P + \rho \boldsymbol{g}$$

In the axial direction, as derived in "Transport phenomena [235]", the equation can be written as:

$$\rho \frac{Du}{Dt} = -\frac{\partial P}{\partial x} - \left(\frac{1}{r}\frac{\partial}{\partial r}(r\,\tau_{rx}) + \frac{\partial \tau_{xx}}{\partial x}\right)$$

where Du/Dt is the substantive derivative and the stress tensors are defined as:

$$\tau_{rx} = -\mu\left(\frac{\partial u}{\partial r} + \frac{\partial v}{\partial x}\right)$$

$$\tau_{xx} = -\mu\left(2\frac{\partial u}{\partial x} - \frac{2}{3}\nabla\vec{u}\right)$$

If we substitute these expressions and the functions above defined in the momentum equation in the axial direction we obtain:

$$\frac{\partial P}{\partial x} = -4F\frac{\partial}{\partial x}\left(\frac{F}{\rho}\right) - 2\mu\frac{\partial}{\partial x}\left(\frac{1}{\rho}\frac{\partial F}{\partial x}\right) + \frac{4}{3}\frac{\partial}{\partial x}\left[2\mu\frac{\partial}{\partial x}\left(\frac{F}{\rho}\right) + \nu\frac{\partial F}{\partial x}\right]$$

Similarly, in the radial direction:

$$\rho \frac{Dv}{Dt} = -\frac{\partial P}{\partial r} - \left(\frac{1}{r}\frac{\partial}{\partial r}(r\,\tau_{rr}) - \frac{\tau_{\theta\theta}}{r} + \frac{\partial \tau_{rx}}{\partial x}\right)$$

where the stress tensor components have the following expressions:

$$\tau_{rr} = -\mu\left(2\frac{\partial v}{\partial r} - \frac{2}{3}\nabla\vec{u}\right)$$

$$\tau_{\theta\theta} = -\mu\left(2\frac{v}{r} - \frac{2}{3}\nabla\vec{u}\right)$$

$$\tau_{rx} = -\mu\left(\frac{\partial u}{\partial r} - \frac{\partial v}{\partial x}\right)$$

The final form becomes:

$$\frac{1}{r}\frac{\partial P}{\partial r} = \frac{\partial}{\partial x}\left(\frac{2F}{\rho}\frac{\partial F}{\partial x}\right) - \frac{3}{\rho}\left(\frac{\partial F}{\partial x}\right)^2 - \frac{\partial}{\partial x}\left[\mu\frac{\partial}{\partial x}\left(\frac{1}{\rho}\frac{\partial F}{\partial x}\right)\right]$$

From the final forms of the conservation equations in the two directions it is evident that $\frac{\partial P}{\partial x}$ and $\frac{1}{r}\frac{\partial P}{\partial r}$ depend on the coordinate x only. This means that the only possibility is:

$$\frac{1}{r}\frac{\partial P}{\partial r} = H = const$$

H is an eigenvalue of the resulting system. After some rearrangements, the equation of conservation of momentum in the radial direction becomes:

$$\frac{\partial}{\partial x}\left[\mu\frac{\partial}{\partial x}\left(\frac{G}{\rho}\right)\right] - 2\frac{\partial}{\partial x}\left(\frac{FG}{\rho}\right) + \frac{3}{\rho}G^2 + H = 0$$

Conservation of species

For the species, the quantity ϕ is the mass of the species k ($\rho_k = \rho\,\omega_k$, where ω_k is the mass fraction). The flux **Fl** = 0 and the transport flux is due to convection and diffusion, hence $m\boldsymbol{V} = \rho_k\vec{u} + \overrightarrow{J_k}$, with $\overrightarrow{J_k}$ being the molecular diffusive flux of the k species. The source term $R = \dot{\Omega}_k$, where $\dot{\Omega}_k$ is the mass reaction rate per unit volume.

The mass conservation equation can be thus written as:

$$\frac{\partial}{\partial t}(\rho\omega_k) + \nabla(\rho\vec{u}\omega_k) = -\nabla\overrightarrow{J_k} + \dot{\Omega}_k \qquad k = 1 \dots N_s$$

where N_S is the number of species.

The molecular diffusive flux is usually written in terms of a diffusion velocity $\vec{V}_k$:

$$\overrightarrow{J_k} = \rho\omega_k\vec{V}_k$$

This diffusion velocity is the sum of three contributions that will be analyzed in detail later in the chapter.

The final form of the equation can be found by using the last expression and the definition of the variable F:

$$\rho\left[\frac{\partial\omega_k}{\partial t} + \frac{2F}{\rho}\frac{\partial\omega_k}{\partial x}\right] = -\frac{\partial}{\partial x}(\rho\omega_k V_k) + \dot{\Omega}_k \qquad k = 1 \dots N_s$$

Conservation of energy

For a single phase material, the amount of heat per unit volume is ϕ = $\rho C_P T$ where C_P is the specific heat at constant pressure and T is the temperature. The heat flux in the absence of transport is $\boldsymbol{Fl} = -\lambda\nabla T$, where λ is the thermal conductivity. The transport flux is $\rho C_P T\mathbf{V}$. Since the Mach number in the counterflow diffusion flames is very small, we neglect the terms associated to the viscous dissipation and to the pressure. Also the kinetic and potential energy can be neglected.
The source term is therefore the radiative heat flux $R = \dot{Q}$.

The simplest conservation of heat equation is:

$$\frac{\partial\rho C_P T}{\partial t} + \nabla\,(\rho C_P T\boldsymbol{V}) = \nabla\,\lambda\nabla T + \dot{Q}$$

Manipulating the equation considering also the mass conservation and the definition of variable F we obtain:

$$\rho\hat{C}_P\left[\frac{\partial T}{\partial t}+\frac{2F}{\rho}\frac{\partial T}{\partial x}\right]=\frac{\partial}{\partial x}\left[\lambda\frac{\partial T}{\partial x}\right]-\rho\sum_{k=1}^{N_S}\hat{C}_{P,k}\omega_k V_k\frac{\partial T}{\partial x}+\dot{Q}-\sum_{k=1}^{N_S}\widehat{H}_k\dot{\Omega}_k$$

$\widehat{H}_k$ is the specific enthalpy for the species k, so the term $R=\sum_{k=1}^{N_S}\widehat{H}_k\,\dot{\Omega}_k$ represents the heat released by combustion.

2. Diffusivity

As mentioned earlier, the molecular diffusion flux is usually expressed in terms of a diffusive velocity V_k, which is the sum of three contributions: Fick's, Soret's and thermophoretic's diffusion. It is interesting to analyze them to understand how differently they contribute to the species' transport.

Fick diffusivity

The first driving force for species diffusion is a concentration gradient. This is the dominant mode of transport. The diffusion velocities should be obtained by solving the system [236]:

$$\nabla X_P=\sum_{k=1}^{N_S}\frac{X_pX_k}{\Gamma_{pk}^{(m)}}\left(V_k-V_p\right)+\left(Y_p-X_p\right)\frac{\nabla P}{P}+\frac{\rho}{p}\sum_{k=1}^{N_S}Y_pY_k\left(f_p-f_k\right)\qquad for\ p=1\dots N_S$$

where $\Gamma_{pk}^{(m)}$ is the binary mass diffusion coefficient of the species *k* in species *p* and X_k is the mole fraction of species *k*.

This is a linear system of size N_S^2 which must be solved in each direction at each point and at each instant for unsteady flows. This is computationally very costly, but usually a simplified approach based on Fick's law is acceptable. According to Fick's law the diffusion velocity can be written as:

$$\omega_k\vec{V}_k^{(m)}=-\Gamma_{k,mix}^{(\mathrm{m})}\nabla\omega_k$$

with $\Gamma_{k,mix}^{(\mathrm{m})}$ mass diffusion coefficient of the species k in the mixture.

From this definition, it derives that the diffusive molecular flux is:

$$\overrightarrow{J_k}^{(m)} = -\rho\Gamma_{k,mix}^{(\mathrm{m})}\nabla\omega_k$$

As it can be noticed, Fick's diffusion depends on the species' mass fractions, since it is related to a composition gradient.

Soret diffusivity

The Soret effect is a phenomenon of mass diffusion in the presence of a temperature gradient, it acts sensibly only on species with a very small molecular mass (for example hydrogen). The hydrogen plays a fundamental role in the reactivity of the system, hence, if the hydrogen profile is modified, by consequence also the heavier species' profiles are modified and the soot production cannot be described properly.

The diffusive flux due to the Soret effect is defined analogously to the Fick one:

$$\overrightarrow{J_k}^{(T)} = -\rho\Gamma_{k,mix}^{(\mathrm{T})}\nabla lnT$$

where $\Gamma_{k,mix}^{(\mathrm{T})}$ is the thermal diffusion coefficient of the species k into the mixture.

Thermophoretic diffusion

Thermophoresis is the term describing the phenomenon wherein small particles, such as soot particles, suspended in a gas characterized by a temperature gradient ∇T, drift in the direction opposite to that of ∇T. It can be seen as a particular case of the Soret effect acting on aerosols. Therefore, also the expression of the thermophoretic diffusive flux reflects this similarity and it is defined as:

$$\overrightarrow{J_k}^{(Th)} = -\rho\Gamma_{k,mix}^{(\mathrm{Th})}\nabla lnT$$

The only difference with respect to the Soret flux lies in the definition of the thermophoretic diffusion coefficient of the species k into the mixture, $\Gamma_{k,mix}^{(\mathrm{Th})}$.

Assuming spherical particles in free molecular regime (Kn_p >>1), which is the case of soot particles, the thermophoretic diffusivity (D_T) can be expressed as [237]:

$$D_T = \left(\frac{3}{4}\right)\left[1 + \left(\frac{\pi}{8}\alpha\right)\right]^{-1} \nu$$

where:

- α, the momentum accommodation coefficient, can be set equal to unity.
- ν is the momentum diffusivity (kinematic viscosity) of the prevailing gas mixture.

The thermophoretic velocity becomes then:

$$\vec{V}_k^{(Th)} = -0.538\,\nu\frac{\nabla T}{T}$$

As shown by the formulas, the thermophoretic velocity does not depend on particles size.

3. Radiative heat losses

In the energy conservation equation the term $\dot{Q}$ represents the radiative heat loss from the flame to the environment and it can be seen as the gradient of a heat flux vector:

$$\dot{Q} = -\nabla \boldsymbol{q^{rad}}$$

An optically thin radiation model is used to represent the gas phase. For the mixtures here considered, it is assumed that the only significant radiating species are H_2O, CO, CO_2 and CH_4. In the optically thin model the self-absorption is neglected, hence the divergence of the net radiative flux can be written as:

$$\nabla \boldsymbol{q^{rad}} = -4\sigma a_g (T^4 - T_{env}^4)$$

where σ is the Stefan-Boltzmann constant and T_{env} the environment temperature.

The Planck mean absorption coefficient a_P is evaluated according to the following expression:

$$a_g = p_{H_2O} a_{P,H_2O} + p_{CO_2} a_{P,CO_2} + p_{CO} a_{P,CO} + p_{CH_4} a_{P,CH_4}$$

where p_k is the partial pressure of species *k*. The extinction coefficient $a_{P,k}$ of species *k* is derived from calculations performed by the RADCAL software [172, 214].

In sooty flames, the radiation absorption coefficient has to include the effect of soot concentration. The absorption coefficient of a mixture of soot and an absorbing gas is calculated as the sum of the absorption coefficients of pure gas and pure soot:

$$a_{s+g} = a_g + a_s$$

Where a_g is the absorption coefficient of gas without soot calculated as explained above and the absorption coefficient of pure soot is:

$$a_s = b_1 \rho_m [1 + b_T (T - 2000)]$$

with $b_1 = 1232.4$ m^2/kg and $b_T \approx 4.8\ 10^{-4}$ K^{-1}. ρ_m is the soot density.

The coefficients b_1 and b_T result from a fitting [215] of the soot absorption coefficient to data based on the Taylor-Foster approximation and data based on the Smith et al. approximation [238]. This model is similar to the one implemented in FLUENT.

Appendix B

Experimental uncertainties: interpretation of temperature measurements

Interestingly, earlier measurement on the same benchmark flame [53] yielded different results from the latest measurements [213] especially in the early stage of the soot formation process. As compared in Figure 5.19, the nucleation burst occurs substantially later in the data report by Abid et al. [53]. The spatial offset is roughly 0.15 cm. The final volume fraction and number density are however the same in both studies. This discrepancy clearly deserves an explanation especially in light of the agreement across all facility and the fact that the current Stanford measurements [213] also used the same 7.6-cm burner as in the old measurement [53].

After a concerted study that eliminated many possible causes, one explanation stands out as our final conclusion. That is, the porous plug of the burner must have changed its pore density distribution after a lengthy use during the period of experiments of [53]. To illustrate this problem, we first plot in Figure B1 the radial temperature distributions determined at a distance of 0.18 cm from the burner surface with H_p = 1.0 cm.

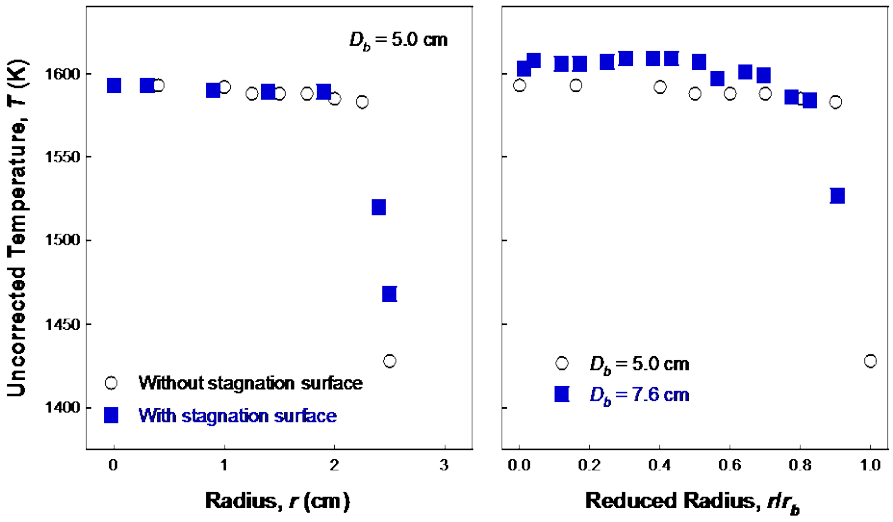

Figure B1. Radial profile of the uncorrected temperature measured at a distance of 0.18 cm from the burner surface for the burner-to-stagnation separation H_p = 1.0 cm, comparing with or without the probe (stagnation surface) (left panel) and for two burner sizes (right panel). The measurement was done at Stanford University.

The left panel of the plot examines the potential impact of the stagnation surface on the radial temperature profile for the 5.0-cm burner. It is seen that the temperature stays roughly a constant until it reaches the edge of the flame, as expected, and that the stagnation surface does not impact the temperature in the radial direction. The right panel shows that the 7.6-cm burner exhibits the same behavior and that the two burners generated flames of temperature that are within 10 K of each other. Suffice to note that the measurements shown were made when the porous plugs in both burners were relatively fresh, and the radial temperature variation seen in Figure B1 is an indicator that the burner is operated properly. Two specific issues can occur when the burner is not operated properly and/or the porous plug is aged due to repeated use. Neither can be detected visually. The problem is best detected by examining the radial temperature distribution in the main flame zone.

As Figure B2 shows, how the porous plug form a tight fit with burner body can impact the radial temperature distribution and thus the centerline temperature.

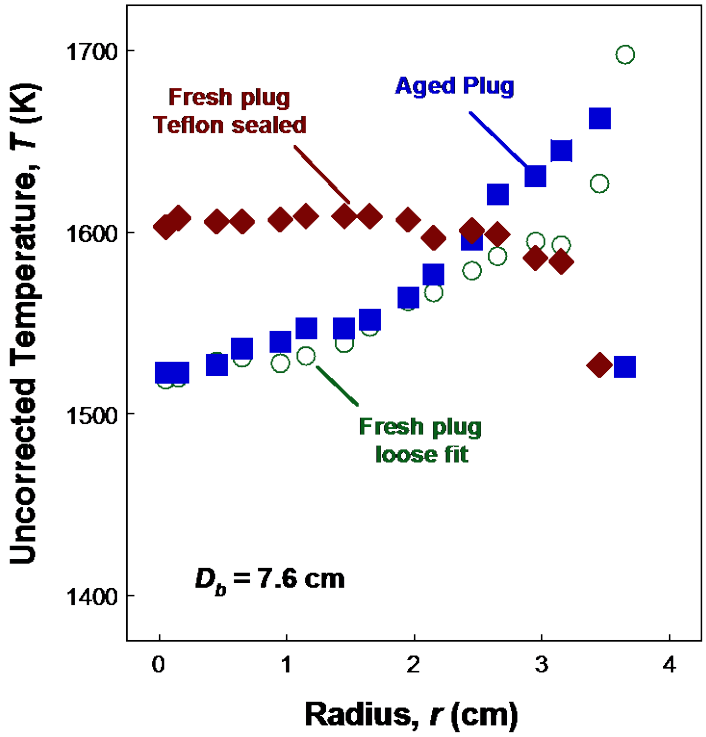

Figure B2. Radial profile of the uncorrected temperature measured at a distance of 0.18 from the burner surface for H_p = 1.0 cm, comparing an aged porous plug, a fresh but loose-fitting porous plug and the same fresh porous plug with edges sealed with Teflon tape.

Loose fits create bad seal, causing the unburned gas to flow preferentially near the plug rim, a non-uniform distribution of enthalpy rate and a lower temperature along the center of the flame than the edge. As shown in the same figure, the problem is removed when a tight seal is achieved with Teflon tape wrapped around the circumference of the porous plug. The second problem is more difficult to detect, but it yields the same result as a loosely fit porous plug: as the porous plug ages the repeated heating and cooling causes the center of the plug to contract and the outer edge to expand. The smaller pore sizes of the plug center produce a smaller local flow rate and thus enthalpy injection rate, which again leads to a lower temperature along the centerline of the flame and a higher temperature towards the flame edge, as shown in Figure B2. The centerline temperature measured by Abid et al. [53] is nearly identical to those of the current study (Figure 5.14). The probe sampling/SMPS analysis of that study was done after the temperature measurement was complete. Therefore, either the porous plug was aged or it was not properly mounted when they carried out the SMPS experiment. The lower centerline temperature that resulted causes the soot to nucleate later in the flame and produced the differences in the f_v and N

profiles seen in Figure 5.18. The lesson learned here indicates that for all experiments that use a flat flame burner, the uniformity of the radial temperature should be checked routinely to ensure the flame is actually flat. Presently, it is unclear whether the porous plug in the McKenna burner exhibits the same aging behavior.